UNIVERSIDADE ESTADUAL DE CAMPINAS

Faculdade de Engenharia Química

JOSIEL MARTINS COSTA

DESENVOLVIMENTO DE ELETROCATALISADORES DE Co-W, Ag-Co E Zn-Co
PARA REAÇÕES DE REDUÇÃO / EVOLUÇÃO DE OXIGÊNIO EM BATERIAS DE
Li-O$_2$ E Zn-AR

DEVELOPMENT OF Co-W, Ag-Co, AND Zn-Co ELECTROCATALYSTS FOR OXYGEN
REDUCTION / EVOLUTION REACTIONS IN Zn-AIR AND Li-O$_2$ BATTERIES

CAMPINAS

2020

JOSIEL MARTINS COSTA

DEVELOPMENT OF Co-W, Ag-Co, AND Zn-Co ELECTROCATALYSTS FOR OXYGEN REDUCTION / EVOLUTION REACTIONS IN Zn-AIR AND Li-O$_2$ BATTERIES

DESENVOLVIMENTO DE ELETROCATALISADORES DE Co-W, Ag-Co E Zn-Co PARA REAÇÕES DE REDUÇÃO / EVOLUÇÃO DE OXIGÊNIO EM BATERIAS DE Li-O$_2$ E Zn-AR

Tese de doutorado apresentada à Faculdade de Engenharia Química da Universidade Estadual de Campinas como parte dos requisitos exigidos para a obtenção do título de Doutor em Engenharia Química.

Thesis presented to the Faculty of Chemical Engineering of the University of Campinas in partial fulfillment of the requirements for the degree of Doctor in Chemical Engineering.

Orientador: PROF. DR. AMBRÓSIO FLORÊNCIO DE ALMEIDA NETO

ESTE TRABALHO CORRESPONDE À VERSÃO FINAL DA TESE DEFENDIDA PELO ALUNO JOSIEL MARTINS COSTA E ORIENTADO PELO PROF. DR. AMBRÓSIO FLORÊNCIO DE ALMEIDA NETO.

CAMPINAS

2020

Ficha catalográfica
Universidade Estadual de Campinas
Biblioteca da Área de Engenharia e Arquitetura
Rose Meire da Silva - CRB 8/5974

Informações para Biblioteca Digital

FOLHA DE APROVAÇÃO

Tese de doutorado defendida por JOSIEL MARTINS COSTA, aprovado em 27 de novembro de 2020, pela banca examinadora constituída pelos professores doutores:

Prof. Dr. Ambrósio Florêncio de Almeida Neto – Presidente e Orientador
(FEQ/UNICAMP)
Videoconferência

Profa. Dra. Mariana Conceição da Costa
(FEQ/UNICAMP)
Videoconferência

Prof. Dr. Rubens Maciel Filho
(FEQ/UNICAMP)
Videoconferência

Prof. Dr. Marcelino Luiz Gimenes
(DEQ/UEM)
Videoconferência

Profa. Dra. Vanessa de Freitas Cunha Lins
(DEQ/UFMG)
Videoconferência

A Ata da defesa com as respectivas assinaturas dos membros encontra-se no SIGA/Sistema de Fluxo de Dissertação/Tese e na Secretaria do Programa da Unidade.

ACKNOWLEDGMENT

RESUMO

Conhecidas pela elevada energia específica teórica, as baterias de lítio-ar compreendem uma tecnologia atrativa para o armazenamento de energia elétrica e podem tornar os veículos elétricos amplamente acessíveis. Adicionalmente, as baterias de Zn-ar possuem aplicações no setor médico e de telecomunicações, como aparelhos auditivos em miniatura e dispositivos de mensagens sem fio. Ambas as tecnologias exigem catodos de ar para acelerar as lentas taxas de reações de redução (descarga) e evolução (carga) de O_2. Apesar dos esforços dos pesquisadores, os eletrocatalisadores atuais carecem de atividade e estabilidade suficientes. Nesse contexto, esta tese propôs avaliar os parâmetros envolvidos na eletrodeposição de catalisadores bimetálicos e na ciclagem da bateria de $Li-O_2$. No estudo com Co-W foram avaliados a influência da densidade de corrente elétrica e da concentração de W na eletrodeposição em espuma de níquel e malha de aço com posterior aplicação na bateria de $Li-O_2$. O estudo com Ag-Co propôs avaliar a influência da densidade de corrente elétrica e pressão de O_2 durante a ciclagem na bateria de $Li-O_2$. Para Zn-Co, foi proposto avaliar a influência da temperatura do banho eletrolítico e da velocidade de rotação catódica durante a eletrodeposição e como essa configuração impactava na ciclagem dos eletrodos na células de $Li-O_2$. No sistema de Zn-ar foram avaliados como o pH da solução de W-Co e o tempo de eletrodeposição influenciavam a eficiência da bateria. A análise estatística para a eletrodeposição de Co-W demonstrou que maiores concentrações de W e densidade de corrente elétrica aumentaram a eficiência de eletrodeposição, no entanto as quantidades de depósito nos substrato não se mostraram benéficas para o sistema de $Li-O_2$. Para a eletrodeposição de Ag-Co, a pressão de O_2 de 2 atm e densidade de corrente elétrica de 50 $\mu A\ cm^{-2}$ na bateria de $Li-O_2$ apresentaram os maiores valores de capacidade de descarga, sendo 336 mAh g^{-1}_c (malha de aço) e 115 mAh g^{-1}_c (espuma de níquel). Os eletrodos contendo Zn-Co apresentaram resultados benéficos para a reação de evolução de oxigênio, de acordo com o valores obtidos por voltametria cíclica de voltametria de varredura linear. Para o substrato de espuma de níquel a temperatura de 70 °C e velocidade de rotação catódica de 100 rpm demonstrou o maior valor de capacidade de carga, sendo de 182 mAh g^{-1}_c. Para a malha de aço os parâmetros a 25 °C e 30 rpm forneceu uma capacidade de carga de 399 mAh g^{-1}_c. Para o estudo com Co-W em baterias de Zn-ar, o tempo de eletrodeposição de 15 min e pH do banho eletrolítico com valor de 7.5 proporcionou eficiência próxima de 60% a 20 mA cm^{-2}, sendo um excelente eletrocatalisador bifuncional para ambas

as reações de O_2 com resultado superior ao catalisador comercial de Pt-Ru. A análise de energia dispersiva de raios-X demonstrou que W foi solubilizado durante a ciclagem na bateria de Zn-ar e pelo microscópio eletrônico de transmissão foi verificado que houve a formação de uma estrutura de espinélio de $ZnCo_2O_4$, devido a presença de Zn na composição do eletrólito.

Palavras-chave: Armazenamento de energia; Eletrodeposição; Baterias; Eletrólitos; Catalisadores.

ABSTRACT

Known for their high theoretical specific energy, lithium-air batteries comprise an attractive technology for storing electric energy that can make electric vehicles widely accessible. Additionally, Zn-air rechargeable batteries have medical and telecommunication applications such as miniature hearing aids and wireless messaging devices. Both technologies require air cathodes to accelerate slow rates of O_2 reduction (discharge) and evolution (charge) reactions. Despite the researchers' efforts, current electrocatalysts lack sufficient activity and stability. In this context, this thesis proposed to evaluate the parameters involved in the electrodeposition of bimetallic catalysts and in the Li-O_2 battery cycling. In the Co-W study, the influence of electric current density and W concentration on the electrodeposition in nickel foam and steel mesh was evaluated with subsequent application on the Li-O_2 battery. The Ag-Co study proposed to evaluate the influence of electric current density and O_2 pressure during cycling on the Li-O_2 battery. For Zn-Co, it was proposed to evaluate the influence of electrolytic bath temperature and cathodic rotation speed during electrodeposition and how this configuration impacted the cycling in Li-O_2 cell. In the Zn-air system were evaluated how the pH of the W-Co solution and the electrodeposition time influenced the battery efficiency. Statistical analysis for Co-W electrodeposition demonstrated that higher W concentrations and electric current density increased the electrodeposition efficiency, however the amount of deposition on the substrates was not beneficial for the Li-O_2 system. For the electrodeposition of Ag-Co, the O_2 pressure of 2 atm and electrical current density of 50 μA cm^{-2} in the Li-O_2 battery presented the highest discharge capacity values, being 336 mAh g^{-1}$_c$ (steel mesh) and 115 mAh g^{-1}$_c$ (nickel foam). The electrodes containing Zn-Co showed beneficial results for the oxygen evolution reaction, according to the values obtained by linear scanning voltammetry and cyclic voltammetry. For the nickel foam substrate the temperature of 70 °C and cathodic rotation speed of 100 rpm showed the highest load capacity value, being 182 mAh g^{-1}$_c$. For the steel mesh the parameters at 25 °C and 30 rpm provided a charge capacity of 399 mAh g^{-1}$_c$. For the study with Co-W in Zn-air batteries, the electrodeposition time of 15 min and pH of the electrolytic bath with a value of 7.5 provided efficiency close to 60% at 20 mA cm^{-2}, being an excellent bifunctional electrocatalyst for both O_2 reactions with better results than the commercial Pt-Ru catalyst. Energy dispersive X-ray showed that W was solubilized during cycling in the Zn-air battery

and by transmission electron microscope it was verified that a spinel structure of $ZnCo_2O_4$ was formed due to the presence of Zn in the electrolyte composition.

LIST OF FIGURES

LIST OF TABLES

SUMMARY

CHAPTER 1

General Introduction, Justification, Objectives and Thesis Structure

1. 1. General Introduction

With the increase of population income, the automobile industry is experiencing numerous sales of vehicles composed of internal combustion engine, which consume fossil fuels and emit harmful gases to the environment such as carbon oxides, hydrocarbons and nitrogen oxides (TIE; TAN, 2013). In order to overcome environmental and energy issues, electric vehicles have been developed in recent years, however, they are less accessible to the population due to the high cost. Electric vehicles provide a significant improvement in fuel cost savings and contribute against the emission of greenhouse gases. Electric cars can be fully electric or battery powered cars that are powered by one or several electric motors and extract their propulsion energy from only one electric battery. Plug-in hybrid cars are vehicles that: (1) are equipped with an internal combustion engine and one or multiple electric motors, (2) extract their fuel propulsion energy and / or electricity, and (3) may be charged from an external source of electricity (WEISS; ZERFASS; HELMERS *et al.*, 2019).

The rechargeable Li-air battery is considered one of the most promising technologies for electric vehicles due to its high theoretical specific energy (over 3500 Wh kg^{-1}), which could allow a longer driving distance (greater than 300 miles). The Zn-air battery has the advantages of low cost, excellent safety, environmentally friendly properties and flexibility with theoretical specific energy of 1350 Wh kg^{-1}, approximately three times higher than current Li-ion batteries (PARK; PARK; NAM; LEE *et al.*, 2015).

The issue related to decreased efficiency in the Li-O$_2$ system is due to the overpotential generated after the discharge, which impairs the kinetics of the O$_2$ reactions, which is caused by the irreversibility of the formed discharge product (usually Li$_2$O$_2$). Discharge product, if not decomposed, may clog the air electrode pores after a few discharge and charge cycles, impairing battery performance (FREUNBERGER; CHEN; DREWETT; HARDWICK *et al.*, 2011; FREUNBERGER; CHEN; PENG; GRIFFIN *et al.*, 2011). Dendrite formation, which is a limiter for Li-O$_2$ batteries is also a limiter for Zn-air batteries. Zinc oxide solid powder that acts as an insulator leads to dendrite formation, affecting Zn-air cell charge-discharge cycles (LEE; TAI KIM; CAO; CHOI *et al.*, 2011). Experimental research has shown that the use of additives such as potassium fluoride and surfactants may inhibit zinc dendrite growth (LAN; LEE; CHIN, 2007).

In order to achieve high efficiency and cycle stability, metal electrocatalysts are introduced into the metal-air battery cathode. Electrocatalysts can be deposited by several

techniques, such as electroplating (XIONG; IVEY, 2018), sonochemical (ANGELUCCI; D'VILLA SILVA; NART, 2007), sol-gel (HU; CHEN; XIA, 2014), ultrasonic (RONG; JIANG; SARNEY; CHU, 2010), co-reduction (XU; SONG; LIU; ZHANG *et al.*, 2018), among others. The electroplating stands out and presents as advantages: (1) fast deposition speed, (2) profitability and (3) simplicity of control over the thickness of metallic films. The morphology and properties of coatings can be adjusted by electrolyte composition (solution types, metal salt concentration and additives) or by electrochemical parameters including deposition potential and electric current density (LIU; DENG; HAN; HU *et al.*, 2016; SIMKA; PUSZCZYK; NAWRAT, 2009).

Transition metal oxides have been considered an alternative to conventional noble metal electrocatalysts for air battery applications due to reasonable activity and alkaline electrolyte stability, low cost and wide availability (YUAN; WU; XIE; LOU, 2014). Among them, MnO_x has a relevant catalytic activity for the O_2 reduction reaction in the non-aqueous Li-air system (CHENG; SCOTT, 2010) and Zn-air (XIONG; CLARK; LABBE; IVEY, 2018). The reduction reaction activity is mainly related to the occupation of the s* orbital and the extent of oxygen transition metal covalence at site B, which serves as a descriptor of secondary activity[1] (SUNTIVICH; GASTEIGER; YABUUCHI; NAKANISHI *et al.*, 2011). Hybridization affects performance and in order to improve it, multivalence transition metals, e.g. cobalt, are used as electrocatalysts (XIONG; IVEY, 2017).

Silver nanoparticles supported on reduced graphene oxide embedded in cobalt and nitrogen had detachable catalytic activity for oxygen reduction reaction (QASEEM; CHEN; WU; ZHANG *et al.*, 2017). The electrocatalyst showed platinum-like activity and superior stability in an alkaline environment, providing an excellent specific capacity of 789 mAh g^{-1}_{Zn} with an energy density of 947 Wh Kg^{-1} at a current density of 20 mA cm^{-2} at a Zn-air battery. Zn-Co electrocatalysts have also been applied to O_2 reduction reactions (LU; WANG; HU; LIU *et al.*, 2019). Coordinated Zn-Co atomic pairs on nitrogen-doped carbon support exhibited good performance under alkaline and acidic conditions, with a maximum power density of 230 mW cm^{-2}. In this context, this thesis proposes to study the influence of electrodeposition and cycling parameters in different cobalt-based electrocatalysts for application in Li-O_2 and Zn-air systems aiming at high system efficiency and stability.

---

[1] The transition metals present in the electrode surface control the ORR steps due to their electronic structure that allows the control of the catalytic activity. The study reflects the influences of s* orbital and metal-oxygen covalence on the competition between O_2^{2-}/OH^- displacement and OH^- regeneration on surface transition metal ions as limiting steps of ORR.

1.2. Justification

The purpose of this thesis was to use electrodeposition, a simple technique capable of depositing active material on substrates, making them suitable for application in $Li-O_2$ and Zn-air batteries by controlling operating parameters that modify several characteristics, like morphology, composition and catalytic activity.

Commercial Pt-Ru and IrO_2 electrocatalysts are known for their high catalytic activity, good retention, and cycle stability. However, they are expensive, as are Au-based electrocatalysts.

Therefore, the justification for this thesis was to consider cobalt-based electrocatalysts with other metals, such as W, Ag, and Zn to become a viable alternative to conventional electrocatalysts. Especially the application of the Co-W electrocatalyst, which is not addressed in the literature with applications for catalysis of oxygen evolution and reduction reactions.

The prospect is that in future these electrocatalysts will be applied in the development and technology of electric vehicles.

1.3. Objectives

1.3.1. General Objective

This thesis proposed the evaluation of the electrodeposition of tungsten, silver and zinc cobalt binary alloys in three different substrates (nickel foam, steel mesh, and carbon), and the characterization of these alloys, aiming at their applications as catalysts in $Li-O_2$ and Zn-air batteries.

1.3.2. Specific Objectives

The research involved electrodeposition assays, physicochemical characterization and catalytic activity of electrocatalysts, $Li-O_2$ and Zn-air battery charge and discharge assays, and electrochemical impedance spectroscopy analysis, according to the following specific objectives:

• To perform tungsten, silver or zinc cobalt electroplating testing for two types of substrates, nickel foam and steel mesh

• To characterize Co-W, Ag-Co and Zn-Co alloys by Scanning Electron Microscope (SEM) with chemical analysis by X-ray Dispersive Energy (EDX) and X-ray Diffraction (XRD)

• To characterize the discharge products with Raman spectroscopy

• To evaluate the catalytic activity of electrocatalysts by cyclic voltammetry (CV) and linear sweep voltammetry (LSV)

• Indirectly to estimate the electrochemically active surface area through electrical double layer capacitance (DLC)

• To evaluate charging and discharging performance on Li-O_2 and Zn-air batteries by varying cathode electrodeposition and cycling parameters

• To determine the most effective electrocatalyst for the Zn-air battery and perform carbon electroplating tests

• To characterize the W-Co electrocatalyst by Transmission Electron Microscopy (TEM) and Field Emission Scan Electron Microscopy (FESEM)

• To evaluate the interfacial changes that occur on the Zn-air battery cathode electrode using the Electrochemical Impedance Spectroscopy (EIS) technique

1.4. Thesis Structure

The steps of this thesis are presented in 8 chapters. In **Chapter 1 - General Introduction, Justifications, Objectives and Thesis Structure** were presented in detail the theme of the thesis, the justification, the proposed objectives and the steps for its realization. Figures 1.1 and 1.2 highlights the procedures developed in each chapter and the stage of the thesis. Li-O_2 battery-related experiments were developed at UNICAMP, LabPEA (Laboratory of Electrochemical Processes and Anticorrosion). The experiments involving Zn-air batteries were conducted at the University of Alberta at the Donadeo Innovation Centre for Engineering.
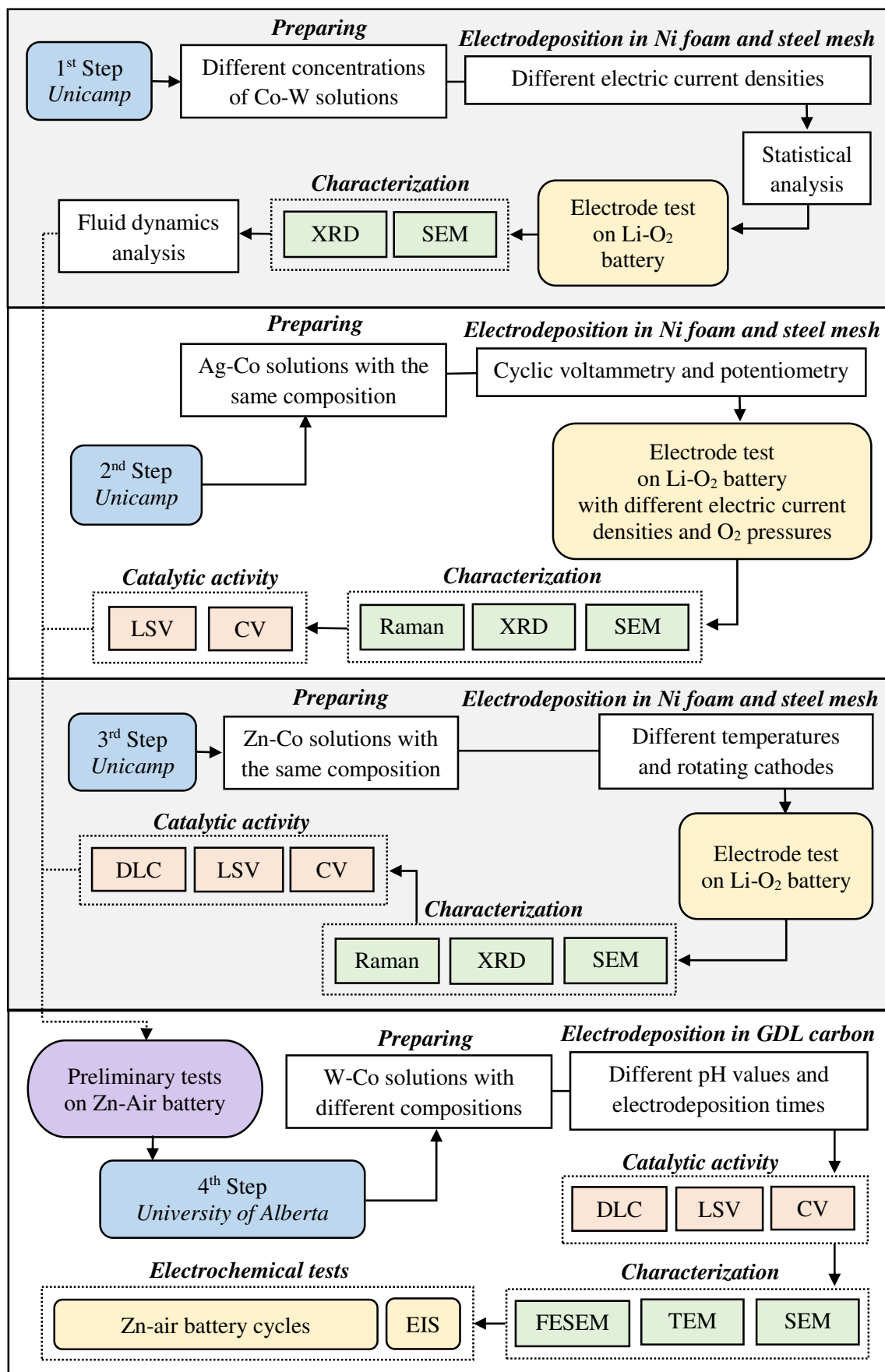
Figure 1.1. Flowchart of the proposals performed in this thesis.

1 **Introduction, justification, objectives and thesis structure**

To present the main theme

To justify the theme of the thesis

To present the research objectives

To present the thesis sctructure

2 **Literature review**

To introduce $Li-O_2$ and Zn-air battery concepts

To report challenges related to $Li-O_2$ and Zn-air batteries

To address the electrocatalysts used in O_2 evolution / oxidation reactions in $Li-O_2$ and Zn-air batteries

3 **Co-W electroplating**

To deposit Co-W on nickel foam and steel mesh

To discuss the influence of electric current density and W concentration on Co-W electrodeposition

To carry out electrode cycling in the $Li-O_2$ battery

4 **Ag-Co electroplating**

To deposit Ag-Co on nickel foam and steel mesh

To discuss the effect of O_2 pressure and electric current density during cycling in the $Li-O_2$ battery

To demonstrate Ag-Co catalytic activity

THESIS STRUCTURE

To deposit Zn-Co on nickel foam and steel mesh

To discuss the influence of solution temperature and rotating cathode on Zn-Co electrodeposition

To evaluate Zn-Co catalytic activity

Zn-Co electroplating **5**

To evaluate the electrodes on the Zn air battery

To verify the influence of pH and electrodeposition time on W-Co oxide deposition

To present the memory of the doctorate period

To suggest perspectives for future work

To display the research findings

Conclusions, suggestions and memory of the doctorade period **8**

To perform a general analysis of the results

General discussion **7** **6** **W-Co oxide electroplating**

Figure 1.2. Representation of the chapters approach in this thesis.

In **Chapter 2 - Literature Review - Electrocatalysts for Li-O$_2$ and Zn-air batteries**, the trends of electrocatalysts used in energy storage systems are contextualized. The chapter reports the basic composition of a Li-O$_2$ and Zn-air battery, the challenges regarding these technologies, and the importance of battery development for electric vehicles and the environment. Several high-performance electrocatalysts compositions have been shown over the last 10 years, emphasizing that the research area is in broad development, looking for innovative and efficient solutions.

In **Chapter 3 - Co-W electroplating for Li-O$_2$ battery application**, the influence of electric current density and tungsten concentration on Co-W electrodeposition on steel mesh and nickel foam substrates is reported. The objective of applying Co-W bimetallic alloy as an electrocatalyst in Li-O$_2$ batteries arose from studies by the research group, which studied the alloy's application as an anti-corrosion coating. The article reports a statistical analysis involving the electrodeposition parameters, the alloy characterization, a fluid-dynamic analysis, and the electrodes' application in the Li-O$_2$ battery, in need of improvement for more effective cycling.

In **Chapter 4 - Ag-Co electroplating for Li-O$_2$ battery application** the influence of O$_2$ pressure and the applied electrical current density during cycling is studied. The cycled electrodes were characterized by relation and morphology and composition, exhibiting the presence of AgCoO$_2$. The article shows that the steel mesh electrodes presented more effective maximum discharge capacities than the nickel foam substrate. The cyclic voltammetry and linear sweep voltammetry techniques showed the catalytic activity of Ag-Co when compared to the pure substrate.

Chapter 5 - Zn-Co electroplating for Li-O$_2$ battery application is a study of the influence of cathodic rotation and solution temperature on the Zn-Co electrodeposition on steel mesh and nickel foam substrates. Consequently, these electrodes influenced the cycling results in the Li-O$_2$ battery. The article addresses the morphological characterization and composition of the electrodes after cycling, showing the presence of Zn$_{21}$Co$_5$ and Co$_3$O$_4$. Catalytic activity is demonstrated by cyclic voltammetry and linear sweep voltammetry. The found electric double layer capacitance for nickel foam (3.10 mF cm^{-2}) and steel mesh 1.34 (mF cm^{-2}) compared to the null value of non-deposited substrate, demonstrated an estimate of electrochemically active surface area for these materials. The maximum load capacity was obtained using steel mesh, proving appropriate for the O$_2$ evolution reaction.

Chapter 6 - W-Co oxide electrodeposition for Zn-air batteries application reports the influence of W and Co ratio, annealing at 300 °C, solution pH, and electrodeposition time on the catalytic activity of the electrodes. The article discusses the characterization of W-Co oxide deposition on carbon, demonstrating that the catalytic activity also occurred due to $ZnCo_2O_4$ nanoparticles formed during cycling. Cycling tests lasting 50 h presented the electrocatalyst's excellent activity and stability against the O_2 reduction and evolution reaction.

Chapter 7 - General Discussion broadly addresses the results obtained during the doctorate period, bringing relevant discussions from Chapter 2 to 6.

Chapter 8 - Conclusions, suggestions, and memory of the doctoral period are presented the main conclusions of the thesis, suggestions for future research in search of results, and discoveries that provide advances in research. The doctorate period's memory listed the activities performed by the doctoral student, such as courses attended and teaching internships. Listed are bibliographic production, such as book chapters, expanded abstract, articles published, submitted, and in partnership with the LabPEA research group.

Appendix A presents the electrodeposition and cycling parameters of chapters 3, 4, 5, and 6.

Appendix B presents an expanded abstract published in the Proceedings of the International Congress on Chemical Reaction Engineering in Mexico.

Appendix C discusses the effect of electric current density and forced convection on the Zn-Fe-Mo ternary alloy electrodeposition. The article is the result of the co-orientation of an undergraduate student (July/2017 to June/2018).

Appendix D presents an article about the effect of Co and W concentration on the anticorrosion properties of Co-W alloys.

Appendix E presents a review published on the use of ultrasound on the coating electrodeposition process.

Appendix F brings a review addressing supercritical carbon dioxide technology for the synthesis of nanocatalysts with applications in energy storage systems.

Appendix G presents a chapter book published on the influence of operating parameters on the electrodeposition process of the Ni-Co-W ternary alloy.

Attachments are the copyright-related publications in this thesis.

References

ANGELUCCI, C. A.; D'VILLA SILVA, M.; NART, F. C. Preparation of platinum–ruthenium alloys supported on carbon by a sonochemical method. **Electrochimica Acta**, 52, n. 25, p. 7293-7299, 2007/09/01/ 2007.

CHENG, H.; SCOTT, K. Carbon-supported manganese oxide nanocatalysts for rechargeable lithium–air batteries. **Journal of Power Sources**, 195, n. 5, p. 1370-1374, 2010/03/01/ 2010.

FREUNBERGER, S. A.; CHEN, Y.; DREWETT, N. E.; HARDWICK, L. J. *et al.* The Lithium–Oxygen Battery with Ether-Based Electrolytes. **Angewandte Chemie International Edition**, 50, n. 37, p. 8609-8613, 2011/09/05 2011.

FREUNBERGER, S. A.; CHEN, Y.; PENG, Z.; GRIFFIN, J. M. *et al.* Reactions in the Rechargeable Lithium–O_2 Battery with Alkyl Carbonate Electrolytes. **Journal of the American Chemical Society**, 133, n. 20, p. 8040-8047, 2011/05/25 2011.

HU, W.; CHEN, S.; XIA, Q. IrO_2/Nb–TiO_2 electrocatalyst for oxygen evolution reaction in acidic medium. **International Journal of Hydrogen Energy**, 39, n. 13, p. 6967-6976, 2014/04/24/ 2014.

LAN, C. J.; LEE, C. Y.; CHIN, T. S. Tetra-alkyl ammonium hydroxides as inhibitors of Zn dendrite in Zn-based secondary batteries. **Electrochimica Acta**, 52, n. 17, p. 5407-5416, 2007/05/05/ 2007.

LEE, J.-S.; TAI KIM, S.; CAO, R.; CHOI, N.-S. *et al.* Metal–Air Batteries with High Energy Density: Li–Air versus Zn–Air. **Advanced Energy Materials**, 1, n. 1, p. 34-50, 2011/01/01 2011.

LIU, F.; DENG, Y.; HAN, X.; HU, W. *et al.* Electrodeposition of metals and alloys from ionic liquids. **Journal of Alloys and Compounds**, 654, p. 163-170, 2016/01/05/ 2016.

LU, Z.; WANG, B.; HU, Y.; LIU, W. *et al.* An Isolated Zinc–Cobalt Atomic Pair for Highly Active and Durable Oxygen Reduction. **Angewandte Chemie International Edition**, 58, n. 9, p. 2622-2626, 2019/02/25 2019.

PARK, J.; PARK, M.; NAM, G.; LEE, J.-s. *et al.* All-Solid-State Cable-Type Flexible Zinc–Air Battery. **Advanced Materials**, 27, n. 8, p. 1396-1401, 2015/02/01 2015.

QASEEM, A.; CHEN, F.; WU, X.; ZHANG, N. *et al.* Ag, Co/graphene interactions and its effect on electrocatalytic oxygen reduction in alkaline media. **Journal of Power Sources**, 370, p. 1-13, 2017/12/01/ 2017.

RONG, C.; JIANG, R.; SARNEY, W.; CHU, D. Ultrasound-assisted micro-emulsion for synthesis of Pt and PtCo nano-particles. **Electrochimica Acta**, 55, n. 22, p. 6872-6878, 2010/09/01/ 2010.

SIMKA, W.; PUSZCZYK, D.; NAWRAT, G. Electrodeposition of metals from non-aqueous solutions. **Electrochimica Acta**, 54, n. 23, p. 5307-5319, 2009/09/30/ 2009.

SUNTIVICH, J.; GASTEIGER, H. A.; YABUUCHI, N.; NAKANISHI, H. *et al.* Design principles for oxygen-reduction activity on perovskite oxide catalysts for fuel cells and metal–air batteries. **Nature Chemistry**, 3, p. 546, 06/12/online 2011.

TIE, S. F.; TAN, C. W. A review of energy sources and energy management system in electric vehicles. **Renewable and Sustainable Energy Reviews**, 20, p. 82-102, 2013/04/01/ 2013.

XIONG, M.; CLARK, M. P.; LABBE, M.; IVEY, D. G. A horizontal zinc-air battery with physically decoupled oxygen evolution/reduction reaction electrodes. **Journal of Power Sources**, 393, p. 108-118, 2018/07/31/ 2018.

XIONG, M.; IVEY, D. G. Electrodeposited Co-Fe as an oxygen evolution catalyst for rechargeable zinc-air batteries. **Electrochemistry Communications**, 75, p. 73-77, 2017/02/01/ 2017.

XIONG, M.; IVEY, D. G. Composition effects of electrodeposited Co-Fe as electrocatalysts for the oxygen evolution reaction. **Electrochimica Acta**, 260, p. 872-881, 2018/01/10/ 2018.

XU, H.; SONG, P.; LIU, C.; ZHANG, Y. *et al.* Facile construction of ultrafine nickel-zinc oxyphosphide nanosheets as high-performance electrocatalysts for oxygen evolution reaction. **Journal of Colloid and Interface Science**, 530, p. 58-66, 2018/11/15/ 2018.

WEISS, M.; ZERFASS, A.; HELMERS, E. Fully electric and plug-in hybrid cars - An analysis of learning rates,user costs, and costs for mitigating CO_2 and air pollutant emissions. **Journal of Cleaner Production**, 212, p. 1478-1489, 2019.

YUAN, C.; WU, H. B.; XIE, Y.; LOU, X. W. Mixed Transition-Metal Oxides: Design, Synthesis, and Energy-Related Applications. **Angewandte Chemie International Edition**, 53, n. 6, p. 1488-1504, 2014/02/03 2014.

CHAPTER 2

Literature review

New approaches for renewable energy using metal electrocatalysts for lithium-O$_2$ and zinc-air batteries

New approaches for renewable energy using metal electrocatalysts for lithium-O₂ and zinc-air batteries

Josiel Martins Costa and Ambrósio Florêncio de Almeida Neto

Abstract

By 2050, electricity is expected to shift from 18 to 50 percent of the world's energy resources, renewable energy sources will enlarge approximately four times the current deployed capacity, and meanwhile, the expectation is that the release of carbon dioxide will be reduced by 50 percent of the current value. In this panorama, it is relevant to propose new set-up and systems for energy storage that are not yet available and that can handle the expected requests. The lithium-O₂ and zinc-air batteries, based on their performances and availability of raw material, comprise an alternative and revolutionary technology for application in electric vehicles in an accessible way. In this context, the development of materials, in particular, electrocatalysts that enable a catalytic activity capable of promoting efficient charge transport, during the process of reducing oxygen and allowing the housing of the discharge products are of scientific and technological relevance. To understand the technology of rechargeable systems, it is necessary to know what materials and chemical reactions in a battery occur. Specifically, the air electrode architecture composed of different materials, such as alloys, metal oxides, carbon nanotubes, and gas diffusion layer has been widely used in both catalytic systems to allow the efficient transfer of charge and the synergistic effect in the triple electrical layer, speeding-up the relevant reactions in the process. In this sense, the objective of the chapter is to report the current trends related to electrocatalysts that reduce the overpotential generated during charge and discharge in the lithium-O₂ and zinc-air batteries.

Keywords: Air electrode; Alloys; Carbon nanotubes; Oxygen reduction reaction; Challenge; Electrochemical performance; Energy storage materials; Metal oxides; Oxygen evolution reaction; New materials.

2.1. Introduction

Global warming and energy demand from fossil fuels characterize two issues pressing the traditional vehicle industry. Unlike gasoline-powered vehicles, electric vehicles, which use rechargeable batteries, not only reduce fossil fuel consumption, but also eradicate the pollution generated in the exhaust, giving credit to the auto industry (Yang et al. 2011). Indicatives in Figure 2.1 demonstrate the rise of 2011 to 2017 of plug-in electric vehicles, which are hybrid vehicles composed of higher capacity batteries.
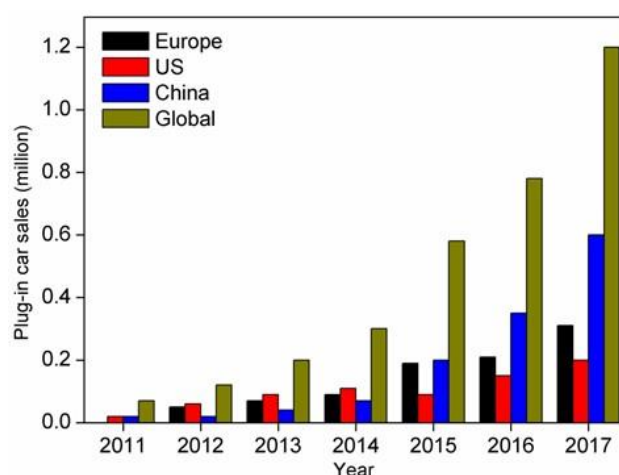
Figure 2.1. Plug-in vehicles sold annually, including global number. Modified after (Pelegov and Pontes 2018) Copyright 2018, Batteries. There is an increase in the number of sales of plug-in vehicles, as a result of concern for the environment and the development of new technologies. With the advancement of battery technology, the tendency is to decrease the sale of combustion engine-powered cars.

Among the technologies available, lead-acid batteries have a shorter useful life cycle of 3 to 4 years; however, it is still used as a source of renewable energy. Nickel-cadmium batteries have a longer life cycle than lead-acid, however, the cost of this technology is expensive. Concerning lithium-ion batteries, the energy density limitation occurs due to the chemical intercalation of the electrode material. Thus, this type of battery does not present relevant applications in electric vehicles[2] (Akhtar and Akhtar 2015).

---

[2] In addition, the specific energy and power density of the lithium-ion battery, even when applied to electric vehicles as a power source, deficiencies in the lithium-ion battery, and ongoing research and development on rechargeable batteries have led to the fundamentals of Li-air battery.

Scientific advances are fundamental to understanding the reactions that occur in rechargeable batteries, as well as the development of new materials to overcome the challenges related to energy storage (Bruce et al. 2011; Christensen et al. 2011; Imanishi and Yamamoto 2014). In this way, it is necessary to develop more efficient and safe rechargeable batteries from economically more accessible technologies.

Specifically, metal-air cells, which electrochemical reactions occur between electrodes that consume air or O_2, have been studied (Girishkumar et al. 2010; Neburchilov et al. 2010). In this sense, this chapter aims to discuss the main challenges and current trends in the architecture of cathode electrodes of lithium-O_2 and zinc-air batteries, with a focus on electrocatalysts that hold-up the oxygen reduction and evolution reactions.

2.2. Li-O₂ batteries

In 2009 the Battery 500 Project was initiated by scientists from the International Business Machines Almaden Research Center which aimed to develop a Li-air battery that had a capacity of 500 miles per charge. For Li-O_2 systems, in the cathode of nanostructured carbon or other metallic materials (nickel foam, steel mesh), oxygen is extracted and is where reactions of lithium ions with electrons occur to generate electricity. When connected to the car, oxygen is released into the atmospheric air. It is intended to transform this technology into a complete product by 2030 (Wilcke and Kim 2016). The authors reported that in an ideal cell, the amount of oxygen consumed during the flush should be exactly equal to the amount released in the refill. The separation of Li_2O_2 in the recharge was attacking the cell's electrolyte during the polls, which caused it to be replaced by another. There is no solvent that is stable for commercially available Li-O_2 cells; however, the authors stated that a combination of solvents worked suitably.

In recent years, two types of reversible Li-O_2 batteries classified as aqueous and non-aqueous systems have been proposed (Bruce et al. 2011; Zhang et al. 2011). Equation 1 shows the reaction for non-aqueous systems:

$$2Li + O_2 \rightarrow Li_2O_2 \tag{1}$$

For aqueous systems, Equation 2 describes the redox reaction of the air cathode that occurs with the presence of water molecules:

4Li + 6H₂O + O₂ → 4 (LiOH·H₂O)   (2)

The voltage of the cell is influenced by the OH^- concentration; meanwhile, it was observed that the OH^- concentration increases during the discharge process. The first studies on Li-air rechargeable cells used an anode composed of Li metallic, a polymeric electrolyte, and a porous carbon-based electrode as a catalyst (Abraham and Jiang 1996; Li and Dai 2014; Read 2006).

The electrolyte serves to promote the transport of lithium ions, the dissolution of gaseous oxygen, and the transfer to the reaction sites and also to protect the lithium anode. The water present in the aqueous electrolytes also participates in the electrochemical reactions, acting as reagent (Tan et al. 2017). An ideal non-aqueous electrolyte for the Li-O₂ system must: (1) be stable with the lithium anode and lithium salts, (2) have superior oxidation potential, and (3) present a lower vapor pressure and a superior boiling point. The formulation of the electrolyte influences the ability to charge and discharge. As examples of electrolytes, there may be mentioned gel-type polymer of $LiPF_4$, carbonates, ethers, ionic liquids at room temperature, sulfoxides and nitrites (Abraham and Jiang 1996; Read 2006).

In the electrode is the place where the oxygen evolution and reduction reaction occur. The objective is to achieve superior energy density and capacity, as well as reversibility. The electrochemical processes involved in the electrode, composed of the interaction between gaseous and ionic species, should remain in contact long enough to result in high capacity.

In general, structures composed of pores are more effective to promote the transport of oxygen in the electrodes, in addition to a large surface to react and facilitate electrical conductivity. The product of the lithium reaction with oxygen gives rise to Li_2O_2, which is in the solid phase. The solid present inside the porous cathode impairs oxygen transport and lowers battery capacity in non-aqueous systems. Even in aqueous systems, such as hybrid batteries, in which Li_2O_2 can be dissolved, the electrochemical reactions can be affected, directly impacting the capacity. Therefore, the structural shape of the electrode also is a major problem for porous cathodes (Tan et al. 2017). Examples of materials used as electrodes are: mesoporous carbon, carbon nanotubes, graphene and macroporous foams (Ding et al. 2014). However, carbon

instability has led to the search of non-carbon cathodes capable of being used in non-aqueous Li-air batteries, for example, a nickel foam, which with potentials above 3.5 V promoted the degradation of carbonate electrolytes (Veith and Dudney 2011).

The kinetics of oxygen reduction limits the performance of LiO_2 systems. The formation of Li_2O_2 and/or Li_2O depends on the reduction of O_2, according to Equations 3, 4, and 5.

$$Li^+ + e^- + O_2 \rightarrow LiO_2 \qquad U° = 3.00\ V \tag{3}$$

$$2Li^+ + 2e^- + O_2 \rightarrow Li_2O_2 \qquad U° = 2.96\ V \tag{4}$$

$$4Li^+ + 4e^- + O_2 \rightarrow 2Li_2O \qquad U° = 2.91\ V \tag{5}$$

Some authors suggest that Equation 4 does not occur directly (Bruce et al. 2011), and is divided into three stages, according to Equations 6, 7 and 8.

$$O_2 + e^- \rightarrow O_2^- \tag{6}$$

$$O_2^- + Li^+ \rightarrow LiO_2 \tag{7}$$

$$2LiO_2 \rightarrow Li_2O_2 + O_2 \tag{8}$$

A voltage range for charge-discharge potentials can be obtained through these different oxygen reduction reactions. From the formation of LiO_2, the mechanism becomes dependent on the type of material of the electrode. Materials in which O_2 adsorb weakly, for example, carbon, reaction with LiO_2 rapidly generates Li_2O_2. However, for surfaces that have strong adsorption of oxygen, such as in platinum, the reaction can trigger the formation of Li_2O, being similar to the process that occurs in an aqueous medium (Lu et al. 2010).

2.2.1. Li-O$_2$ batteries challenge

Several factors contribute to decreasing energy storage in the practice of Li-O$_2$ batteries. A porous conductive matrix, generally composed of carbon, is used as a cathode, in which with the discharge, electrode mass and volume are increased due to the accumulation of product generated. Larger quantities of the Li metal are added than necessary for the stoichiometric ratio to suppose the regeneration inefficiency. Besides, energy storage can also be reduced with the use of electric current collectors, and in particular for Li-O$_2$ batteries, gas diffusion channels (Bruce et al. 2011).

There are other factors such as the following: the instability of organic electrolytes, the behavior of the electrode and Li metal anode when in contact with reduced oxygen species, specifically the superoxide radical anion; and overpotentials during oxygen reduction/evolution reactions, which characterize a technological challenge to be overcome (Ottakam Thotiyl et al. 2013; Zou et al. 2016).

Regarding the use of Li metallic anode, the impregnation of non-homogeneous ions leads to the formation of Li dendrites during the cycle, promoting the neglect of Li metal. The dendrites pierce the separator giving rise to short circuits, as well as causing the contact with the electrode to be lost. The battery cycle duration is reduced as the dendrites grow and the solid electrolytic interface consumes electrolyte. The distribution of uneven current can cause this phenomenon (Bai et al. 2016). Seeking to increase anode stability, materials have been developed that involve homogeneous artificial layers of protection, highly conductive Li-ion, to reduce the formation of dendrites during the cycles. For example, polymer electrolytes and thin ceramic films present a promising direction to minimize problems of formation of such lithium dendrites (Girishkumar et al. 2010).

Another relevant issue in the batteries is the high polarization of the electrode, which results in the loss of energy efficiency, during the discharge of the cell, approximately 2.7 V, which is significantly lower than the standard potential (U$_o$). This potential difference is the overpotential discharge (η_{des}). The same analysis is valid for recharging, where the voltage increases up to 4.0 V, which results in the overpotential charge (η_{car}). The deviation from the standard potential is greater than the current flowing through the system and is known as electrode polarization. In this condition, the electrode is polarized (Girishkumar et al. 2010).

Three types of polarization are reported: concentration polarization or mass transport when it is the result of the depletion of the reactant gas at the electrode/electrolyte interface, which emphasizes the need for electrodes with high surface area and porosity that allow easy access to the reagents gaseous; the activation polarization, caused by the high concentration of reagent that forms a barrier to electron transfer; and the polarization by ohmic fall, which is the result of the electrical resistance inside the cell, being the process conditioned by Ohm's law, which distances the potential of balance electrode (Zheng et al. 2016; Zouhri and Lee 2016).

The stability of the electrolyte is also an aggravating factor since the non-aqueous electrolyte must be conductive, have electrochemical stability, and have considerable oxygen solubility (Balaish et al. 2014). Even with ongoing research, the instability of the solvent and lithium salts characterizes issues that require studies. To improve this instability, additives have been used to increase cell performance (Tan et al. 2017).

Electrolytes based on ionic liquids are currently a strategy aimed at improving the cycling of the Li-O$_2$ battery with high discharge rate. Monaco et al. (2013) analyzed the O$_2$ reduction reaction on a mesoporous carbon electrode using an ionic liquid as an electrolyte. The study demonstrated that the response of the oxygen electrode under high currents was governed by mass transport of O$_2$. The current density used was 0.2 mA cm^{-2}, and a value of 600 mAh g^{-1} of specific capacity was obtained.

2.3. Zn-air batteries

Known for detachable energy density, such as 1086 Wh kg^{-1}, Zn-air batteries also stand out for the low cost of production, lower than 10 \$ kW^{-1} h^{-1}, which is approximately two times lower compared to lithium systems. Zn-air batteries become an alternative to lithium-air batteries, which may come to fruition in the future due to the higher available energy density when compared to any rechargeable system. However, as well as other metal-air cells, problems related to the metallic Zn electrode and the catalyst impair the performance of this system.

Among the applications of Zn-air batteries, in the medical and telecommunication sector, it has already been tested. Even with superior energy densities, Zn-air batteries have lower power, less than 10 mW for devices applied to the hearing aid, due to the inefficiency of

the available catalysts. Furthermore, dissolution of zinc and inadequate bifunctional catalysts have also hindered the life cycle (Li and Dai 2014).

A negative zinc electrode, an air electrode (generally porous), and a separation membrane both in contact through an alkaline electrolyte make up a Zn-air battery. During the discharge, oxidation of the zinc occurs, solubilizing the Zn in the electrolyte, giving rise to ions $Zn(OH)_4^{-2}$ (Lee et al. 2011). This reaction occurs until the electrolyte is supersaturated. After supersaturation, zinc ions are presented as insoluble zinc oxide, described by the equations (Meng et al. 2018):

$$\text{Negative electrode: } Zn^{2+} + 4OH^- \rightarrow Zn(OH)_4^{-2} + 2\,e^- \tag{9}$$

$$Zn(OH)_4^{-2} \rightarrow ZnO + H_2O + 2OH^- \tag{10}$$

$$\text{Positive electrode: } O_2 + 4\,e^- + 2H_2O \rightarrow 4OH^- \tag{11}$$

$$\text{General reaction: } 2Zn + O_2 \rightarrow 2ZnO \tag{12}$$

$$\text{Parasitic reaction: } Zn + 2H_2O \rightarrow Zn(OH)_2 + H_2 \tag{13}$$
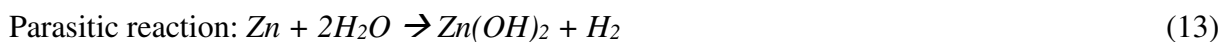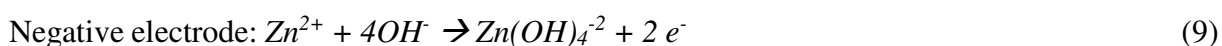
Thermodynamically, the evolution and oxidation reactions occur spontaneously and have a voltage value of 1.65 V. Meanwhile, during the charge and discharge cycles, they are kinetically slow, requiring catalysts to accelerate the process (Park et al. 2017).

During the heterogeneous catalysis process, the reactions occur on the surface of the catalyst. In this way, the catalytic activity depends on the mass transport that proceeds between the catalyst surface and the bulk phase. Both oxygen evolution and oxygen reduction reactions are composed of electron transfer and gas/liquid diffusion (Tang et al. 2018). To enhance the reactions, gas diffusion layers are used as the air electrode. However, the material must have high electrical conductivity, be hydrophobic, and have considerable porosity and surface area (Danner et al. 2016). These diffusers are usually composed of thin porous films manufactured of carbon materials, meshes or metal foam (Chen et al. 2018).

The gas diffusion layer must allow uniform contact between the air and the catalyst and, simultaneously, serve as a barrier for electrolyte penetration, which justifies

hydrophobicity and the formation of interpenetrating subsystems capable of facilitating the diffusion of O_2 to the catalyst site, where a three-phase electrolyte-gas-catalyst interface is created (Fu et al. 2017; Su et al. 2017).

The morphology of the electrocatalyst must be designed to expose the active sites to electrolyte and sources of oxygen. Vertically aligned macropores and matrices grown on carbon nanotubes, for example, increase ionic transport and facilitate the diffusion of oxygen. Metal nanoparticles provide regions for reactions to occur on the surface (Jia et al. 2017).

2.3.1. Zn-air batteries challenge

The Zn electrodes have performance impaired due to several factors, such as dendrite growth, mass change, passivation, and hydrogen evolution. Battery performance is decreased when one or more of these phenomena occur simultaneously. Retention of charge and discharge cycles, a considerable utilization rate of Zn, and high efficiency with minimum hydrogen evolution are expected on an ideal Zn electrode. To obtain these characteristics, researches have been developed by varying the design of the Zn electrode structure, the air-electrode, and the electrolyte composition. The incorporation of heavy metals in the Zn electrodes, for example, suppresses these three phenomena, just as the electrolyte optimization can suppress the effect of the shape change, the dendrite growth, and the evolution of hydrogen[3] (Chen et al. 2018).

Due to the slow kinetics, the electrocatalysts are applied to reduce the overpotentials and facilitate the occurrence of oxygen reduction and evolution reactions. The most efficient and usual electrocatalysts are the base of precious metals and compounds, usually Pt, IrO_2, and RuO_2 (Chen et al. 2019). High efficiencies in these two reactions depend on the different reactions associated with the electronic structure and adsorption energy, which consequently has electrolyte pH dependence (Jiao et al. 2015; Vij et al. 2017). Moreover, unavailability, high cost, and the poisonous effect caused by precious metals the hindered practical applications. It is important to seek alternative multifunctional electrocatalysts than conventional (Chen et al. 2019).

As the reactions have different demands for the active sites, the bifunctional catalysts need to be adequate to regulate the intrinsic activity, in addition to the enlarged surface

---

[3] However, the incorporation of heavy metal in the Zn electrodes are not ideal due to their environmental toxicity.

area, the diffusion, and the electron transport being accelerated, expounding the active sites in the catalytic process (Kuang and Zheng 2016).

Zinc-air batteries work in an alkaline environment, such as Na and K hydroxides, for a better activity for the zinc electrode and cathode, since Zn can react quickly in acid solution and generate anodic corrosion (Lee et al. 2016). KOH is generally more appropriate over NaOH due to its low viscosity, high O_2 diffusion coefficient, and better ionic effect. However, since these are open systems, the loss of water from the liquid electrolyte is a relevant cause of performance reduction. Research has been carried out aiming at electrolyte gelling to minimize loss and improve battery performance and life cycle (Othman et al. 2001). The function of the gelling agent is to immobilize and store the KOH electrolyte with a retention capacity of 20 to 100 times its weight. Besides, the use of gel can improve the specific capacity, according to the study of Mohamad (2006).

2.4. Electrocatalysts for Li-O₂ and Zn-air batteries

In rechargeable systems, the heterogeneous electrocatalysis has the function of reducing the overpotential generated during the oxygen reduction and evolution reaction, since this overpotential decreases the energy storage (McCloskey et al. 2011). In order to accelerate the reactions that occur in the discharge and charge steps, catalysts are incorporated, as shown in Figure 2.2.
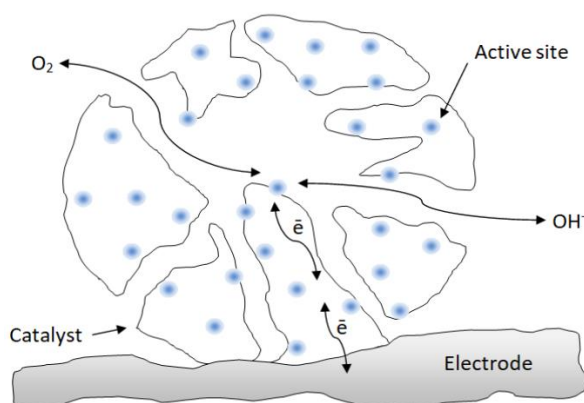
Figure 2.2. Catalytic process diagram in air electrodes. Modified after (Tang et al. 2018) Copyright 2018, American Chemical Society. The active site is the region where the reactions involved in the charge-discharge process of the batteries occurred. More porous materials favor the catalysis of the reactions.

In aqueous electrolytes, developing bifunctional catalysts with significant catalytic activity compared to noble metals is still a challenge. For non-aqueous Li-O$_2$ systems, understanding the catalyst function concerning the formed and decomposed solid product is indispensable for the development of effective catalysts. As the discharge process in non-aqueous electrolytes is followed by the generation of solid Li$_2$O$_2$, which can cover the catalyst surface over time. To shorten this time and improve the discharge, electrocatalysts that are repeatedly adsorbed against the increasing formation of Li$_2$O$_2$ are required (Tan et al. 2017).

Song et al. (2017) developed Co-W-C nanocomposites containing encapsulated functional species doped with nitrogen. The nanoparticles of cobalt and tungsten carbide were encapsulated using induced evaporation and heat treatment. The oxygen reduction reaction was facilitated, showing higher yield and good transferability of electrons with the material obtained.

Cho et al. (2017) studied Ag-Co catalysts with varied stoichiometric ratios. The alloys were obtained by electrodeposition with Triton X-100 (surfactant), Ag and Co, and KNO$_3$ in an aqueous solution. The alloy composed of Ag$_1$Co$_7$ electrodeposited for 200 s, with 14% Co, revealed the superior catalytic activity to the oxygen reduction reaction, with a similar or better result to platinum.

Yu et al. (2016) manufactured nanotubes of cobalt oxide (Co$_3$O$_4$) by electro-spinning and subsequent air calcination. Cobalt oxide nanotubes were reduced to cobalt by calcination under H$_2$ and argon atmosphere and served as a model to react with the silver precursor (silver nitrate), through galvanic substitution, giving rise to the AgCo nanotubes. Several AgCo nanotubes were prepared under different conditions, varying the reduction reaction time and the galvanic substitution. The reduction time of 1 h and galvanic substitution of 3 h were shown to be better for the discharge, demonstrated by the higher current density and the detachable number of electrons that were transferred during the reaction. In addition, the discharge performance using AgCo nanotubes was better than cobalt, bare platinum, and silver nanowires.

Reduced graphene and AgCo oxidized electrocatalyst was synthesized by an electrochemical method. The synthesis of the AgCo alloy in the reduced graphene catalyst was performed using polyethylene glycol as an additive. The electrocatalyst presented the superior activity of electrochemical surface area and mass, resulting from well-dispersed nano-linked nanoparticles that provided transfer rate during the oxygen reduction reaction. The AgCo in

reduced graphene electrocatalyst showed higher oxygen reduction reaction current density, in addition to being stable and selective when compared to the other catalysts tested (Joo et al. 2017).

As shown in Table 2.1, there is a trend of carbon-based electrocatalysts and their respective discharge and charge capacities in the last 6 years. The values of the capacities vary according to the method used for the synthesis of nanotubes, the use or not of heat treatment and the metallic elements that make up the cathode. As an example, the study of Gao et al. (2017) used a layer of carbon-doped with nitrogen and encapsulated with hybrid W_2C. The authors obtained high capacity in both O_2 reactions, with an initial capacity close to 11000 mAh g^{-1}, smaller overpotential and greater life cycle, which was assigned to the synergic effect between the nanoparticles of W_2C and the layers of carbon-doped with nitrogen. The specific cathode architecture allowed the decomposition of the undesired $LiCO_3$ product and the effective conduction of electrons and Li^+.

Table 2.1. Main bifunctional electrocatalysts used in rechargeable Li-O₂ systems

Electrocatalyst	Discharge capacity (mAh g$_c^{-1}$)	Charge capacity (mAh g$_c^{-1}$)	Current density (mA g$_c^{-1}$)	Reference
Fe_3O_4 at CoO	5100	5100	40	Shang et al. (2018)
Co@CoO carbon nanofibers	4427	4427	100	Cao et al. (2019)
Ru/N carbon nanotubes	7100	7100	100	Zhang et al. (2019b)
δ-MnO_2 at multi-walled carbon nanotubes	~28400	-	100	Ma et al. (2019)
W_2C carbon layers	11000	11000	100	Gao et al. (2017)
Fe/Fe_3C N-doped graphene	7150	~7000	100	Lai et al. (2016)
V_2O_5/Al_2O_3	2875	2875	100	Lim et al. (2013)
$LaMnO_3$	6852	6852	100	Li et al. (2018)
Ag/NiO-Fe_2O_3	5138	5138	200	Lu et al. (2019a)
Ta_2O_5 nanoparticles	~15000	~15000	200	Zhang et al. (2018)
Pd-Cu	12000	-	200	Choi et al. (2014)
RuO_2 at $NiCo_2O_4$	17633	~16500	200	Zou et al. (2018)

Cobalt nanoparticles immobilized internally in CoO and moored in nitrogen-doped porous carbon nanofibers were produced using a coaxial electrospinning process and thereafter a heat treatment (Cao et al. 2019). The cathode Co showed a porous hierarchical structure of a high surface area, composed by a large amount of active sites that showed synergistic interactions between the two chemical species, Co and CoO. The petal-shaped Li_2O_2 discharge

products from the Co and CoO cathode were easily decomposed when compared to the film-type Li_2O_2. The results provided a model for the design of Co in CoO cathodes with charge and discharge capacity of 4427.3 mAh g^{-1}.

Ultrafine bimetallic Fe-Co nanoparticles fixed on nitrogen-doped porous carbon were used in Zn-air batteries (Zhong et al. 2019). The catalyst exhibited superior performance for the discharge with a half-wave potential = 0.84 V and limiting current density = -5.3 mA cm^{-2}. A high potential circuit = 1.50 V and high specific capacity = 726.2 mAh g^{-1} with stability, even higher than the Pt in C catalyst, were also observed.

The Fe-Co-Ni ternary alloy electrodeposited by electrophoresis was used in mesoporous carbon nanofibers to catalyze the charge reaction (Li et al. 2019b). After carbonization, the morphology of fibrous appearance with a diameter of 250 nm was maintained. In the Zn-air battery, the alloy presented a differential charge voltage of 0.88 V at 20 mA cm^{-2}, considerable stability, and superior power density of 73 mW cm^{-2} at a current density of 80 mA cm^{-2}, having surpassed the results of electrodes containing Pt in C.

To further enhance the discharge reaction activities, Cu-Co bimetallic alloys were incorporated by doping by immersion in carbon-containing carbon nanotubes containing Co (Li et al. 2019c). The synergistic effect observed between the Cu-Nx and Co-Nx species increased the O_2 reduction reaction activities, being applied as a cathode of Zn-air cell. The specific capacity achieved was 760 mAh g^{-1}, which equates to an energy density of 821 Wh kg^{-1}, with a discharge rate of 100 mA cm^{-1}. The superior result of the bimetallic catalyst proposed a viable option for the production of energy conversion cells.

In the electrodes of Zn-air systems, the electrode architecture is also extremely relevant, according to Table 2.2, which shows the trends of the electrocatalysts of the last 2 years. A strategy developed with carbon-supported nitrogen-doped Zn-Co demonstrated the ease of O-O bond cleavage, presenting an overpotential of 0.335 V for the discharge process (Lu et al. 2019b). As shown in Table 2.2, the cathodic catalyst showed a power density of 230 mW cm^{-2}. Furthermore, the authors concluded that the catalytic activity can be sustained even in the acid medium and that the Zn-air battery presented detachable power density and stability.

In addition to alloys and metal oxides, the composites are also applicable to the Zn-air electrode. According to Table 2.2, Co_9S_8/S and nitrogen dual-doped graphene composite showed detachable electrochemical kinetics for O_2 reactions, with better activity parameters such as lower Tafel slope of 47.7 mV dec^{-1} for reduction reaction and 69.2 mV dec^{-1} for

evolution reaction than traditional Pt in C and RuO$_2$ catalysts (Shao et al. 2019). To extend the practical application, the Zn-air battery demonstrated excellent charge-discharge results and cycle stability and was fully prepared in the solid state.

Table 2.2. Main bifunctional electrocatalysts used in rechargeable Zn-air systems

Electrocatalyst	Oxygen reduction reaction activity	Oxygen evolution reaction activity	Battery performance	Electrolyte	Reference
(Ni, Co)S_2 nanosheets	Onset potential: 0.82 V	Onset potential: 1.47 V	Power density: 153.5 mW cm^{-2}	6 M KOH	Zhang et al. (2019a)
B-N co-doped porous carbon	Onset potential: 0.894 V	Onset potential: 1.38 V	Cycling ability: 600 cycles (100 h) at 2 mA cm^{-2}	6 M KOH	Qian et al. (2017)
Co_9S_8/S and N dual doped graphene composite	Onset potential:0.92 V Tafel slope: 47.7 mV dec^{-1}	Tafel slope: 69.2 mV dec^{-1}	Power density: 36.2 mW cm^{-2}	6 M KOH	Shao et al. (2019)
(Ni, Co)Se_2	Onset potential: 0.70 V	Onset potential ~ 1.58V	Power density: 110 mW cm^{-2}	6 M KOH with 0.2 M zinc acetate	Sun et al. (2019)
Fe/Co-N-C nanofibers with embedding Fe-Co alloy nanoparticles	Tafel slope: 80 mV dec^{-1}	Tafel slope: 78 mV dec^{-1}	Power density: 115 mW cm^{-2}	6 M KOH with 0.2 M zinc acetate	Li et al. (2019a)
Co-Ni nitrogen-doped graphitic carbon	Tafel slope: 51 mV dec^{-1}	Tafel slope: 78 mV dec^{-1}	Power density: 130.5 mW cm^{-2}	6 M KOH with 0.2 M ZnO	Yang et al. (2019)
FeCoNi alloy	-	Tafel slope: 78 mV dec^{-1}	Power density: 130.5 mW cm^{-2}	6 M KOH with 0.2 M ZnO	Li et al. (2019b)
Zn/CoN-C	Onset potential: 1.004 V	-	Power density: 230 mW cm^{-2}	6 M KOH	Lu et al. (2019b)
Iron-Imidazolate	Onset potential: 0.90 V	Onset potential: 0.56 V	Cycling ability: 600 cycles (160 h) at 2 mA cm^{-2}	6 M KOH with 0.2 M ZnO	Lee et al. (2019)
$NiFe_2O_4$	Onset potential: 0.83 V	Onset potential: 1.56 V	Power density: 211 mW cm^{-2}	KOH with 0.2 M $ZnCl_2$	Naik and Sampath (2018)
$Co_2P_2O_7$ particles	Onset potential: 0.90 V	Onset potential: 1.45 V	Power density: 138 mW cm^{-2}	6 M KOH	Ren et al. (2018)

2.5. Conclusions

Significant research has been developed on materials and structural designs to obtain better results of electrochemically rechargeable Li-O$_2$ and Zn-air batteries in the last ten years. Despite the significant effort, the technology of rechargeable Li and Zn batteries are still not finalized enough for widespread applications. It is suggested the use of computational simulation and screening on the high yield, aiming to accelerate the development of electrocatalysts with high catalytic activity. Active sites should be more exposed, reducing the impediment of mass transfer; for this, the geometric structures of the electrodes must be controlled. The temperature must be considered since for practical applications the batteries will be used in a temperature range, not at a fixed temperature.

Even with several efficient bifunctional metal catalysts, carbon materials are essential, due to applications such as substrates, catalysts or additives. However, the high oxidation potential generates carbon corrosion during charge, reducing performance and stability. An alternative to this issue has been to use graphitized carbon, foam or mesh metal material to restrict the effect of corrosion. Therefore, the control of morphology is necessary, due to influence on the properties of the material, such as the specific surface area, which determines the catalytic activity. We hope that these approaches in this chapter will be used for researchers and motivate the innovation on catalysts and that in the future occurs the commercialization of rechargeable Li-O$_2$ and Zn-air batteries.

Acknowledgements

References

Abraham KM, Jiang Z (1996) A Polymer Electrolyte-Based Rechargeable Lithium/Oxygen Battery Journal of The Electrochemical Society 143:1-5 doi:10.1149/1.1836378

Akhtar N, Akhtar W (2015) Prospects, challenges, and latest developments in lithium-air batteries International Journal of Energy Research 39:303-316 doi:10.1002/er.3230

Bai P, Li J, Brushett FR, Bazant MZ (2016) Transition of lithium growth mechanisms in liquid electrolytes Energy & Environmental Science 9:3221-3229 doi:10.1039/C6EE01674J

Balaish M, Kraytsberg A, Ein-Eli Y (2014) A critical review on lithium-air battery electrolytes Physical Chemistry Chemical Physics 16:2801-2822 doi:10.1039/C3CP54165G

Bruce PG, Freunberger SA, Hardwick LJ, Tarascon JM (2011) Li-O$_2$ and Li-S batteries with high energy storage Nature materials 11:19-29 doi:10.1038/nmat3191

Cao Y et al. (2019) Synthesis of Ag/Co@CoO NPs anchored within N-doped hierarchical porous hollow carbon nanofibers as a superior free-standing cathode for LiO$_2$ batteries Carbon 144:280-288 doi:10.1016/j.carbon.2018.12.048

Chen J et al. (2019) Chitin-derived porous carbon loaded with Co, N and S with enhanced performance towards electrocatalytic oxygen reduction, oxygen evolution, and hydrogen evolution reactions Electrochimica Acta 304:350-359 doi:10.1016/j.electacta.2019.03.028

Chen X, Zhou Z, Karahan HE, Shao Q, Wei L, Chen Y (2018) Recent Advances in Materials and Design of Electrochemically Rechargeable Zinc-Air Batteries Small 14:1801929 doi:10.1002/smll.201801929

Cho Y-B, Moon S, Lee C, Lee Y (2017) One-pot electrodeposition of cobalt flower-decorated silver nanotrees for oxygen reduction reaction Applied Surface Science 394:267-274 doi:10.1016/j.apsusc.2016.10.068

Choi R et al. (2014) Ultra-low overpotential and high rate capability in Li-O$_2$ batteries through surface atom arrangement of PdCu nanocatalysts Energy & Environmental Science 7:1362-1368 doi:10.1039/C3EE43437K

Christensen J et al. (2011) A Critical Review of Li/Air Batteries Journal of The Electrochemical Society 159:R1-R30 doi:10.1149/2.086202jes

Danner T, Eswara S, Schulz VP, Latz A (2016) Characterization of gas diffusion electrodes for metal-air batteries Journal of Power Sources 324:646-656 doi:10.1016/j.jpowsour.2016.05.108

Ding N, Chien SW, Hor TSA, Lum R, Zong Y, Liu Z (2014) Influence of carbon pore size on the discharge capacity of Li-O$_2$ batteries Journal of Materials Chemistry A 2:12433-12441 doi:10.1039/C4TA01745E

Fu J, Cano ZP, Park MG, Yu A, Fowler M, Chen Z (2017) Electrically Rechargeable Zinc-Air Batteries: Progress, Challenges, and Perspectives Advanced materials 29:1604685 doi:10.1002/adma.201604685

Gao R, Zhou Y, Liu X, Wang J (2017) N-Doped Defective Carbon Layer Encapsulated W_2C as a Multifunctional Cathode Catalyst for High Performance Li-O₂ Battery Electrochimica Acta 245:430-437 doi:10.1016/j.electacta.2017.05.177

Girishkumar G, McCloskey B, Luntz AC, Swanson S, Wilcke W (2010) Lithium-Air Battery: Promise and Challenges The Journal of Physical Chemistry Letters 1:2193-2203 doi:10.1021/jz1005384

Imanishi N, Yamamoto O (2014) Rechargeable lithium–air batteries: characteristics and prospects Materials Today 17:24-30 doi:10.1016/j.mattod.2013.12.004

Jia G, Zhang W, Fan G, Li Z (2017) Three-Dimensional Hierarchical Architectures Derived from Surface-Mounted Metal-Organic Framework Membranes for Enhanced Electrocatalysis 56:13781-13785 doi:10.1002/anie.201708385

Jiao Y, Zheng Y, Jaroniec M, Qiao SZ (2015) Design of electrocatalysts for oxygen- and hydrogen-involving energy conversion reactions Chemical Society Reviews 44:2060-2086 doi:10.1039/C4CS00470A

Joo Y, Ahmed MS, Han HS, Jeon S (2017) Preparation of electrochemically reduced graphene oxide-based silver-cobalt alloy nanocatalysts for efficient oxygen reduction reaction International Journal of Hydrogen Energy 42:21751-21761 doi:10.1016/j.ijhydene.2017.07.123

Kuang M, Zheng G (2016) Nanostructured Bifunctional Redox Electrocatalysts Small 12:5656-5675 doi:10.1002/smll.201600977

Lai Y, Chen W, Zhang Z, Qu Y, Gan Y, Li J (2016) Fe/Fe₃C decorated 3-D porous nitrogen-doped graphene as a cathode material for rechargeable Li-O₂ batteries Electrochimica Acta 191:733-742 doi:10.1016/j.electacta.2016.01.134

Lee J-S, Tai Kim S, Cao R, Choi N-S, Liu M, Lee KT, Cho J (2011) Metal-Air Batteries with High Energy Density: Li-Air versus Zn-Air Advanced Energy Materials 1:34-50 doi:10.1002/aenm.201000010

Lee J-SM, Sarawutanukul S, Sawangphruk M, Horike S (2019) Porous Fe-N-C Catalysts for Rechargeable Zinc-Air Batteries from an Iron-Imidazolate Coordination Polymer ACS

Sustainable Chemistry & Engineering 7:4030-4036 doi:10.1021/acssuschemeng.8b05403

Lee J, Hwang B, Park M-S, Kim K (2016) Improved reversibility of Zn anodes for rechargeable Zn-air batteries by using alkoxide and acetate ions Electrochimica Acta 199:164-171 doi:10.1016/j.electacta.2016.03.148

Li C, Wu M, Liu R (2019a) High-performance bifunctional oxygen electrocatalysts for zinc-air batteries over mesoporous Fe/Co-N-C nanofibers with embedding FeCo alloy nanoparticles Applied Catalysis B: Environmental 244:150-158 doi:10.1016/j.apcatb.2018.11.039

Li C, Yu Z, Liu H, Chen K (2018) High surface area $LaMnO_3$ nanoparticles enhancing electrochemical catalytic activity for rechargeable lithium-air batteries Journal of Physics and Chemistry of Solids 113:151-156 doi:10.1016/j.jpcs.2017.10.039

Li C, Zhang Z, Wu M, Liu R (2019b) FeCoNi ternary alloy embedded mesoporous carbon nanofiber: An efficient oxygen evolution catalyst for rechargeable zinc-air battery Materials Letters 238:138-142 doi:10.1016/j.matlet.2018.11.160

Li Y, Dai H (2014) Recent advances in zinc–air batteries Chemical Society Reviews 43:5257-5275 doi:10.1039/C4CS00015C

Li Z et al. (2019c) Structural Modulation of Co Catalyzed Carbon Nanotubes with Cu-Co Bimetal Active Center to Inspire Oxygen Reduction Reaction ACS Applied Materials & Interfaces 11:3937-3945 doi:10.1021/acsami.8b18496

Lim SH, Kim DH, Byun JY, Kim BK, Yoon WY (2013) Electrochemical and catalytic properties of V_2O_5/Al_2O_3 in rechargeable Li-O₂ batteries Electrochimica Acta 107:681-685 doi:10.1016/j.electacta.2013.06.045

Lu X et al. (2019a) 3D Ag/NiO-Fe₂O₃/Ag nanomembranes as carbon-free cathode materials for Li-O₂ batteries Energy Storage Materials 16:155-162 doi:10.1016/j.ensm.2018.05.002

Lu Y-C, Gasteiger HA, Crumlin E, McGuire R, Shao-Horn Y (2010) Electrocatalytic Activity Studies of Select Metal Surfaces and Implications in Li-Air Batteries Journal of The Electrochemical Society 157:A1016-A1025 doi:10.1149/1.3462981

Lu Z et al. (2019b) An Isolated Zinc-Cobalt Atomic Pair for Highly Active and Durable Oxygen Reduction Angewandte Chemie International Edition 58:2622-2626 doi:10.1002/anie.201810175

Ma L, Meng N, Zhang Y, Lian F (2019) Improved electrocatalytic activity of δ-MnO$_2$@MWCNTs by inducing the oriented growth of oxygen reduction products in Li-O$_2$ batteries Nano Energy 58:508-516 doi:10.1016/j.nanoen.2019.01.089

McCloskey BD, Scheffler R, Speidel A, Bethune DS, Shelby RM, Luntz AC (2011) On the Efficacy of Electrocatalysis in Nonaqueous Li-O$_2$ Batteries Journal of the American Chemical Society 133:18038-18041 doi:10.1021/ja207229n

Meng F-L, Liu K-H, Zhang Y, Shi M-M, Zhang X-B, Yan J-M, Jiang Q (2018) Recent Advances toward the Rational Design of Efficient Bifunctional Air Electrodes for Rechargeable Zn–Air Batteries Small 14:1703843 doi:10.1002/smll.201703843

Mohamad AA (2006) Zn/gelled 6M KOH/O$_2$ zinc–air battery Journal of Power Sources 159:752-757 doi:10.1016/j.jpowsour.2005.10.110

Monaco S, Soavi F, Mastragostino M (2013) Role of Oxygen Mass Transport in Rechargeable Li/O$_2$ Batteries Operating with Ionic Liquids The Journal of Physical Chemistry Letters 4:1379-1382 doi:10.1021/jz4006256

Naik KM, Sampath S (2018) Two-step oxygen reduction on spinel NiFe$_2$O$_4$ catalyst: Rechargeable, aqueous solution- and gel-based, Zn-air batteries Electrochimica Acta 292:268-275 doi:10.1016/j.electacta.2018.08.138

Neburchilov V, Wang H, Martin JJ, Qu W (2010) A review on air cathodes for zinc–air fuel cells Journal of Power Sources 195:1271-1291 doi:10.1016/j.jpowsour.2009.08.100

Othman R, Basirun WJ, Yahaya AH, Arof AK (2001) Hydroponics gel as a new electrolyte gelling agent for alkaline zinc–air cells Journal of Power Sources 103:34-41 doi:10.1016/S0378-7753(01)00823-0

Ottakam Thotiyl MM, Freunberger SA, Peng Z, Bruce PG (2013) The Carbon Electrode in Nonaqueous Li-O$_2$ Cells Journal of the American Chemical Society 135:494-500 doi:10.1021/ja310258x

Park J, Park M, Nam G, Kim MG, Cho J (2017) Unveiling the Catalytic Origin of Nanocrystalline Yttrium Ruthenate Pyrochlore as a Bifunctional Electrocatalyst for Zn-Air Batteries 17:3974-3981 doi:10.1021/acs.nanolett.7b01812

Pelegov VD, Pontes J (2018) Main Drivers of Battery Industry Changes: Electric Vehicles - A Market Overview Batteries 4 doi:10.3390/batteries4040065

Qian Y et al. (2017) A metal-free ORR/OER bifunctional electrocatalyst derived from metal-organic frameworks for rechargeable Zn-Air batteries Carbon 111:641-650 doi:10.1016/j.carbon.2016.10.046

Read J (2006) Ether-Based Electrolytes for the Lithium/Oxygen Organic Electrolyte Battery Journal of The Electrochemical Society 153:A96-A100 doi:10.1149/1.2131827

Ren J-T, Yuan G-G, Chen L, Weng C-C, Yuan Z-Y (2018) Rational Dispersion of Co$_2$P$_2$O$_7$ Fine Particles on N,P-Codoped Reduced Graphene Oxide Aerogels Leading to Enhanced Reversible Oxygen Reduction Ability for Zn-Air Batteries ACS Sustainable Chemistry & Engineering 6:9793-9803 doi:10.1021/acssuschemeng.8b00873

Shang C et al. (2018) Fe$_3$O$_4$@CoO mesospheres with core-shell nanostructure as catalyst for Li-O$_2$ batteries Applied Surface Science 457:804-808 doi:10.1016/j.apsusc.2018.07.026

Shao Q, Liu J, Wu Q, Li Q, Wang H-g, Li Y, Duan Q (2019) In Situ Coupling Strategy for Anchoring Monodisperse Co$_9$S$_8$ Nanoparticles on S and N Dual-Doped Graphene as a Bifunctional Electrocatalyst for Rechargeable Zn-Air Battery Nano-Micro Letters 11:4 doi:10.1007/s40820-018-0231-3

Song L et al. (2017) Functional Species Encapsulated in Nitrogen-Doped Porous Carbon as a Highly Efficient Catalyst for the Oxygen Reduction Reaction Chemistry - A European Journal 23:3398-3405 doi:10.1002/chem.201605026

Su H, Xu Q, Chong J, Li H, Sita C, Pasupathi S (2017) Eliminating micro-porous layer from gas diffusion electrode for use in high temperature polymer electrolyte membrane fuel cell Journal of Power Sources 341:302-308 doi:10.1016/j.jpowsour.2016.12.029

Sun C, Guo X, Zhang J, Han G, Gao D, Gao X (2019) Rechargeable Zn-air batteries initiated by nickel-cobalt bimetallic selenide Journal of Energy Chemistry 38:34-40 doi:10.1016/j.jechem.2019.01.001

Tan P et al. (2017) Advances and challenges in lithium-air batteries Applied Energy 204:780-806 doi:10.1016/j.apenergy.2017.07.054

Tang C, Wang H-F, Zhang Q (2018) Multiscale Principles To Boost Reactivity in Gas-Involving Energy Electrocatalysis Accounts of Chemical Research 51:881-889 doi:10.1021/acs.accounts.7b00616

Veith GM, Dudney NJ (2011) Current Collectors for Rechargeable Li-Air Batteries Journal of The Electrochemical Society 158:A658-A663 doi:10.1149/1.3569750

Vij V et al. (2017) Nickel-Based Electrocatalysts for Energy-Related Applications: Oxygen Reduction, Oxygen Evolution, and Hydrogen Evolution Reactions ACS Catalysis 7:7196-7225 doi:10.1021/acscatal.7b01800

Wilcke WW, Kim H (2016) The 800-km battery lithium-ion batteries are played out. Next up: lithium-air IEEE Spectrum 53:42-62 doi:10.1109/MSPEC.2016.7420398

Yang L, Wang D, Lv Y, Cao D (2019) Nitrogen-doped graphitic carbons with encapsulated CoNi bimetallic nanoparticles as bifunctional electrocatalysts for rechargeable Zn-Air batteries Carbon 144:8-14 doi:10.1016/j.carbon.2018.12.008

Yang Z, Zhang J, Kintner-Meyer MC, Lu X, Choi D, Lemmon JP, Liu J (2011) Electrochemical energy storage for green grid Chem Rev 111:3577-3613 doi:10.1021/cr100290v

Yu A, Lee C, Lee N-S, Kim MH, Lee Y (2016) Highly Efficient Silver-Cobalt Composite Nanotube Electrocatalysts for Favorable Oxygen Reduction Reaction ACS Applied Materials & Interfaces 8:32833-32841 doi:10.1021/acsami.6b11073

Zhang J et al. (2019a) Bimetallic Nickel Cobalt Sulfide as Efficient Electrocatalyst for Zn-Air Battery and Water Splitting Nano-Micro Letters 11:2 doi:10.1007/s40820-018-0232-2

Zhang P-F et al. (2019b) High-performance rechargeable Li-CO$_2$/O$_2$ battery with Ru/N-doped CNT catalyst Chemical Engineering Journal 363:224-233 doi:10.1016/j.cej.2019.01.048

Zhang RH, Zhao TS, Wu MC, Jiang HR, Zeng L (2018) Mesoporous ultrafine Ta$_2$O$_5$ nanoparticle with abundant oxygen vacancies as a novel and efficient catalyst for non-aqueous Li-O$_2$ batteries Electrochimica Acta 271:232-241 doi:10.1016/j.electacta.2018.03.164

Zhang T, Imanishi N, Takeda Y, Yamamoto O (2011) Aqueous Lithium/Air Rechargeable Batteries Chemistry Letters 40:668-673 doi:10.1246/cl.2011.668

Zheng Q, Xing F, Li X, Ning G, Zhang H (2016) Flow field design and optimization based on the mass transport polarization regulation in a flow-through type vanadium flow battery Journal of Power Sources 324:402-411 doi:10.1016/j.jpowsour.2016.05.110

Zhong B, Zhang L, Yu J, Fan K (2019) Ultrafine iron-cobalt nanoparticles embedded in nitrogen-doped porous carbon matrix for oxygen reduction reaction and zinc-air batteries Journal of Colloid and Interface Science 546:113-121 doi:10.1016/j.jcis.2019.03.038

Zou L, Jiang Y, Cheng J, Chen Y, Chi B, Pu J, Jian L (2018) Bifunctional catalyst of well-dispersed RuO_2 on $NiCo_2O_4$ nanosheets as enhanced cathode for lithium-oxygen batteries Electrochimica Acta 262:97-106 doi:10.1016/j.electacta.2018.01.005

Zou L, Jiang Y, Cheng J, Gong Y, Chi B, Pu J, Jian L (2016) Dandelion-like $NiCo_2O_4$ hollow microspheres as enhanced cathode catalyst for Li-oxygen batteries in ambient air Electrochimica Acta 216:120-129 doi:10.1016/j.electacta.2016.08.151

Zouhri K, Lee S-y (2016) Evaluation and optimization of the alkaline water electrolysis ohmic polarization: Exergy study International Journal of Hydrogen Energy 41:7253-7263 doi:10.1016/j.ijhydene.2016.03.119

CHAPTER 3

Influence of current density and W concentration on Co-W alloys used as catalysts in electrodes for Li-O$_2$ battery

**Influence of current density and W concentration on Co-W alloys
used as catalysts in electrodes for Li-O₂ battery**

Josiel Martins Costa, Thayane Carpanedo de Morais Nepel,
and Ambrósio Florêncio de Almeida Neto

Abstract

In this study, we verified the influence of tungsten (W) concentrations and current density for the electroplating of the cobalt-tungsten (Co-W) alloy on two substrates (nickel foam and steel mesh). The statistical evaluation showed a mathematical model that related the efficiency of deposition with the parameters analyzed. The efficiency varied from 0 to 60.05% for the nickel foam and 0 to 64.39% for the steel mesh. Scanning electron microscopy showed that to increase the current density made the surface less uniform, due to the size of the grains formed and X-ray diffraction pointed to the formation of amorphous coating alloys. Electrodeposition of the alloy in the steel mesh occurred with greater contribution by forced convection, as opposed to the nickel foam that had a smaller contribution, according to the effects of fluid dynamics. The Co-W alloys evidenced by energy-dispersive X-rays spectroscopy were tested in the cell with a constant pressure of O_2 and presented an alternative for the use of catalysts in Li-O₂ batteries.

Keywords: coating materials; Co-W alloy; electroplating; nickel foam; steel mesh.

3.1. Introduction

Electrodeposited cobalt-tungsten (Co-W) alloys are of great importance because of their exceptional hardness, wear resistance, corrosion in acid and alkaline media, in addition to their magnetic behavior between the cobalt (Co) alloys (Wang et al. 2006). In the electronics industry, they are used as barriers to prevent the diffusion of copper into gold. Due to its high melting point (3410 °C) and the excellent thermal stability, tungsten can provide excellent properties as an element in the Co-W alloy, being a material that can replace the chromium coatings, which have high toxicity and carcinogenic effects (Bera et al. 2012), and generally presents in the form of particles dispersed in the alloy uniformly within the network (Li et al. 2019). Another possible applicability of Co alloys is related to the use as catalysts in batteries (Cho et al. 2017; Sivagami et al. 2017).

Hybrid electrical vehicles (HEVs) and electric vehicles (EVs) have been gaining significant importance because they are environmentally efficient in fuel usage due to the reduction of CO_2 emissions by using recuperated kinetic vehicle energy stored as electric energy in a system battery (Taymaz and Benli 2014). Thus, lithium-air (Li-air) batteries are promising because of their high energy density, compared to other types of batteries available (lead-acid, nickel-cadmium, lithium-ion). Heterogeneous electrocatalysis became the object of study in rechargeable lithium batteries due to the reduction of the overpotential in both oxygen reduction (discharge) and oxygen evolution (load) reactions, since the overpotential generates a low storage of energy, i.e., the energy required to charge the battery is greater than the amount released during discharge (McKloskey et al 2011).One of the obstacles to its development has been the absence of a high-performance and low-cost catalyst. In response, research has been carried out using metal oxides (Oh et al., 2012), metal nitrides (Li et al. 2013), metallic nanoparticles (Choi et al. 2014), organometallic compounds (Ren et al. 2011) and carbon nanotubes (Awadallah 2015) as electrocatalysts on the O_2 electrode.

Studies have involved the development of tungsten carbide-cobalt (WC-Co) nanocomposites with functional species (WC-Co nanoparticles) encapsulated in a nitrogen-doped porous carbon structure through the induced evaporation method combined with subsequent heat treatment. The material demonstrated benefits to the active sites, higher yield, electron transferability and excellent electrocatalytic performance for the oxygen reduction reactions (Song et al. 2017). Cobalt-tungsten alloy layer containing 2.4 at % tungsten was

electroplated on type 430 stainless steel. This alloy can be converted to their oxides by oxidation under solid oxide fuel cells (SOFCs) operating conditions (Gan et al. 2018). In this context, the development of low-cost electrocatalysts with high efficiency is of relevant scientific and technological importance to obtain rechargeable $Li-O_2$ batteries. The characterization of catalytic materials impacts on the quantification of the reversible capacity (Cameán et al. 2010). This research proposes to verify the development, characterization and fluid dynamics effects of rotation in the synthesis of electrocatalysts with application in $Li-O_2$ batteries, by varying electric current density, concentration of sodium tungstate and substrate (nickel foam and steel mesh).

3.2. Material and methods

3.2.1. Preparation of substrates and electrolytic bath

The alloys of this study were deposited on a Sigma-Aldrich nickel foam with a diameter of 1 cm. Considering the foam as a solid, the deposition area for a circle with a diameter of 1 cm is 1.57 cm²; however, the foam is highly porous, which characterizes a higher surface area (Banhart 2001), being beneficial for the electroplating of Co-W and the discharge products of $Li-O_2$ cells (Lu et al. 2010). Taking into consideration that the steel mesh is not a material with great porosity when compared to nickel foam, 10 circles with a diameter of 1 cm were used. These circles were joined by its ends and folded one over the other to visualize only a single circle, allowing the electroplating on both sides of each circle. Thus, the available surface area was slightly larger, with at least 15.7 cm², since the material had an opening of 400 mesh.

The nickel foam and steel mesh were coupled to the rotating disk electrode using a rod of the same material. However, the rod, with a length of 2.5 cm × 0.3 mm in width, was superimposed on a copper filament, with a length of 1.5 cm × 0.3 mm in width, for better coupling to the rotating disk electrode. The nickel foam surfaces were subjected to a thorough cleaning process. Chemical treatment was carried out, first with 10% NaOH, for degreasing and then with 1% H_2SO_4, for surface activation. Because the steel mesh is a non-acid and base resistant material, the chemical treatment was restricted to nickel foam. After the chemical treatment, the substrate was dried in the drying oven at 100 °C and placed in the desiccator.

Electrochemical baths were based on previous studies (Porto et al. 2017; Vernickaite et al. 2016ᵃ, Zemanová et al. 2012) and prepared with: sodium tungstate ($Na_2WO_4 \cdot 2H_2O$) ranging from 0.1 to 0.3 mol·L^{-1}; cobalt sulfate ($CoSO_4 \cdot 7H_2O$) at 0.3 mol·L^{-1}; Ammonium citrate [$(NH_4)_2C_6H_6O_7$], a complexing agent, at 0.3 mol·L^{-1}; sodium tetraborate decahydrate ($Na_2B_4O_7 \cdot 10H_2O$), an amorphizing agent, at 3.75×10^{-2} mol·L^{-1}; and sodium dodecyl sulfate ($NaC_{12}H_{25}SO_4$) at 1.04×10^{-4} mol·L^{-1}, so that the H_2 released during the electroplating detached with greater velocity, avoiding the formation of bubbles in the adhered alloy.

3.2.2. Electroplating

For electroplating tests, a pH meter was used in addition to the rotating disk electrode (pattern 616A, Princeton Applied Research), with a potentiostat/galvanostat (VersaStat 3, Princeton Applied Research), which controlled the current density between the working electrode and the counter electrode. The electric current density ranged from 2 to 10 mA·cm^{-2}, the cathode rotation was maintained at 45 rpm and the experiment was performed at room temperature. The potentiostat was used in galvanostatic mode, and hollow cylindrical mesh of platinum as counter electrode. Each electrolysis lasted 60 minutes[4].

The faradaic efficiency (ε) was calculated based on the mass obtained by the load used and the chemical composition of the coating obtained by energy-dispersive X-ray (EDX) according to Equation (1):

$$\varepsilon = \frac{m.F}{I.t} \sum \frac{n_j.W_j}{M_j} \tag{1}$$

where *m* is the measured mass of coating (g), *t* is the deposition time (s), *I* is the total current passed (A), W_j is the weight fraction of the element in the coating obtained by EDX, n_j is the number of electrons transferred per atom of each metal, M_j is the atomic mass of that element (g·mol^{-1}), and *F* is the Faraday constant (96,485 C·mol^{-1}).

To quantitatively evaluate the influence of the input variables, concentration of sodium tungstate (C_W) and electric current density (I), and qualitatively the substrate (S), on the

---

[4] See Appendix A.

deposition efficiency (ε), as well as its possible interactions, a complete factorial design 2^3 was perfomed, with 4 experiments at the central point (level 0), totaling 16 experiments to be randomly performed, avoiding systematic errors. Table 3.1 shows the input variables used in the experimental design, their coding and real levels of each variable in the electroplating system for the Co-W alloy.

Table 3.1. Actual and coded values of variables in the 2^3 experimental design

Variables	Level (-1)	Level (0)	Level (+1)
Current density (mA·cm^{-2})	2	6	10
Concentration of $Na_2WO_4·2H_2O$ (mol·L^{-1})	0.1	0.2	0.3
Substrate	nickel foam	-	steel mesh

3.2.3. Characterization

The X-ray diffraction (XRD) and the scanning electron microscopy with chemical analysis using EDX characterized the substrate samples containing Co-W alloys. The XRD was obtained with a Philips device (X'PERT model) with copper Kα radiation, at a voltage of 40 kV, current of 40 mA, wavelength of 1.52 Å, step size of 0.02 2θ and a time per step of 1 s. The micrographs of the nickel foam and steel mesh substrates containing metal alloys of tungsten were obtained using the scanning electronic microscope (SEM) of the LEO brand (LEO 440i model) with EDX detector.

3.2.4. Analysis of the fluid dynamics of the electroplating

The approximate correlation of mass transfer for the system of forced convection[5] provided by cathode rotation is given by Equation 2 (Welty et al. 2007).

$$\frac{k_c d}{D_{AB}} = 0.62 Re^{1/2} Sc^{1/3} \tag{2}$$

where k_c is the convective mass transfer coefficient and:

---

[5] These correlations were appropriate for systems with rotation.

$$Re = \frac{d^2\omega}{\nu} \tag{3}$$

$$Sc = \frac{\nu}{D_{AB}} \tag{4}$$

where ω is the cathode rotation, ν is the kinematic viscosity of the solution, d is the agitator diameter and D_{AB} is the diffusivity of species A (Co or W) with respect to species B (solution). Thus, the deposition rate (W_A) was calculated by Equation 5.

$$W_A = Ak_c\left(C_{A0} - C_{Af}\right) \tag{5}$$

where A is the area of the electrode, C_{A0} and C_{Af} are, respectively, the initial and final concentrations of the chemical species A (g·cm⁻³). Final concentrations of species A were estimated by its material balance in the bath and masses deposited at the cathode, according to Equation 6.

$$V\left(C_{A0} - C_{Af}\right) = m_{Af} - m_{A0} \tag{6}$$

where V is the volume of the electrolytic bath, and m_{Ao} and m_{Af} are the masses of the chemical species A deposited at the cathode.

3.2.5. Electrochemical tests on Li-O₂ cell

The stainless steel cell was composed of a metal lithium anode of 1.6 cm in diameter and 0.5 mm thick, a glass fiber filter (Whatman®) with 2 centimeters of diameter, a gas diffusion catalyst (steel mesh or nickel foam electrode), and 100 µL of electrolyte - 0.1 M LiClO₄ in anhydrous dimethyl sulfoxide (DMSO) (Gittleson et al. 2014). A porous stainless steel screen was placed on the electrode and a stainless steel spring (Lu et al. 2010). The cell was closed between two stainless steel plates, containing the terminals for insertion of oxygen, both of which were isolated from each other by a teflon ring. The cell had an input for oxygen at the cathode, as well as current collectors, which were connected to the potentiostat / galvanostat, to control the charge and discharge current.

The assembly of the cell was carried out in a Glove-Box (MBRAUN-LABstar Workstation) in argon atmosphere. After assembly the cell remained in the glovebox for 4 hours prior to the start of the electrochemical tests. Cell were tested using a two-catalyst configuration. In this configuration, the counter electrode was connected to the reference electrode (Li / Li$^+$), which was connected to the cell. The other terminal was connected to the cell in the region of the working electrode[6]. Once connected to the galvanostat, the cell were evaluated in cycles, with constant pressure of O_2 (99.9%). The electrochemical tests were performed galvanostatically with electric current density of 0.05 mA.cm^{-2} and O_2 pressure of 1.5 atm, with potentials higher than 2.2 V and lower than 4.0 V (Yang and Xia 2010). The galvanostat was programmed to carry out 20 loading and unloading cycles.

3.3. Results and discussion

3.3.1. Electroplating of Co-W alloy

Table 3.2 shows the results of faradaic efficiency (ε) obtained for the 2^3 experimental design matrix used in the study of synthesized electrolytic bath prepared in laboratory. These results were analyzed using nonlinear regression. The mass of Co and W was obtained from the percentages of the metals evidenced by the EDX analysis and by the total deposit mass.

---

[6] New assays have shown that a time of 72 h allows OCP stability and proximity to the value of 2.96 V in the Li-O₂ cell.

Table 3.2. Matrix of 2^3 factorial experimental design plus faradaic efficiency

Exp.	I (mA·cm^{-2})	C_W (mol·L^{-1})	Substrate	m_{Co} (g)	m_W (g)	ε (%)
1	2 (-1)	0.1 (-1)	nickel foam (-1)	0	0	0
2	10 (+1)	0.1 (-1)	nickel foam (-1)	0.000 32	0.000 08	2.30
3	2 (-1)	0.3 (+1)	nickel foam (-1)	0.000 30	0.000 13	12.46
4	10 (+1)	0.3 (+1)	nickel foam (-1)	0.008 36	0.002 09	60.05
5	2 (-1)	0.1 (-1)	steel mesh (+1)	0	0	0
6	10 (+1)	0.1 (-1)	steel mesh (+1)	0.009 28	0.001 41	6.16
7	2 (-1)	0.3 (+1)	steel mesh (+1)	0.008 59	0.001 58	29.28
8	10 (+1)	0.3 (+1)	steel mesh (+1)	0.097 59	0.014 16	64.39
9	6 (0)	0.2 (0)	nickel foam (-1)	0.000 86	0.000 22	10.42
10	6 (0)	0.2 (0)	steel mesh (+1)	0.017 99	0.002 21	19.41
11	6 (0)	0.2 (0)	nickel foam (-1)	0.000 54	0.000 14	6.56
12	6 (0)	0.2 (0)	steel mesh (+1)	0.017 45	0.002 14	18.83
13	6 (0)	0.2 (0)	nickel foam (-1)	0.000 77	0.000 20	9.26
14	6 (0)	0.2 (0)	steel mesh (+1)	0.016 97	0.002 09	18.32
15	6 (0)	0.2 (0)	nickel foam (-1)	0.000 48	0.000 12	5.79
16	6 (0)	0.2 (0)	steel mesh (+1)	0.018 73	0.002 30	20.21

The faradaic efficiency (ε) can be estimated by Equation (7) at a 95% confidence level. The regression coefficient (R^2) obtained was 0.9360, which means that 93.60% of the variation around the average may be estimated by Equation (7). To obtain this model, the adjusted R² was observed and through the backward elimination tool of the *Statistica 7* software the highest adjusted R² value was sought, because this value is only higher in a model with more terms if these terms contribute the most to describe the response more than it would be expected by chance.

$$\varepsilon = 17.71 + 11.39 \cdot I + 19.71 \cdot C_W + 4.36 \cdot S + 9.28 \cdot I \cdot C_W + 2.16\, C_W \cdot S \tag{7}$$

where I is current density (mA·cm^{-2}), C_W is the concentration of Na₂WO₄·2H₂O (mol·L^{-1}) and S is the substrate (nickel foam or steel mesh).

Fig. 3.1 shows the linear distribution of predicted values compared to those observed. Assuming that the model follows a regular distribution, Equation (7) is suitable for the data interpretation. The Fisher's exact test was performed for analysis of variance (ANOVA) and the model obtained was significant according to the test. The ANOVA was used by several authors (Porto et al. 2017; Santana et al. 2007) to quantify the influence of the parameters on electroplating.
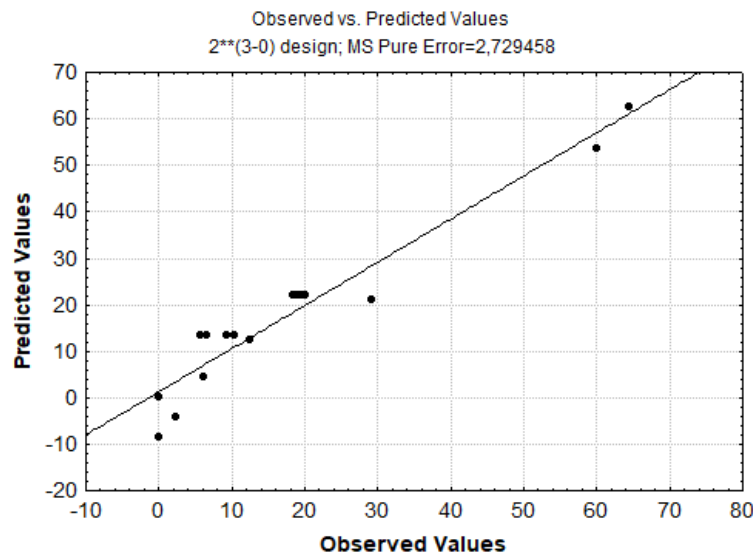
Figure 3.1. Representative graph of the values observed in comparison to the predicted values.

Table 3.3 shows that current density (1), concentration of sodium tungstate (2), substrate (3), the interaction between current density (1) and concentration (2), and the interaction between concentration (2) and substrate (3) had significant effects at a 95% confidence interval.

Table 3.3. Results of ANOVA for deposition efficiency

Source	Sum of squares	Degree of freedom	F	p
Current density (1)	1038.77	1	380.58	0.000001
Concentration of $Na_2WO_4.2H_2O$ (2)	3109.45	1	1 139.22	0.000000
Substrate (3)	304.15	1	111.43	0.000043
Interaction between 1 and 2	688.95	1	252.41	0.000004
Interaction between 2 and 3	37.41	1	13.71	0.010062

Fig. 3.2 shows the response surfaces methods for the nickel foam and steel mesh when varying the current density and sodium tungstate concentration. The increase of the current density and sodium tungstate concentration contributed to the increase of the electroplating efficiency for both substrates, however the greater efficiency occurred in the steel mesh. This result is the inverse of that obtained by other studies (Ghaferi et al. 2011; Ibrahim et al. 2003), which verified that the increase in current density decreases the amount of deposited tungsten. Reduction of tungsten is an activation-controlled reaction with low current densities, whereas diffusion becomes controlled by increasing current density (Obradovic et al.

2003). However, the current density applied in this research is small when compared to the research of the authors.
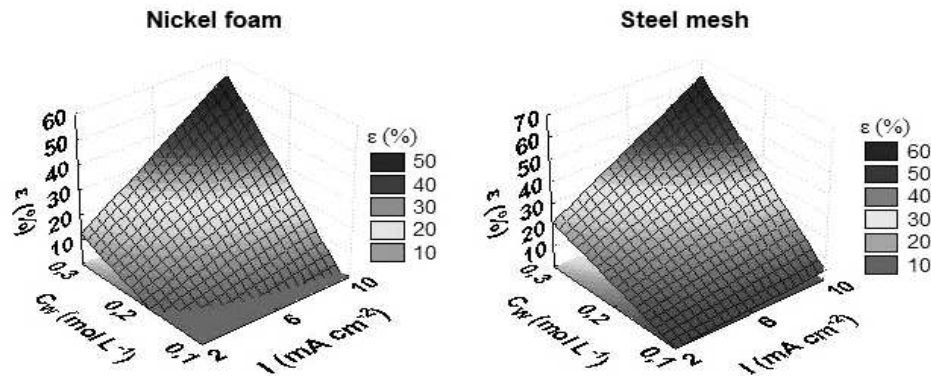
Figure 3.2. Response surfaces for the faradaic efficiency obtained on *Statistics 7* at a 95% confidence interval.

Comparing experiments 4 and 8, there was a higher mass of deposited Co-W in the steel mesh when compared to the nickel foam. The literature reports no studies with electroplating in nickel foam and steel mesh containing Co-W. Considering the steel coupons as substrate, there are several studies with deposition efficiencies: the Fe-Co-W alloy has 48 – 55 % iron (Fe), 39 – 42 % cobalt and 4 – 12 % tungsten, obtained by galvanostatic electrolysis (Yermolenko et al. 2017); and the Co-W-P alloy has 81 % cobalt, 10 % tungsten and 9 % phosphorus (P), obtained by potentiostatic electrolysis (Yun et al. 2008).

The pH values of the electrolytic bath also influenced on the electroplating and significantly affected the structure and properties of the electrodeposited alloys (Gómez et al. 2003; Dulal et al. 2007). For the sodium tungstate concentrations of 0.1, 0.2, and 0.3 mol·L⁻¹, the pH values of the electrolytic bath were 3.41, 4.27 and 5.79, respectively. The maximum mass percentages of W evidenced by the EDX analysis obtained for these pH values were 0.00141, 0.00221 and 0.00209 g in experiments 6, 10 and 4, respectively. Depending on the pH used for Co-W electroplating, a different percentage of W content and structure may be obtained. The increase in pH contributes to the evolution from lenticular to nodular growth (Tsyntaru 2016).

The tungsten chemical species that appear in the pH range of the cobalt complexes are predominantly the para-tungsten A (Prasad et al. 2007). According to the tungsten species graphs obtained by the Hydra-Medusa software showed that the range of this species was

between the pH values of 6 and 9.3, according to the concentrations of sodium tungstate in the bath. The electroplating of tungsten was possible even when using a bath with pH values lower than 6, because the Co-W alloy was formed, which may have occurred by the species $HW_6O_{21}^{5-}$.

Studies on Co-W-P film deposited from acid solution demonstrated higher amounts of tungsten and phosphorus and were amorphous; while films deposited from an almost neutral solution were polycrystalline and contained hexagonal cobalt (Dulal et al. 2007). Su et al. (2012) observed the influence of the pH and the complexing agent on the formation of Co-W coatings and verified that at pH 3 the alloy showed a lower hardness, and according to the SEM analysis, there was the formation of needle-type crystallites with crystallite size below 1.0 µm, demonstrating effects on the microstructure and tribological properties of the coatings. The deposition time can also influence the formed alloy. Studies with electrodeposition of nickel on porous aluminum substrates have observed that the increased deposition time caused excessive oxidation of the substrate, which was proved by TEM (Zamora et al. 2011). The properties of multilayer deposits are influenced by the electrolyte composition, deposition currenty, additives, pH of the solution and substrates (Turoňová et al. 2015).

3.3.2. Crystallinity of Co-W coating

Fig. 3.3 shows the X-ray patterns of Co-W coatings deposited that had a hexagonal close-packed structure. To observe the Co-W characteristic peaks, the diffractograms of the nickel foam and steel mesh substrates were also added. The peak due to nickel (Ni) metal was observed at 45.07, 52.55 and 77.55° corresponding respectively to crystallographic planes (111), (200) and (220) (Wang et al. 2013). For the steel mesh substrate the peak of Cr at 44.39° (011), Fe at 50.92° (011) and Fe-C 74.68° (220) (JCPDS card N° 00-0221, 00-6657, 23-0298), was observed. Due to the thin deposition layer[7], most of the samples show the substrate peaks. However, samples with higher deposition showed amorphous characteristics. The Co-W coatings exhibit a hexagonal close-packed structure at room temperature (Su et al. 2012). The increase of the sodium tungstate concentration and the current density generated peaks of Co in the background of spectra according to experiment 8, which allowed the observation with 41.73 and 47.51°, corresponding respectively to crystallographic planes (100) and (101) (Ghaferi et

---

[7] Thin deposit layers need high resolution equipment.

al. 2015). The peaks found in these alloy are characteristic of cobalt, which indicates a complete dissolution of tungsten in cobalt and, therefore, formation of a solid monophasic solution[8]. Studies with Co-25 wt·% W alloys also observed the presence of this monophase (Tsyntaru et al. 2009). For experiment 8, Co-10.77 wt·% W alloy were obtained using EDX analysis, which was the sample that had the largest amount of mass of electrodeposited alloy.
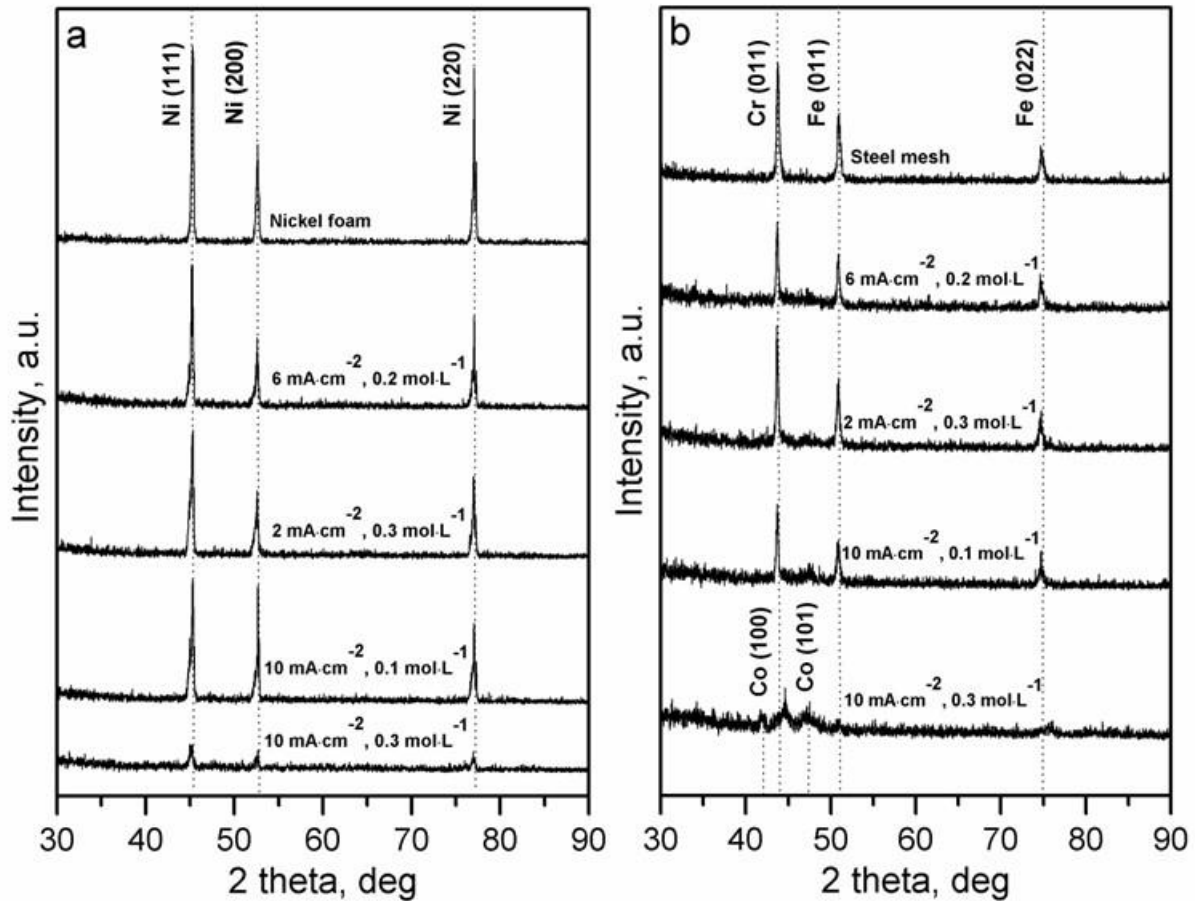
Figure 3.3. X-ray diffraction (XRD) patterns of cobalt-tungsten (Co-W) electrodeposited coatings in a) nickel foam and b) steel mesh.

Due to the introduction of refractory metal, the Co-W alloy consisted of an amorphous coating. In addition, the amorphizing agent was added to the electrolytic bath. Co-W alloys can form thermodynamically stable intermetallic compounds, such as Co_3W, which are generally amorphous and hard (Gómez et al. 2003; Tsyntaru et al. 2013).

---

[8] By XRD was not found W, however the EDX indicated peaks of metal W.

3.3.3. Coating morphology and Co-W distribution in the alloy

Fig. 3.4 shows the SEM of four samples that had varied current density. For both substrates, nickel foam and steel mesh, the increase of current density made the surface less uniform due to larger grain size (Ghaferi et al. 2015). The electrodeposited alloys adhered well to the substrate. The deposits could be folded without evident peeling and some cracks could occur, as shown in Fig. 3.4b-d (Gáliková et al. 2006; Vernickaite et al. 2016[b]), which are the samples that had the largest amounts of mass of electrodeposited alloy.
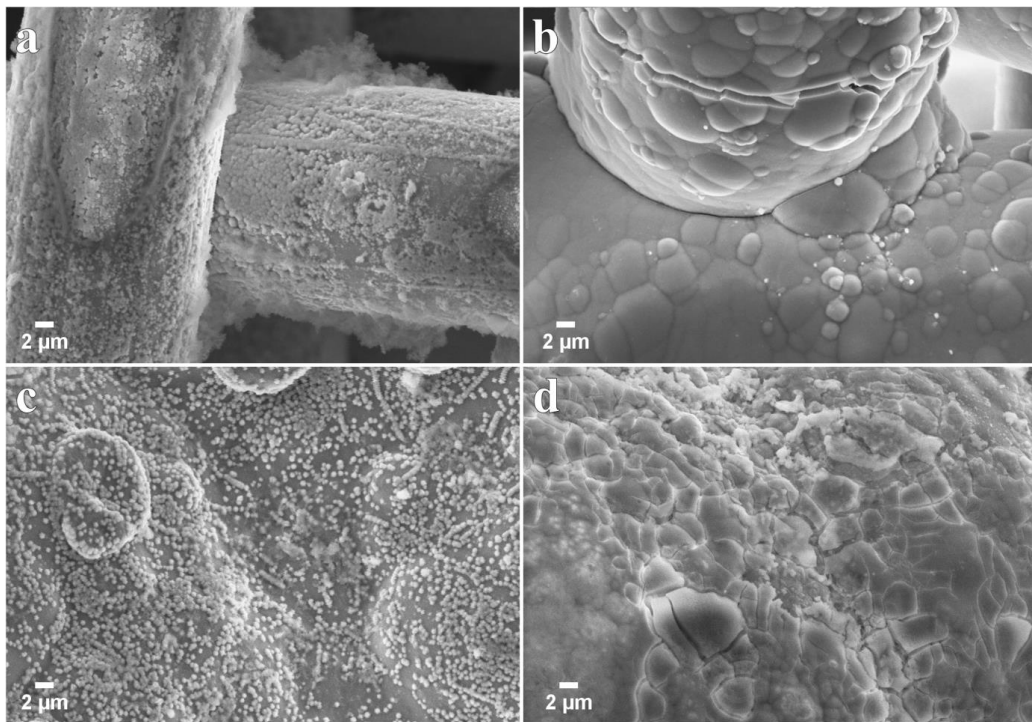
Figure 3.4. Scanning electronic microscope (SEM) micrographs of cobalt-tungsten (Co-W) coatings produced at (a) 2 mA·cm^{-2} (exp. 7) and (b) 10 mA·cm^{-2} (exp. 8) in steel mesh; (c) 2 mA·cm^{-2} (exp. 3) and (d) 10 mA·cm^{-2} (exp. 4) in nickel foam.

The surface morphology showed semi-spherical clusters of cauliflower type that are typical of low-concentration W alloys, as reported in previous studies (Della Noce et al. 2014; Oliveira et al. 2015). The size of the cauliflower nodule can decrease by increasing the current density and bath temperature, which promotes the increase in microhardness (Vernickaite et al. 2016[b]). In Fig. 3.4b-d, the cauliflower-type nodule is larger for higher current density applied.

3.3.4. Deposition rate and fluid dynamic effects

Study on the influence of cathode rotation was performed by evaluating the actual deposition rate in comparison with the deposition rate obtained by forced convection applied to the system. For this, the convective heat transfer coefficient (K_c) was calculated for each test and for each component of the alloy (Co and W). The diffusivity values of Co^{2+} and WO_4^{2-} in relation to water and the kinematic viscosity of water at 25°C were obtained from tabulated values (Li and Gregory 1974; Crittenden et al. 2012). As the speed of rotation did not vary, values for all experiments were obtained: K_{cCo} – 1.08×10^{-3} cm·s⁻¹, K_{cW} – 1.30×10^{-3} cm·s⁻¹, Re – 527.70, S_{cCo} – 1277.54 and S_{cW} – 967.50. The value of the deposition rate (W_A) was calculated using Equation 5. The real deposition rate (W_{real}) was calculated by dividing the final mass of each element "A" in the alloy by the deposition time (3,600 seconds). The results obtained for the deposition rate parameters are in Table 3.4.

Table 3.4. Results of deposition rate parameters

Exp.	C_f (10^{-2} g·cm⁻³)		W_A (g·s⁻¹)		W_{real} (g·s⁻¹)	
	Co	W	Co	W	Co	W
1	1.77	1.84	-	-	-	-
2	1.77	1.84	1.09×10^{-8}	0.33×10^{-8}	8.89×10^{-8}	2.22×10^{-8}
3	1.77	5.51	1.02×10^{-8}	0.53×10^{-8}	8.33×10^{-8}	3.61×10^{-8}
4	1.75	5.51	0.28×10^{-6}	0.85×10^{-7}	2.32×10^{-6}	5.81×10^{-7}
5	1.77	1.84	-	-	-	-
6	1.75	1.84	1.57×10^{-6}	2.88×10^{-7}	2.58×10^{-6}	3.92×10^{-7}
7	1.75	5.51	1.46×10^{-6}	3.23×10^{-7}	2.39×10^{-6}	4.39×10^{-7}
8	1.57	5.49	1.66×10^{-5}	2.89×10^{-6}	2.71×10^{-5}	3.93×10^{-6}
9	1.77	3.68	0.29×10^{-7}	0.90×10^{-8}	2.39×10^{-7}	6.11×10^{-8}
10	1.73	3.67	3.05×10^{-6}	4.51×10^{-7}	5.00×10^{-6}	6.14×10^{-7}
11	1.77	3.68	0.18×10^{-7}	0.57×10^{-8}	1.50×10^{-7}	3.89×10^{-8}
12	1.73	3.67	2.96×10^{-6}	4.37×10^{-7}	4.85×10^{-6}	5.94×10^{-7}
13	1.77	3.68	0.26×10^{-7}	0.82×10^{-8}	2.14×10^{-7}	5.56×10^{-8}
14	1.73	3.67	2.88×10^{-6}	4.27×10^{-7}	4.71×10^{-6}	5.81×10^{-7}
15	1.77	3.68	0.16×10^{-7}	0.49×10^{-8}	1.33×10^{-7}	3.33×10^{-8}
16	1.73	3.67	3.18×10^{-6}	4.70×10^{-7}	5.20×10^{-6}	6.39×10^{-7}

According to Table 3.4, the forced convection provided by the cathode rotation is one of the main phenomena related to the deposition rate, having significant values of the actual deposition rates. For the steel mesh substrate, the deposition occurred in great proportion due to the phenomenon of forced convection, evidenced by W_A values, having for Co: 60.85 – 61.25

%, and W: 73.45 – 73.58 % of W_{real} value. As for the nickel foam substrate, the forced convection contributed in a lower proportion to the deposition, which can be explained by other factors that govern the system, such as the reaction speed. The larger surface area of the steel mesh substrate favored the increase in mass transfer.

3.3.5. Open circuit potential and electrode performance in the cell

After the time of 4 hours in the glove box, the open circuit potential (OCP) values varied for all experiments as shown in Figure 5. The standard thermodynamic potential for LiO_2 formation is 2.96 V (Imanish and Yamamoto 2014), which considers conditions for the growth of Li_2O_2 crystals on a Li_2O_2 surface. However, the equilibrium potential for the surface reaction of the Co-W alloy on the nickel or steel substrate can often be different from this value. OCP of Li-O₂ cells is a function of the assembly method, temperature, load / discharge conditions, exposure to different O_2 partial pressures, ranging from 2.8 to 3.3 V, however there are studies with lower OCP values (Sevim et al. 2016).

The discharge capacities for the electrodes with the highest amounts of Co-W alloy were the lowest values. For electrodes containing small amounts of catalyst, for example, experiment 2 (0.4 milligrams), the maximum discharge capacity was 14.01 $mAh.g_c^{-1}$. The same result was observed by another study (Xiao et al. 2010) that attributed the decrease of the capacity related to the fall of the porosity of the nickel foam, due to the greater filling of the catalyst, which made it difficult to diffuse O_2[9]. As for the substrate used, there was a certain similarity of the obtained capacities, for example, the comparison between experiment 4 and 8, and between 3 and 7 as shown in Fig. 3.5, which suggests that the steel mesh can be used as an electrode instead of nickel foam due to the lower cost.

---

[9] The authors found that electrode porosity decreased significantly after discharge. This reduction can be attributed due to pore occupancy by the Li_2O or Li_2O_2 reaction product. In addition, the wettability of the electrolyte may not have been adequate to allow stability with the air electrode.
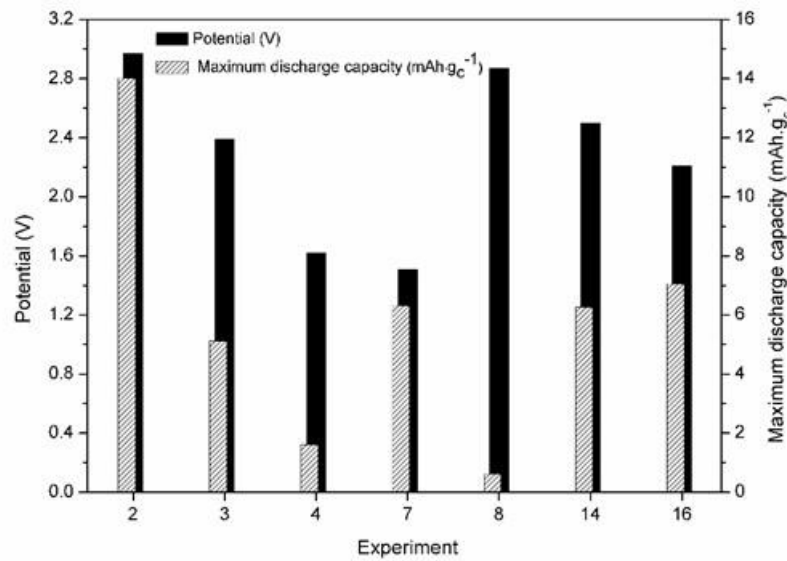
Figure 3.5. OCP values and maximum discharge capacity of the electrodes.

3.4. Conclusions

The studied variables affect the composition of coating alloys, crystallinity, morphology and deposition efficiency. The substrates used showed similar electroplating efficiencies, even though they had different composition and morphology. Amorphous coatings were obtained in the experiments. The higher surface area of the electrode favored the mass transfer by forced convection, according to the results of the Co-W deposition rate in the steel mesh. The electrodes presented characteristics for application in batteries, as OCP and capacity of reversibility. Thus, the alloy obtained in these materials presents an alternative for Li-O₂ catalytic systems, being coatings deposited in substrates with high surface area that have morphological and structural capacity to house discharge products of the battery.

Acknowledgements

References

Awadallah EA (2015) Promoting effect of group VI metals on Ni/MgO for catalytic growth of carbon nanotubes by ethylene chemical vapour deposition. Chem Pap 69:316-324. doi: 10.1515/chempap-2015-0029

Banhart J (2001) Manufacture, characterisation and application of cellular metals and metal foams. Prog Mater Sci 46:559-632. doi: 10.1016/S0079-6425(00)00002-5

Bera P, Seenivasan H, Rajam KS, Grips VKW (2012) XRD, FESEM and XPS studies on heat treated Co-W electrodeposits. Mater Lett 76:103-105. doi: 10.1016/j.matlet.2012.02.046

Cameán I, Lavela P, Tirado JL, García AB (2010) On the electrochemical performance of anthracite-based graphite materials as anodes in lithium-ion batteries. Fuel 89:986-991. doi: 10.1016/j.fuel.2009.06.034

Cho Y-B, Moon S, Lee C, Lee Y (2017) One-pot electrodeposition of cobalt flower-decorated silver nanotrees for oxygen reduction reaction. App Surf Sci 394:267-274. doi: 10.1016/j.apsusc.2016.10.068

Choi R, Jung J, Kim G, Song K, Kim Y-I, Jung SC, Han Y-K, Song H, Kang Y-M (2014) Ultra-low overpotential and high rate capability in Li-O₂ batteries through surface atom arrangement of PdCu nanocatalysts. Energy Environ Sci 7:1362-1368. doi: 10.1039/c3ee43437k

Crittenden JC, Trussell RR, Hand DW, Howe KJ, Tchobanoglous G (2012) MWH's Water Treatment: Principles and Design. 3 rd ed. Hoboken: Jhon Wiley and Sons.

Della Noce R, Benedetti AV, Magnani M, Passamani EC, Kumar H, Cornejo DR, Ospina CA (2014) Structural, morphological and magnetic characterization of electrodeposited Co-Fe-W alloys. J Alloys Compd 611:243-248. doi: 10.1016/j.jallcom.2014.05.157

Dulal SMSI, Yun HJ, Shin CB, Kim C-K (2007) Electrodeposition of CoWP film: III. Effect of pH and temperature. Electrochim Acta 53:934-943. doi: 10.1016/j.electacta.2007.08.006

Gan L, Murakami H, Saeki I (2018) High temperature oxidation of Co-W electroplated type 430 stainless steel for the interconnect of solid oxide fuel cells. Corros Sci 134:162-168. doi: 10.1016/j.corsci.2018.02.026

Gáliková Z, Chovancová M, Danielik V (2006) Properties of Ni-W alloy coatings on steel substrate. Chem Pap 60:353-359. doi: 10.2478/s11696-006-0064-2

Ghaferi Z, Raeissi K, Golozar MA, Edris H (2011) Characterization of nanocrystalline Co-W coatings on Cu substrate, electrodeposited from a citrate-ammonia bath. Surf Coat Techn 206:497-505. doi: 10.1016/j.surfcoat.2011.07.074

Ghaferi Z, Sharafi S, Bahrololoom ME (2015) Effect of current density and bath composition on crystalline structure and magnetic properties of electrodeposited FeCoW alloy. Appl Surf Sci 355:766-773. doi 10.1016/j.apsusc.2015.07.083

Gittleson FS, Sekol RC, Doubek G, Linardi M, Taylor AD (2014) Catalyst and electrolyte synergy in Li-O₂ batteries. Phys Chem Chem Phys 16:3230-3237. doi: 10.1039/c3cp54555e

Gómez E, Pellicer E, Vallés E (2003) Influence of the bath composition and the pH on the induced cobalt–molybdenum electrodeposition. J Electroanal Chem 556:137-145. doi: 10.1016/S0022-0728(03)00339-5

Ibrahim MAM, Abd El Rehim SS, Moussa SO (2003) Electrodeposition of noncrystalline cobalt-tungsten alloys from citrate electrolytes. J Appl Electrochem 33:627-633. doi: 10.1023/A:1024916903544

Imanishi N, Yamamoto O (2014) Rechargeable lithium-air batteries: characteristics and prospects. Mater Today 17:24-30. doi: 10.1016/j.mattod.2013.12.004

Li F, Ohnishi R, Yamada Y, Kubota J, Domen K, Yamada A, Zhou H (2013) Carbon supported TiN nanoparticles: an efficient bifunctional catalyst for non-aqueous Li-O₂ batteries. Chem Comm 49:1175-1177. doi: 10.1039/c2cc37042e

Li J, Deng N, Wu P, Zhou Z (2019) Elaborating the Cu-network structured of the W-Cu composites by sintering intermittently electroplated core-shell powders. J Alloys Compd 770:405-410. doi: 10.1016/j.jallcom.2018.08.158

Li Y-H, Gregory S (1974) Diffusion of ions in sea water and in deep-sea sediments. Geochim Cosmochim Ac 38:703-714. doi: 10.1016/0016-7037(74)90145-8

Lu YC, Gasteiger HA, Crumlin E, McGuire R, Horn S (2010) Electrocatalytic activity studies of select metal surfaces and implications in Li-air batteries. J Electrochem Soc 157:1016-1025. doi: 10.1149/1.3462981

McKloskey BD, Scheffler R, Speidel A, Bethune DS, Shelby RM, Luntz AC (2011) On the efficacy of electrocatalysis in nonaqueous Li-O₂ batteries. J Am Chem Soc 133: 18038-18041. doi: 10.1021/ja207229n

Obradovic MD, Stevanovic RM, Despic AR (2003) Electrochemical deposition of Ni-W alloys from ammonia-citrate electrolyte. J Electroanal Chem 552:185-196. doi: 10.1016/S0022-0728(03)00151-7

Oh SH, Black R, Pomerantseva E, Lee J-H, Nazar LF (2012) Synthesis of a metallic mesoporous pyrochlore as a catalyst for lithium-O₂ batteries. Nat Chem 4:1004-1010. doi: 10.1038/nchem.1499

Oliveira ALM, Costa JD, de Sousa MB, Ja J, Alves N, Campos ARN, Santana RAC, Prasad S (2015) Studies on electrodeposition and characterization of the Ni-W-Fe alloys coatings. J Alloys Compd 619:697-703. doi: 10.1016/j.jallcom.2014.09.087

Prasad S, Santana RAC, Campos ARN, Leite VD (2007) Potentiometric and conductometric studies on the system acid-isopolytungstate and the formation of lanthanum tungstates. Eclet Quím 32:71-78. doi: 10.1590/S0100-46702007000100010

Porto MB, Alvim LB, de Almeida Neto AF (2017) Nickel removal from wastewater by induced co-deposition using tungsten to formation of metallic alloys. J Clean Prod 142:3293-3299. doi: 10.1016/j.jclepro.2016.10.140

Ren X, Zhang SS, Tran DT, Read J (2011) Oxygen reduction reaction catalyst on lithium/air battery discharge performance. J Mater Chem 21:10118-10125. doi: 10.1039/c0jm04170j

Santana RAC, Campos ARN, Prasad S, Leite VD (2007) Optimization of the electrolytic bath for electrodeposition of corrosion resistant Fe-W-B alloys. Quím Nova 30:360-365. doi: 10.1590/S0100-40422007000200023

Sevim M, Francia C, Amici J, Vankova S, Sener T, Metin O (2016) Bimetallic MPt (M: Co, Cu, Ni) alloy nanoparticles assembled on reduced graphene oxide as high performance cathode catalysts for rechargable lithium-oxygen batteries. J Alloy Compd 683:231-240. doi: 10.1016/j.jallcom.2016.05.094

Sivagami IN, Prasanna K, Santhoshkumar P, Jo YN, Seo GY, Lee CW (2017) Agar templated electrodeposition of binary zinc-cobalt alloy and formation of zinc-cobalt-carbon nanocomposite for application in secondary lithium batteries. J Alloys Compd 697: 450-460. doi: 10.1016/j.jallcom.2016.08.177

Song L, Wang T, Ma Y, Xue H, Guo H, Fan X, Xia W, Gong H, He J (2017) Functional species encapsulated in nitrogen-doped porous carbon as a highly efficient catalyst for the oxygen reduction reaction. Chem Eur J 23:3398-3405. doi: 10.1002/chem.201605026

Su F-H, Liu C-S, Huang P (2012) Effect of complexing agents and pH on microstructure and tribological properties of Co-W coatings produced by double pulse electrodeposition. Appl Surf Sci 258:6550-6557. doi: 10.1016/j.apsusc.2012.03.075

Taymaz I, Benli M (2014) Emissions and fuel economy for a hybrid vehicle. Fuel 115:812-817. doi: 10.1016/j.fuel.2013.04.045

Tsyntaru N (2016) Electrodeposition of cobalt-tungsten alloys and their application for surface engineering. Russian J Electrochem 52:1041-1047. doi: 10.1134/S1023193516110136

Tsyntsaru N, Dikusar A, Cesiulis H, Celis JP, Bobanova Zh, Sidelnikova S, Belevskii S, Yapontseva Yu, Bersirova O, Kublanovskii V (2009) Tribological and corrosive characteristics of electrochemical coatings based on cobalt and iron superalloys. Powder Metall Met Ceram 48:419-428. doi: 10.1007/s11106-009-9150-7

Tsyntsaru N, Cesiulis H, Pellicer E, Celis J-P, Sort J (2013) Structural, magnetic, and mechanical properties of electrodeposited cobalt–tungsten alloys: Intrinsic and extrinsic interdependencies. Electrochim Acta 104:94-103. doi: 10.1016/j.electacta.2013.04.022

Turoňová AM, Capik M, Oriňaková R, Gál M (2015) Electrolytic preparation of nanosized Cu/Ni-Cu multilayered coatings. Chem Pap 69:462-469. doi: 10.1515/chempap-2015-0035

Vernickaite E, Tsyntsaru N, Cesiulis H (2016[a]) Electrodeposited Co-W alloys and their prospects as effective anode for methanol oxidation in acidic media. Surf Coat Techn 307:1322-1328. doi: 10.1016/j.surfcoat.2016.07.049

Vernickaite E, Tsyntsaru N, Cesiulis H (2016[b]) Electrochemical co-deposition of tungsten with cobalt and copper: Peculiarities of binary and ternary alloys coatings formation. Surf Coat Techn 307:1341-1349. doi: 10.1016/j.surfcoat.2016.07.025

Wang L, Li D, Koike M, Watanabe H, Xu Y, Nakagawa K, Tomishige K (2013) Catalytic performance and characterization of Ni-Co catalysts for the steam reforming of biomass tar to synthesis gas. Fuel 112:654-661. doi: 10.1016/j.fuel.2012.01.073

Wang L, Gao Y, Xu T, Xue Q (2006) A comparative study on the tribological behavior of nanocrystalline nickel and cobalt coatings correlated with grain size and phase structure. Mater Chem Phys 99:96-103. doi: 10.1016/j.matchemphys.2005.10.014

Welty JR, Wicks CE, Wilson RE, Rorrer GL (2007) Fundamentals of Momemtum, Heat and Mass Transfer." 5 th ed. Hoboken: Jhon Wiley and Sons, pp. 589-591

Xiao J, Wang D, Xu W, Wang D, Williford RF, Liu J, Zhang J-G (2010) Optimization of Air Electrode for Li/Air Batteries. J Electrochemical Soc 157:A487-A492. doi: 10.1149/1.3314375

Yang X-H, Xia Y-Y (2010) The effect of oxygen pressures on the electrochemical profile of lithium/oxygen battery. J Solid State Eletrochem 14:109-114. doi: 10.1007/s10008-009-0791-8

Yermolenko IY, Ved MV, Sakhnenko ND, Sachanova YI (2017) Composition, morphology, and topography of galvanic coatings Fe-Co-W and Fe-Co-Mo. Nanoscale Res Lett 12:1-9. doi: 10.1186/s11671-017-2128-3

Yun HJ, Dulal SMSI, Shin CB, Kim C-K (2008) Characterisation of electrodeposited Co-W-P amorphous coatings on carbon steel. Electrochim Acta 54:370-375. doi: 10.1016/j.electacta.2008.07.068

Zamora G, Arurault L, Winterton P, Bes R (2011) Impact of the type of anodic film formed and deposition time on the characteristics of porous anodic aluminium oxide films containing Ni metal. Chem Pap 65:460-468. doi: 10.2478/s11696-011-0039-9

Zemanová M, Kurinec R, Jorík V, Kadleĉiková (2012) Ni-W alloy coatings deposited from a citrate electrolyte. Chem Pap 66:492-501. doi: 10.2478/s11696-011-0116-0

CHAPTER 4

Ag-Co electrocatalysts for rechargeable lithium-O₂ batteries: O₂ pressure and current density effects

Ag-Co electrocatalysts for rechargeable lithium-O₂ batteries:
O₂ pressure and current density effects

Josiel Martins Costa and Ambrósio Florêncio de Almeida Neto

Abstract

In this study, we evaluated the Ag-Co alloy as a catalyst in the Li-O₂ battery electrode aiming to improve the electrochemical performance of the energy system. Ag-Co alloys were obtained by cyclic voltammetry from an electrolytic bath. The influence of O₂ pressure (1.5, 2.0 and 2.5 atm) and current density (25, 50 and 75 $\mu A \cdot cm^{-2}$) on the charge and discharge on cell were studied. It was observed that a medium value of O₂ pressure and current density was favorable to obtain a high capacity. Energy-dispersive X-ray presented that the cyclic voltammetry technique did not favor cobalt deposition. Scanning electron microscopy showed homogeneity of the deposits with the presence of cracks and small crystals. X-ray diffraction evidenced Li_2O as well as Raman spectra for nickel foam electrode. Oxygen evolution reaction was improved with Ag-Co catalyst according linear sweep voltammetry and cyclic voltammetry analysis. Steel mesh electrode showed higher discharge capacity (336 $mAh \cdot g_c^{-1}$) when compared to nickel foam (115 $mAh \cdot g_c^{-1}$) which suggests that materials with lower cost can be used as electrodes in Li-O₂ batteries.

Keywords: Storage system; Electrodeposition; Alloy; New material.

4.1. Introduction

The global energy demand from fossil fuels is unsustainable due to their increasing cost and fast depletion, as well as the greenhouse effect caused by the continuous consumption and application of these fuels [1]. Global warming and finite oil reserves characterize two problems that are pressing the traditional vehicle industry [2]. The search for cleaner energy sources is required to shift focus to the generation of energy from electrochemical systems, batteries and fuel cells, solar cells, and super capacitors, among others.

In this sense, oxygen reduction reaction (ORR) and oxygen evolution reaction (OER) is an important cathodic phenomenon in proton exchange membrane fuel cells and batteries to obtain energy [3]. Therefore, the development of non-platinum electrocatalysts with high electroactivity for these reactions has been the main objective of the study on electrocatalysts, because Pt-based catalysts are expensive, rare, and unstable for long-term applications. Recently, Ag-Mn, Ag-Cd, Ag-Cu and Ag-Co alloyed electrocatalysts have been shown to possess good electrocatalytic activity toward ORR [4-7]. Specifically the Ag-Co alloy, studies showed the electrocatalytic effect of silver is enhanced by the addition of cobalt, which was able to break the O–O bond of molecular oxygen, thus accelerating the first step of the reduction mechanism. At the same time, research was to further reduce the cost of catalyst, reducing the amount of Ag, which, even though being much less expensive than Pt, is still a noble metal [8].

Studies evaluated the ORR-OER using a Co-P bifunctional catalyst. The high discharge capacity, excellent rate capability and cycle stability of the Co-P based in LiO_2 batteries was obtained [9]. Ag-Co catalysts with varying stoichiometric proportions by electrodeposition were synthesized [10]. The electrode with Ag: Co ratio of 1:7 showed the best ORR activity. The alloy composed of Ag_1Co_7 electrodeposited for 200 s, with approximately 14% Co, showed the highest catalytic activity of ORR, being better or comparable to platinum.

In addition the catalyst, the oxygen pressure and the current density also impact on the capacity and reversibility of the system. When the oxygen pressure increases from 1 to 10 atm, the discharge capacity increases drastically, especially at high current densities [11]. The effects of O_2 pressure on Li-O₂ was investigated with values of 1 to 25 atm [12]. Transitioning from 1 up to 10 atm increased the discharge capacity 50% at 100 $\mu A \cdot cm^{-2}$, however the performance of the cell saw diminishing returns for the cell at pressures above 10 atm, with 25

atm cells not showing a significant difference in performance over 10 atm. Thus, in this study, we synthesized Ag-Co alloy on two electrodes (nickel foam and steel mesh) and evaluated the influence of O$_2$ pressure and current density on the cycling of Li-O$_2$ using Ag-Co as catalysts. Furthermore, the electrocatalyst were characterized by linear sweep voltammetry (LSV), cyclic voltammetry (CV), scanning electron microscopy (SEM), energy dispersive spectrometry (EDX), X-ray diffraction (XRD), Raman spectra, based on the performance of experiments in a Li-O$_2$ cell.

4.2. Experimental

4.2.1. Preparation of cathodes

The alloys of this study were deposited in 1 cm diameter nickel foam and steel mesh (400 mesh). This size allows the addition of the circle in the Li-O$_2$ cell. Steel mesh electrodes were used with 3 circles of 1 cm in diameter joined by the ends and folded one over the other. The surfaces of the nickel foam and the steel mesh were cleaned with 10% NaOH and 1% H$_2$SO$_4$, lasting 1 min. After the chemical treatment, the substrate was dried in an oven at 100°C and placed in the desiccator, for subsequent measurement of initial mass.

4.2.2. Electrolytic bath and electrodeposition of the Ag-Co alloy

Electrolytic baths were prepared from salts of high analytical purity. Silver nitrate, AgNO$_3$, silver source salt 0.002 mol·L^{-1}; cobalt sulfate, CoSO$_4$.7H$_2$O, cobalt source salt 0.1 mol·L^{-1} and sodium chloride, NaCl 3.5 mol·L^{-1} [13]. For the electrodeposition tests, a rotating disk electrode was used (pattern 616A, Princeton Applied Research), a potentiostat/galvanostat (VersaStat 3, Princeton Applied Research) and a pH meter. The Ag-Co alloy was synthesized at room temperature using cyclic voltammetry (CV) with a scanning rate of 50 mV·s^{-1}, with a potential range of -1.0 to +0.2 V (V vs Ag$^+$/AgCl). The number of cycles was determined from preliminary tests, in order to deposit small amounts, close to 1 mg. For each bath 3 samples were synthesized, using 12, 15 and 20 cycles, respectively. The initial pH was adjusted to 2.80 using nitric acid and the cathodic rotation was maintained at 100 rpm. A cell composed of three electrodes was used: the working electrode (nickel foam or steel mesh), the reference electrode (Ag$^+$/AgCl) and counter electrode (cylindrical hollow platinum mesh).

4.2.3. Preparation of Li-O₂ battery and electrochemical measurements

The battery was assembly in a Glove-Box (MBRAUN-LABstar Workstation) under argon atmosphere in this order: a lithium blade (1.6 cm diameter), 50 µL of electrolyte (anhydrous dimethylsulfoxide with lithium perchlorate 0.1 $mol \cdot L^{-1}$) [14], a gas fiber filter sheet (2 cm diameter), 50 µL of electrolyte, an electrode (nickel foam or steel mesh), a porous stainless steel screen and a stainless steel spring for electric contact [15, 16].

After assembly and proper sealing, a rest time of at least 4 h was waited before the electrochemical tests began. Cells were tested using a two-catalyst configuration with constant O_2 pressure of (99.9%). The electrochemical tests were performed galvanostatically, with potentials higher than 2.2 V and lower than 4.0 V. For this study was used a factorial design 2^2 with triplicate at the central point, with three different values of current density (25, 50 and 75 $\mu A \cdot cm^{-2}$), O_2 pressures (1.5, 2.0 and 2.5 atm) [17] and two substrates (nickel foam and steel mesh)[10].

The OER linear sweep voltammetry (LSV) curves were recorded at a scan rate of 5 $mV \cdot s^{-1}$, and CV at a scan rate of 20 $mV \cdot s^{-1}$ in 1 M KOH purged with pure O_2 gas at room temperature. A spiral platinum and Hg/HgO (0.098 V vs. SHE) electrodes were used as counter electrode and reference electrode, respectively[11].

4.2.4. Chemical, microstructural and physical characterization

4.2.4.1 Microstructure and chemical composition

The microstructure and chemical composition of the alloys were obtained by SEM, model Leo 440i, equipped with X-Ray Energy Dispersion Spectrometer (LEO Electron Microscopy/Oxford, Cambridge, England) model 6070. It was made magnifications of 5000 times. In addition, the discharge products were investigated by a Raman spectroscopy (Renishaw InVia), using an excitation wavelength of 633 nm.

---

[10] See Appendix A.

[11] Although the electrode environment in the Li-O₂ cell is different from the alkaline environment tests, the catalytic activity is measured using KOH as electrolyte.

4.2.4.2 Physical properties

XRD analysis was performed to visualize peaks of metal and discharge products, and to calculate crystallite size. It was used the K-alpha copper scanning method, 40 kV voltage, 40 mA current, 2θ ranging from 20 to 90° with a pitch of 0.02°, speed $0.033° \cdot s^{-1}$ and length of wave of 1.54 Å on a Philips Analytical X Ray diffractometer and X'Pert-MPD model.

4.3. Results and discussion

4.3.1. Morphology and Li-O₂ battery performance

Table 4.1 shows the 14 electrodes, being represented by the letter E, the nickel foam and M, the steel mesh. Other variables are arranged, such as the electric current density applied (I), the O₂ pressure (P). The mass of the catalyst in the electrode (m_{cat}), the open circuit potential (OCP) and maximum charge capacity (MCC) are also arranged.

Table 4.1. Variables (I, P) and results (m_{cat}, OCP, MCC, number of cycles) of the electrodes

Electrode	I ($\mu A \cdot cm^{-2}$)	P (atm)	m_{cat} (mg)	OCP (V)	MCC ($mAh \cdot g_c^{-1}$)	Number of cycles
E1	25	1.5	1.2	3.06	14	4
E2	25	2.5	1.0	2.98	14	20
E3	75	1.5	1.0	2.28	263	2
E4	75	2.5	1.6	2.89	74	1
E5	50	2.0	1.3	2.99	39	15
E6	50	2.0	1.0	3.06	45	12
E7	50	2.0	1.0	1.75	278	2
M1	25	1.5	3.9	2.95	7.6	10
M2	25	2.5	1.0	2.48	127	3
M3	75	1.5	1.0	2.88	125	15
M4	75	2.5	1.2	2.11	101	20
M5	50	2.0	1.1	3.16	170	7
M6	50	2.0	1.6	2.83	220	8
M7	50	2.0	1.1	3.09	130	20
M8	50	2.0	1.0	2.87	155	20

From the data in Table 4.1 it was verified that the amount of mass deposited in each electrode remained practically constant, close to 1 mg using cyclic voltammetry. Through the Statistica software it was verified that no variables had significant effect, and also did not

interact. The standard thermodynamic potential for the formation of Li-O_2 is 2.96 V [18], which was the value obtained by some electrodes. However due to the non-homogeneity of the electrodes and the interaction at the electrode-electrolyte interface, some values ranged from 2.96 V. The OCP slightly higher than the theoretical 2.96 V can be due to residual water adsorbed to the steel wall of the chamber and / or the residual water present in the oxygen gas [19]. In general, all the cycles were programmed to occur in the initial 15 s of the OCP measurement, followed by discharge and subsequent loading, for another 19 cycles, totaling 20 cycles. However, the electrodes E3, E4 and E7 performed the discharge rapidly, which can be observed by in Fig. 4.1 - a. The first discharge showed low capacity, the first charge showed high capacity. The charge (O_2 evolution reaction, OER) varies significantly and depends on the discharge rate, the excess potential and the discharge depth, as well as the configuration of the cell (electrolyte, catalyst and cathode material) [20].

According to Table 1, samples E3 and E4 had between 1 and 2 cycles, which is not beneficial to the system, since reversibility is expected after each loading and unloading. This low reversibility may be related to the current applied in these two samples, which was 75 $\mu A \cdot cm^{-2}$. The discharge of the Li-O_2 battery depends on the O_2 reduction reaction (ORR) that produces solid Li_2O_2 on the positive electrode, which, after a reasonably constant voltage plateau, is often terminated by a sharp voltage drop, offering a capacity [21, 22]. Fine films of Li_2O_2 of the order of 5 - 10 nm may result in the end of the cycling in the discharge due to a limited electronic conductivity of Li_2O_2 which prevents the transport of electrons from the cathode surface to the reactive site expected to be at the electrolytic interface $Li_2O_2 \,|\, Li^+$ [23].

Observing the foam E1 and E2 data, it was verified that for the same applied current, however, with different O_2 pressures the discharge capacity was higher for a lower O_2 pressure, being 104 $mAh \cdot g_c^{-1}$. For a higher applied current density of 75 $\mu A \cdot cm^{-2}$ (samples E3 and E4), however with different O_2 pressures, the load capacity presented a higher result also for a lower O_2 pressure, with a value of 263 $mAh \cdot g_c^{-1}$, that can be observed in Fig. 4.1 - a. The steel mesh electrodes presented higher discharge capacity when compared to nickel foam, as shown in Fig. 4.1 - b.
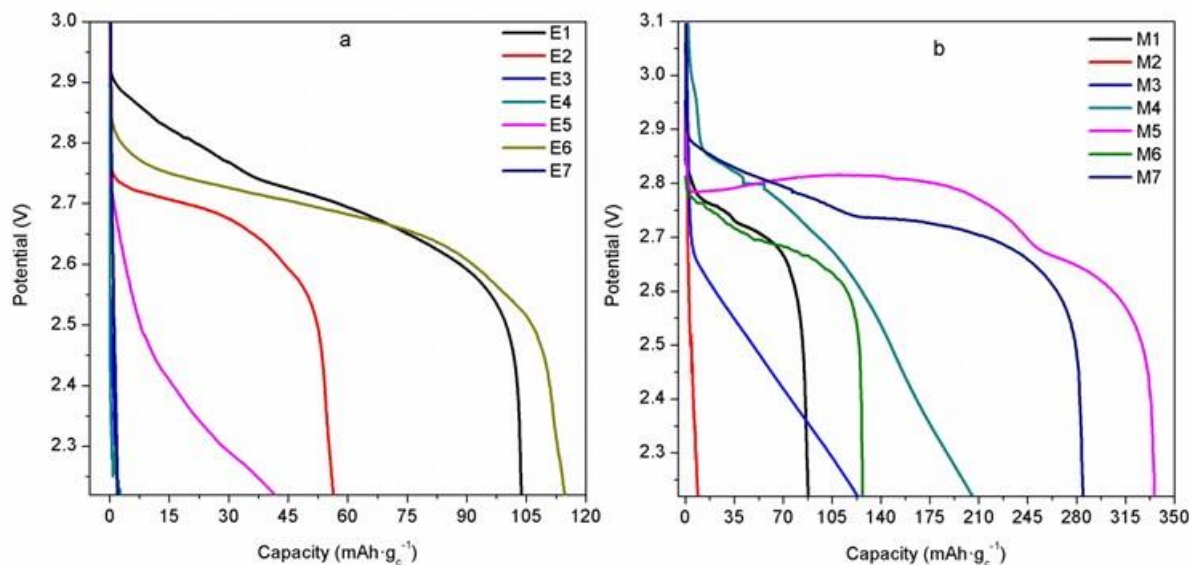
Figure 4.1. Maximum discharge capacity in a - nickel foam and b - steel mesh electrodes.

Regarding the morphology of the nickel foam electrodes, micrographs were performed by the SEM in the samples with lower and higher discharge capacity, according to Fig. 4.2 - a and b. E3 sample had a low discharge capacity of only 2.00 mAh·g_c^{-1}. Fig. 4.2 - a shows the heterogeneous regions in the electrode, the opposite of the sample E6 (Fig. 4.2 - b), which showed homogeneity with the presence of cracks.

SEM micrographs of the electrodes with lower and higher discharge capacity showed the electrode that obtained the highest discharge capacity (Fig. 4.2 - d) presented homogeneous surface. The electrode with lower discharge capacity (Fig. 4.2 - c) presented a similar distribution however with less amount of material. In both Fig. 4.2 - c) and d) small crystals are formed which are related to smaller applied potentials, which results in a lower nucleation rate, as observed by Nineva et al. (2011) [24]. The Li_2O_2 discharge products can be seen on the electrode surface as bright material in Fig. 4.2 a) and c). The electrode surface was not heavily covered with discharge products, seen as small white particles on the electrode surface, as reported for other study [12].
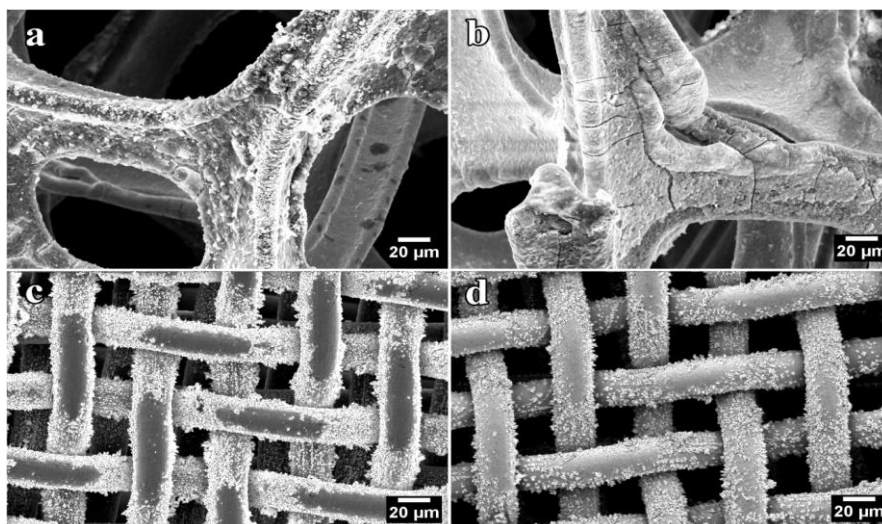
Figure 4.2. SEM micrographs of electrodes after cell tests: a - 75 µA·cm⁻², 1.5 atm (E3); b - 50 µA·cm⁻², 2 atm (E6); c - 25 µA·cm⁻², 2.5 atm (M2), d - 50 µA·cm⁻², 2.0 atm (M5).

The Ag and Co metals were mapped on the electrodes that were cycled in the battery (E3, E6, M2 and M5) in order to quantify the percentage of Ag and Co present in the substrate evidenced by EDX, as shown in Table 4.2. Since minimum amounts of alloy were electrodeposited, two samples with superior electrodeposition time were synthesized by electrodeposition. However, it was found that even with a longer time and different deposition technique, the mass of the deposit remained close to 1 mg.

E8 electrode was synthesized using the same technique mentioned in item 4.2.2, however, 20 cycles were used in the cyclic voltammetry technique, instead of 12 cycles, which were used for the synthesis of the first electrode in the electrolytic bath. For the electrode M8 the electrodeposition occurred with the same composition of the electrolytic bath, however a cell composed of two electrodes was used, in which the platinum electrode acted as reference and counter electrode. A potential of 6 V with duration of 200 s was applied [25].

Table 4.2. Percentage of mass of Ag and Co elements as evidenced by EDX

Electrode	Ag (%)	Co (%)
E3	61	36
E6	45	54
M2	100	0
M5	100	0
E8	80	20
M8	69	31

According to Table 4.2 the Ag metal was in a higher proportion in all the alloys, except the E6 sample, due to heterogeneous regions in the sample. The increase in the number of cycles used in voltammetry favored the increase in the percentage of Ag in the alloy, according to the percentage of the electrode E8. M2 and M5 steel mesh electrodes did not present cobalt deposits, indicating that the cyclic voltammetry technique was not beneficial for the electrodeposition of the alloy in this type of substrate. However, it may have occurred that the three points analyzed by EDX of samples M2 and M5 did not represent the sample as a whole. For the potentiostatic technique (electrode M8), deposition of both metals occurred, as visualized by the Table 4.2.

The metals Ag and Co present a reduction potential of +0.80 V and -0.28 V, which demonstrates that Ag^+ has a greater tendency to acquire electrons and that it reduces in the form Ag^0 more easily than Co^{2+} reduces to Co^0. Through the graphs generated by the VersaStudio software it was verified that during cyclic voltammetry on the substrate nickel foam, the maximum current values reached were 145 mA, while in the substrate steel mesh the maximum values reached were 83 mA, which supports the hypothesis that a higher current applied to the electrodeposition of Co occurs in the mesh, that is, another electrodeposition technique in which the electron flux is greater than that obtained by cyclic voltammetry. One can also attribute the absence of Co deposited due to the number of cycles, since the maximum deposition time was 960 s (20 cycles).

In the potentiostatic technique used in the electrode M8, the current range obtained by the graph was 500 - 700 mA. From the M8 electrode cycling it was concluded that the presence of cobalt in the electrode did not significantly affect the results, obtaining a charge capacity of 155 mAh·g_c^{-1} and discharge of 121 mAh·g_c^{-1}, with duration of the 20 programmed cycles. These results are lower, for example, to the electrode M5, which presented capacities of charge and discharge of 170 mAh·g_c^{-1} and 336 mAh·g_c^{-1} respectively.

4.3.2. Electrochemical activity of Ag-Co catalysts

CV plots for both substrates with and without Ag-Co catalyst are shown in Fig. 4.3 - a. The bare Ni foam and steel mesh presented the same behavior for OER, as shown in Fig. 4.3 - b, with onset potential of 0.63 a 10 µA·cm^{-2}. For the electrodes before the ORR-OER the values obtained were 0.56 and 0.59 V for the electrode E6 and M5 respectively,

demonstrating the OER is improved with the Ag-Co catalyst, since the onset potential was 70 and 40 mV higher with the absence of the catalyst. After the ORR-OER the electrodes presented values 0.56 and 0.61 V evidencing the stability and reversibility of the system[12]. Studies with catalysts for ORR and OER compared the results with Pt-Ru catalyst [26]. The onset potential obtained was 0.58 V for the OER at 10 $\mu A \cdot cm^{-2}$ which demonstrate that the values obtained for the Ag-Co catalysts are similar to the values of Pt-Ru catalysts.
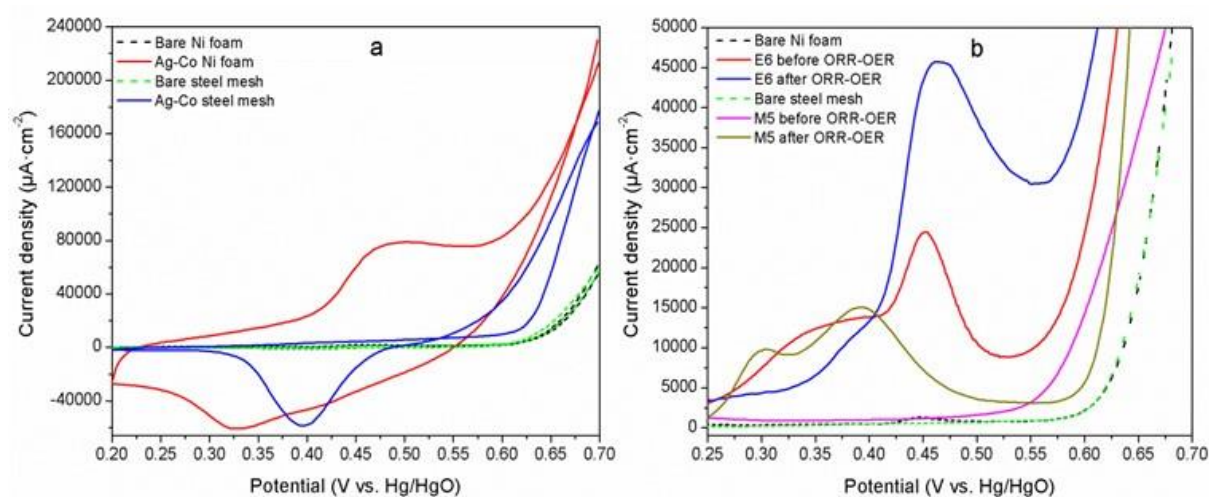
Figure 4.3. a - CV plots of the electrodes with and without catalysts at a scan rate of 20 $mV \cdot s^{-1}$ in O₂ saturated 1M KOH electrolyte; b - OER LSV plots for the electrodes at a scan rate of 5 $mV \cdot s^{-1}$ in O₂ saturated 1M KOH electrolyte.

4.3.3. Characterization of the electrodes

It was observed the formation of five different peaks for samples of nickel and steel mesh, as shown in Fig. 4.4, which shows the diffractogram of the substrates without deposits. The diffractogram of the nickel foam samples exhibited Ni_4 characteristic peaks, being (111) - 44.83 °, (002) - 52.25 ° and (022) - 77.02 ° (JCPDS Nº 01-1604). Peak 111 may be superimposed on the lithium-cobalt oxide ($LiCoO_2$) peak with planes (hkl) equal to (104) at 45.26 °. Formation of $LiCoO_2$ may occur due to the presence of the lithium salt ($LiClO_4$) in the assembly of the cell. The stainless steel mesh showed characteristic peaks of the material composition, $Fe_{24}C$ (101) - 44.02°, known as martensitic structure and chromium carbide C_3Cr_7

---

[12] The peaks in Figure 4.3. of nickel foam and steel mesh samples after ORR/OER indicated Ag-Co electrode oxidation.

(116) - 51.09 ° (JCPDS Nº 44-1291 and 65 -1347, respectively). The obtaining of the peaks with composition of the substrate was already expected due to the small amounts of deposit and products of the discharge.
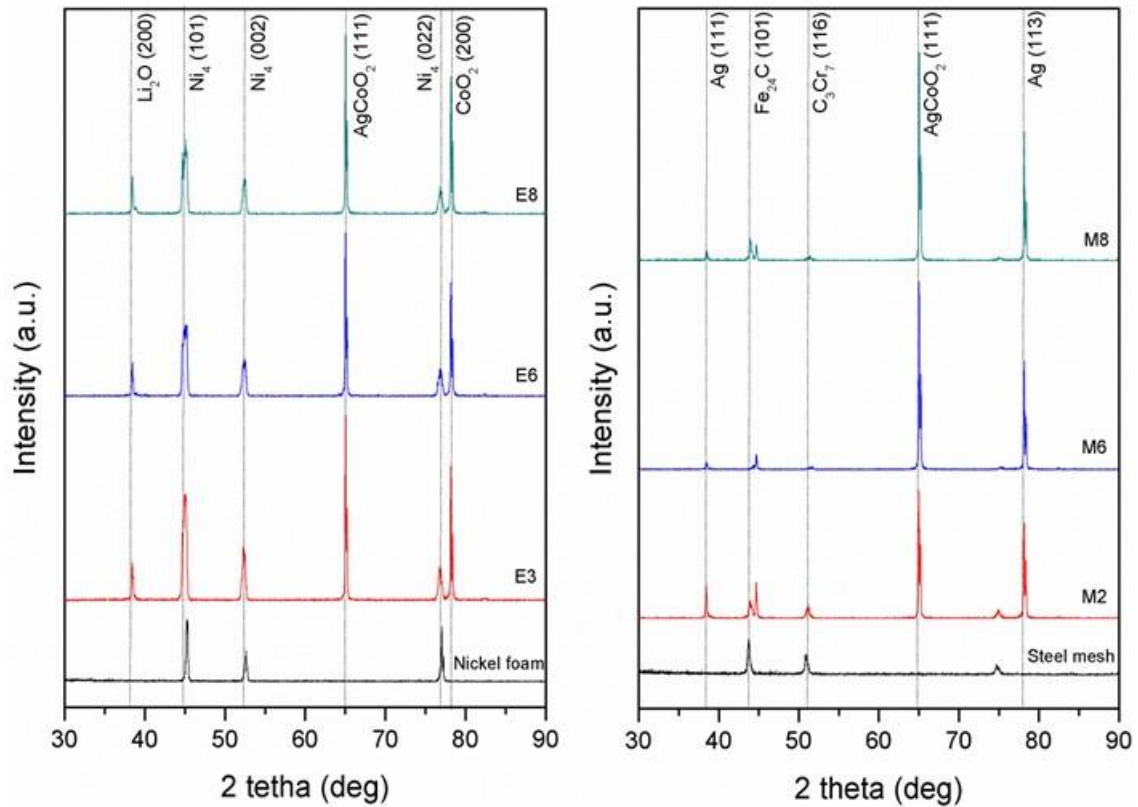
Figure 4.4. XRD patterns of the nickel foam and steel mesh samples containing the Ag-Co alloy after tests in the cell.

In the nickel samples the peak of Li_2O (200) at 39.03° was obtained, as reported by Kobayashi et al. (2017) [27], which used copper doped with Li_2O as cathodic material in lithium ion battery. Lithium oxide (Li_2O) as evidenced by the diffractogram indicates that the performance of the Li-O₂ battery is limited by cathode kinetics, that is, by the formation and decomposition of lithium oxide or peroxide [28].

The peak of $AgCoO_2$ (111) at 65.29° was obtained on both substrates. The size of the crystallite (*Tc*) of $AgCoO_2$ was calculated by Equation 1, known as the Scherrer equation:

$$Tc = {K\lambda}/{\beta\cos\theta} \tag{1}$$

where K is the Scherrer constant (0.91), λ is the wavelength of the radiation used (0.154156 nm), β is the width of the half height of the peak of diffraction (rad) and θ is the Bragg (rad) angle. The value of Tc obtained was 3.23 nm for the substrate of nickel and 2.64 nm for the steel mesh, which corroborate with studies which was obtained $AgCoO_2$ catalysts having crystallite size of 5.14 nm by the coprecipitation method [29].

Raman spectroscopy analysis was carried out to identify the chemical composition of discharge products, being useful for distinguishing between different metal oxides with the same elements. Raman spectrum of Li_2O_2 and Li_2O was obtained with peaks at 802 [30] and 521 cm^{-1} [31] as shown in Fig. 4.5. Characteristic peaks of Li_2CO_3 (1091 cm^{-1}) and LiOH (3662 cm^{-1}) are not detected [32].
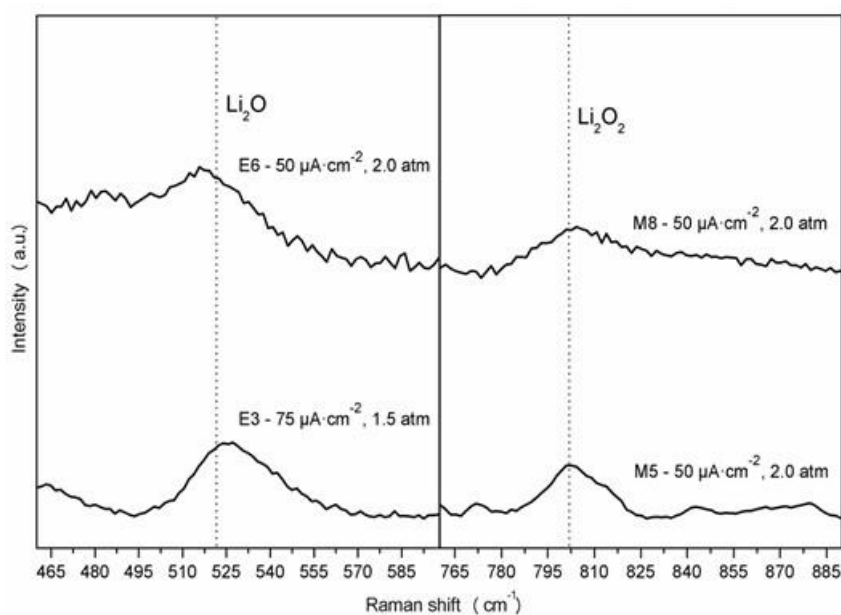
Figure 4.5. Raman spectra of samples E3, E6, M5 and M8 at an excitation wavelength of 633 nm.

4.4. Conclusions

Li-O₂ battery with Ag-Co as catalyst in steel mesh and nickel foam as electrode has been studied. We found that the O₂ pressure and current density affected the charge and discharge capacity of the electrochemical storage system, having a medium value of O₂ pressure

(2.0 atm) and current density (50 $\mu A \cdot cm^{-2}$) the favored the high capacity obtained. By Raman spectroscopy, formation of Li_2O_2 and Li_2O is confirmed from the discharged cathode surface, and characteristic peaks of Li_2CO_3 and $LiOH$ are not detected. XRD patterns evidenced the peaks of Li_2O and $AgCoO_2$. OER was improved in both substrates, demonstrating the high catalytic activity. Sample that the presence of cobalt was not detected did not affect the capacity. The values of capacity for nickel foam and steel foam suggest the use of the latter because of its considerable cost and accessibility.

Acknowledgements

References

[1] U.R. Farooqui, A.L. Ahmad, N.A. Hamid, Renewable and Sustainable Energy Reviews, 77 (2017) 1114-1129.

[2] Z. Yang, J. Zhang, M.C.W. Kintner-Meyer, X. Lu, D. Choi, J.P. Lemmon, J. Liu, Chemical Reviews, 111 (2011) 3577-3613.

[3] Q. Yi, L. Song, Electroanalysis, 24 (2012) 1655-1663.

[4] K. Lee, M.S. Ahmed, S. Jeon, Journal of Power Sources, 288 (2015) 261-269.

[5] Q. Wang, H. Yang, Z. Zhou, L. Wang, W. Yan, W. Wu, S. Chen, Z. Liu, Z. Tang, International Journal of Hydrogen Energy, 42 (2017) 11295-11303.

[6] Y. Jin, F. Chen, Electrochimica Acta, 158 (2015) 437-445.

[7] Y. Joo, M.S. Ahmed, H.S. Han, S. Jeon, International Journal of Hydrogen Energy, 42 (2017) 21751-21761.

[8] C. Zafferoni, G. Cioncoloni, M.L. Foresti, L. Dei, E. Carretti, F. Vizza, A. Lavacchi, M. Innocenti, Molecules (Basel, Switzerland), 20 (2015) 14386-14401.

[9] F. Zhang, M. Wei, J. Sui, C. Jin, Y. Luo, S. Bie, R. Yang, Journal of Alloys and Compounds, 750 (2018) 655-658.

[10] Y.-B. Cho, S. Moon, C. Lee, Y. Lee, Applied Surface Science, 394 (2017) 267-274.

[11] H.J. Kwon, H.C. Lee, J. Ko, I.S. Jung, H.C. Lee, H. Lee, M. Kim, D.J. Lee, H. Kim, T.Y. Kim, D. Im, Journal of Power Sources, 364 (2017) 280-287.

[12] E.J. Nemanick, R.P. Hickey, Journal of Power Sources, 252 (2014) 248-251.

[13] J. Garcia-Torres, E. Vallés, E. Gómez, Materials Letters, 65 (2011) 1865-1867.

[14] F.S. Gittleson, R.C. Sekol, G. Doubek, M. Linardi, A.D. Taylor, Physical Chemistry Chemical Physics, 16 (2014) 3230-3237.

[15] Y.-C. Lu, H.A. Gasteiger, E. Crumlin, R. McGuire, Y. Shao-Horn, Journal of The Electrochemical Society, 157 (2010) A1016-A1025.

[16] J.M. Costa, T.C. de Morais Nepel, A.F. de Almeida Neto, Chemical Papers, (2018).

[17] X.-h. Yang, Y.-y. Xia, Journal of Solid State Electrochemistry, 14 (2009) 109.

[18] N. Imanishi, O. Yamamoto, Materials Today, 17 (2014) 24-30.

[19] Y. Suzuki, K. Kami, K. Watanabe, N. Imanishi, Solid State Ionics, 278 (2015) 222-227.

[20] P. Adelhelm, P. Hartmann, C.L. Bender, M. Busche, C. Eufinger, J. Janek, Beilstein journal of nanotechnology, 6 (2015) 1016-1055.

[21] J. Lu, L. Li, J.-B. Park, Y.-K. Sun, F. Wu, K. Amine, Chemical Reviews, 114 (2014) 5611-5640.

[22] A.C. Luntz, B.D. McCloskey, Chemical Reviews, 114 (2014) 11721-11750.

[23] V. Viswanathan, K.S. Thygesen, J.S. Hummelshøj, J.K. Nørskov, G. Girishkumar, B.D. McCloskey, A.C. Luntz, The Journal of Chemical Physics, 135 (2011) 214704.

[24] S. Nineva, T. Dobrovolska, I. Krastev, Journal of Applied Electrochemistry, 41 (2011) 1397-1406.

[25] I.N. Sivagami, K. Prasanna, P. Santhoshkumar, Y.N. Jo, G.Y. Seo, C.W. Lee, Journal of Alloys and Compounds, 697 (2017) 450-460.

[26] M. Xiong, M.P. Clark, M. Labbe, D.G. Ivey, Journal of Power Sources, 393 (2018) 108-118.

[27] H. Kobayashi, M. Hibino, T. Makimoto, Y. Ogasawara, K. Yamaguchi, T. Kudo, S.-i. Okuoka, H. Ono, K. Yonehara, Y. Sumida, N. Mizuno, Journal of Power Sources, 340 (2017) 365-372.

[28] Y.-C. Lu, H.A. Gasteiger, M.C. Parent, V. Chiloyan, Y. Shao-Horn, Electrochemical and Solid-State Letters, 13 (2010) A69-A72.

[29] S. Dey, G.C. Dhal, D. Mohan, R. Prasad, Polyhedron, 155 (2018) 102-113.

[30] L. Johnson, C. Li, Z. Liu, Y. Chen, S.A. Freunberger, P.C. Ashok, B.B. Praveen, K. Dholakia, J.-M. Tarascon, P.G. Bruce, Nature Chemistry, 6 (2014) 1091.

[31] F.S. Gittleson, K.P.C. Yao, D.G. Kwabi, S.Y. Sayed, W.-H. Ryu, Y. Shao-Horn, A.D. Taylor, ChemElectroChem, 2 (2015) 1446-1457.

[32] S. Higashi, Y. Kato, K. Takechi, H. Nakamoto, F. Mizuno, H. Nishikoori, H. Iba, T. Asaoka, Journal of Power Sources, 240 (2013) 14-17.

CHAPTER 5

Zn-Co electrocatalysts in lithium-O$_2$ batteries: Temperature and rotating cathode effects on the electrodeposition

Zn-Co electrocatalysts in lithium-O$_2$ batteries:
Temperature and rotating cathode effects on the electrodeposition

Josiel Martins Costa and Ambrósio Florêncio de Almeida Neto

Abstract

In this study, we developed Zn-Co catalyst by electrodeposition process in nickel foam and steel mesh electrodes for application as a cathode in Li-O$_2$ batteries. The electrodes were synthesized from an electrolytic bath varying the temperature (25 to 70 °C) and rotating cathode (30 to 100 rpm) by the potentiostatic method. The results of capacities in the Li-O$_2$ cell and catalytic activity measurements showed that the Zn-Co alloy is a promising catalyst for the O$_2$ evolution reaction (OER). Sharp surfaces composed for nanoflakes and heterogeneous surfaces with whitish agglomerates which may have increased the surface area for the housing of the discharge products was observed by scanning electron microscopy (SEM). X-ray diffraction (XRD) evidenced Zn$_{21}$Co$_5$ composition and Raman spectra evidenced discharge product Li$_2$O$_2$. The maximum charge capacity of 399 mAh g$_c^{-1}$ for steel mesh and 182 mAh g$_c^{-1}$ for nickel foam electrode suggests the use of this alloy as catalysts in Li-O$_2$ batteries.

Keywords: Energy storage materials; Electrochemical performance; Alloys; Oxygen evolution reaction.

5.1. Introduction

Greenhouse gas reductions, energy demand from fossil fuels and the search for sustainable energy promote the development of innovative energy storage technologies. Lithium-air, lithium-ion batteries and supercapacitors are examples of promising high-performance energy storage systems [1-3]. Batteries with high energy density lead to safe use and low cost for electric vehicles. This characteristic can be obtained in lithium-air batteries, due to the non-storage of the oxygen, but its extraction directly from the ambient atmosphere, which generates a theoretical density of 13 kWh kg^{-1} [4]. However, this system is verified that low efficiency results from the overpotential during the oxygen evolution reaction (OER) and the oxygen reduction reaction (ORR) at the O_2 diffusion cathodes. Particularly, the higher overpotentials are observed during the OER in comparison with the ORR, which impairs the kinetics of the system [5].

OER corresponds to O-O bonds and presents four electron transfer processes inserted into protons so that OER has slow kinetics and is predominant in overall efficiency [6,7]. Therefore, the development of high-efficiency electrocatalysts is necessary to accelerate OER or reduce overpotential in order to improve the cyclability [8]. Recently, materials based on metals have been used as electrocatalysts in OER [9], as for both reactions reduced graphene oxide, metal oxide and nanocomposites have been also applied in catalytic process in Li-O_2 cells [10-13].

Particularly, the materials based on cobalt have been outstanding due to their abundance, low cost, and catalytic activity when compared to RuO_2 and IrO_2 [14]. Electrocatalysts can be obtained by carbonizing, electrospinning, precipitation, hydrothermal method and electrodeposition process [15-20]. For the electrodeposition, the composition of the bath, temperature and stirring velocity generates differences on homogeneity, porosity, and structures that modify the electrochemical behavior and directly impact on the catalytic activity of the material [21].

Mesoporous $ZnCo_2O_4$ was used as bifunctional electrocatalysts for application in energy storage systems [22]. The material impregnated on the carbon (Ketjen black) had a high specific capacity, greater than using only pure carbon. The high surface area of 127.2 m^2 g^{-1} and 3D mesoporous structure justified the good catalytic performance in the Li-O_2 battery.

Thus, in this study, we proposed to verify the impact of temperature and rotating cathode on the electrodeposition bath of the Zn-Co catalyst used as cathodes in Li-O$_2$ batteries. Furthermore, the Zn-Co alloys obtained were characterized by linear sweep voltammetry (LSV), cyclic voltammetry (CV), X-ray diffraction (XRD), scanning electron microscopy (SEM), energy dispersive spectrometry (EDS) and Raman spectra based on the performance of experiments in Li-O$_2$ cell.

5.2. Materials and methods

5.2.1. Chemical treatment of the electrodes

Zn-Co alloys were electrodeposited in nickel foam and steel mesh with 1 cm in diameter, both with rod length 2.5 cm by 0.3 mm wide. Three circles with 1 cm diameter joined by the ends and folded over one another were used for the steel mesh electrode. A 1.5 cm by 0.3 mm wide copper filament was superimposed on the substrate rod to facilitate the insertion in the rotating electrode. The electrodes were cleaned through a chemical treatment using 10% NaOH and subsequently 1% H$_2$SO$_4$. Thus, the electrodes were washed and dried at 100 °C in the oven and then placed in the desiccator [23].

5.2.2. Electrodeposition of the Zn-Co alloy

For this study was used a factorial design 2^2 with triplicate at the central point, with three different values of temperature (25, 47.5 and 70 °C), cathode rotation of electrodeposition (30, 65 and 100 rpm), and two electrodes (nickel foam and steel mesh)[13]. The electrolytic bath was composed of cobalt sulfate, CoSO$_4 \cdot$7H$_2$O, source salt of cobalt 0.1 mol L^{-1} and zinc sulfate, ZnSO$_4 \cdot$7H$_2$O, source salt of zinc 0.2 mol L^{-1}. A rotating disk electrode (pattern 616A, Princeton Applied Research), a pH meter and a potentiostat/galvanostat (VersaStat 3, Princeton Applied Research) were used in electroplating tests. The initial pH was adjusted to 6.40 using ammonium hydroxide. For the tests at 25 °C, the potentiostatic technique was used with a two-electrode cell: the working electrode (nickel foam or steel mesh) and the counter electrode (cylindrical hollow platinum mesh). A potential of 4 V for 60 seconds was applied to obtain

---

[13] See Appendix A.

about 1 mg of deposit in the substrate [24]. For the electrodepositions performed at 47.5 and 70 °C, the three electrode cell, composed of the reference electrode ($Ag^+/AgCl$) was used. A potential of -1.15 V for 200 seconds was applied [25] to obtain deposits with values close to 1 mg.

5.2.3. *Li-O₂ cell measurements and electrocatalytic activity*

The lithium disk with a diameter of 1.6 cm and thickness of 0.5 mm was positioned on the stainless steel chain collector of the cell; 50 µL of electrolyte (anhydrous dimethylsulfoxide containing lithium perchlorate 0.1 mol L^{-1}) was added on this slide. A fiberglass membrane with 2 cm of diameter was placed and another 50 µL of the electrolyte was added thereon [26]. The electrode was positioned on the membrane moistened with the electrolyte. Lastly, a stainless steel screen and a stainless steel spring were added. The cell was assembled in a Glove-Box (MBRAUN-LABstar Workstation) with H_2O and O_2 concentrations less than 1 ppm.

A time of 4 hours for stabilization of the system was expected after the use of the cell. For the electrochemical tests, the configuration of two electrodes was used, in which one of the terminals was composed of the reference electrode and the counter electrode, and the other terminal by the working electrode. Cells were evaluated in cycles, with an electric current density of 50 µA cm^{-2}, O_2 pressure of 2 atm (99.9%), potential upper limit 2.2 V and potential lower limit 4.0 V.

In order to confirm the catalytic activity of the Zn-Co alloy in the OER, LSV curves were recorded at a scan rate of 5 mV s^{-1}, and CV at a scan rate of 20 mV s^{-1} in 1 M KOH purged with pure O_2 gas at room temperature. A spiral platinum and Hg/HgO (0.098 V vs. SHE) electrodes were used as a counter electrode and a reference electrode, respectively.

5.2.4. *Chemical, microstructural and physical characterization*

The chemical composition and microstructure of the catalysts were obtained by SEM, model Leo 440i, equipped with X-Ray Energy Dispersion Spectrometer (LEO Electron Microscopy/Oxford, Cambridge, England) model 6070. It was made magnifications of 5000 times. XRD analysis was performed to visualize peaks of metal and discharge products and to calculate crystallite size. It was used the K-alpha copper scanning method, 40 kV voltage, 40

mA current, 2θ ranging from 20 to 90° with a pitch of 0.02°, speed 0.033° s^{-1} and wavelength of 1.54 Å on a Philips Analytical X-Ray diffractometer and X'Pert-MPD model. In addition, the discharge products were investigated by a Raman spectroscopy (Renishaw InVia), using an excitation wavelength of 633 nm.

5.3. Results and discussion

5.3.1. Catalytic performance of Zn-Co and cathode morphology

Table 5.1 shows the 14 electrodes, being represented by the letter F, the nickel foam and N, the steel mesh. Other variables are arranged, such as the temperature (T), the cathode rotation (v). The mass of the catalyst in the electrode (m_{cat}), the open circuit potential (OCP) the maximum discharge capacity (MDC) and the number of cycles are also arranged.

Table 5.1. Variables and results of the electrodes

Electrodes	T (°C)	v (rpm)	m_{cat} (mg)	OCP (V)	MDC (mAh g_c^{-1})	Number of cycles
F1	25	30	1.0	2.21	2	11
F2	25	100	1.0	2.83	63	1
F3	70	30	1.0	2.81	41	1
F4	70	100	1.0	2.67	8	20
F5	47.5	65	1.0	2.59	1	5
F6	47.5	65	1.0	2.71	50	5
F7	47.5	65	1.0	2.91	11	5
N1	25	30	1.1	2.70	28	16
N2	25	100	1.2	2.21	9	10
N3	70	30	1.0	2.58	0	4
N4	70	100	1.0	2.69	4	5
N5	47.5	65	1.0	2.67	63	6
N6	47.5	65	1.0	2.72	10	6
N7	47.5	65	1.0	2.20	3	6

According to the data in Table 5.1, the deposited catalyst mass remained constant, close to 1 mg in most samples. *OCP* values were varied; however, they did not impair cell cycling. The cycling was programmed with 15 seconds initial of *OCP* measurement and 20 charge and discharge cycles with a potential lower limit of 2.2 V and higher of 4.0 V applying a current of 50 μA cm^{-2} with an O₂ pressure of 2 atm. Comparing samples F1 and F2, it was

observed at 25 °C the increase in the rotating cathode from 30 to 100 rpm favored the increase of the discharge capacity, which was 63 mAh g_c^{-1} in sample F2.

The maximum charge capacity values were higher than the maximum discharge capacity in all electrodes, as compared with Figure S1- a and b, which shows that the Zn-Co alloy is a promising catalyst for the O_2 evolution reaction (OER), which occurs during charge. This assumption is valid since the discharge was performed after the 15 seconds of OCP measurement, and even then lower values of discharge capacity were obtained. Regarding the influence of the temperature of the electrolytic bath, the charge and discharge capacities decreased and increased according to the rotating cathode. For example, by comparing sample F1 and F3, increasing the temperature from 25 to 70 °C lowered the load capacity from 144 to 128 mAh g_c^{-1} for the rotating cathode of 30 rpm. However, for a rotation of 100 rpm, the increase in temperature increased the charge capacity from 160 to 182 mAh g_c^{-1}, as shown in Figure 5.1 - a.
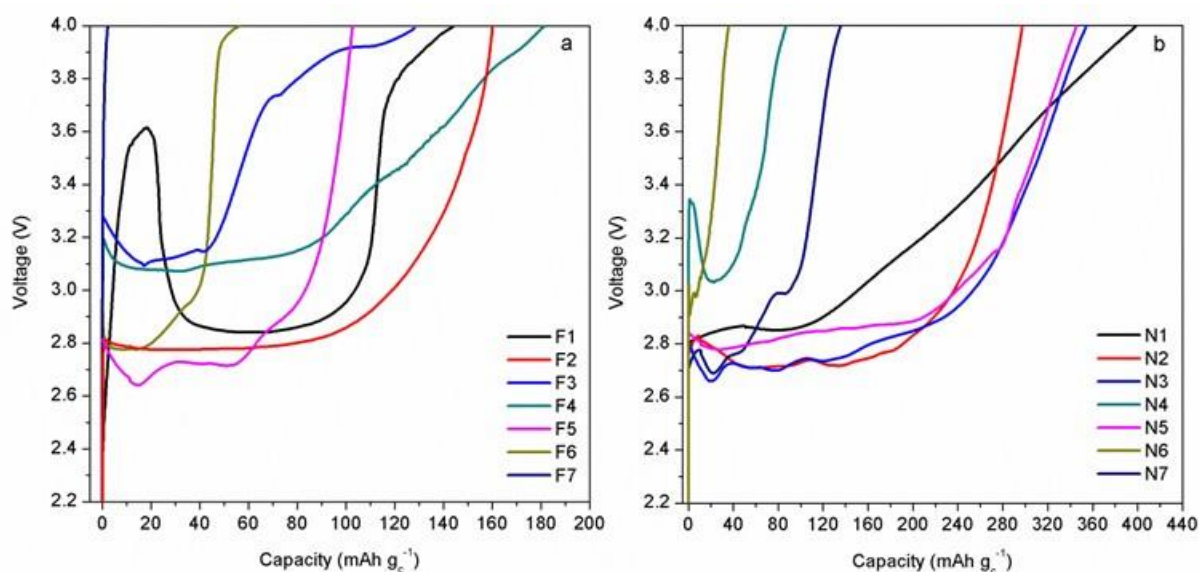
Figure 5.1. Maximum charge capacity in a) nickel foam and b) steel mesh electrodes.

In the steel mesh electrodes, it was verified that the increase in temperature and rotating cathode did not affect higher values of maximum charge capacity since the highest capacity value observed was the N1 sample with cathode rotation of 30 rpm at 25 °C with a value of 399 mAh g_c^{-1}, that suggest a higher number of active sites of the Zn-Co catalyst and the absence of parallel reactions that could decrease the decomposition reaction rate of Li_2O_2.

The reproducibility of the experiments with non-similar values is related to the non-formation of the triple electric layer, in which it depends on the gas oxygen diffused in the dimethylsulfoxide, the electrolyte permeating the electrode and the oxygen flow diffused inside the cell. The resting time of 4 hours occurs for stabilization of the open circuit potential and for the electrolyte to diffuse completely inside the electrode. However, because they are porous materials, some specific regions may present a greater quantity of electrolyte, which generates heterogeneity of the system. The initial reduction peak in Figure 5.1 - a and b can be attributed to the collapse of the crystalline structure of the catalyst and to the formation of the solid electrolyte interface layer. From this peak, the capacity increases, revealing the electrochemical reaction. The irreversible capacity for the other cycles is generated by the formation of solid electrolyte interface films, the irreversible formation of Li_2O, and the irreversible decomposition of the electrolyte [27].

Comparing the micrographs obtained in the SEM of the samples with high (F4) and lower (F7) charge capacity, it was observed according to Figure 5.2 - a the formation of sharp surfaces composed for nanoflakes, which may have increased the surface area for the housing of the product discharge the battery. Similar results in the microstructure were obtained by other studies that electrodeposited Zn-Co alloys using a bath with 0.0074 mol L^{-1} of agar in the composition [22]. Therefore, the nanoflakes structure limited the change in electrode volume and avoided spraying during the cycles of lithiatization and delitiation [28,29].

For the F7 sample, a more homogeneous surface is observed with no sharp structures and whitish clusters that may be related to the formation of lithium peroxide. The annealing treatment with the acetate hydrate led to the formation of a porous structure of $Zn_{0.3}Co_{2.7}O_4$ willow leaves. This compound demonstrated good electrocatalytic oxygen evolution reaction and had morphology and structure similar to Figure 5.2 - a [30].
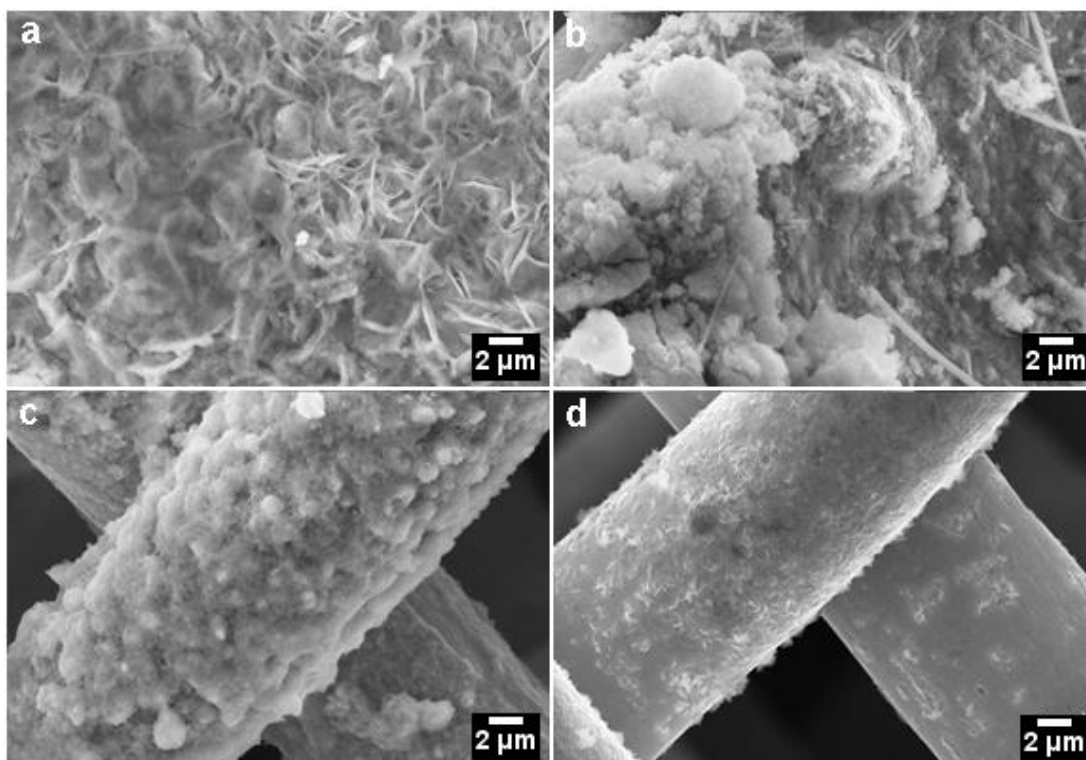
Figure 5.2. SEM micrographs of electrodes after cell tests: a - 70 °C, 100 rpm (F4); b - 47.5 °C, 65 rpm (F7); c - 25 °C, 30 rpm (N1), d - 47.5 °C, 65 rpm (N6).

Micrographs of the samples with higher (N1) and lower (N6) maximum charge capacity showed regions with heterogeneous surfaces with whitish agglomerates that may be associated to the product of the ORR, lithium peroxide, according to Figure 5.2 - c. For sample N6, homogeneous regions were observed with the absence of agglomerates, as shown in Figure 5.2 - d. When the cobalt proportion of the alloy increases, the coating structure becomes more uniform in crystallite size [31]. The crystallite form with low cobalt content is rounded, as shown in Figure 5.2 - c with a Co percentage mass of 14%.

The increase in temperature increased the proportion of Co in the alloy for both substrates, as shown in Table 5.2, by EDS analysis.

Table 5.2. Percentage of the mass of Zn and Co elements as evidenced by EDS

Electrode	Zn (%)	Co (%)
F4	87	13
F7	95	5
N1	86	14
N6	78	22

The composition reference, representing the percentage of Co in the deposits equals to that of the electrolytic bath [32], with a value of 7%. The Co content in the deposits is always above this value, indicating that the co-deposition of Zn and Co is a normal type [33]. Values below 7% indicate that cobalt is deposited by an anomalous process, as in electrode F7.

CV plots for both substrates with and without Zn-Co catalyst are shown in Figure 5.3 - a. The bare Ni foam and steel mesh presented the same value for OER, as shown in Figure 5.3 - b, with an onset potential of 0.63 at 10000 μA cm^{-2}. For the electrodes before the ORR-OER the values obtained were 0.62 and 0.58 V for the electrode F4 and N1 respectively, demonstrating the OER was optimized with the Zn-Co catalyst since the onset potential was 10 and 50 mV higher with the absence of the catalyst. After the ORR-OER the electrodes presented values 0.60 and 0.58 V evidencing the stability and reversibility of the system[14].
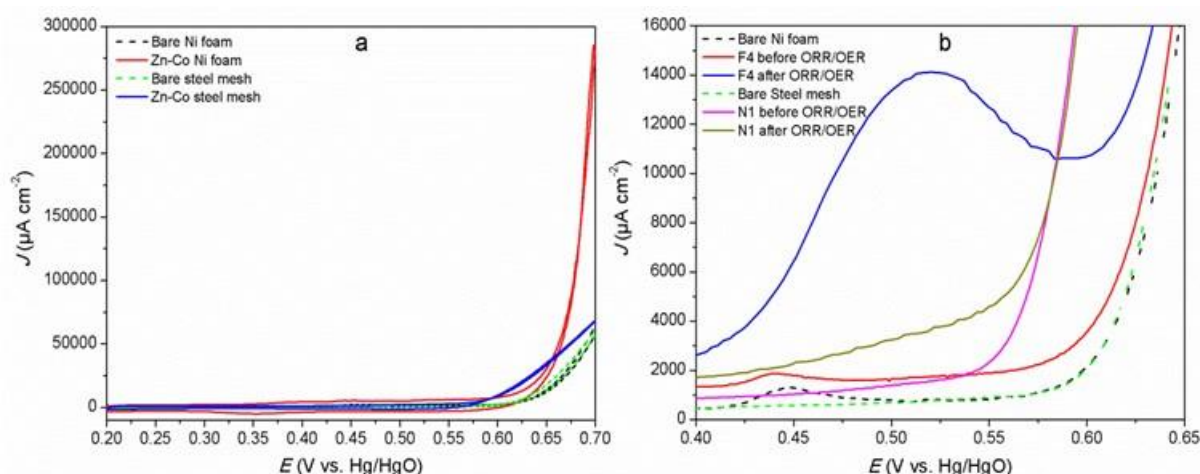
Figure 5.3. a - CV plots for Zn-Co catalysts at a scan rate of 20 mV s^{-1} in O₂ saturated 1M KOH electrolyte; b - OER LSV plots for catalysts at a scan rate of 5mV s^{-1} in O₂ saturated 1M KOH electrolyte.

CV plots in the potential range of 0.0 to 0.1 V at different rates (10, 20, 40, 60, 80, 100, and 120 mV s^{-1}) were studied to evaluate the double layer capacitance (C_{dl}) (Figure S2). The charge of the double layer q_{dl} is estimated by the extrapolation of q to $v = \infty$ (v is the scanning rate) in a graph of q vs. $v^{-1/2}$, according to the method reported in [34] (Figure 5.4 - a). The total charge q$_t$ was obtained by the inverse of the reciprocal voltammetric charge (q^{-1})

---

[14] The peak in Figure 5.3. of nickel foam sample after ORR / OER may indicate dissolution of the Zn-Co electrode.

(Figure 5.4 - b). C_{dl} values can be obtained by dividing half of the q_{dl} by the potential window of the CV curve.
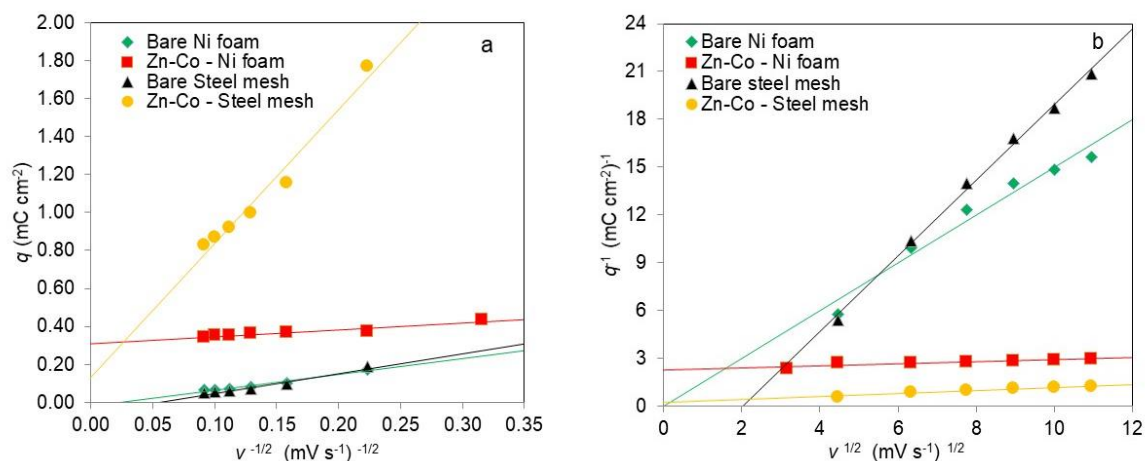
Figure 5.4. a - Voltammetric charge (q) plotted against the square root of the scan rate ($v^{-1/2}$); b - The reciprocal of voltammetric charge (q^{-1}) plotted against the square root of the scan rate ($v^{1/2}$).

The role of capacitance measurements is a measure of the electrochemically active surface area that is required for the evaluation of the catalytic activity. Table 5.3 shows the capacitance values of the electrodes. Electrodes with the absence of Zn-Co demonstrate that the bare substrates have no electrochemically active surface area. The double layer capacitance value of 3.10 and 1.34 mF cm^{-2}, respectively for experiment F4 and N1 before the battery test, characterize the higher electrochemically active surface area of the Zn-Co alloy.

Table 5.3. Capacitance values of the electrodes

Electrodes	q_t (mC cm^{-2})	q_{dl} (mC cm^{-2})	C_t (mF cm^{-2})	C_{DL} (mF cm^{-2})	C_P (mF cm^{-2})
Bare Ni foam	N/A	N/A	N/A	N/A	N/A
Zn-Co Ni foam (F4)	0.444	0.310	4.44	3.10	1.34
Bare Steel mesh	N/A	N/A	N/A	N/A	N/A
Zn-Co Steel mesh (N1)	4.805	0.134	48.05	1.34	46.71

5.3.2. XRD and Raman analysis

The Ni substrate peaks are present in all samples (F) with the composition Ni_4, in the crystallographic planes (111) - 44.83°, (002) - 52.25° and (022) - 77.02° (JCPDS n° 01-1604) being according to Figure 5.5. Formation of cobalt oxide (Co_3O_4) according to the plane (044) at 65.25° (JCPDS n° 90-5888) was observed. The Zn-Co alloy was evidenced by the peak at 77.55° with the crystallographic plane (510) corresponding to the $Zn_{21}Co_5$ composition (JCPDS n° 04-0882). A study of Zn-Co alloys electrodeposited from oxalate electrolytes evidenced the $Zn_{21}Co_5$ composition [31]. The alloys were obtained using a bath with a temperature of 45-50 °C and pH value 6.1 with a cathodic current density of 1 A dm^{-2}.
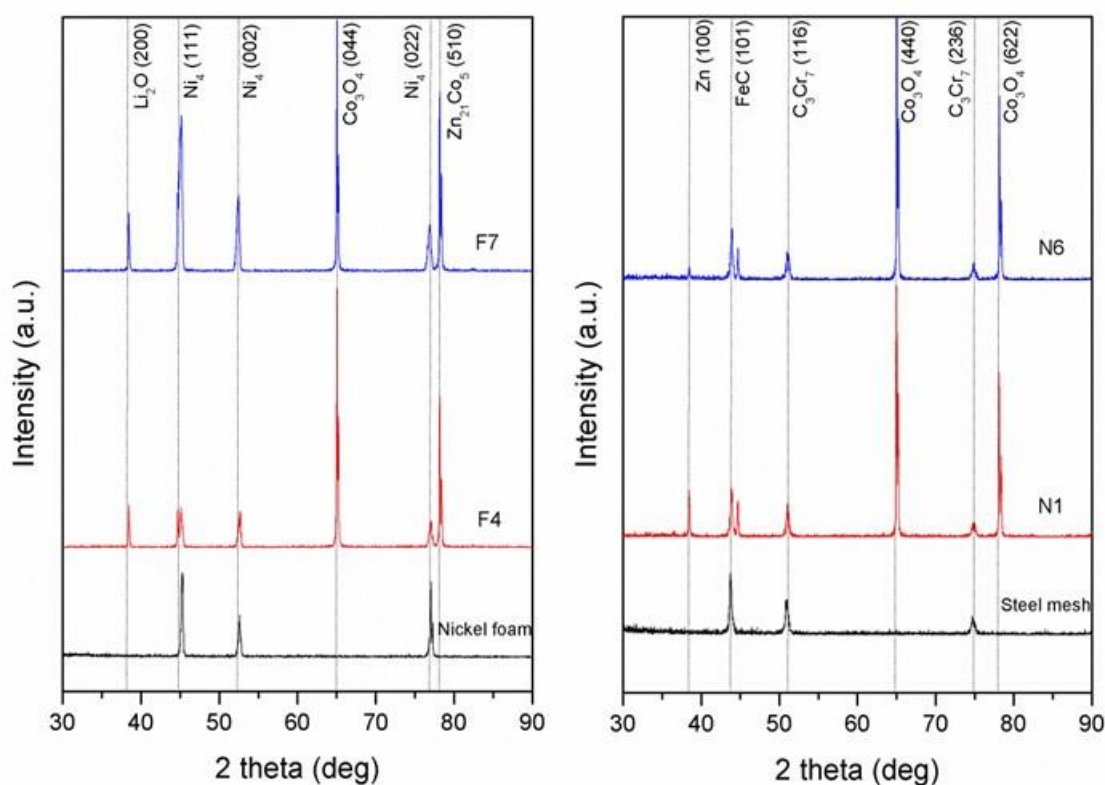
Figure 5.5. XRD patterns of the electrodes with Zn-Co alloy after tests in the cell.

In the substrate of the steel mesh, the substrate peaks remained present, such as FeC (101) - 44.02° and C_3Cr_7 (116) - 51.09°, with addition of another peak that refers to the substrate, chromium carbide (C_3Cr_7) at 74.86° with plane (236) (JCPDS n° 65-1347). The peak of cobalt oxide (Co_3O_4) was found to be 65.25 (440) and 78.39° (622), however, it is possible

that the zinc peak may be above the peak of Co_3O_4 at 38.54° per peak at 38.99°. As well, the $LiCoO_2$ peak may be superimposed on the Co_3O_4 peak at 78.39 °, as it has a peak at 78.69°.

The crystallite size (Tc) was calculated by Equation 1, known as the Scherrer equation:

$$T_c = \frac{K\lambda}{\beta \cos\theta} \tag{1}$$

where K is the Scherrer constant (0.91), λ is the wavelength of the radiation used (0.154156 nm), β is the width of the half height of the peak of diffraction (rad) and θ is the Bragg angle (rad). The value of Tc obtained for cobalt oxide Co_3O_4 with planes (044) and (400) was 2.42 and 5.05 nm respectively. A study obtained cobalt oxide catalysts with a crystallite size of 5 to 38 nm with a focus on the catalysis of chlorinated volatile organic compounds [35]. The authors reported that this oxide is effective in the low-temperature combustion of non-chlorinated hydrocarbons, carbon monoxide, and diesel soot. Besides this application, Co_3O_4 has been used as a bifunctional catalyst in LiO_2 battery, according to several studies [17-19]. The rugged surface enriched with ultra-fine nanosheets Co_3O_4 reinforced both ORR and OER, with a higher initial capacity, a lower overpotential and a longer life cycle [18]. For the $Zn_{21}Co_5$ alloy, the obtained crystallite size was 3.49 nm, which is similar to the value obtained by a study that produced Zn-Co coatings from an electrolytic bath composed of sodium citrate, and salts of metals Zn and Co by pulsed electrodeposition [36].

In the nickel samples, the peak of Li_2O (200) at 39.03° was obtained, as reported by [37], which investigate polyisobutylene as a new binder for application in Li-air cells. Lithium oxide (Li_2O) as evidenced by the diffractogram indicates that the performance of the Li-O₂ battery is limited by cathode kinetics, that is, by the formation and decomposition of lithium oxide or peroxide [38]. To identify the chemical composition of the discharge products and to distinguish the metal oxides with the same elements, Raman spectroscopy analysis was used. Raman spectrum of Co_3O_4 and Li_2O_2 was obtained with peaks at 626, 695 [39] and 783 cm^{-1} [40,41] as shown in Figure 5.6.
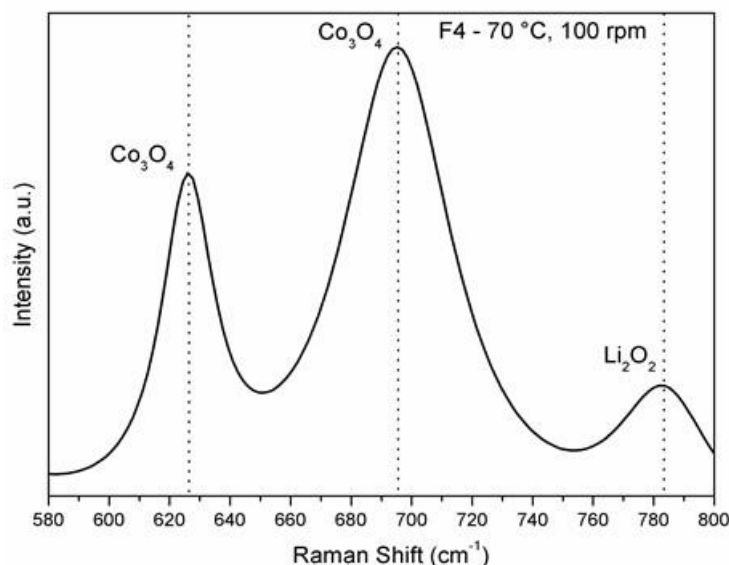
Figure 5.6. Raman spectra of sample F4 at an excitation wavelength of 633 nm.

5.4. Conclusions

Zn-Co alloys have been successfully electrodeposited in steel mesh and nickel foam for application as an electrode in Li-O₂ battery. We found that this catalyst favored OER (charge) with greater capacities than ORR (discharge). LSV and CV plots and the values of double layer capacitance confirmed the high catalytic activity. A high temperature of electrodeposition produced sharp surfaces composed for nanoflakes which suggested a place to house discharge products. The rotating cathode did not affect the maximum charge capacity since the highest capacity value observed was 399 mAh g_c^{-1} at 25 °C and 30 rpm. The peaks obtained in the diffractogram allowed to calculate the crystallite size, which is in agreement with the literature for the use as catalysts. The charge capacity values using electrodes with Zn-Co suggest their use in catalytic processes of energy storage due to its considerable performance.

Acknowledgments

References

1. Deosarkar MP, Pawar SM, Bhanvase BA (2014) In situ sonochemical synthesis of Fe_3O_4-graphene nanocomposite for lithium rechargeable batteries. Chem Eng Process 83:49-55

2. Yang X, Leng J, Wang D, Wang Z, Wang J-X, Pu Y, Shui J, Chen J-F (2017) Synthesis of flower-shaped V_2O_5:Fe^{3+} microarchitectures in a high-gravity rotating packed bed with enhanced electrochemical performance for lithium ion batteries. Chem Eng Process 120:201-206

3. Li Y, Gao H, Sun Z, Li Q, Xu Y, Ge C, Cao Y (2018) Tuning morphology and conductivity in two-step synthesis of zinc-cobalt oxide and sulfide hybrid nanoclusters as highly-performed electrodes for hybrid supercapacitors. J Solid State Electrochem 22:3197-3207

4. Moureaux F, Stevens P, Toussaint G, Chatenet M (2013) Development of an oxygen-evolution electrode from 316L stainless steel: Application to the oxygen evolution reaction in aqueous lithium–air batteries. J Power Sources 229:123-132

5. Lu Y-C, Gallant BM, Kwabi DG, Harding JR, Mitchell RR, Whittingham MS, Shao-Horn Y (2013) Lithium-oxygen batteries: Bridging mechanistic understanding and battery performance. Energ Environ Sci 6:750-768

6. Suen N-T, Hung S-F, Quan Q, Zhang N, Xu Y-J, Chen HM (2017) Electrocatalysis for the oxygen evolution reaction: recent development and future perspectives. Chem Soc Rev 46:337-365

7. Tan P, Chen B, Xu H, Zhang H, Cai W, Ni M, Liu M, Shao Z (2017) Flexible Zn- and Li-air batteries: Recent advances, challenges, and future perspectives. Energ Environ Sci 10:2056-2080

8. Zhu K, Zhu X, Yang W (2019) Application of in situ techniques for the characterization of NiFe-based oxygen evolution reaction (OER) electrocatalysts. Ang Chem Int Ed 58:1252-1265

9. Sakita AMP, Noce RD, Vallés E, Benedetti AV (2018) Pulse electrodeposition of CoFe thin films covered with layered double hydroxides as a fast route to prepare enhanced catalysts for oxygen evolution reaction. Appl Surf Sci 434:1153-1160.

10. Zhao G, Zhang L, Pan T, Sun K (2013) Preparation of NiO/multiwalled carbon nanotube nanocomposite for use as the oxygen cathode catalyst in rechargeable Li–O_2 batteries. J Solid State Electrochem 17:1759-1764

11. Wang F, Wu X, Shen C, Wen Z (2016) Facile synthesis of Fe@Fe$_2$O$_3$ core-shell nanowires as O$_2$ electrode for high-energy Li-O$_2$ batteries. J Solid State Electrochem 20:1831-1836

12. Zeng J, Amici J, Monteverde Videla AHA, Francia C, Bodoardo S (2017) Synthesis of mesoporous carbons and reduced graphene oxide and their influence on the cycling performance of rechargeable Li-O$_2$ batteries. J Solid State Electrochem 21:503-514

13. Yang J, Li Y, Mi H, Zhang P, Deng L, Sun L, Ren X (2018) Enhanced electrocatalytic performance of Fe-TiO$_2$/N-doped graphene cathodes for rechargeable Li-O$_2$ batteries. J Solid State Electrochem 22:909-917

14. Wang J, Cui W, Liu Q, Xing Z, Asiri AM, Sun X (2016) Recent Progress in Cobalt-Based Heterogeneous Catalysts for Electrochemical Water Splitting. Adv Mater 28:215-230

15. Anis SF, Lalia BS, Mostafa AO, Hashaikeh R (2017) Electrospun nickel–tungsten oxide composite fibers as active electrocatalysts for hydrogen evolution reaction. J Mater Sci 52:7269-7281

16. Zhang M, Gao J, Hong W, Wang X, Tian Q, An Z, Wang L, Yao H, Liu Y, Zhao X, Qiu H (2019) Bimetallic Mn and Co encased within bamboo-like N-doped carbon nanotubes as efficient oxygen reduction reaction electrocatalysts. J Colloid Interface Sci 537:238-246

17. Gao R, Yang Z, Zheng L, Gu L, Liu L, Lee Y, Hu Z, Liu X (2018) Enhancing the Catalytic Activity of Co$_3$O$_4$ for Li–O$_2$ Batteries through the Synergy of Surface/Interface/Doping Engineering. ACS Catal 8:1955-1963

18. Gao R, Shang Z, Zheng L, Wang J, Sun L, Hu Z, Liu X (2019) Enhancing the Catalytic Activity of Co$_3$O$_4$ Nanosheets for Li-O$_2$ Batteries by the Incoporation of Oxygen Vacancy with Hydrazine Hydrate Reduction. Inorg Chem 58:4989-4996

19. Zheng Y, Gao R, Zheng L, Sun L, Hu Z, Liu X (2019) Ultrathin Co$_3$O$_4$ Nanosheets with Edge-Enriched {111} Planes as Efficient Catalysts for Lithium–Oxygen Batteries. ACS Catal 9:3773-3782

20. Wang X, Hou X, Wang Q, Ge W, Guo S (2019) In situ fabrication of flaky-like NiMn-layered double hydroxides as efficient catalyst for Li-O$_2$ battery. J Solid State Electrochem 23:1121-1128

21. Pushpavanam M, Natarajan SR, Balakrishnan K, Sharma LR (1991) Corrosion behaviour of electrodeposited zinc-nickel alloys. J Appl Electrochem 21:642-645

22. Li P, Sun W, Yu Q, Guan M, Qiao J, Wang Z, Rooney D, Sun K (2015) An effective three-dimensional ordered mesoporous $ZnCo_2O_4$ as electrocatalyst for Li-O₂ batteries. Mater Lett 158:84-87.

23. Costa JM, de Morais Nepel TC, de Almeida Neto AF (2019) Influence of current density and W concentration on Co–W alloys used as catalysts in electrodes for Li–O₂ batteries. Chem Pap 73:1103-1112

24. Sivagami IN, Prasanna K, Santhoshkumar P, Jo YN, Seo GY, Lee CW (2017) Agar templated electrodeposition of binary zinc-cobalt alloy and formation of zinc-cobalt-carbon nanocomposite for application in secondary lithium batteries. J Alloys and Comp 697:450-460.

25. Sulciute A, Baltrusaitis J, Valatka E (2015) Structure, morphology and electrochemical properties of zinc-cobalt oxide films on AISI 304 type steel. J Appl Electrochen 45:405-417

26. Lu Y-C, Gasteiger HA, Crumlin E, McGuire R, Shao-Horn Y (2010) Electrocatalytic activity studies of select metal surfaces and implications in Li-air batteries. J Electrochem Soc 157:A1016-A1025.

27. Wang X, Xue H, Na Z, Yin D, Li Q, Wang C, Wang L, Huang G (2018) Metal organic frameworks route to prepare two-dimensional porous zinc-cobalt oxide plates as anode materials for lithium-ion batteries. J Power Sources 396:659-666

28. Liang S, Cao X, Wang Y, Hu Y, Pan A, Cao G (2016) Uniform $8LiFePO_4 \cdot Li_3V_2(PO_4)_3$/C nanoflakes for high-performance Li-ion batteries. Nano Energy 22:48-58

29. Liu X, Shi S, Xiong Q, Li L, Zhang Y, Tang H, Gu C, Wang X, Tu J (2013) Hierarchical $NiCo_2O_4$@$NiCo_2O_4$ Core/Shell nanoflake arrays as high-performance supercapacitor materials. ACS Appl Mater Interfaces 5:8790-8795

30. Zhang J, Yuan B, Ma J, Wei J, Wang J, Zhou J, Zhang R, Zhang D (2017) Synthesis of $Zn_{0.3}Co_{2.7}O_4$ porous willow-leaf like structure for enhanced electrocatalytic oxygen evolution reaction. Mater Lett 198:196-200

31. Shekhanov RF, Gridchin SN, Balmasov AV (2017) Electroplating of zinc–cobalt alloys from oxalate electrolytes. Prot Met Phys Chem Surf 53:483-487

32. Higashi K, Fukushima H, Urakawa T, Adaniya T, Matsudo K (1981) Mechanism of the electrodeposition of zinc alloys containing a small amount of cobalt. J Electrochem Soc 128:2081-2085

33. Chu Q, Liang J, Hao J (2014) Electrodeposition of zinc-cobalt alloys from choline chloride–urea ionic liquid. Electrochim Acta 115:499-503

34. Lee Y-H, Chang K-H, Hu C-C (2013) Differentiate the pseudocapacitance and double-layer capacitance contributions for nitrogen-doped reduced graphene oxide in acidic and alkaline electrolytes. J Power Sources 227:300-308

35. de Rivas B, López-Fonseca R, Jiménez-González C, Gutiérrez-Ortiz JI (2011) Synthesis, characterisation and catalytic performance of nanocrystalline Co_3O_4 for gas-phase chlorinated VOC abatement. J Catal 281 (1):88-9727

36. Garcia JR, do Lago DCB, Cesar DV, Senna LF (2016) Pulsed cobalt-rich Zn–Co alloy coatings produced from citrate baths. Surf Coat Technol 306:462-472

37. Heine J, Rodehorst U, Badillo JP, Winter M, Bieker P (2015) Chemical stability investigations of polyisobutylene as new binder for application in lithium-air batteries. Electrochim Acta 155:110-115

38. Lu Y-C, Gasteiger HA, Parent MC, Chiloyan V, Shao-Horn Y (2010) The influence of catalysts on discharge and charge voltages of rechargeable Li-oxygen batteries. Electrochem Solid State Lett 13:A69-A72

39. Tang C-W, Wang C-B, Chien S-H (2008) Characterization of cobalt oxides studied by FT-IR, Raman, TPR and TG-MS. Thermochim Acta 473 (1):68-7331. Dilimon VS, Lee D-G, Yim S-D, Song H-K (2015) Multiple roles of superoxide on oxygen reduction reaction in Li$^+$-containing nonaqueous electrolyte: Contribution to the formation of oxide as well as peroxide. J Phys Chem C 119:3472-3480

40. Dilimon VS, Lee D-G, Yim S-D, Song H-K (2015) Multiple Roles of Superoxide on Oxygen Reduction Reaction in Li$^+$-Containing Nonaqueous Electrolyte: Contribution to the Formation of Oxide as Well as Peroxide. J Phys Chem C 119:3472-3480

41. Gittleson FS, Ryu W-H, Taylor AD (2014) Operando observation of the gold-electrolyte interface in Li-O₂ batteries. ACS Appl Mater Interfaces 6:19017-19025

Supplementary material
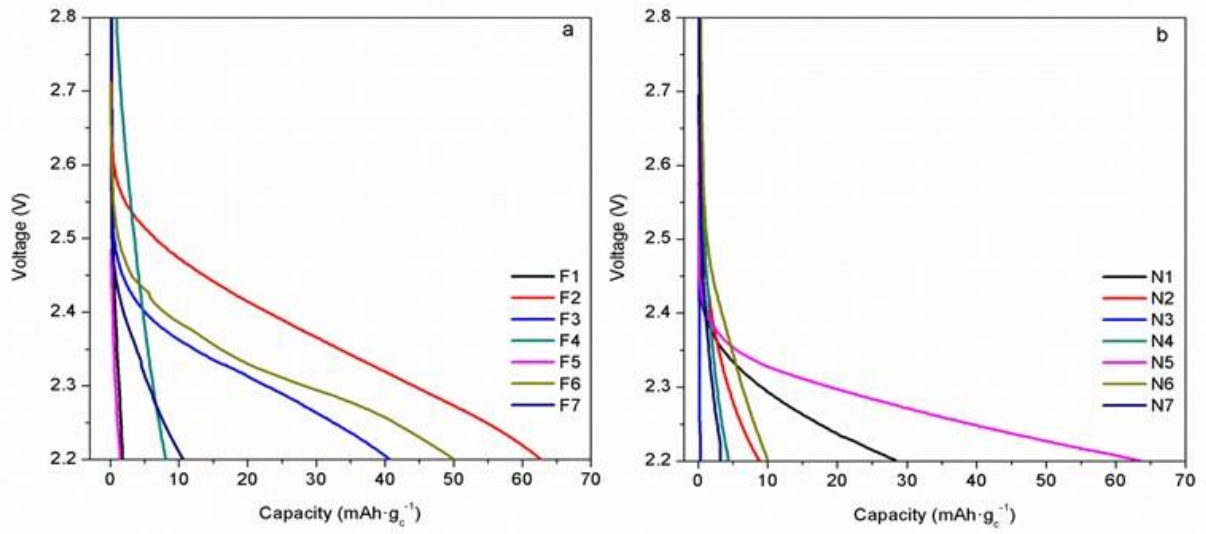
Figure S1. Maximum discharge capacity in a) nickel foam and b) steel mesh electrodes.
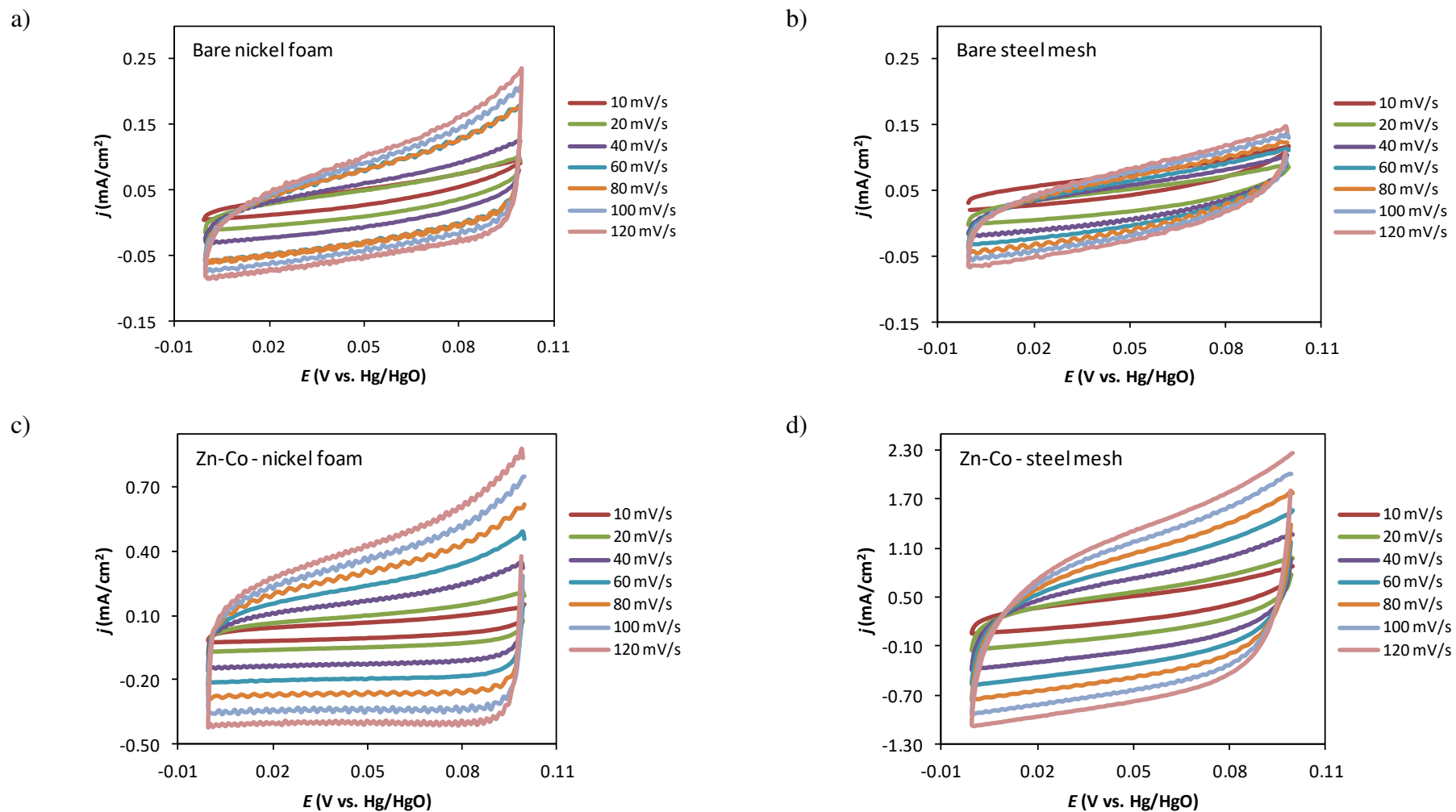
Figure S2. CV curves at different scan rates in a potential window of 0.0 to 0.1 V vs. Hg/HgO in Ar saturated 1 M KOH for different samples: (a) bare nickel foam; (b) bare steel mesh; (c) Zn-Co - nickel foam; (d) Zn-Co - steel mesh.

CHAPTER 6

In-situ transformation of electrodeposited W-Co oxide to ZnCo₂O₄ nanoparticles as an effective bifunctional catalyst in Zn-air batteries

In-situ transformation of electrodeposited W-Co oxide to ZnCo$_2$O$_4$ nanoparticles as an effective bifunctional catalyst in ZABs

Josiel Martins Costa, Michael Patrick Clark,

Ambrósio Florêncio de Almeida Neto, and Douglas Gordon Ivey

Abstract

W-Co was cathodically electrodeposited on gas diffusion layer (GDL) electrodes for application as a bifunctional catalyst Zn-air batteries. The electrodes were synthesized galvanostatically at various pH values (4.5 and 7.5) and deposition times (5, 15 and 25 min). TEM analysis showed that the deposits oxidized in contact with air, forming a conformal layer of W-Co oxide with a thickness of ~10 nm. During battery cycling, most of the W dissolved in the electrolyte. The remaining Co oxide agglomerated, forming nanoparticles < 100 nm in size. Zn^{2+} (present in the electrolyte as ZnO) was incorporated into the Co oxide nanopartcles. As such, the conformal layer of W-Co oxide transformed into cubic spinel ZnCo$_2$O$_4$ nanoparticles which provided excellent bifunctional catalytic activity. The ZnCo$_2$O$_4$ catalyst demonstrated good performance in two-electrode and three-electrode full-cell Zn-air battery tests. In three-electrode tests at 10 mA cm^{-2}, a round trip efficiency of 62% was achieved, exceeding the efficiency of Pt/Ru-C (61%). In two-electrode tests at 10 mA cm^{-2}, an initial efficiency of 61% was obtained and the stability exceeded that of Pt/Ru-C. The final efficiencies were 59% for the three-electrode and 56% for the two-electrode configuration (after 100 cycles). The high maximum power density (216 mW cm^{-2}) and stability during cycling demonstrates that electrodeposited W-Co oxide is well suited as a Zn-air battery catalyst.

Keywords: Energy storage materials; electrocatalysts; W-Co oxide; bifunctional catalyst.

6.1. Introduction

With increasing utilization of renewable energy sources, such as wind and solar, comes the need for improved chemical energy storage technologies. Metal-air batteries are an attractive option due to their high energy density and low cost [1]. Specifically, Zn-air batteries (ZABs), which are environmentally friendly, have high energy densities and are made from abundant and economical raw materials, are a promising solution for grid-scale energy storage. However, widespread application of ZABs has been hampered by poor cycle life and low charge-discharge efficiencies. These problems are largely associated with the air electrode [2].

The oxygen reduction reaction (ORR) and the oxygen evolution reaction (OER) are the discharge and charge reactions occurring at the air electrode, respectively. Equation (1) shows ORR (left to right) and OER (right to left).

$$O_2 + 2H_2O + 4e^- \leftrightarrow 4OH^- \tag{1}$$

Both ORR and OER suffer from slow kinetics, which reduces battery efficiency and necessitates the use of effective catalysts. Because of their high activity towards ORR or OER, noble metal-based catalysts such as Pt (ORR), IrO_2 (OER) and RuO_2 (OER) are considered as benchmarks for catalytic activity. However, these materials are expensive and are not individually bifunctionally active (i.e., catalyze both ORR and OER) [3, 4]. It is essential to develop and study inexpensive, high-efficiency bifunctional catalysts with performance on-par with or better than their noble metal counterparts.

The OER activity and cycling stability of Co oxides have been shown to improve with the addition of other transition metals, such as Fe [5, 6]. Additionally, oxides composed of two, or even more, transition metals have been applied as effective bifunctional catalysts [7]. When combining multiple transition metals to form a mixed oxide, the resultant electronic structure is a combination of the individual oxides. By carefully selecting the optimum elements and composition, the electronic structure of mixed oxides can easily be tailored in order to maximize catalytic performance [8]. The performance of transition metal oxides can be further improved by forming nanostrucutres to enhance surface area. A number of mixed transition metal oxide nanoparticles have been studied for ORR [9]. Nanoparticles allow for enhanced performance because they improve surface area and help to reduce the impact of transition

metal oxide's poor conductivity [10]. Toh et al. prepared $NiCo_2O_4$ and $ZnCo_2O_4$ spinel oxides that had onset potentials of -147 and -239 mV vs. Ag/AgCl, respectively. These results demonstrate the potential of Co containing mixed transition metal oxides for use as ORR catalysts [11].

Transition metal oxide catalysts can be manufactured by a variety different techniques, such as hydrothermal, sol-gel, and thermal decomposition methods [12-14]. Electrodeposition is a simple alternative capable of depositing active material on electrodes without the need for binders, additives, or conductive agents, making it well suited for the synthesis of bifunctional catalysts. Electrodeposition has a wide range of parameters which can be tuned in order to achieve optimal deposits. These parameters include metal concentration in the electrolyte, pH, electrodeposition time, temperature, agitation/stirring and electrolyte additives, all of which can affect deposit morphology and catalytic activity [15].

In this work, a novel W-Co oxide, which transitions to $ZnCo_2O_4$ nanoparticles during battery cycling, bifunctional catalyst for the air electrode for ZABs is studied. To the authors' knowledge, W has not been utilized as either an ORR or OER catalyst for ZABs, likely due to tungsten's high solubility in alkaline solutions; however, W-Co oxide has been used in supercapacitors and lithium ion batteries [16, 17]. W-Co is cathodically electrodeposited under variable pH conditions and deposition periods. The metallic W-Co film immediately oxidizes upon contact with air. The catalyst is electrochemically characterized using linear sweep voltammetry (LSV) and cyclic voltammetry (CV). Microstructural characterization is done through scanning, transmission, and scanning transmission electron microscopy (SEM, TEM, STEM), coupled with energy dispersive x-ray (EDX) spectroscopy. The best candidates are assembled into batteries and cycled at 10 and 20 mA cm^{-2}, in either two-electrode or three-electrode configurations.

6.2. Materials and methods

6.2.1. Catalyst preparation

The solutions for the electrodeposition of W-Co contained (0.0125, 0.025, 0.03, 0.035, and 0.05 M cobalt sulfate heptahydrate ($CoSO_4 \cdot 7H_2O$ - Fisher scientific (98.1%)), 0.05 M sodium tungstate dehydrate ($Na_2WO_4 \cdot 2H_2O$ - Acros Organics (>99%)) and 0.05 M

ammonium citrate tribasic ($C_6H_{17}N_3O_7$ - Alfa Aesar (>97%)), which is a complexing agent [18]. All chemicals were used as received. Electrodeposition was performed in a two-electrode setup, with polytetrafluoroethylene (PTFE) coated porous carbon paper (SGL 39BC gas diffusion layer or GDL) as the working electrode and Pt mesh as the counter electrode[15]. The deposition area was 2 cm × 2 cm. W-Co was cathodically deposited according to Equations (2) and (3) at a current density of 50 mA cm^{-2}, using a potentiostat (Biologic VSP-300).

$$Co^{+2}_{(aq)} + 2\bar{e} \rightarrow Co_{(s)} \qquad\qquad \text{E}^o = \text{-0.28 V vs SHE} \qquad\qquad (2)$$

$$WO_{3(aq)} + 6H^+ + 6\bar{e} \rightarrow W_{(s)} + 3H_2O \qquad\qquad \text{E}^o = \text{-0.09 V vs SHE} \qquad\qquad (3)$$

Because electrodeposition was conducted cathodically, it would be expected that the deposited films would be metallic in natures. However, the deposited films quickly oxidize upon contact with air. The films in this work will be referred to as W-Co oxide. The effects of solution pH and electrodeposition time on ZAB efficiency were investigated in duplicate with pH values of 4.5 and 7.5 and electrodeposition times of 5, 15 and 25 min. Deposition solution pH was adjusted with nitric acid. After deposition, all samples were rinsed with deionized water and dried in air. The samples were also annealed at 300 °C in air for 0.5 h.

The benchmark Pt-Ru bifunctional catalyst was prepared by ink spraying. The ink contained 30 wt% Pt and 15 wt% Ru with carbon black (Alfa Aesar) and was dispersed in a suspension of 2 mL of deionized water, 1 mL of isopropanol, 0.1 ml of 5% Nafion (D- 521) and 0.2 mL of 5% PTFE binder. The ink was sonicated for 0.5 h and applied to the GDL using an air gun. The mass loading of Pt/Ru-C on the GDL was ~1.2 mg cm^{-2} (360 μg Pt cm^{-2} and 180 μg Ru cm^{-2}) after annealing at 300 °C for 0.5 h.

6.2.2. Microstructural characterization

Scanning electron microscopy (Tescan VEGA3 SEM and Zeiss Sigma FESEM) and transmission electron microscopy (JEOL JEM-ARM200CF TEM), along with energy dispersive X-ray (EDX) spectroscopy, were used to characterize the microstructure and

---

[15] See Appendix A.

composition of the samples. TEM samples were prepared by scraping off some of the catalyst from the GDL and dispersing the catalyst in ethanol using ultrasonic agitation. One or two drops of the suspension were placed onto a carbon coated, copper grid and the ethanol was allowed to evaporate.

6.2.3. Electrochemical measurements and battery testing

Linear sweep voltammetry (LSV) and cyclic voltammetry (CV) in 1 M KOH were performed with the W-Co oxide catalyst coated GDL as the working electrode, Pt mesh as the counter electrode and Hg/HgO (0.098 V vs. SHE) as the reference electrode. Potentials reported for half-cell tests are all vs. Hg/HgO. The electrolyte was purged with pure O_2 gas for 15 min prior to testing to ensure O_2 saturation. The current densities were normalized to the geometric surface area.

ZAB tests were performed in a home-made cell using a two-electrode (bifunctional) (Figure S1-a) or three-electrode configuration (Figure S1-b). All electrochemical testing was performed using a Biologic VSP-300 potentiostat. W-Co oxide coated GDL acted as the discharge-charge electrode with an area of 1 cm^2 exposed to the electrolyte (6 M KOH + 0.25 M ZnO). The Zn electrode was bent in an L shape (dimensions 8.5 × 1.8 cm) with one segment placed horizontally in the lower part of the cell (Figure S1). The distance between the horizontal Zn plate and the air electrode was 2 cm. Electrochemical impedance spectroscopy (EIS) was performed at 1.2 V with 10 mV AC potential from 100 kHz to 50 mHz. Discharge-charge cycling was performed at a current density of 10 or 20 mA cm^{-2}, with each cycle consisting of a 10 min charge and 10 min discharge period; a 5 min rest period was implemented after each charge or discharge segment. The test duration was 50 h (100 full cycles). The efficiency was calculated from Equation 4.

$$Efficiency\ (\%) = \frac{Discharge\ potential}{Charge\ potential} \qquad (4)$$

6.3. Results and discussion

6.3.1. Electrochemical analysis

In order to determine the solution W:Co ratio that provided the best efficiency at 20 mA cm^{-2} in a ZAB, different proportions were tested according to Table 1. The 1:1 ratio had the highest efficiency, however, insoluble precipitates formed in the electrodeposition solution. SEM EDX analysis showed that the precipitates contained both W and Co, but were Co-rich (Co:W ratio ~2 - Figure S2-a and S2-e). The maximum W:Co ratio in which there was no precipitate formation was 1:0.7. Lower W:Co electrodeposition solution ratios led to increased OER potentials, decreasing the efficiency. OER rate tests were not stable for 1:0.5 and 1:0.25 ratios. From this initial study, electrodeposition solutions containing a W:Co ratio of 1:0.7 were used for further studies involving electrodeposition time and solution pH due to the better performance for ORR and OER in the two-electrode configuration. Charge-discharge tests were also performed with air electrodes fabricated from pure Co deposits (0.035 M CoSO$_4$ 7H$_2$O) and pure W (0.05 M Na$_2$WO$_4$ 2H$_2$O); both deposits were annealed. The efficiencies at 20 mA cm^{-2} were 57.1% (Co) and 46.6% (W), demonstrating that W and Co combined provides a synergistic effect. Pure W electrodes were unstable during OER testing. Figure S2-b-d shows SEM images of the surface morphology for the pure W, pure Co and W-Co oxide electrodes (before cycling). EDX spectra show that W is the main component for electrodes containing both W and Co (Figure S2-e).

Table 6.1. Battery charge/discharge efficiency for different W:Co proportions (15 min electrodeposition time, annealed electrodes)

W:Co proportion	pH	Final charge potential* (V)	Final discharge potential* (V)	Efficiency (%)
1:1 (0.05 M:0.05 M)	8.0	2.08	1.24	59.6
1:0.7 (0.05 M:0.035 M)	7.5	2.08	1.23	59.1
1:0.6 (0.05 M:0.03 M)	7.6	2.17	1.21	55.8
1:0.5 (0.05 M:0.025 M)	8.0	2.18	1.19	54.6
1:0.5 (0.05 M:0.025 M)	6.0	2.49	1.15	46.2
1:0.25 (0.05 M:0.0125 M)	4.0	2.49	1.13	45.4
1:0 (0.05 M:0 M)	9.2	2.49	1.16	46.6
0:1 (0 M:0.035 M)	5.5	2.10	1.20	57.1

*Potentials were taken at a discharge/ charge current density of 20 mA cm^{-2}

The influence of solution pH and electrodeposition time for W-Co oxide deposits on the efficiency of a ZAB was investigated and the results are shown in Table 2; all samples were annealed before testing. Lower efficiency values were obtained at a pH of 4.5, compared with a pH of 7.5, and can be attributed to hydrogen evolution occurring in parallel with electrodeposition. Hydrogen evolution was confirmed by the observation of H_2 bubbles during deposition; the bubbles negatively impact the morphology of the deposited material [19]. Additionally, H^+ ions are consumed during H_2 evolution, causing the pH to increase during deposition. Electrodepositions for 15 min were also done at a pH of 10.5 with addition of ammonium hydroxide (0.05 M) to determine whether a further increase in efficiency could be achieved. The efficiency of deposits prepared at pH of 10.5 was 58.6 ± 1.3 %, indicating no improvement relative to the natural solution pH (7.5).

Table 6.2. Battery efficiencies for W-Co electrodes electrodeposited under different conditions

pH	Deposition time (min)	Final pH	Efficiency (%)
	5	4.7 ± 0.1	47.1 ± 0.5
4.5	15	4.9 ± 0.1	46.2 ± 0.1
	25	4.9 ± 0.1	47.3 ± 0.3
	5	7.5 ± 0.0	57.6 ± 0.0
7.5	15	7.4 ± 0.1	58.8 ± 0.4
	25	7.5 ± 0.0	58.5 ± 0.3
10.5	15	10.5 ± 0.1	58.6 ± 1.3

Discharge potentials were determined for a range of current densities (2, 5, 10 and 20 mA cm^{-2}) and are shown in Figure 1-a for annealed samples. The results at all current densities confirm that the bifunctional activity of W-Co oxide is comparable to Pt-Ru. According to Table 2, it was determined that the optimum deposition conditions were a solution pH of 7.5 and a deposition time of 15 min.

Figure 1-b shows CV plots for annealed and unannealed samples deposited from solutions at pH values of 4.5 and 7.5 in O_2-saturated 1 M KOH. Annealing improved the ORR activity for both samples. LSV plots for ORR in O_2-saturated 1 M KOH are shown in Figure 1-c. The 7.5 pH, annealed sample showed activity very close to that for the Pt-Ru baseline material with an onset potential (at 10 mA cm^{-2}) of -0.11 V. According to several studies, annealing can improve electrocatalytic activity [20-24] and ensured that the W-Co, which was deposited as a metallic film, was completely oxidized. Because of the results shown in Figure 1-b and 1-c the unannealed films were not investigated further.

Double layer capacitance is directly proportional to electrode surface area and was used to compare the relative surface area of deposits. The double layer capacitance (C_{dl}) was evaluated by the integral method using CV plots at different scanning rates (v) in Ar-saturated 1 M KOH (Figure S3). The potential range used for capacitance measurements was determined from CV plots taken in Ar-saturated 1 M KOH (Figure 1-d). The potential range used for C_{dl} measurement was $0 - 0.1$ V because of the absence of faradaic reactions in this region. The double layer charge (q_{dl}) was estimated from a plot of q vs. $v^{-1/2}$, using linear regression to extrapolate v to ∞ (Figure 1-e) [25]. C_{dl} was calculated by dividing q_{dl} by the potential window (0.1 V). The total charge (q_t) was also estimated by linear regression using the same method; instead by extrapolating v to 0 on a plot of q^{-1} vs. $v^{1/2}$ (Figure S4). The pseudocapacitance C_p was calculated by subtracting C_{dl} from C_t. Capacitance results are summarized in Table 3. Annealing improved C_{dl} for both the pH 4.5 and 7.5 deposits; since no additional material has been incorporated, the cause of the C_{dl} increase is not immediately apparent. The increase in C_{dl} can be attributed to one or both of the following effects: the fully oxidized film may provide greater capacitance per unit area than the unannealed film [26], and/ or annealing may introduce some surface roughness/ facets. The highest C_{dl} was achieved for the annealed pH 7.5 sample, with $C_{dl} = 38.4$ mF cm^{-2}. The relatively high surface area of this deposit helps facilitate its excellent catalytic activity. Comparing the C_{dl} value (38.4 mF cm^{-2}) of the annealed, 7.5 pH sample with other catalysts prepared by our group and reported in literature, such as electrodeposited Co (10.4 mF cm^{-2}) [6], electrodeposited MnO$_x$ (8.3 mF cm^{-2}) [24], and atomic layer deposited MnO$_x$ (20.4 mF cm^{-2}) [27] illustrates the high surface area of the 7.5 pH W-Co oxide film. Capacitance values were not attainable from the unannealed pH 4.5 sample as well as the bare GDL, due to their hydrophobic nature preventing electrolyte penetration. Figure 1-f presents OER LSV plots for the annealed 7.5 pH sample, as well as for Pt-Ru and bare GDL. The OER activity was increased with the W-Co oxide coating compared with bare GDL, which has no catalytic activity. The onset potential (at 10 mA cm^{-2}) for Pt-Ru is 73 mV lower than the value for W-Co oxide.
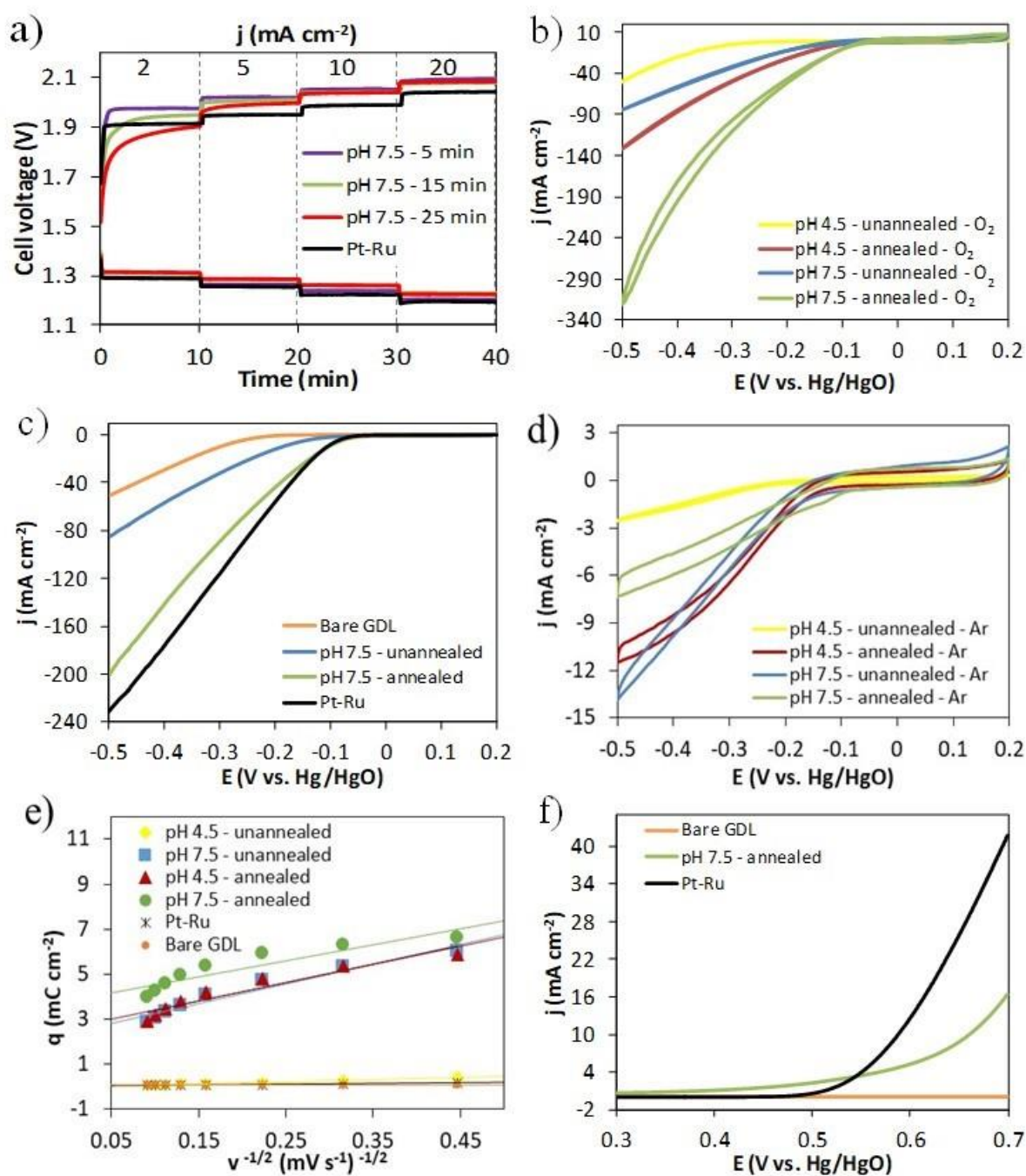
Figure 6.1. Electrochemical measurements for W-Co oxide catalysts: a) Rate discharge-charge curves for various electrodes in Zn-air batteries; b) CV plots (20 mV s^{-1} in O$_2$-saturated 1 M KOH); c) ORR LSV plots (5 mV s^{-1} in O$_2$-saturated 1 M KOH); d) CV plots (20 mV s^{-1} in Ar-saturated 1 M KOH) ; e) Results for C$_{dl}$ measurement (voltammetric charge (q) plotted against the square root of the scan rate (v$^{-1/2}$)); f) OER LSV plots (5 mV s^{-1} in O$_2$-saturated 1 M KOH).

Table 6.3. Capacitance measurement results

Electrode	q_t (mC cm^{-2})	q_{dl} (mC cm^{-2})	C_t (mF cm^{-2})	C_{dl} (mF cm^{-2})	C_p (mF cm^{-2})
Bare GDL	N/A	0.06	N/A	0.6	N/A
Pt-Ru	0.26	0.03	2.6	0.3	2.3
pH 4.5 - unannealed	N/A	N/A	N/A	N/A	N/A
pH 4.5 - annealed	8.18	2.60	81.8	26.0	55.8
pH 7.5 - unannealed	8.41	2.38	84.1	23.8	60.3
pH 7.5 - annealed	8.27	3.84	82.7	38.4	44.3

6.3.2. Morphology and composition of the catalysts

W-Co oxide samples deposited from a solution with a pH of 7.5 for 15 min and then annealed, were examined using TEM/STEM (Figure 2). TEM/STEM results for the unannealed deposit are shown in Figure S5. Figure 2-a and 2-b show STEM bright field (BF) and annular dark field (ADF) images of GDL carbon particles coated with the electrodeposited W-Co oxide. Due to the relatively high density and atomic number of the W-Co oxide, the film appears as darker regions in the BF image (3 regions are circled in Figure 2-a) and bright contrast regions in the ADF image. STEM imaging clearly shows that the W-Co oxide film coats the GDL particles conformally, which facilitates the high surface area of the electrode. The conformal nature of this deposit was surprising, as electrodeposition is commonly considered a directional deposition technique [28]. The conformal nature of the W-Co oxide is very similar to MnO_x films prepared by the much more complicated, expensive, and slow technique of atomic layer deposition [27]. A high resolution TEM image is shown in Figure 2-c, showing a film thickness of ~10 nm or less. EDX maps from the area shown in Figure 2-a and 2-b are shown in Figure 2-d and 2-e. STEM EDX spectra for cycled and uncycled deposits are shown in Figure S6. The STEM EDX spectra and mapping demonstrate that the deposit is clearly composed of W and O, with a small amount of Co. TEM/STEM analysis shows no significant differences between annealed and unannealed samples.
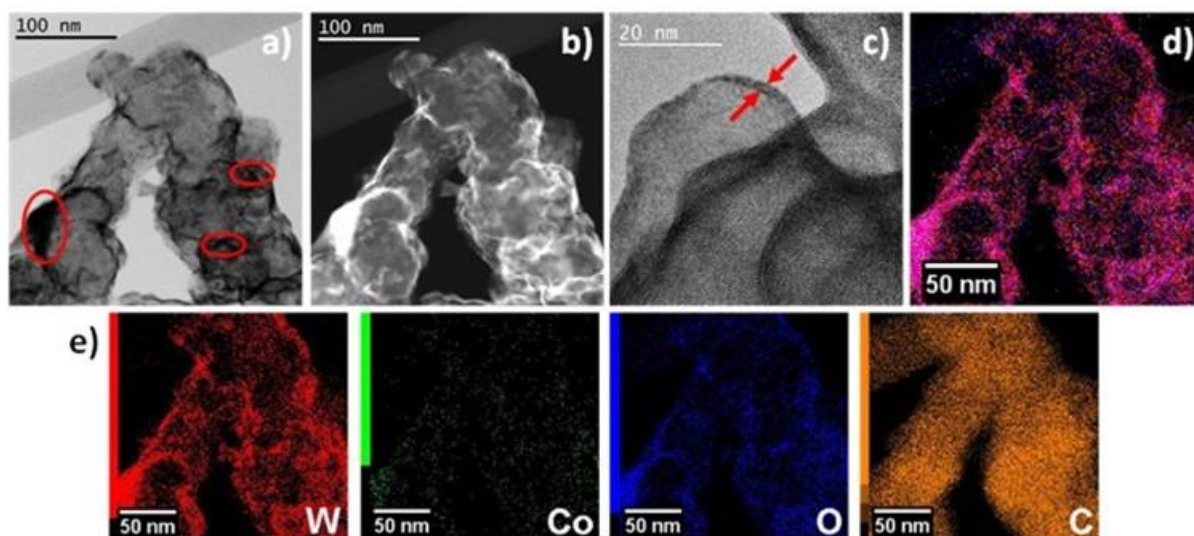
Figure 6.2. TEM/ STEM analysis of the annealed, 7.5 pH sample before electrochemical testing: a) STEM BF image; b) STEM ADF image; c) high resolution TEM image; d) EDX map overlay of W (red), Co (green) and O (blue); e) individual EDX maps for W, Co, O and C.

Samples were examined in the SEM before and after ZAB testing; images are shown in Figure 3-a to 3-h. The electrode prepared at pH 4.5 (Figure 3-a) has a heterogeneous morphology, with particles scattered across the electrode surface. The sample prepared at 7.5 pH (Figure 3-b) has a much more homogeneous morphology, the surface of the GDL appears unchanged after deposition; the presence of a W-Co oxide deposit is confirmed by STEM/ TEM as well as SEM EDX analysis. Samples cycled in a ZAB (both bifunctional and three-electrode) do not retain their homogeneous morphology, particles are present across the electrode surface. Relatively large particles (> 1 μm) were observed on all cycled samples (arrows in Figure 3-f), which were identified as KOH using EDX analysis. Samples that were exposed to OER potentials (Figure 3-c, 3-e, and 3-g) had smaller and more abundant particles across the surface, as indicated by arrows in Figure 3-g. These small particles had relatively large Co content, suggesting that they are composed of Co oxide.

EDX spectra were taken from multiple areas from each sample. The EDX spectra all contain large C and F signals due to the C based GDL (F is present in the PTFE binder). All battery cycled samples were thoroughly rinsed with deionized water prior to SEM and EDX analysis; however, significant K and Zn peaks from the electrolyte were still detected for these samples. Plan view secondary electron (SE) images of annealed samples before battery testing (solution pH of 4.5 and 7) are shown in Figure 3-a and 3-b. The deposit from the pH 4.5 solution

contains W, but no Co, while the deposit from the pH 7.5 solution contains W plus a small amount of Co. After 50 h of bifunctional cycling (Figure 3-c), W is no longer observed in the EDX spectrum. W dissolution was investigated by exposing electrodes to a number of cycling conditions. Electrodes were cycled in a three-electrode configuration, using separate electrodes for ORR and OER. Two pairs of electrodes were cycled, one pair for 2.5 h (5 cycles), and another pair for 50 h (100 cycles). EDX spectra for the cycled samples all show a drop in W intensity during cycling, with most electrodes having no W intensity at all. An electrode submerged in electrolyte for 50 h also showed no W intensity, demonstrating that W passively dissolves in the electrolyte. This is confirmed by the W-H_2O Pourbaix diagram [29]. In alkaline solutions, soluble WO_4^{-2} is the stable W species, i.e., WO_3 dissolves in the KOH + ZnO electrolyte. At the OER electrode, the applied potentials are higher than at the ORR electrode, providing a large overpotential for oxidation. This leads to faster dissolution at the OER electrode compared with the ORR electrode.
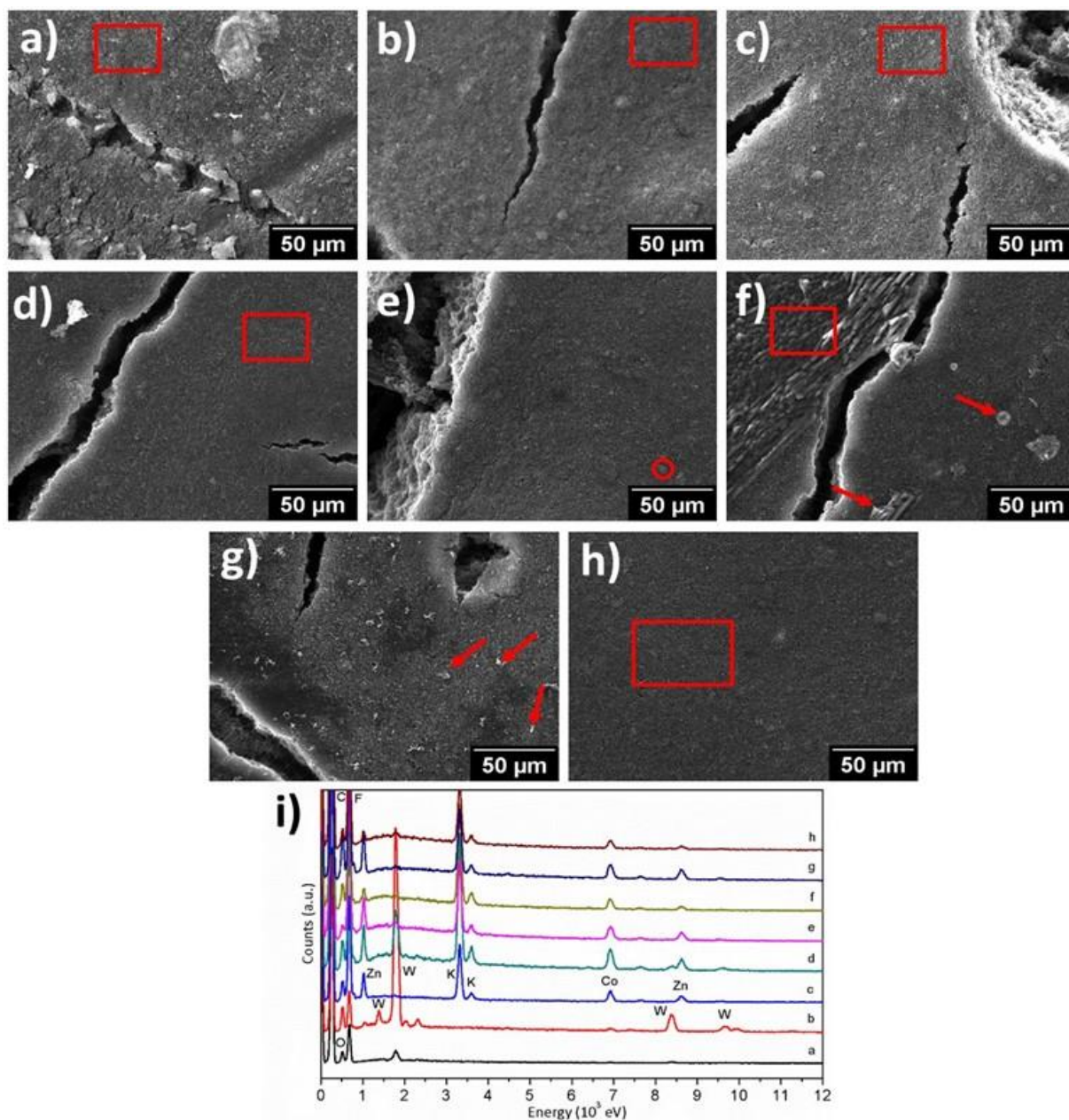
Figure 6.3. SEM secondary electron (SE) images of various W-Co oxide coated electrodes: a) 4.5 pH, annealed and before testing; b) 7.5 pH, annealed and before testing; c) 7.5 pH, annealed after cycling 50 h (bifunctional - two-electrode at 10 mA cm^{-2}); d) ORR electrode - 7.5 pH, annealed and after 5 cycles - three-electrode at 10 mA cm^{-2}; e) OER electrode - 7.5 pH, annealed and after 5 cycles - three-electrode at 10 mA cm^{-2}; f) ORR electrode - 7.5 pH, annealed and after cycling for 50 h - three-electrode at 10 mA cm^{-2}; g) OER electrode - 7.5 pH, annealed and after cycling 50 h - three-electrode at 10 mA cm^{-2}; h) immersed in the electrolyte (6M KOH + 0.25 ZnO) for 50 h. i) EDX spectra for the various electrodes from the regions indicated by the rectangles, arrows or points.

The annealed sample, after battery cycling for 50 h (100 cycles) at 10 mA cm^{-2} in the two-electrode (bifunctional) configuration, was examined by TEM/STEM (Figure 4). The deposit changed significantly during cycling. First of all, the deposit has coalesced forming discrete particles on the carbon substrate. The particles show up bright in the STEM ADF image (Figure 4-a) and dark in the STEM BF image (Figure 4-b). The particle size varies considerably, from a few nm up to ~100 nm. Secondly, most of the W is dissolved into the electrolyte and Zn is incorporated into the particles. This is evident from the EDX maps in Figure 4-d and 4-e and EDX spectra shown in Figure S6. The particles are nanocrystalline; a selected area diffraction (SAD) pattern taken from the region (Figure 4-c) can be indexed to a $ZnCo_2O_4$ cubic spinel structure (a = 0.8095 nm – PDF #23-1390). The presence of small ammounts of W in the EDX map suggests that the $ZnCo_2O_4$ is doped with a small amount of W. Spinel structures of ternary transition metal oxides, including $ZnCo_2O_4$ [11], have been utilized for ORR/OER processes, showing synergistic effects between the two transition metal elements [30]. Liu et al. prepared N-doped nanotubes coupled with $ZnCo_2O_4$ for use as a bifunctional electrocatalysts in Zn-air batteries [31]. Their $ZnCo_2O_4$-NCNT catalyst had excellent bifunctional performance, with a stable discharge voltage of 1.35 V (at 10 mA cm^{-2}), and a stable charge voltage of 2.19 V (at 100 mA cm^{-2}).
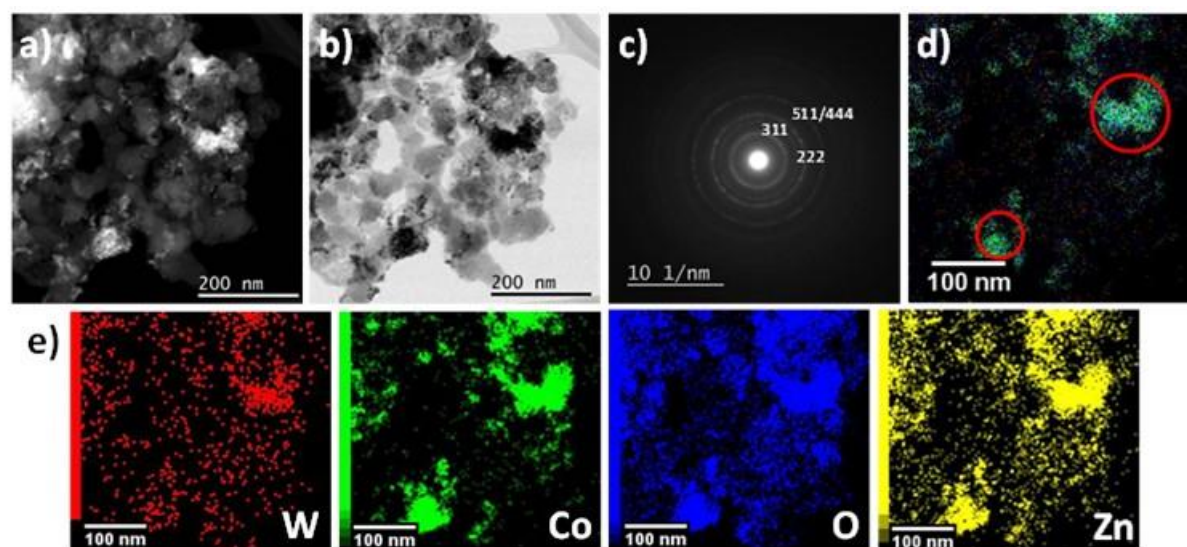
Figure 6.4. STEM images, SAD pattern and EDX analysis of sample electrodeposited at 7.5 pH and annealed, after 50 h of cycling: a) STEM ADF image; b) STEM BF image; c) SAD pattern. d) EDX map overlay of W (red), Co (green) and O (blue); e) individual EDX maps for Co, W, O and Zn.

The formation of $ZnCo_2O_4$ nanoparticles from the initial W-Co oxide deposit can help explain why despite W being dissolved, the W-Co oxide deposit out performs deposits prepared using only Co. By co-depositing W and Co, Co is well distributed in a conformal layer across the GDL surface. Upon cycling, the W oxide scaffold is dissolved, and the remaining Co oxide coalesces into nanoparticles while simultaneously incorporating Zn to form $ZnCo_2O_4$. The high surface area of the spinel nanoparticles provide excellent catalytic activity. Deposits prepared without W do not achieve the finely dispersed nanoparticle morphology, and as such, have inferior ZAB performance.

In order to investigate the distribution of catalyst within the porosity of the GDL, cross sections for the SEM were prepared by freezing as prepared electrodes (before testing) in liquid nitrogen and then fracturing them. SEM EDX line scans were done across the fractured surfaces; examples are shown in Figure 5. Both Co and W were detected at depths into the GDL of up to ~80 μm. An interesting feature of the line scans is that the composition reaches a maximum at ~40 μm (Figure 5-a and 5-b), which appears to be counter intuitive. The maximum Co and W concentrations are expected to be at the surface. The observed distribution is an artifact of EDX analysis in the SEM. The carbon substrate is porous and has a low atomic number ($z = 6$), which generates a large interaction volume for x-ray generation. The GDL fracture surfaces during imaging were not oriented exactly normal to the electron beam, but were tiled by ~15°. The regions closest to the deposition surface did not generate as many x-rays, due to electrons escaping from the sample surface, leading to lower W and Co composition. This effect accounts for the lower apparent surface concentration of Co and W and is illustrated in Figure 5-d. The presence is catalyst deep within the GDL helps to enhance ZAB performance. Deep catalyst distribution allows for greater surface area than techniques such as spray coating which load catalyst only on the GDL surface. This catalyst distribution also helps to maintain three phase boundaries between catalyst, electrolyte, and air during extended cycling. During cycling, it is common for the electrolyte to soak into the structure of the GDL; if catalyst is not effectively distributed this causes a loss of three phase boundaries and reduces battery performance.
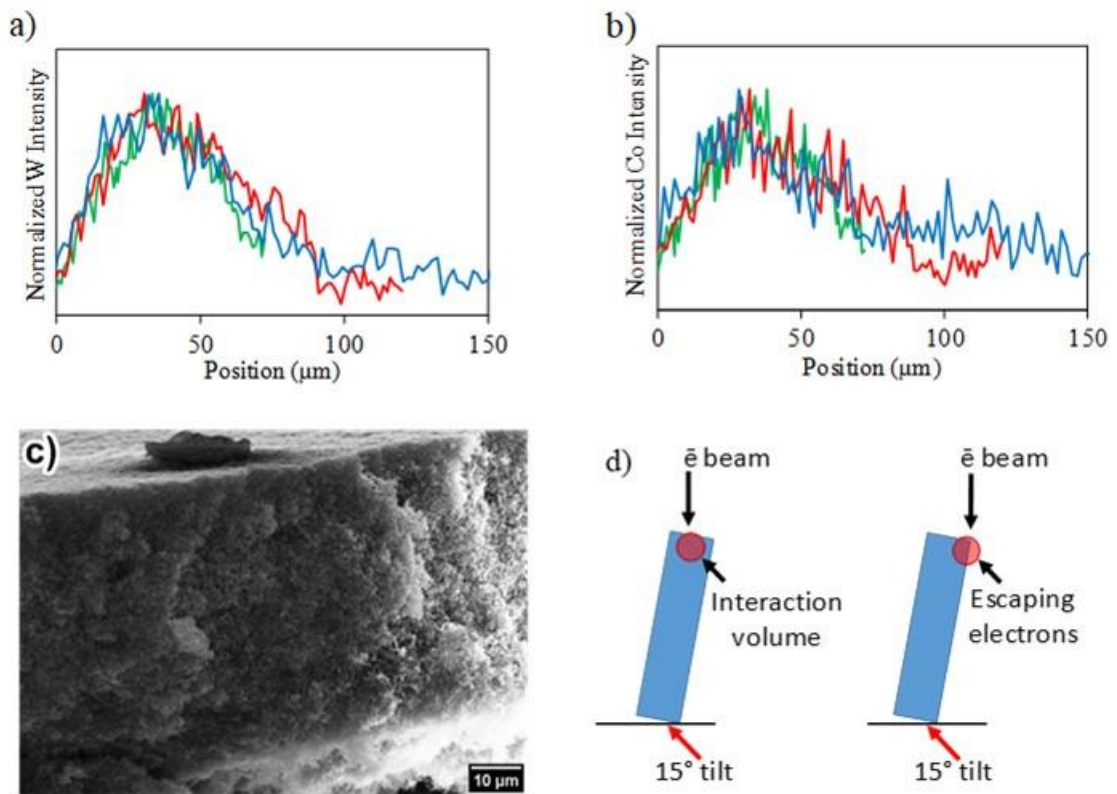
Figure 6.5. SEM EDX cross-section line scans for a) W and b) Co. Three separate scans were taken from different areas. c) FESEM SE cross-section image of GDL. d) Schematic showing electron beam interaction with the cross-section sample.

6.3.3. Zn-air battery measurements

Figure 6-a shows charge and discharge polarization curves for bare GDL, Pt-Ru and W-Co oxide (annealed, pH 7.5 deposit). W-Co oxide exhibits much better performance than bare GDL and better discharge performance than Pt-Ru at all but the lowest current densities. The charge performance is superior to Pt-Ru at current densities less than 10 mA cm^{-2} and comparable at higher current densities.

Polarization and power curves, during discharge, for the annealed and unannealed W-Co oxide samples are shown in Figure 6-b. The maximum power density was 216.4 mW cm^{-2} for the annealed electrode and 189.6 mW cm^{-2} for the unannealed electrode. These values are superior to those for other air electrode catalysts in Zn-air batteries reported in the recent literature: Fe$_3$O$_4$ encapsulated in porous carbon nanobowls - 156.8 mW cm^{-2} [32], N and Cu codoped CoS$_{1.97}$ nanowires - 68.6 mW cm^{-2} [33], N and P co-doped carbon spheres -

79 mW cm^{-2} [34], Co nanoparticles encapsulated in N-doped, C nanofibers - 51.7 mW cm^{-2} [35].

Three-electrode charge-discharge cycle tests at 10 mA cm^{-2} are shown in Figure 6-c for W-Co oxide (annealed, pH 7.5 sample). The initial efficiency is 61.8% (discharges at 1.26 V and charges at 2.04 V) while the final efficiency after 50 h (100 cycles) is 59.1% (discharges at 1.23 V and charges at 2.08 V). In the three-electrode battery, there are separate electrodes for ORR and OER, both with W-Co oxide as the catalyst, as shown in the schematic in Figure S1-a. Results for Pt-Ru, with the same three-electrode configuration are shown in Figure 6-d; the initial and final efficiencies are 61.0% (discharges at 1.25 V and charges at 2.05 V) and 60.4% (discharges at 1.25 V and charges at 2.07 V), respectively, for the same cycling period, which is slightly better than for W-Co oxide. A Zn-air battery, with W-Co oxide catalyzed electrodes was also tested in a three electrode configuration at a current density of 20 mA cm^{-2} (Figure S7). The initial efficiency is 58.0% (discharges at 1.23 V and charges at 2.12 V) and the final efficiency is 55.9% (discharges at 1.19 V and charges at 2.13 V), which demonstrates the stability of the catalyst even under higher current density conditions. The excellent performance of the electrodes prepared in this work is attributed to the structure of the catalyst (spinel $ZnCo_2O_4$), the small particle size (< 100 nm), and the good distribution of catalyst throughout the GDL. These factors allow for performance which exceeds most of the results in literature, including current studies that have used $NiCo_2O_4$ ultrathin nanosheets with oxygen vacancies [36] and hollow cobalt oxide nanoparticles embedded in nitrogen-doped carbon [37] as bifunctional electrocatalysts in which they obtained initial efficiency of 52.9 and 58.5%, respectively at 10 mA cm^{-2}.

Electrodes were also cycled at 10 mA cm^{-2} in a two-electrode (bifunctional) configuration (Figure S1-b), with a single electrode used for both OER and ORR. Results for W-Co oxide are shown in Figure 6-e and for Pt-Ru in Figure S8. The initial and final efficiencies for W-Co oxide are 60.3% (discharges at 1.23 V and charges at 2.04 V) and 56.3% (discharges at 1.17 V and charges at 2.08 V), respectively. Pt-Ru had initial and final efficiency values of 62.6% (discharges at 1.24 V and charges at 1.98 V) and 54.3% (discharges at 1.14 V and charges at 2.10 V), respectively. This result demonstrates that the bifunctional cycling stability of W-Co oxide electrodes far exceeds that of Pt-Ru. The three-electrode configuration with separate electrodes for OER and ORR exhibits better cycling stability, as well as higher efficiency than the bifunctional configuration. The improved stability is a result of the smaller

potential window experienced by each electrode. Large potential variations can promote changes in morphology, oxidation state and crystal structure. The cyclic and repetitive nature of these changes causes gradual degradation of the catalyst. The narrow potential window afforded by the three-electrode configuration minimizes this degradation, leading to better efficiency and stability.

The performance of the Zn-air battery was evaluated through the discharge-charge voltage gap ($\Delta\eta$) [38]. The initial difference in discharge-charge potential for the Wo-Co oxide (annealed, pH 7.5 sample) at 10 mA cm^{-2} was 0.81 V ($\Delta\eta_{initial}$). The difference in discharge-charge potential at the end of cycling was 0.91 V ($\Delta\eta_{end}$). This small drop of 0.10 V shows that the catalyst was stable during cycling and the value is comparable to and lower than values found in the literature for the same current density (10 mA cm^{-2}) according to Table S2.

The electrical properties of the electrodes were evaluated at 1.2 V by electrochemical impedance spectroscopy (EIS), as shown in Figure S9 and Table S1. An equivalent circuit composed of R_s (R_f Q_f) (R_{ct} Q_{dl}) was used to fit the experimental data [39], where R_s, R_f and R_{ct} are the electrolyte resistance, catalyst layer resistance and charge transfer resistance, respectively. The catalyst layer resistance for W-Co oxide electrodes is significantly lower than that of the Pt-Ru electrodes (~0.2 vs. ~0.8 Ω cm^2); this is due to the thin and conformal morphology of the W-Co oxide, all of the catalyst is in intimate contact with the conductive C substrate. Since the Pt-Ru was prepared by spray coating, the contact between catalyst and GDL electrode is not as electronically conductive. Before cycling, the charge transfer resistance for W-Co oxide (annealed, pH 7.5) was 0.6 Ω cm^2, which increased after cycling (50 h or 100 cycles for the three electrode configuration) to 1.0 Ω cm^2 and 1.3 Ω cm^2 at current densities of 10 and 20 mA cm^{-2}, respectively. The R_{ct} for W-Co oxide, even after cycling, is still superior to R_{ct} for the Pt-Ru (3.4 Ω cm^2 before cycling).
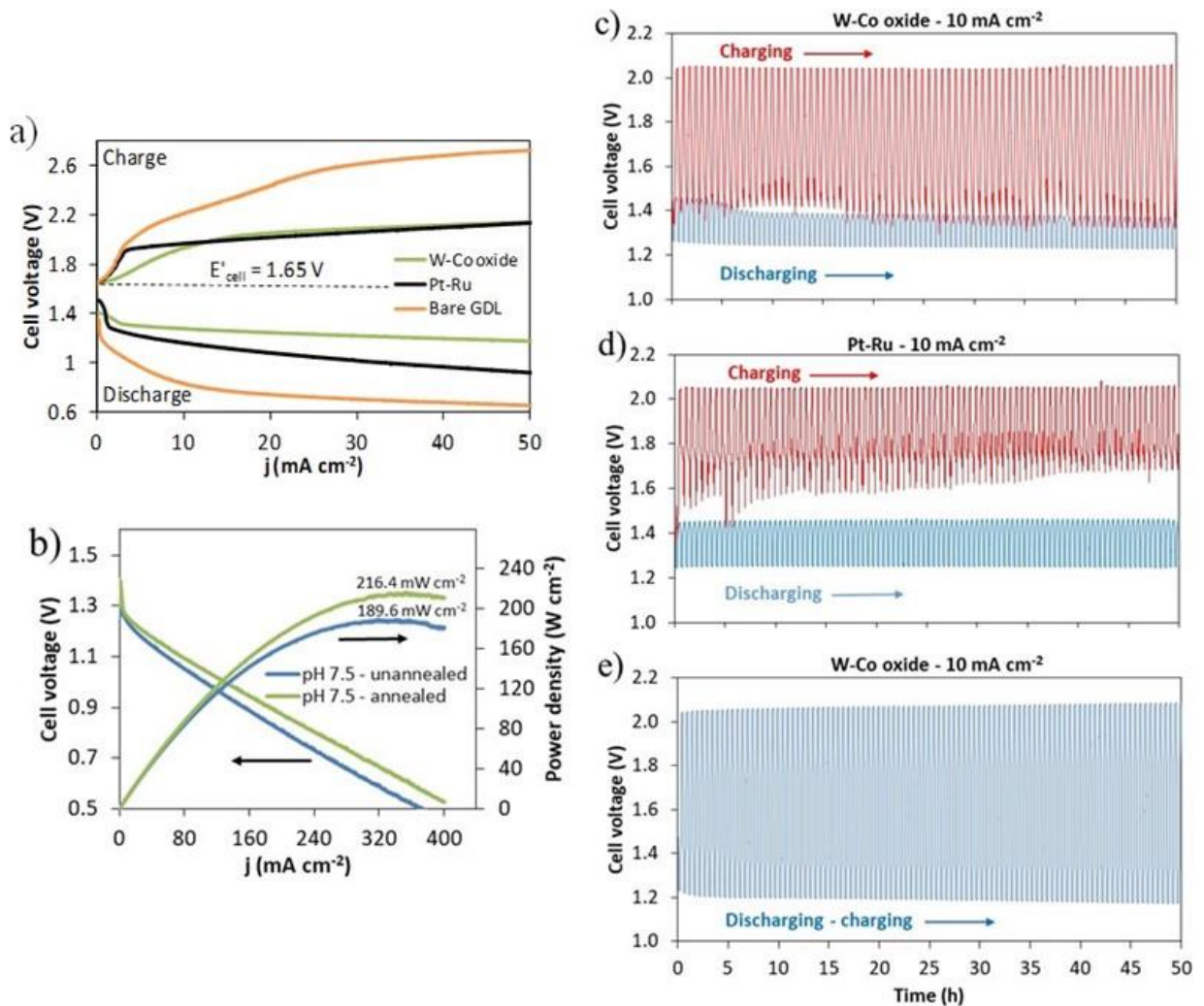
Figure 6.6. a) Discharge-charge polarization curves for bare GDL, W-Co oxide and Pt-Ru electrodes. b) Polarization and power density curves for annealed and unannealed W-Co oxide electrodes. Discharge-charge cycling performance for Zn-air batteries at 10 mA cm^{-2}: c) W-Co oxide three-electrode; d) Pt-Ru three electrode and e) W-Co oxide electrode (bifunctional) configurations.

6.4. Conclusions

Bifunctional W-Co oxide catalysts for the air electrode in a ZAB were synthesized by electrodeposition onto a gas diffusion layer (GDL)conditions were optimized by varying electrodeposition conditions including time, solution composition, and solution pH. An electrodeposition time of 15 min and a solution pH of 7.5 produced the best performing catalysts, with a charge/ discharge efficiency of 58.8% at a current density of 20 mA cm^{-2}.

Electron microscopy analysis was used to identify the deposited film as W-Co oxide; the oxide conformally coated the GDL with a thickness of ~10 nm. During exposure to the battery electrolyte (KOH + ZnO), W dissolved leaving behind Co, which combined with Zn from the electrolyte to form $ZnCo_2O_4$ nanoparticles with sizes less than ~100 nm. $ZnCo_2O_4$ was ultimately responsible for the bifunctional activity of the electrode. The air electrode demonstrated stable cycling behavior in a three-electrode configuration for 50 h (100 cycles) at 10 and 20 mA cm^{-2}, with final efficiencies of 59.1 and 55.9%, respectively. The electrodes also demonstrated good bifunctional activity and stability, with a final efficiency of 56.3% after 100 cycles (50 h) at 10 mA cm^{-2}.

Acknowledgements

References

[1] J. Suntivich, H.A. Gasteiger, N. Yabuuchi, H. Nakanishi, J.B. Goodenough, Y. Shao-Horn, Design principles for oxygen-reduction activity on perovskite oxide catalysts for fuel cells and metal–air batteries, Nature Chemistry, 3 (2011) 546.

[2] Y. Li, H. Dai, Recent advances in zinc–air batteries, Chemical Society Reviews, 43 (2014) 5257-5275.

[3] J. Choi, J.-H. Jang, C.-W. Roh, S. Yang, J. Kim, J. Lim, S.J. Yoo, H. Lee, Gram-scale synthesis of highly active and durable octahedral PtNi nanoparticle catalysts for proton exchange membrane fuel cell, Applied Catalysis B: Environmental, 225 (2018) 530-537.

[4] G.-F. Chen, T.Y. Ma, Z.-Q. Liu, N. Li, Y.-Z. Su, K. Davey, S.-Z. Qiao, Efficient and Stable Bifunctional Electrocatalysts Ni/Ni$_x$M$_y$ (M = P, S) for Overall Water Splitting, Advanced Functional Materials, 26 (2016) 3314-3323.

[5] W. Ahn, M.G. Park, D.U. Lee, M.H. Seo, G. Jiang, Z.P. Cano, F.M. Hassan, Z. Chen, Hollow Multivoid Nanocuboids Derived from Ternary Ni–Co–Fe Prussian Blue Analog for

Dual-Electrocatalysis of Oxygen and Hydrogen Evolution Reactions, Advanced Functional Materials, 28 (2018) 1802129.

[6] M. Xiong, D.G. Ivey, Composition effects of electrodeposited Co-Fe as electrocatalysts for the oxygen evolution reaction, Electrochimica Acta, 260 (2018) 872-881.

[7] T. Ishihara, K. Yokoe, T. Miyano, H. Kusaba, Mesoporous MnCo2O4 spinel oxide for a highly active and stable air electrode for Zn-air rechargeable battery, Electrochimica Acta, 300 (2019) 455-460.

[8] J. Suntivich, K.J. May, H.A. Gasteiger, J.B. Goodenough, Y. Shao-Horn, A Perovskite Oxide Optimized for Oxygen Evolution Catalysis from Molecular Orbital Principles, Science, 334 (2011) 1383.

[9] H. Osgood, S.V. Devaguptapu, H. Xu, J. Cho, G. Wu, Transition metal (Fe, Co, Ni, and Mn) oxides for oxygen reduction and evolution bifunctional catalysts in alkaline media, Nano Today, 11 (2016) 601-625.

[10] C. Goswami, K.K. Hazarika, P. Bharali, Transition metal oxide nanocatalysts for oxygen reduction reaction, Materials Science for Energy Technologies, 1 (2018) 117-128.

[11] R.J. Toh, A.Y.S. Eng, Z. Sofer, D. Sedmidubsky, M. Pumera, Ternary Transition Metal Oxide Nanoparticles with Spinel Structure for the Oxygen Reduction Reaction, ChemElectroChem, 2 (2015) 982-987.

[12] Y. Wang, Y. Zhang, Z. Liu, C. Xie, S. Feng, D. Liu, M. Shao, S. Wang, Layered Double Hydroxide Nanosheets with Multiple Vacancies Obtained by Dry Exfoliation as Highly Efficient Oxygen Evolution Electrocatalysts, Angewandte Chemie International Edition, 56 (2017) 5867-5871.

[13] B. Zhang, X. Zheng, O. Voznyy, R. Comin, M. Bajdich, M. García-Melchor, L. Han, J. Xu, M. Liu, L. Zheng, F.P. García de Arquer, C.T. Dinh, F. Fan, M. Yuan, E. Yassitepe, N. Chen, T. Regier, P. Liu, Y. Li, P. De Luna, A. Janmohamed, H.L. Xin, H. Yang, A. Vojvodic, E.H. Sargent, Homogeneously dispersed multimetal oxygen-evolving catalysts, Science, 352 (2016) 333.

[14] P. Cai, S. Ci, E. Zhang, P. Shao, C. Cao, Z. Wen, FeCo Alloy Nanoparticles Confined in Carbon Layers as High-activity and Robust Cathode Catalyst for Zn-Air Battery, Electrochimica Acta, 220 (2016) 354-362.

[15] M. Xiong, D.G. Ivey, Electrodeposited Co-Fe as an oxygen evolution catalyst for rechargeable zinc-air batteries, Electrochemistry Communications, 75 (2017) 73-77.

[16] X. Xiao, T. Ding, L. Yuan, Y. Shen, Q. Zhong, X. Zhang, Y. Cao, B. Hu, T. Zhai, L. Gong, J. Chen, Y. Tong, J. Zhou, Z.L. Wang, WO_{3-x}/MoO_{3-x} Core/Shell Nanowires on Carbon Fabric as an Anode for All-Solid-State Asymmetric Supercapacitors, Advanced Energy Materials, 2 (2012) 1328-1332.

[17] D.-M. Kim, S.-J. Kim, Y.-W. Lee, D.-H. Kwak, H.-C. Park, M.-C. Kim, B.-M. Hwang, S. Lee, J.-H. Choi, S. Hong, K.-W. Park, Two-dimensional nanocomposites based on tungsten oxide nanoplates and graphene nanosheets for high-performance lithium ion batteries, Electrochimica Acta, 163 (2015) 132-139.

[18] J.M. Costa, T.C. de Morais Nepel, A.F. de Almeida Neto, Influence of current density and W concentration on Co–W alloys used as catalysts in electrodes for Li–O_2 batteries, Chemical Papers, 73 (2019) 1103-1112.

[19] S. Banbur-Pawlowska, K. Mech, R. Kowalik, P. Zabinski, Analysis of electrodeposition parameters influence on cobalt deposit roughness, Applied Surface Science, 388 (2016) 805-808.

[20] D. Kaewsai, S. Yeamdee, S. Supajaroon, M. Hunsom, ORR activity and stability of PtCr/C catalysts in a low temperature/pressure PEM fuel cell: Effect of heat treatment temperature, International Journal of Hydrogen Energy, 43 (2018) 5133-5144.

[21] S. Hussain, H. Erikson, N. Kongi, M. Merisalu, P. Ritslaid, V. Sammelselg, K. Tammeveski, Heat-treatment effects on the ORR activity of Pt nanoparticles deposited on multi-walled carbon nanotubes using magnetron sputtering technique, International Journal of Hydrogen Energy, 42 (2017) 5958-5970.

[22] P. Gokuladeepan, A. Karthigeyan, Effect of annealing temperature on oxygen reduction reaction of reduced graphene oxide incorporated cobalt oxide nanocomposites for fuel cell applications, Applied Surface Science, 449 (2018) 705-711.

[23] L. Liu, G. Zeng, J. Chen, L. Bi, L. Dai, Z. Wen, N-doped porous carbon nanosheets as pH-universal ORR electrocatalyst in various fuel cell devices, Nano Energy, 49 (2018) 393-402.

[24] M. Xiong, M.P. Clark, M. Labbe, D.G. Ivey, A horizontal zinc-air battery with physically decoupled oxygen evolution/reduction reaction electrodes, Journal of Power Sources, 393 (2018) 108-118.

[25] Y.-H. Lee, K.-H. Chang, C.-C. Hu, Differentiate the pseudocapacitance and double-layer capacitance contributions for nitrogen-doped reduced graphene oxide in acidic and alkaline electrolytes, Journal of Power Sources, 227 (2013) 300-308.

[26] P. Germain, W. Pell, B. Conway, Evaluation and origins of the difference between double-layer capacitance behaviour at Au-metal and oxidized Au surfaces, Electrochimica Acta - ELECTROCHIM ACTA, 49 (2004) 1775-1788.

[27] M.P. Clark, T. Muneshwar, M. Xiong, K. Cadien, D.G. Ivey, Saturation Behavior of Atomic Layer Deposition MnOx from Bis(Ethylcyclopentadienyl) Manganese and Water: Saturation Effect on Coverage of Porous Oxygen Reduction Electrodes for Metal–Air Batteries, ACS Applied Nano Materials, 2 (2019) 267-277.

[28] M. Xiong, D.G. Ivey, Synthesis of Bifunctional Catalysts for Metal-Air Batteries Through Direct Deposition Methods, Batteries & Supercaps, 2 (2019) 326-335.

[29] E. Patrick, M.E. Orazem, J.C. Sanchez, T. Nishida, Corrosion of tungsten microelectrodes used in neural recording applications, Journal of Neuroscience Methods, 198 (2011) 158-171.

[30] Y.-T. Lu, Y.-J. Chien, C.-F. Liu, T.-H. You, C.-C. Hu, Active site-engineered bifunctional electrocatalysts of ternary spinel oxides, $M_{0.1}Ni_{0.9}Co_2O_4$ (M: Mn, Fe, Cu, Zn) for the air electrode of rechargeable zinc–air batteries, Journal of Materials Chemistry A, 5 (2017) 21016-21026.

[31] Z.-Q. Liu, H. Cheng, N. Li, T.Y. Ma, Y.-Z. Su, $ZnCo_2O_4$ Quantum Dots Anchored on Nitrogen-Doped Carbon Nanotubes as Reversible Oxygen Reduction/Evolution Electrocatalysts, Advanced Materials, 28 (2016) 3777-3784.

[32] J. Yin, B. Wei, Y. Li, Y. Li, P. Xi, Construction of surface lattice oxygen in metallic $N-CuCoS_{1.97}$ porous nanowire for wearable Zn−air battery, Journal of Energy Chemistry, 34 (2019) 1-9.

[33] H.-M. Zhang, Y. Zhao, Y. Zhang, M. Zhang, M. Cheng, J. Yu, H. Liu, M. Ji, C. Zhu, J. Xu, Fe_3O_4 encapsulated in porous carbon nanobowls as efficient oxygen reduction reaction catalyst for Zn-air batteries, Chemical Engineering Journal, 375 (2019) 122058.

[34] S. Chen, L. Zhao, J. Ma, Y. Wang, L. Dai, J. Zhang, Edge-doping modulation of N, P-codoped porous carbon spheres for high-performance rechargeable Zn-air batteries, Nano Energy, 60 (2019) 536-544.

[35] H. Li, M. An, Y. Zhao, S. Pi, C. Li, W. Sun, H.-g. Wang, Co nanoparticles encapsulated in N-doped carbon nanofibers as bifunctional catalysts for rechargeable Zn-air battery, Applied Surface Science, 478 (2019) 560-566.

[36] W. Liu, J. Bao, L. Xu, M. Guan, Z. Wang, J. Qiu, Y. Huang, J. Xia, Y. Lei, H. Li, $NiCo_2O_4$ ultrathin nanosheets with oxygen vacancies as bifunctional electrocatalysts for Zn-air battery, Applied Surface Science, 478 (2019) 552-559.

[37] Y. Tian, L. Xu, J. Bao, J. Qian, H. Su, H. Li, H. Gu, C. Yan, H. Li, Hollow cobalt oxide nanoparticles embedded in nitrogen-doped carbon nanosheets as an efficient bifunctional catalyst for Zn–air battery, Journal of Energy Chemistry, 33 (2019) 59-66.

[38] J.-I. Jung, M. Risch, S. Park, M.G. Kim, G. Nam, H.-Y. Jeong, Y. Shao-Horn, J. Cho, Optimizing nanoparticle perovskite for bifunctional oxygen electrocatalysis, Energy & Environmental Science, 9 (2016) 176-183.

[39] Y. Meng, W. Song, H. Huang, Z. Ren, S.Y. Chen, S.L. Suib, Structure-property relationship of bifunctional MnO2 nanostructures: highly efficient, ultra-stable electrochemical water oxidation and oxygen reduction reaction catalysts identified in alkaline media, J Am Chem Soc, 136 (2014) 11452-11464.

Supplementary material
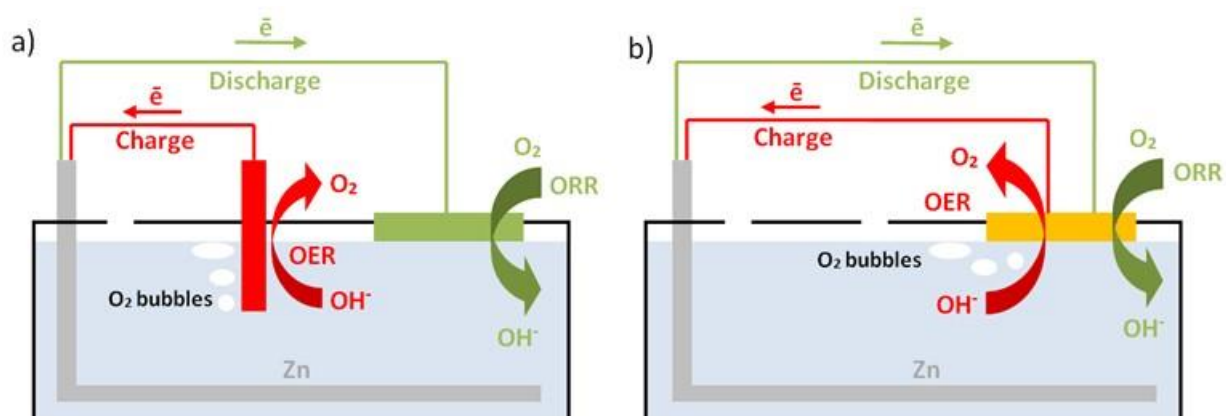
Figure S1. a) Three-electrode Zn-air battery configuration and b) two-electrode Zn-air battery configuration.
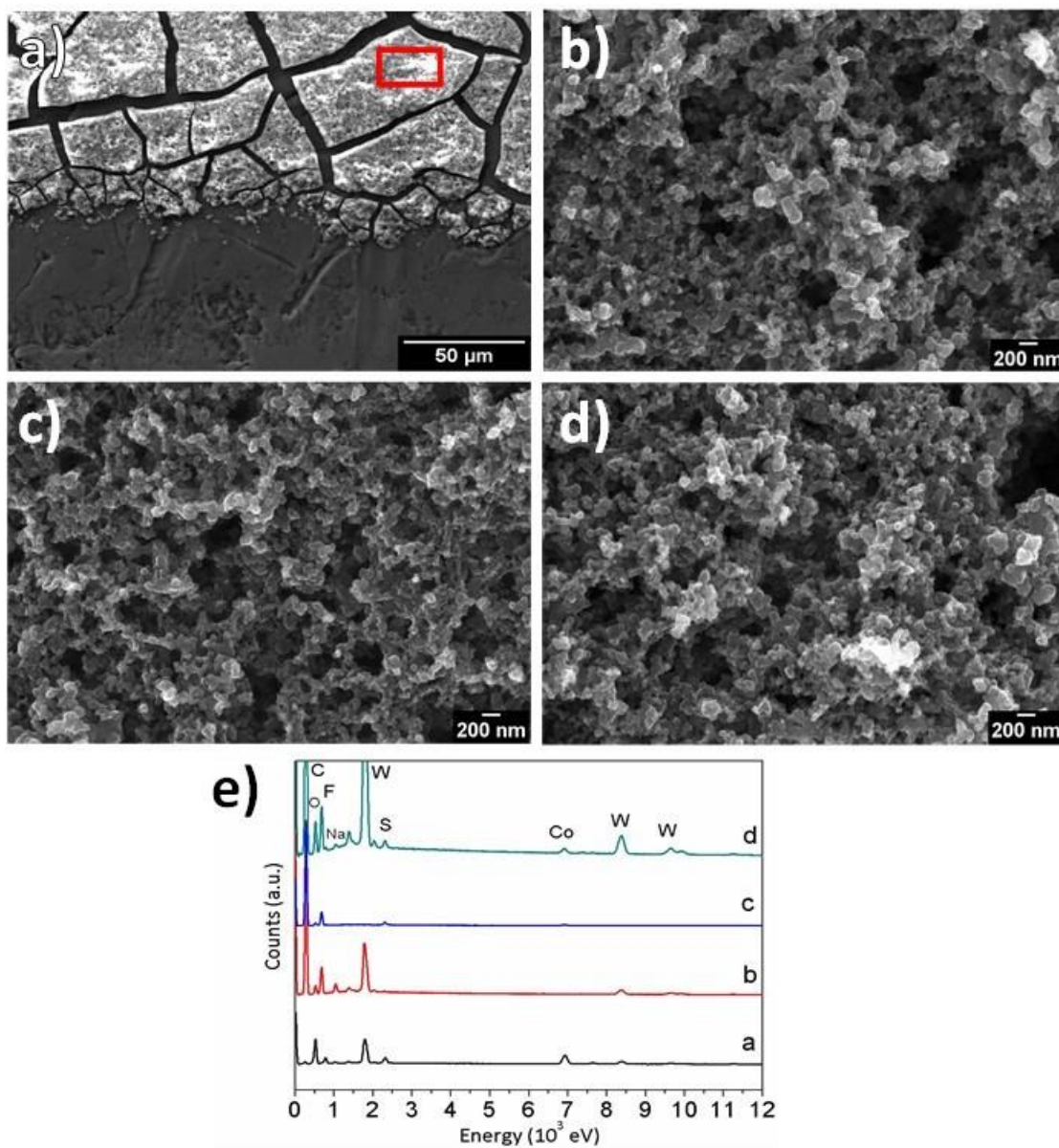
Figure S2. SEM SE images of a) W-Co precipitates (1:1 ratio); b) pure W annealed (0.05 M); c) pure Co annealed (0.035 M), d) W-Co oxide unannealed, 7.5 pH (1:0.7 ratio). d) EDX spectra for the different electrodes.
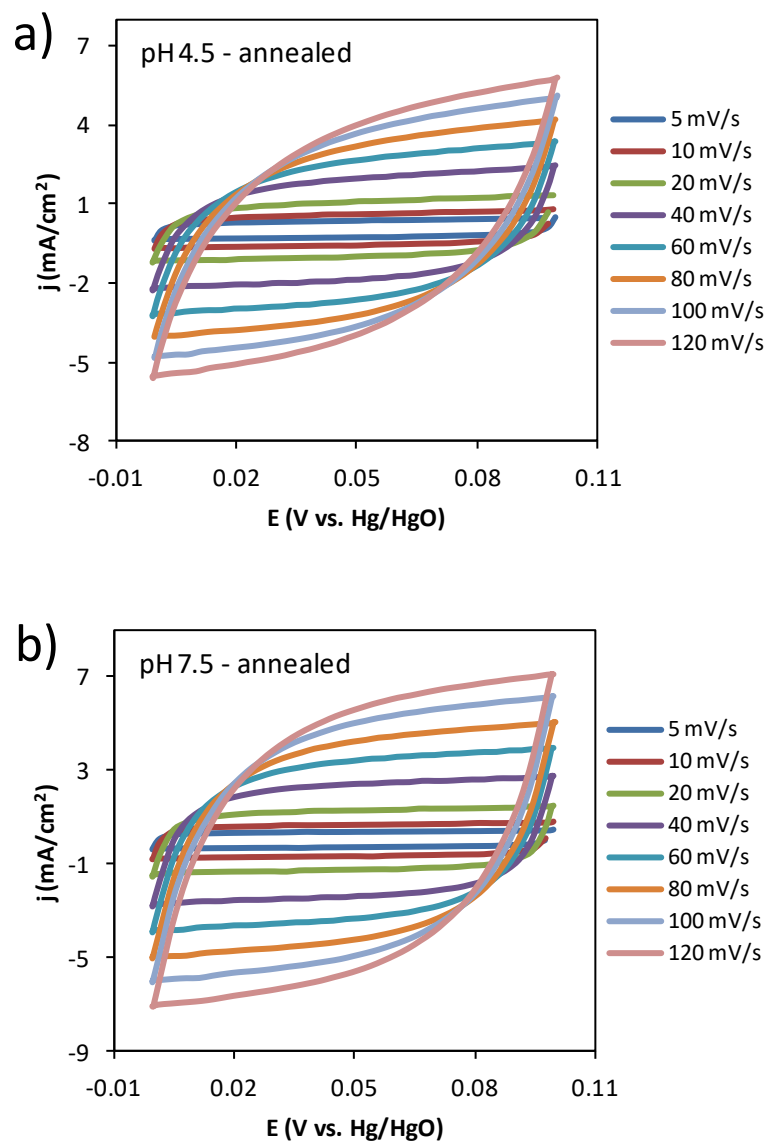
Figure S3. CV curves at different scan rates for a potential window of 0.0 to 0.1 V vs. Hg/HgO in Ar saturated 1 M KOH for different samples: (a) pH 4.5 - annealed and (b) pH 7.5 - annealed.
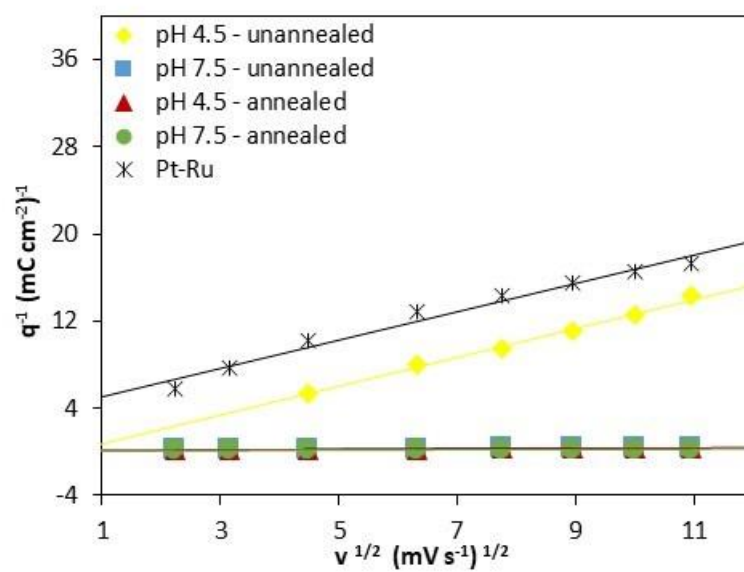
Figure S4. Reciprocal of voltammetric charge (q^{-1}) plotted against square root of the scan rate ($v^{1/2}$).
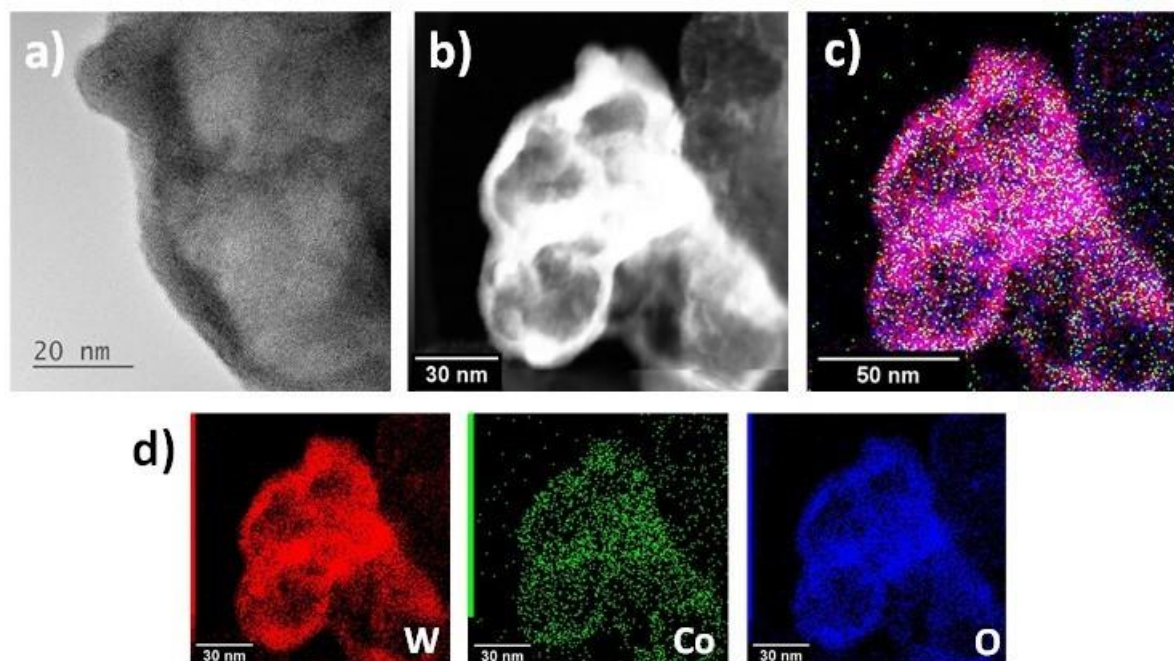
Figure S5. Images of unannealed, 7.5 pH sample before electrochemical testing: a) TEM BF image; b) STEM ADF image; c) EDX map overlay of W (red), Co (green) and O (blue); d) individual EDX maps for W, Co and O.
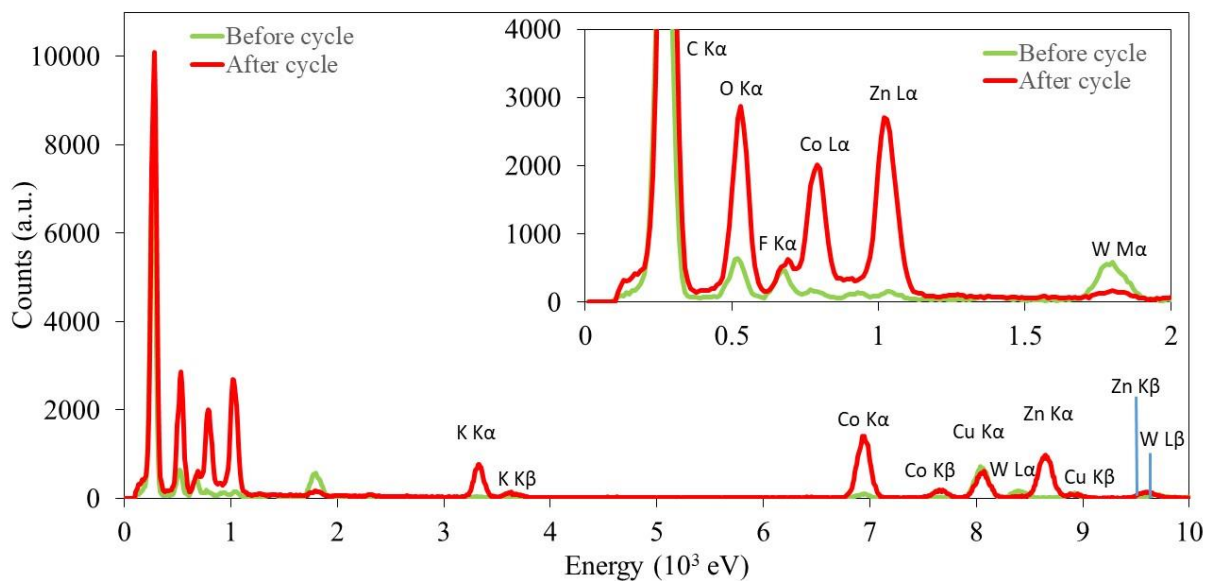
Figure S6. STEM EDX spectra before and after 50 h of cycling of the annealed W-Co oxide, electrodeposited at 7.5 pH for 15 min. The small Cu peak at ~8 kV is an artifact and is due to x-rays generated from the Cu support grid by stray electrons.
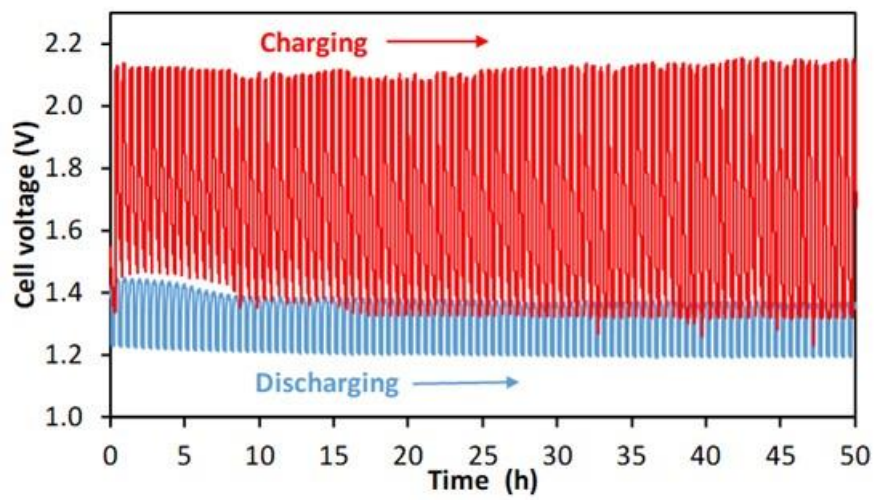
Figure S7. Discharge-charge cycling for a Zn-air battery (three electrode configuration) at 20 mA cm^{-2} with W-Co oxide electrodes.
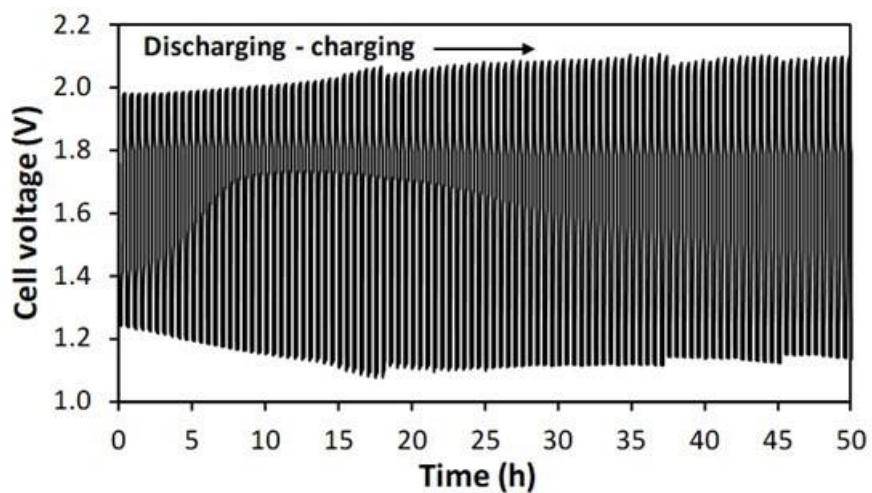
Figure S8. Discharge-charge cycling for a Zn-air battery (two electrode configuration) at 10 mA cm^{-2} with Pt-Ru electrodes.
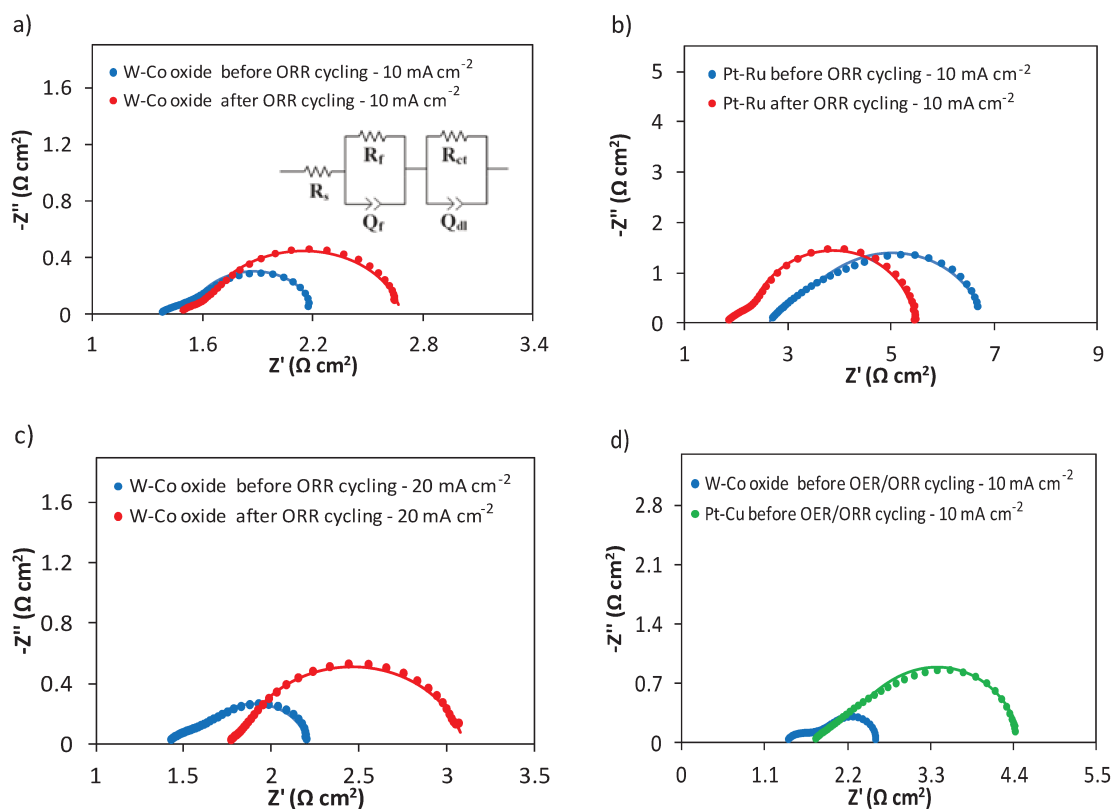
Figure S9. Electrochemical impedance spectra (EIS) for catalysts at different potentials: (a) EIS at 1.2 V for W-Co oxide (annealed, pH 7.5) before and after ORR cycling at 10 mA cm^{-2}. (b) EIS at 1.2 V for Pt-Ru before and after ORR cycling at 10 mA cm^{-2}. (c) EIS at 1.2 V for W-Co oxide (annealed, pH 7.5) before and after ORR cycling at 20 mA cm^{-2}. (d) EIS at 1.2 V for W-Co oxide (annealed, pH 7.5) and Pt-Ru before cycling in the two-electrode cell at 10 mA cm^{-2}.

Table S1 Equivalent circuit parameters based on the EIS spectra shown in Figure S9

Electrode	R_s Ω cm^2	R_f Ω cm^2	Q_f mΩ^{-1} s^n cm^{-2}	R_{ct} Ω cm^2	Q_{dl} mΩ^{-1} s^n cm^{-2}
W-Co oxide before ORR cycling - 10 mA cm^{-2}	1.4	0.2	0.02 (n=0.66)	0.6	0.03 (n=0.95)
W-Co oxide after ORR cycling - 10 mA cm^{-2}	1.5	0.2	0.02 (n=0.75)	1.0	0.03 (n=0.89)
Pt-Ru before ORR cycling - 10 mA cm^{-2}	2.6	0.8	0.003 (n=0.81)	3.4	0.008 (n=0.84)
Pt-Ru after ORR cycling - 10 mA cm^{-2}	1.8	0.6	0.01 (n=0.72)	3.1	0.02 (n=0.94)
W-Co oxide before ORR cycling - 20 mA cm^{-2}	1.4	0.2	0.02 (n=0.70)	0.6	0.04 (n=0.92)
W-Co oxide after ORR cycling - 20 mA cm^{-2}	1.7	0.1	0.01 (n=0.91)	1.3	0.03 (n=0.86)
W-Co oxide before OER/ORR cycling - 10 mA cm^{-2}	1.3	0.6	0.02 (n=0.51)	0.6	0.03 (n=0.97)
Pt-Ru before OER/ORR cycling - 10 mA cm^{-2}	1.7	0.7	0.01 (n=0.63)	2.0	0.01 (n=0.86)

Table S2 Comparison of discharge-charge voltage gap ($\Delta\eta$) between this work and the literature

Catalyst, battery test condition and battery performance	Reference
Two-electrode - 10 mA cm^{-2} for 50 h $\Delta\eta_{initial}$= 0.81 V $\Delta\eta_{end}$= 0.91 V $\Delta\eta_{end}$-$\Delta\eta_{initial}$= 0.10 V	This paper
MnO$_x$ and CoFe (three-electrode) - 10 mA cm^{-2} for 50 h $\Delta\eta_{initial}$= 0.78 V $\Delta\eta_{end}$= 0.89 V $\Delta\eta_{end}$-$\Delta\eta_{initial}$= 0.11 V	[1]
Yttrium ruthenate nanoparticles (two-electrode) - 10 mA cm^{-2} for 33.3 h $\Delta\eta_{initial}$= 0.74 V $\Delta\eta_{end}$= 0.84 V $\Delta\eta_{end}$-$\Delta\eta_{initial}$= 0.10 V	[2]
MnCo$_2$O$_4$ nanoparticles (two electrode) - 10 mA cm^{-2} for 33.3 h $\Delta\eta_{initial}$= 0.55 V $\Delta\eta_{end}$= 0.80 V $\Delta\eta_{end}$-$\Delta\eta_{initial}$= 0.25 V	[3]
Co oxide nanoparticles (two-electrode) - 10 mA cm^{-2} for 5 h $\Delta\eta_{initial}$= 0.87 V $\Delta\eta_{end}$= 1.13 V $\Delta\eta_{end}$-$\Delta\eta_{initial}$= 0.26 V	[4]
NiCo-air (two-electrode) - 10 mA cm^{-2} for 29 h $\Delta\eta_{initial}$= 0.98 V $\Delta\eta_{end}$= 1.12 V $\Delta\eta_{end}$-$\Delta\eta_{initial}$= 0.14 V	[5]

[1] M. Xiong, M.P. Clark, M. Labbe, D.G. Ivey, A horizontal zinc-air battery with physically decoupled oxygen evolution/reduction reaction electrodes, Journal of Power Sources, 393 (2018) 108-118.

[2] J. Park, M. Park, G. Nam, M.G. Kim, J. Cho, Unveiling the Catalytic Origin of Nanocrystalline Yttrium Ruthenate Pyrochlore as a Bifunctional Electrocatalyst for Zn–Air Batteries, Nano Letters, 17 (2017) 3974-3981.

[3] D. Bin, Z. Guo, A.G. Tamirat, Y. Ma, Y. Wang, Y. Xia, Crab-shell induced synthesis of ordered macroporous carbon nanofiber arrays coupled with MnCo$_2$O$_4$ nanoparticles as bifunctional oxygen catalysts for rechargeable Zn–air batteries, Nanoscale, 9 (2017) 11148-11157.

[4] Y. Tian, L. Xu, J. Bao, J. Qian, H. Su, H. Li, H. Gu, C. Yan, H. Li, Hollow cobalt oxide nanoparticles embedded in nitrogen-doped carbon nanosheets as an efficient bifunctional catalyst for Zn–air battery, Journal of Energy Chemistry, 33 (2019) 59-66.

[5] W. Liu, J. Bao, L. Xu, M. Guan, Z. Wang, J. Qiu, Y. Huang, J. Xia, Y. Lei, H. Li, NiCo$_2$O$_4$ ultrathin nanosheets with oxygen vacancies as bifunctional electrocatalysts for Zn-air battery, Applied Surface Science, 478 (2019) 552-559.

CHAPTER 7

General Discussion

7.1. General Discussion

At the beginning of this work, the main focus was to deposit Co-W on substrates with different surface morphology and composition. Thus, from previous studies carried out in the LabPEA research group with Co-W (PORTO, 2016), the composition was optimized, as well as the electrodeposition parameters. As this is a recent research group, the initial parameters of current density and O_2 pressure followed previous studies by the research group (CREMASCO, 2017). In order to seek a statistical correlation on the influence of the electrodeposition parameters (solution composition and electric current density), it was verified that the increase of the current density and the W concentration increased the electrodeposition efficiency, however, did not favor the cycling on the Li-O_2 battery due to clogged pores and cathode surface. In addition, the specific capacity calculation took into account the mass of the deposited material, which contributed to obtain small values.

After observing that deposit amounts in the order of milligrams would be beneficial to the system, Ag-Co was electroplated on the steel mesh and nickel foam substrate. This study aimed to discuss the influence of the applied electric current density and O_2 pressure in the system. The O_2 pressure at 2 atm with current density of 50 μA cm^{-2} presented the highest discharge capacity of 336 mAh g$^{-1}_c$. Although the discharge curves of the E5, M2, M3, M4 and M5 electrodes showed unusual shapes, they were not different from those found in the literature (LIU; XU; YAN; SUN *et al.*, 2016; MA; YUAN; SHA; MA *et al.*, 2013; PENG; FREUNBERGER; CHEN; BRUCE, 2012). If the y-axis scale had been larger, this would be more evident. In this case, it was decided to add the scale within the potential limit of 2.2 to 4.0 V. However, the discharge plateau was evidenced close to the value of 3.0 V.

The alkaline KOH solution mainly served to evaluate the oxygen evolution/reduction of oxygen reaction as used by several studies on Li-O_2 batteries (JO; TAMAKLOE; JIN; LIM *et al.*, 2019; LAI; CHEN; ZHANG; QU *et al.*, 2016; YIN; LI; YU; LV *et al.*, 2019; YU; YU; SUN; WU *et al.*, 2016; ZHAO; HANG; ZHANG; WANG *et al.*, 2017). The voltammograms of the bare electrodes, with catalyst cycled and non-cycled demonstrated that the catalytic activity of the oxygen evolution reaction was also improved with Ag-Co deposition.

Battery cycle stability was not a major point of the Ag-Co study, as the time of each cycle was not limited, only potential limits with a lower limit of 2.2 and greater than 4.0 V. In

general, Li-O_2 studies analyze discharge and charge capacity, but without limiting cycle time, to observe the maximum capacity value obtained according to the following studies (WU; WANG; LIAO; YANG *et al.*, 2015; YUAN; YANG; NAN; SUN *et al.*, 2018). From the parameters obtained in the Ag-Co study, the same electric current density and O_2 pressure were used in the Zn-Co study.

The Zn-Co study sought to verify whether electrodeposition parameters would influence battery cycling. Thus, the temperature of the electrodeposition solution and the rotating cathode were varied. It was verified that the Zn-Co electrocatalyst showed better catalytic activity for the oxygen evolution reaction according to the voltammograms. The determination of the capacitance of the double electric layer for the bare electrodes, with catalyst cycled and non-cycled proved that the Zn-Co deposit by correlation increased the electrochemically active surface area. The electrochemically active surface area can be calculated according to the authors (MCCRORY; JUNG; PETERS; JARAMILLO, 2013; VINCENT, 2016), as the double layer capacitance (C_{dl}) divided by the specific capacitance (C_s). However, the specific capacitance range is wide (0.006 to 0.050 mF cm^{-2}) (BIKKAROLLA; PAPAKONSTANTINOU, 2015; CENTENO; STOECKLI, 2006; KÖTZ; CARLEN, 2000; MCCRORY; JUNG; PETERS; JARAMILLO, 2013; RABBOW; WHITEHEAD, 2017; VINCENT, 2016) and choosing a value directly affects the value of the area found. In addition, the reference values for 1 M KOH are for carbon based substrates. The literature does not report values for different materials, such as nickel foam and steel mesh. Therefore, the electric double layer capacitance is an indirect value of the catalytic activity of the material.

The narrow potential window was suitable for substrates, allowing to identify the presence of pseudocapacitance, which is a faradaic process that contributes to the storage of energy electrochemically. This narrow potential window has been used by several authors (WANG; LIN; TONG; HUANG *et al.*, 2019; XIONG; CLARK; LABBE; IVEY, 2018; XIONG; IVEY, 2018).

The unconventional form of the discharge graph showed the absence of the characteristic plateau around 3.2 - 3.4 V vs Li, which would correspond to the decomposition of Li2O2, which also allows one to suspect that collateral processes occurred. For most samples, the load plateau occurred between 2.7 and 3.2 V, this interval has been reported in some studies. (LU; WANG; JIN; LI *et al.*, 2015; ZHANG; WANG; JIANG; ZHOU *et al.*, 2015). The charge

plateau below 3.2 V was a particular feature of the system. The different behaviors of the curves were due to the electrode specificity, since the solution temperature and the rotating cathode velocity were varied, which changed the morphology and the catalytic properties.

The initial reduction peak cited in Chapter 5 is related to an initial and rapid decrease in potential value, explained as a breakdown of the catalyst crystal structure and the formation of the electrolyte-solid interface layer. Then, an increase in potential (charge) was observed. Tests on Li batteries are generally qualitative and are intended to verify whether or not a parameter change affects electrode behavior. Mathematical models cannot describe the charge/discharge response in Li-O_2 batteries because the system depends on several parameters such as Li^+ transport, O_2 transport, Li_2O_2 formation mechanism, reaction kinetics, catalytic distribution, side reactions and change in electrolyte volume. For example, several papers have done qualitative analysis (CETINKAYA; TOKUR; OZCAN; ALGÜL *et al.*, 2015; KUNANUSONT; SHIMOYAMA, 2017; ZHANG; WANG; JIANG; ZHOU *et al.*, 2015).

After studies with W-Co, Ag-Co and Zn-Co on Li-O_2 batteries it was proposed to apply these catalysts to the nickel foam and steel mesh substrate on Zn-air batteries. It was found that cycling was not possible since the open-circuit potential of the Zn-air cell was equal to 0 V. Thus, it was proposed to electrodeposit the three catalysts on carbon (GDL - gas diffusion layer).

Preliminary studies demonstrated a Zn-air battery efficiency of 59.1, 51.5 and 43.9% at 20 mA cm^{-2}, respectively for Co-W, Ag-Co and Zn-Co. Thus, Co-W was chosen for further studies. The composition of the Co-W solution at the beginning was the same as for the synthesis of the catalysts for the Li-O_2 battery. However, the presence of a precipitate was verified and the optimization of W:Co proportions was necessary. After solubilizing the maximum amount of Co in W, a study of the influence of the pH of the solutions (4.5 and 7.5) and the electrodeposition time (5, 15 and 25 min) on carbon on the Zn-air battery efficiency was performed. Zn-air battery. Annealing at 300 °C for 30 min also influenced the system, promoting the increase of active sites. The battery presented excellent stability during 50 h cycling and high efficiency. Analysis by TEM, SEM and FESEM demonstrated that during cycling tungsten was dissolved in the zinc oxide and potassium hydroxide electrolyte, and that the zinc cobalt oxide ($ZnCo_2O_4$) with spinel structure was responsible for the catalytic activity in the electrode.

References

BIKKAROLLA, S. K.; PAPAKONSTANTINOU, P. CuCo2O4 nanoparticles on nitrogenated graphene as highly efficient oxygen evolution catalyst. **Journal of Power Sources**, 281, p. 243-251, 2015/05/01/ 2015.

CENTENO, T. A.; STOECKLI, F. On the specific double-layer capacitance of activated carbons, in relation to their structural and chemical properties. **Journal of Power Sources**, 154, n. 1, p. 314-320, 2006/03/09/ 2006.

CETINKAYA, T.; TOKUR, M.; OZCAN, S.; ALGÜL, H. *et al.* Graphene Oxide/α-MnO$_2$ Nanocomposite Electrodes Produced Using Planetary Ball Milling for Li-O$_2$ Batteries. **Materials Today: Proceedings**, 2, p. 4223-4228, 12/31 2015.

CREMASCO, L. F. **Development of catalytic systems and electrodes for Lithium-air**. Advisor: DOUBEK, G. 2017. 72 f. Master degree - Department of Chemical Systems Engineering, University of Campinas.

JO, Y. K.; TAMAKLOE, W.; JIN, X.; LIM, J. *et al.* Multilayer Hybrid Nanosheet of Mesoporous Carbon−Layered Metal Oxide as a Highly Efficient Electrocatalyst for Li−O$_2$ Batteries. **Applied Catalysis B: Environmental**, 2019/05/08/ 2019.

KÖTZ, R.; CARLEN, M. Principles and applications of electrochemical capacitors. **Electrochimica Acta**, 45, n. 15, p. 2483-2498, 2000/05/03/ 2000.

KUNANUSONT, N.; SHIMOYAMA, Y. Porous carbon electrode for Li-air battery fabricated from solvent expansion during supercritical drying. **The Journal of Supercritical Fluids**, 133, 09/01 2017.

LAI, Y.; CHEN, W.; ZHANG, Z.; QU, Y. *et al.* Fe/Fe3C decorated 3-D porous nitrogen-doped graphene as a cathode material for rechargeable Li–O$_2$ batteries. **Electrochimica Acta**, 191, p. 733-742, 2016/02/10/ 2016.

LIU, B.; XU, W.; YAN, P.; SUN, X. *et al.* Enhanced Cycling Stability of Rechargeable Li–O$_2$ Batteries Using High-Concentration Electrolytes. **Advanced Functional Materials**, 26, n. 4, p. 605-613, 2016/01/01 2016.

LU, F.; WANG, Y.; JIN, C.; LI, F. *et al.* Microporous La$_{0.8}$Sr$_{0.2}$MnO$_3$ perovskite nanorods as efficient electrocatalysts for lithium–air battery. **Journal of Power Sources**, 293, p. 726-733, 2015/10/20/ 2015.

MA, Z.; YUAN, X.; SHA, H.-D.; MA, Z.-F. *et al.* Influence of cathode process on the performance of lithium-air batteries. **International Journal of Hydrogen Energy**, 38, n. 25, p. 11004-11010, 2013/08/21/ 2013.

MCCRORY, C. C. L.; JUNG, S.; PETERS, J. C.; JARAMILLO, T. F. Benchmarking Heterogeneous Electrocatalysts for the Oxygen Evolution Reaction. **Journal of the American Chemical Society**, 135, n. 45, p. 16977-16987, 2013/11/13 2013.

PENG, Z.; FREUNBERGER, S. A.; CHEN, Y.; BRUCE, P. G. A Reversible and Higher-Rate Li-O_2 Battery. **Science**, 337, n. 6094, p. 563, 2012.

PORTO, M. B. **Optimization of process electroplating and physicochemical characterization of metallic alloy of Fe-W, Ni-W and Co-W**. Advisor: NETO, A. F. d. A. 2016. 90 f. Master degree - Department of Products and Processes Design, University of Campinas.

RABBOW, T. J.; WHITEHEAD, A. H. Deconvolution of electrochemical double layer capacitance between fractions of active and total surface area of graphite felts. **Carbon**, 111, p. 782-788, 2017/01/01/ 2017.

VINCENT, I. Electrochemical Characterization and Oxygen Reduction Kinetics of Cu-incorporated Cobalt Oxide Catalyst. **International Journal of Electrochemical Science**, p. 8002-8015, 09/01 2016.

WANG, X.; LIN, S.; TONG, H.; HUANG, Y. *et al.* Two-dimensional V_4C_3 MXene as high performance electrode materials for supercapacitors. **Electrochimica Acta**, 307, p. 414-421, 2019/06/01/ 2019.

WU, C.; WANG, H.; LIAO, C.; YANG, J. *et al.* Enhanced performance of Li-O_2 battery based on CFx/C composites as cathode materials. **Electrochimica Acta**, 186, p. 631-641, 2015/12/20/ 2015.

XIONG, M.; CLARK, M. P.; LABBE, M.; IVEY, D. G. A horizontal zinc-air battery with physically decoupled oxygen evolution/reduction reaction electrodes. **Journal of Power Sources**, 393, p. 108-118, 2018/07/31/ 2018.

XIONG, M.; IVEY, D. G. Composition effects of electrodeposited Co-Fe as electrocatalysts for the oxygen evolution reaction. **Electrochimica Acta**, 260, p. 872-881, 2018/01/10/ 2018.

YIN, J.; LI, Z.; YU, Y.; LV, Y. *et al.* Facile electrodeposition of MFe2O4 (M=Co, Fe) on carbon cloth as air cathodes for Li-O2 batteries. **Ceramics International**, 45, n. 10, p. 13401-13408, 2019/07/01/ 2019.

YU, Q.; YU, Q.; SUN, W.; WU, H. *et al.* Novel Ni@Co$_3$O$_4$ Web-like Nanofiber Arrays as Highly Effective Cathodes for Rechargeable Li-O2 Batteries. **Electrochimica Acta**, 220, p. 654-663, 2016/12/01/ 2016.

YUAN, M.; YANG, Y.; NAN, C.; SUN, G. *et al.* Porous Co$_3$O$_4$ nanorods anchored on graphene nanosheets as an effective electrocatalysts for aprotic Li-O$_2$ batteries. **Applied Surface Science**, 444, p. 312-319, 2018/06/30/ 2018.

ZHANG, D.; WANG, B.; JIANG, Y.; ZHOU, P. *et al.* Enhanced electrocatalytic performance of Co$_3$O$_4$/Ketjen-black cathodes for Li–O2 batteries. **Journal of Alloys and Compounds**, 653, p. 604-610, 2015/12/25/ 2015.

ZHAO, Y.; HANG, Y.; ZHANG, Y.; WANG, Z. *et al.* Strontium-doped perovskite oxide La$_{1-x}$Sr$_x$MnO$_3$ (x=0, 0.2, 0.6) as a highly efficient electrocatalyst for nonaqueous Li-O$_2$ batteries. **Electrochimica Acta**, 232, p. 296-302, 2017/04/01/ 2017.

CHAPTER 8

General conclusions, suggestions for future work and memory of the doctorate period

8.1. General Conclusions

The bibliographic research discussed in **Chapter 2** allowed us to understand the basic characteristics and configurations that make up $Li-O_2$ and Zn-air batteries, as well as to demonstrate what are the challenges to be overcome in the systems. The literature review involving the results of works of recent years was essential to understand how reactions occur and what are the trends in the composition of electrocatalysts.

Chapter 3 revealed that the statistical analysis was adequate for electrodeposition efficiency, with an adjustment coefficient of 0.936, with a confidence interval of 95%. However, the statistical analysis proved inadequate when the objective was to obtain a high charging and discharging capacity. The increase in electric current density and W concentration favored electrodeposition efficiency, which obtained values of 60.05% for nickel foam and 64.39% for steel mesh. Only Co peaks were identified by X-ray diffraction, indicating a complete dissolution of W into Co, thus forming a solid single-phase solution.

In **Chapter 4**, the electric current density of 50 $\mu A\ cm^{-2}$ and O_2 pressure of 2 atm were the parameters that allowed the highest discharge capacity in the $Li-O_2$ battery. The EDX analysis verified that the cyclic voltammetry technique for the Ag-Co electrodeposition did not favor the Co deposition. The catalytic activity was confirmed by cyclic voltammetry and linear scanning voltammetry. Raman spectra showed the presence of Li_2O and Li_2O_2 after cycling. In general, the steel mesh proved to be a substrate with higher values of charge and discharge capacity in the battery.

In **Chapter 5**, the 30 °C temperature and 30 rpm rotation speed for Zn-Co electroplating gave the $Li-O_2$ battery charge the best result. The double electric layer capacitance indicated that the electrochemically active surface area was increased with the Zn-Co deposit. Raman spectra showed Co_3O_4 and Li_2O_2 after cycling. $Zn_{21}Co_5$ and Co_3O_4 peaks with the crystallographic planes (510) and (044) were obtained by X-ray diffraction.

In **Chapter 6**, after several preliminary studies with the three binary electrocatalysts, it was found that W-Co showed results superior to Zn-Co and Ag-Co. It was observed that the pH of 7.5 and the electrodeposition time of 15 min and the annealing of the sample at 300 °C for 30 min were beneficial for the Zn-air system, with efficiency close to 60%. The TEM analysis indicated that after cycling, there were minimal or no amount of W, and the formation of $ZnCo_2O_4$, indicating that spinning $ZnCo_2O_4$ participated in the catalytic activity.

Regarding which technology is best, Li-O_2 or Zn-air batteries, it should be noted that electrochemical performance, low cost, and high energy density are factors that generate interest in research and development of these products. Zn-air batteries are highly stable to moisture, unlike Li-O_2 cells, which must be assembled in an inert atmosphere. This implies that the Zn-air cells' manufacture is simple and price competitive, as Zn metal and aqueous Zn-air system electrolytes are inexpensive when compared to Li metal and non-electrolytes of the Li-O_2 system. However, Li-O_2 batteries' reversibility is better than Zn-air batteries, which is still an obstacle for practical application to rechargeable Zn-air cells. Additionally, the operating potential and specific capacities of Li-O_2 batteries are greater than the Zn-air battery, which gives a high energy density and is an attractive feature of Li-O_2 batteries. Thus, both technologies have particularities that make them promising energy storage systems.

Therefore, the development of this thesis contributed to the expansion of the frontiers of knowledge, which addressed relevant information regarding the parameters that influence Li-O_2 and Zn-air energy storage devices, such as metal concentration in the solution, density of electrical current applied on electrodeposition, O_2 pressure on the battery, electrical current density applied on battery, electrolytic bath temperature, rotating cathode velocity during electrodeposition, bath pH, annealing, electrodeposition time and metal stoichiometric ratio. The results suggested that certain parameters, such as bath pH and annealing, were crucial for stability and high catalytic activity in the systems.

8.2 Suggestions for future work

The several techniques available for obtaining catalysts and materials that can be used as a cathode, based on the knowledge obtained by this thesis, below are presented some suggestions for stimulating research and achieving improved results:

1. To evaluate the activity of binary electrocatalysts (Co-W, Ag-Co, Zn-Co) combined with carbon nanotubes in the Li-O_2 battery.
2. Seek to decrease the efficiency loss between cycles in the Li-O_2 battery.
3. Using reduced graphene oxide in combination with binary electrocatalysts and therefore, applying another technique for the impregnation of metals on substrates, such as dip coating.

4. Optimize the ratio of Ag, Zn, and Co in order to achieve more efficient Zn-air battery results.

5. To suit the steel mesh and nickel foam substrate to the Zn-air battery for catalytic activity and cyclability.

8.3. Memory of the doctorate period

The chemical engineer Josiel Martins Costa joined as a doctoral student at UNICAMP in 2017 under the guidance of Prof. Dr. Ambrósio Florêncio de Almeida Neto through the selection process of the Department of Product and Process Design (DDPP). With financial aid Capes (n ° 88882.329685 / 2019-01) for 12 months (Mar-17 / Feb-18), attended a compulsory course: IQ-640 Kinetics and Reactors II, two optional courses: IQ-350 Experiment Design and IQ-263 Topics in Chemical Engineering II, and validated by taking advantage of studies, a compulsory course: IQ-130 Transport Phenomena I.

He participated in the Group C Teaching Internship Program (PED C) with activities to partially support the teaching of the discipline EQ-712 Applied Chemical Kinetics, acting as a volunteer between August/2017 to December/2017 (8 hours per week, 0% teaching load) and as a PED B scholarship holder (12 hours per week, 5% teaching load) from February/2018 to July/2018 and from August/2018 to December/2018 in the discipline EQ-801 Chemical Engineering Laboratory III.

Research related to the doctoral project resulted in 3 experimental papers in Brazil, 1 experimental article published in the *Journal of Solid State Electrochemistry*, 1 experimental article published in the journal *Electrocatalysis*, and 1 experimental article published in the journal *Chemical Papers*. There was also 1 chapter book published by *Springer* Publishing and 1 expanded abstract published in the *International-Mexican Congress on Chemical Reaction Engineering (IMCCRE 2018)*.

A review regarding the use of the ultrasound during the eletrodeposition process resulted in a publication in the journal *Ultrasonics Sonochemistry*. Besides, a review of the use of supercritical fluid technology for the synthesis of nanocatalysts resulted in a publication in the journal *Synthetic Metals*.The doctoral student attended the event *VII EPFEQ (Graduate Meeting of the Faculty of Chemical Engineering)* in 2018.

The exchange at the University of Alberta at the Donadeo Innovation Centre for Engineering under the guidance of Prof. Dr. Douglas Ivey resulted in preliminary studies with the three electrocatalysts (Co-W, Ag-Co and Zn-Co) applied to the Zn-air battery and 1 experimental article published in *International Journal of Hydrogen Energy*.

The co-orientation of an undergraduate student resulted in the publication of 1 paper in the journal *Chemical Physics* and 1 abstract published in the UNICAMP Undergraduate Work Magazine. Partnerships with members of LabPEA's research group resulted in 1 chapter book published by *Wiley-Scrivener* Publisher, 1 experimental paper published by the *Journal of Water Process Engineering*, 1 experimental paper published by the journal *Sustainable Chemistry and Pharmacy*, 1, experimental paper by the journal *Materials Science and Engineering B*, 1 experimental paper published by the journal *Environmental Technology,* and 1 experimental paper published by the journal *Surfaces and Interfaces*.

Published papers

1. COSTA, J. M.; ALMEIDA NETO, A. F.. Nanocatalysts deposition assisted by supercritical carbon dioxide technology: A review. **Synthetic Metals**, 116627, 2020. doi.org/10.1016/j.synthmet.2020.116627

2. COSTA, J. M.; ALMEIDA NETO, A. F.. Ultrasound-assisted electrodeposition and synthesis of alloys and composite materials: A review. **Ultrasonics Sonochemistry**, 105193, 2020. doi.org/10.1016/j.ultsonch.2020.105193

3. COSTA, J. M.; CLARK, M. P.; DE ALMEIDA NETO, A. F.; IVEY, D. G.. In-situ transformation of eletrodeposited W-Co oxide into $ZnCo_2O_4$ nanoparticles as an effective bifunctional catalyst in ZABs. **International Journal of Hydrogen Energy**, v. 45, p. 16122-16132, 2020. doi.org/10.1016/j.ijhydene.2020.04.052

4. COSTA, J. M.; PORTO, M. B.; AMANCIO, R. J.; DE ALMEIDA NETO, A. F.. Anticorrosive Co-W alloys: Effects of W and Co concentration on their microstructure and faradaic efficiency. **Surfaces and Interfaces**. v. 20. p. 100626, 2020. doi.org/10.1016/j.surfin.2020.100626

5. PORTELA, D. G.; NEPEL, T. C. M.; **COSTA, J. M.**; ALMEIDA NETO, A. F.. Two-stages electrodeposition for the synthesis of anticorrosive Ni-W-Co coating from a deactivated nickel bath. **Materials Science and Engineering: B**, v. 260, 114611, 2020. doi.org/10.1016/j.mseb.2020.114611

6. NEPEL, T. C. M.; **COSTA, J. M.**; VIEIRA, M. G. A.; ALMEIDA NETO, A. F.. Copper removal kinetic from industrial electroplating industrial wastewater using pulsed electrodeposition technique. **Environmental Technology**, 2020. doi.org/10.1080/09593330.2020.1793005

7. PORTO, M. B.; **COSTA, J. M.**; ALMEIDA NETO, A. F;. Ni-W alloys and their anticorrosive properties: Ni removal efficiency from galvanic wastewater by electrodeposition. **Journal of Water Process Engineering**, v. 36, p. 101250, 2020. doi.org/10.1016/j.jwpe.2020.101250

8. MOREIRA, F. L.; **COSTA, J. M.**; ALMEIDA NETO, A. F.. Anticorrosive Zn-Ni alloys: An alternative for the treatment of electroplating industry wastewater. **Sustainable Chemistry and Pharmacy**, v. 16, p. 100263, 2020. doi.org/10.1016/j.scp.2020.100263

9. COSTA, J. M.; HORI, M. S.; DE ALMEIDA NETO, A. F.. Exploring the electrodeposition of Zn-Fe-Mo alloys: Forced convection and current density effects. **Chemical Physics**, 110502, 2019. doi.org/10.1016/j.chemphys.2019.110502

10. COSTA, J. M.; DE ALMEIDA NETO, A. F.. Zn-Co electrocatalysts in lithium-O_2 batteries: temperature and rotating cathode effects on the electrodeposition. **Journal of Solid State Electrochemistry**, v. 23, p. 2533-2540, 2019. doi.org/10.1007/s10008-019-04334-1

11. COSTA, J. M.; DE ALMEIDA NETO, A. F.. Ag-Co Electrocatalysts for Rechargeable Lithium-O_2 Batteries: O_2 Pressure and Current Density Effects. **Electrocatalysis**, v. 5, p. 532-539, 2019. doi.org/10.1007/s12678-019-00540-7

12. COSTA, J. M.; DE MORAIS NEPEL, T. C.; DE ALMEIDA NETO, A. F.. Influence of current density and W concentration on Co-W alloys used as catalysts in electrodes for Li-O$_2$ batteries. **Chemical Papers**, v. 73, p. 1103-1112, 2019. doi.org/10.1007/s11696-018-0661-x

Chapter book

1. COSTA, J. M.; ALMEIDA NETO, A. F.. New Approaches for Renewable Energy Using Metal Electrocatalysts for Lithium-O$_2$ and Zinc-Air Batteries. In: Inamuddin, Asiri, Abdullah M.. (Org.). Nanotechnology in the Life Sciences. 1ed. Basel: Springer International Publishing, 2020, p. 45-61. doi.org/10.1007/978-3-030-42284-4_3

2. COSTA, J. M.; PORTELA, D. G. ; ALMEIDA NETO, A. F.. Ni-Co-W Alloys: Influence of Operational Process Conditions on Their Electroplating. In: Inamuddin, Rajender Boddula, Mohd Imran Ahamed and Abdullah M. Asiri. (Org.). Alloy Materials and Their Allied Applications. 1ed. Beverly: Wiley Scrivener Publishing, 2020, v. 1, p. 39-60. doi.org/10.1002/9781119654919.ch3

Expanded Abstract

1. COSTA, J. M.; NEPEL, T. C. M.; ALMEIDA NETO, A. F.. Obtaining and characterizing Co-W alloys using nickel foam and steel mesh as substrate. In: International-Mexican Congress on Chemical Reaction Engineering (IMCCRE 2018), 2018, Mazatlán. PROCEEDINGS IMCCRE 2018, 2018. p. 21-22.

Abstract

1. HORI, M. S.; **COSTA, J. M.**; DE ALMEIDA NETO, A. F.. Influence of stirring velocity and current density on electrodeposition of Zn-Fe-Mo alloys. In: Revista dos Trabalhos de Iniciação Científica da UNICAMP. n° 26, 2019. doi.org/10.20396/revpibic262018994

APPENDIX A

Electroplating parameters of experimental articles
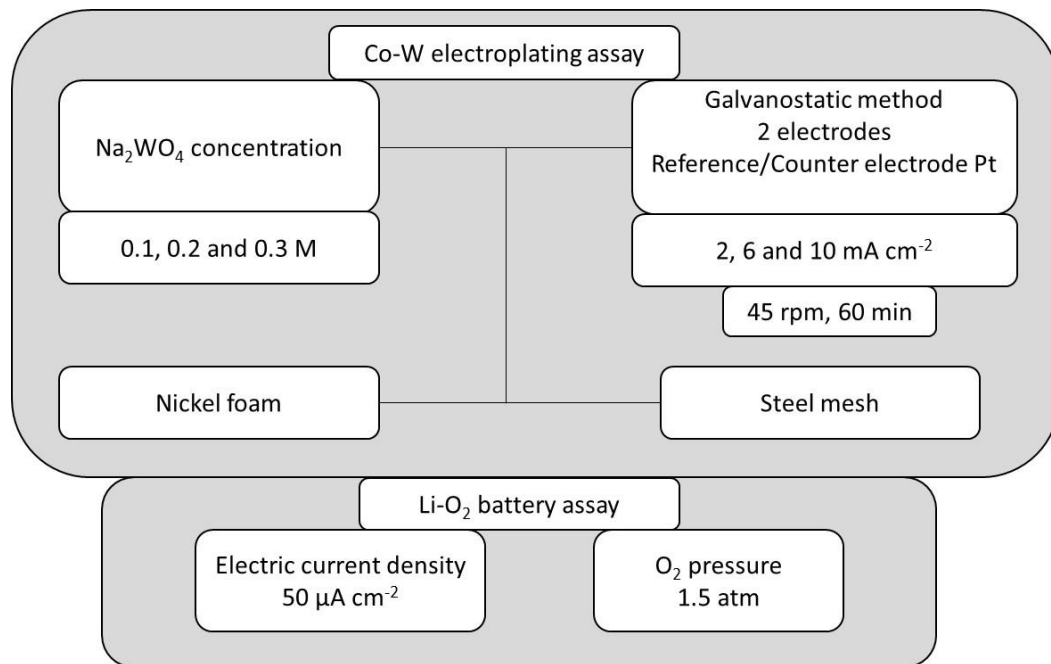
Figure 1. Schematic representation of electroplating assay in Chapter 3.
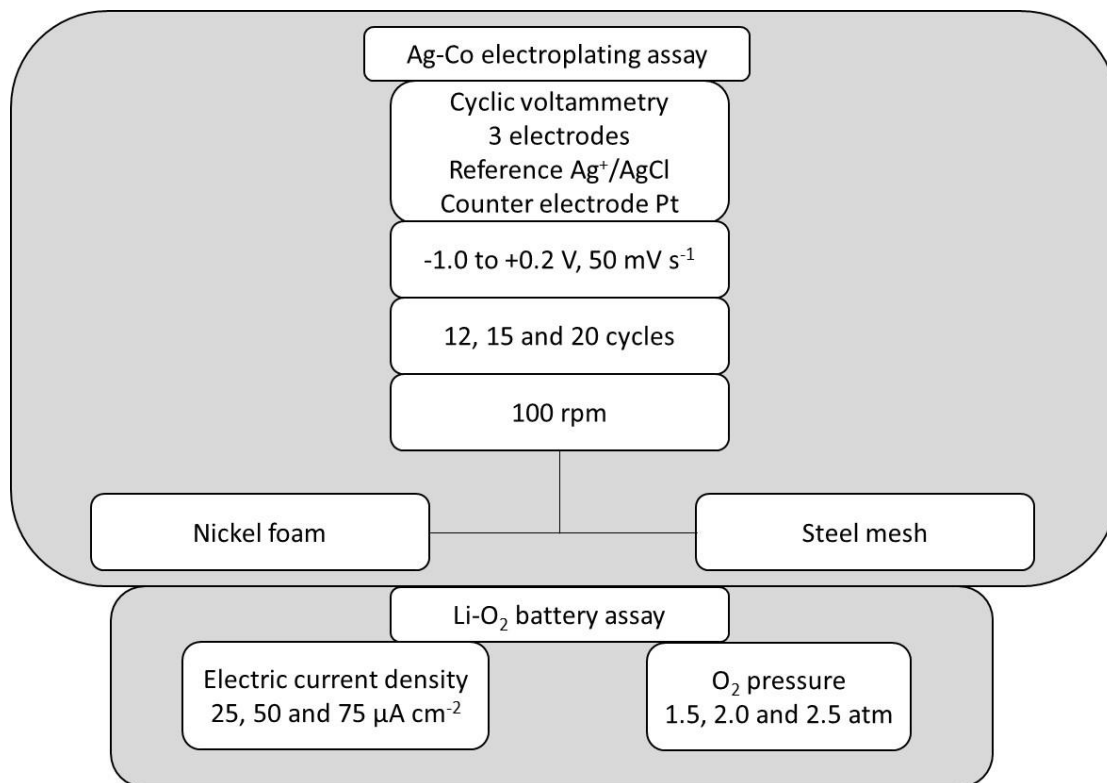
Figure 2. Schematic representation of electroplating assay in Chapter 4.
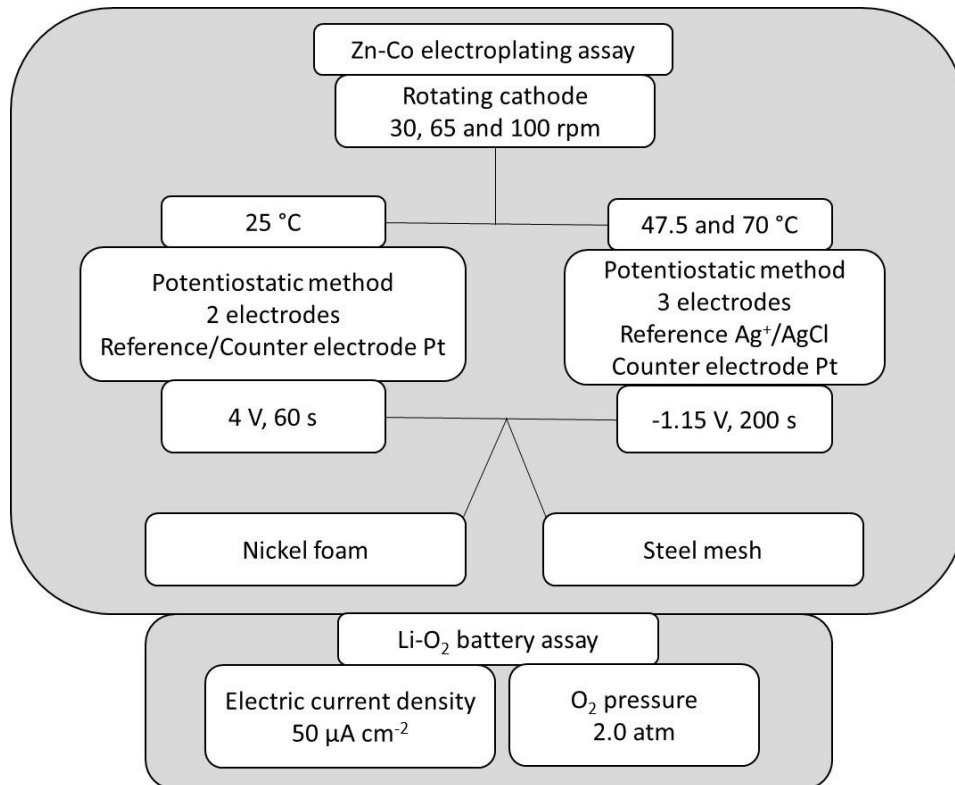
Figure 3. Schematic representation of electroplating assay in Chapter 5.
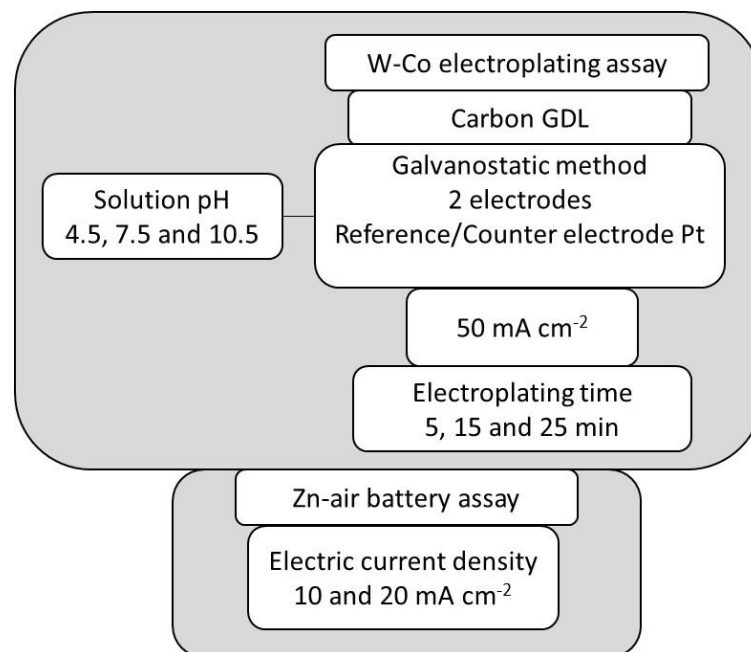
Figure 4. Schematic representation of electroplating assay in Chapter 6.

APPENDIX B

Expanded abstract on the obtaining and characterization of Co-W alloys using nickel foam and steel mesh as substrate

Obtaining and characterizing Co-W alloys using nickel foam and steel mesh as substrate

Josiel Martins Costa, Thayane Carpanedo de Moraes Nepel,
and Ambrósio Florêncio de Almeida Neto

1. Introduction

Co-W electrodeposition alloys are relevant due to exceptional hardness, wear resistance and corrosion [1], and can be used as catalysts in batteries. Heterogeneous electrocatalysis became the object of study in Li-air rechargeable batteries due to the reduction of the overpotential in oxygen reduction (discharge) and oxygen evolution (load) reactions, since the overpotential generates a low storage of energy, ie more energy is needed to charge the battery than the amount released during the discharge [2]. One of the obstacles to its development has been the absence of a high-performance and low-cost catalyst. In this context, the development of low cost electrocatalysts with high efficiency, is of relevant scientific and technological for obtaining rechargeable batteries. This work proposes to verify the development and characterization of electrocatalysts with potential application in battery, varying electric current density, sodium tungstate concentration and substrate (nickel foam and steel mesh).

2. Experimental

Alloys were deposited on 1 cm diameter of nickel foam and steel mesh. Electrochemical baths were prepared containing sodium tungstate, ranged from 0.1 to 0.3 mol L^{-1}; Cobalt sulfate, 0.3 mol L^{-1}; Ammonium citrate, 0.3 mol L^{-1}; Sodium tetraborate decahydrate, 3.75×10^{-2} mol L^{-1}; 1-Na-dodecylsulfate, 1.04×10^{-4} mol L^{-1} [3]. A complete

factorial design 2², with 4 experiments at the central point, totaling 16 experiments to be performed in random order, to avoid systematic error. For the electroplating tests, a galvanostat was used to control the current density between the working electrode and the counter electrode (platinum). The electric current density ranged from 2 to 10 mA cm^{-2}, the cathodic rotation was maintained at 45 rpm and the experiment was performed at room temperature. The electrolysis lasted 60 minutes each. X-ray Diffraction (XRD) and Scanning Electron Microscopy with Chemical Analysis by Energy Dispersive X-ray (EDX) characterized the substrate samples containing Co-W alloys.

3. Results and discussion

The faradic efficiency (ε) obtained for electrodeposition in the nickel foam varied from 0 to 60.05% and for the steel mesh from 0 to 64.39% using EDX analysis and can be estimate by Equation 1, with 95% confidence level, and regression coefficient (R^2) of 0.9360, which means that 93.60% of the variation around average may be estimated by Equation 1. In order to obtain this model, the adjusted R² was observed through the backward elimination tool of the Statistica 7.

$$\varepsilon = 17{,}71 + 11.39 \cdot I + 19.71 \cdot C_W + 4.36 \cdot S + 9.28 \cdot I \cdot C_W + 2.16 \, C_W \cdot S \qquad (1)$$

I is current density (mA cm^{-2}), C_W sodium tungstate concentration (mol L^{-1}) and S is substrate (nickel foam or steel mesh).

The increase of the current density and sodium tungstate concentration contribute to the increase of the electroplating efficiency for both substrates, however the greater efficiency occurred with the steel mesh. This result is the inverse of that obtained by other studies [3,4], which verified that the increase in current density decreases the amount of tungsten deposited. The reduction of tungsten is an activation-controlled reaction with low current densities, whereas diffusion becomes controlled by increasing current density [5]. However the current density applied in this work is small when compared to the work of the authors.

Figure 1 shows the SEM of four samples that were varied the current density. For both substrates, nickel foam and steel mesh, the increase of current density made the surface

less uniform caused by larger grain size [6]. The deposits may be folded without evident peeling and some cracks may occur as shown in Figure 1b-d [7], which are the samples that presented the largest amounts of electrodeposited alloy mass. The surface morphology showed cauliflower-type semi-spherical clusters that are typical of low-concentration W alloys, as reported in previous studies [8,9]. The size of the cauliflower nodule can be decreased by increasing the current density and bath temperature, which promotes the increase in microhardness [7].
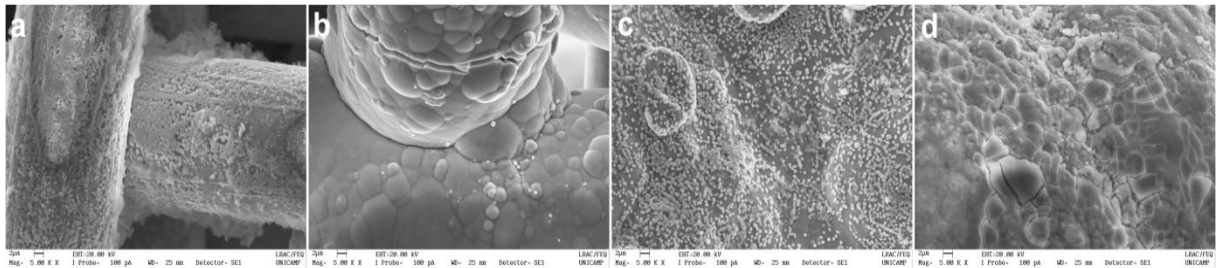
Figure 1. SEM micrographs of Co-W coatings produced at (a) 2 mA cm^{-2} and (b) 10 mA cm^{-2} in steel mesh; (c) 2 mA cm^{-2} and (d) 10 mA cm^{-2} in nickel foam.

The studied variables affected the composition of the coating alloys, crystallinity, morphology and deposition efficiency. The substrates used showed similar electroplating efficiencies, even though they presented different composition and morphology. Amorphous coatings were obtained in most of the experiments; however, it was found that the increase of tungsten concentration in the electrochemical bath and higher applied current density was determinant to obtain coatings with higher crystallinity. Thus, the alloy obtained in these materials presents an alternative for catalytic systems, being coatings deposited in substrates with high surface area that have morphological and structural capacity to house discharge products of the battery.

Acknowledgements

References

[1] L. Wang, Y. Gao, T. Xu, Q. Xue. *Materials Chemistry and Physics.* **2006**, *99*, 96.

[2] F. Li, R. Ohnishi, Y. Yamada, J. Kubota, K. Domen, A. Yamada, H. Zhou, *Chemical Communications*. **49** (2013) 1175.

[3] Z. Ghaferi, K. Raeissi, M.A. Golozar, H. Edris, *Surface and Coatings Technology*. **206** (2011) 497.

[4] M. A. M. Ibrahim, S.S. Abd El Rehim, S.O. Moussa, *Journal of Applied Electrochemistry*. **33** (2003) 627.

[5] M.D. Obradovic, R.M. Stevanovic, A.R. Despic, *Journal of Electroanalytical Chemistry*. **552** (2003) 185.

[6] Z. Ghaferi, S. Sharafi, M. E. Bahrololoom, *Applied Surface Science*. **355** (2015) 766.

[7] E. Vernickaite, N. Tsyntsarua, H. Cesiulis, *Surface and Coatings Technology*. **307** (2016) 1341.

[8] R. Della Noce, A. V. Benedetti, M. Magnani, E. C. Passamani, H. Kumar, D. R. Cornejo, C. A. Ospina, *Journal of Alloys and Compounds*. **611** (2014) 243.

[9] A. L. M. Oliveira, J. D. Costa, M. B. de Sousa, J. Ja, N. Alves, A. R. N. Campos, R. A. C. Santana, S. Prasad, *Journal of Alloys and Compounds*. **619** (2015) 697.

APPENDIX C
Effects of the forced convection and current density on electrodeposition of Zn-Fe-Mo alloys

Effects of the forced convection and current density

on electrodeposition of Zn-Fe-Mo alloys

Josiel Martins Costa, Mariana Sayuri Hori, and Ambrósio Florêncio de Almeida Neto

Abstract

In this study, zinc ternary alloys known for their catalytic application in desulphurization processes, were developed by the electrodeposition process. Zn-Fe-Mo ternary alloy were synthesized from electrolytic bath using copper as a substrate. The influence of forced convection (9 to 51 rpm) and current density (1.72 to 58.28 mA·cm-2) on the electrodeposition of Zn-Fe-Mo alloys was evaluated by using a central composite design. It was observed that the decrease in the electric current density resulted in an increase in electrodeposition efficiency from 36 to 68%. According to statistical analysis, the stirring velocity was not significant, however, it was verified that the forced convection phenomenon contributed to increasing the deposition from 30 to 72% for Zn and Fe, and from 37 to 90% for Mo. In addition, the alloys obtained were characterized by X-ray diffraction and scanning electron microscopy (SEM). Diffractograms evidenced the presence of crystalline structures and the SEM micrographs presented coatings with rough and fibrous appearance.

Keywords: development of new materials; central composite design; electroplating; X-ray diffraction.

1. Introduction

Zinc metal alloys are commonly used as coatings and may have their improved properties from the codeposition of other metals. Zinc and iron alloys, for example, exhibit corrosion resistance, in addition to detachable weldability and paintability [1]. Molybdenum metal alloys have industrial applications, due to resistant to corrosion and ferromagnetic properties. These alloys also have application in the heterogeneous catalysis [2], due to the catalytic properties for the hydrogen production [3]. Although there is no deposition of pure molybdenum in aqueous solution, the electrodeposition of a salt of this metal with alkali metals, in the presence of a metal salt of the iron group and of a complexing agent, is easily carried out, whose phenomenon has been denominated as codeposition induced [4]. Thus, the electrodeposition of the ternary alloy containing zinc, iron and molybdenum has the purpose of obtaining the improved properties of each metal, resulting in increased resistance to corrosion and wear, as compared to binary alloy - without molybdenum - or with other alloys of zinc, although the use of these last alloys still occurs, mainly due to the low cost of synthesis [5].

Studies of zinc, cobalt and molybdenum ternary alloys have shown that the presence of this latter metal has a positive effect on the corrosion resistance due to the property of forming oxides on the surface of the coating [6]. Thus, it was expected that the replacement of cobalt by iron, a metal that also induces molybdenum deposition, may result in equally satisfactory properties [7]. The variation of process conditions, such as sodium molybdate concentration and electrolytic bath pH, directly influence deposition efficiency, homogeneity and deposit morphology. In relation of Zn-Ni-Mo alloys [8], the increase of the MoO_4^{2-} concentration in a Zn-Fe-Mo alloy also leads to a significant reduction of the electrodeposition efficiency [1].

Winiarski, Tylus, Krawczyk and Szczygieł [1] observed that the increase of molybdate concentration from 0.0025 to 0.05 mol·L^{-1}, the efficiency decreased from 82 to 25%, whereas in binary Zn-Fe alloys, at the same conditions of current density and cathodic rotation (800 rpm), the efficiency was high, of approximately 91%. In addition, these same authors reported that baths with a concentration of 0.0025 mol·L^{-1} of MoO_4^{2-}, resulted in a homogeneous and rough-looking alloy. Already in baths with slightly higher concentrations, between 0.01 and 0.025 mol·L^{-1}, alloys were obtained with smooth and homogeneous surfaces. Above this, at 0.05 mol·L^{-1} sodium molybdate, the result was a slightly adherent coating, characterized by small grooves and peeling appearance. Thus, in this study, we adjusted the

concentration of Mo in the electrolytic bath aiming to evaluate the influence of stirring velocity and current density on the electrodeposition of Zn-Fe-Mo alloys. Furthermore, the alloys obtained were characterized by scanning electron microscopy (SEM), energy dispersive spectrometry (EDS) and X-ray diffraction (XRD) based on the performance of experiments in an electrolytic bath system.

2. Material and methods

2.1. Preparation of substrates and electrolytic bath

The tests were performed using a copper substrate in a square shape, whose sides measured 2 cm, which totaled a surface area of 8 cm^2, considering both sides of the plate, in addition to a 3 cm rod to couple the substrate on the rotating electrode. The choice of copper was dictated by the necessity to use a substrate which does not contain in its composition of any of the alloying components of Zn-Fe-Mo coating. The treatment of the substrate occurred in two steps, one mechanical and one chemical. The mechanical treatment consisted of the polishing with three sands of water grain, in the following order: 220, 400 and 1200, for elimination of impurities and oxides on the surface. For the chemical treatment, the substrate was immersed in 10% w/v NaOH solution (sodium hydroxide), to eliminate grease and, after washing with distilled water, in 1% v/v H_2SO_4 solution (sulfuric acid) for surface neutralization and activation.

The composition of the electrolytic bath was prepared from the dissolution of the reagents in the following order [9]: Sodium molybdate, 0.01 and 0.005 mol·L^{-1} Na_2MoO_4, Molybdenum source salt; Sodium borate, $Na_2B_4O_7$ 0.0375 mol·L^{-1}, to obtain amorphous alloy; Ammonium citrate, $(NH_4)_2C_6H_6O_7$ 0.2 mol·L^{-1}, used in the bath as a complexing agent; Iron sulfate, $FeSO_4$ 0.2 mol·L^{-1}, source salt of Iron; Zinc sulphate, $ZnSO_4$ 0.2 mol·L^{-1}, zinc source salt and 1-dodecylsulfate-Na 1.04×10^{-4} mol·L^{-1}, to prevent bubble formation in the adhered alloy.

2.2. Electroplating

The effects of electric current density (mA·cm^{-2}) and rotating cathode (rpm) on the electrodeposition of Zn-Fe-Mo alloys were evaluated using a central composite design, according to Table 1. Central composite design is used when curvature adjustment is significant in the linear model. The center points in this model provide information about axial points for efficient estimation of the pure quadratic terms [10].

Table 1. Actual and coded values of variables in the central composite design

Variables	Level ($-\sqrt{2}$)	Level (-1)	Level (0)	Level ($+1$)	Level ($+\sqrt{2}$)
Current density (I) (mA·cm^{-2})	1.72	10	30	50	58.28
Rotating cathode (R) (rpm)	9	15	30	45	51

The pH was adjusted with ammonium hydroxide to 5.5. The electrolysis occurred at the room temperature (25 °C), lasting 60 min for all experiments, using a rotating electrode pattern 616A Princeton Applied Research and a potentiostat VersaStat3 Princeton Applied Research in the galvanostatic form, to control the difference of the electrical potential between the working electrode and the counter electrode, a hollow cylindrical mesh of platinum.

The faradaic efficiency (ε) was calculated from the mass obtained by the load used and the chemical composition of the coating obtained by EDS according to Equation (1) [11]:

$$\varepsilon = \frac{m.F}{I.t} \sum \frac{n_j.W_j}{M_j} \tag{1}$$

where m is the measured mass of coating (g), t is the deposition time (s), I is the total current passed (A), w_j is the mass fraction of the element in the coating obtained by EDS, n_j is the number of electrons transferred per atom of each metal, M_j is the atomic mass of that element (g·mol^{-1}), and F is the Faraday's constant (96,485 C·mol^{-1}).

2.3. Characterization of Zn-Fe-Mo alloys

2.3.1. Chemical composition and morphology

The topographies and chemical compositions of the alloys were obtained by SEM, model Leo 440i, equipped with X-Ray Energy Dispersion Spectrometer (LEO Electron Microscopy / Oxford, Cambridge, England) model 6070. It was made magnifications of 5000 times.

2.3.2. Physical properties

The XRD analysis was performed by the K-alpha copper scanning method, 40 kV voltage, 40 mA current, 2θ ranging from 20 to 90° with a pitch of 0.02°, speed $0.033°·s^{-1}$ and length of wave of 1.54 Å on a Philips Analytical X Ray diffractometer and X'Pert-MPD model.

The lattice constant of Zn was obtained by the Equation (2):

$$\frac{1}{d^2} = \frac{4}{3}\left(\frac{h^2 + hk + k^2}{a^2}\right) + \frac{l^2}{c^2} \tag{2}$$

where d is interplanar spacing; a and c are the lattice parameters; h, k and l are crystalline plane.

2.4. Fluid dynamics analysis

The purpose of this analysis was to verify the value of the contribution of the forced convection phenomenon for the Zn-Fe-Mo alloy electrodeposition. The approximate correlation of mass transfer for the system of forced convection provided by rotating cathode is given by Equation (3) [12]:

$$\frac{k_c d}{D_{AB}} = 0.62Re^{1/2}Sc^{1/3} \tag{3}$$

where k_c is the convective mass transfer coefficient $(cm·s^{-1})$ and:

$$Re = \frac{d^2\omega}{\nu} \tag{4}$$

$$Sc = \frac{\nu}{D_{AB}} \tag{5}$$

where ω is the cathode rotation (rad·s⁻¹), ν is the kinematic viscosity of the solution (cm²·s⁻¹), *d* is the agitator diameter (cm) and D_{AB} is the diffusivity of species A (Zn, Fe or Mo) with respect to species B (solution) (cm²·s⁻¹), *Re* is the Reynolds number and *Sc* is the Schmidt number. Thus, the deposition rate (W_A) was calculated by Equation (6).

$$W_A = Ak_c(C_{A0} - C_{Af}) \tag{6}$$

where *A* is the area of the electrode (cm²), C_{A0} and C_{Af} are, respectively, the initial and final concentrations of the chemical species A (g·cm⁻³). Final concentrations of species A were estimated by their material balance in the bath and masses deposited at the cathode, according to Equation (7).

$$V(C_{A0} - C_{Af}) = m_{Af} - m_{A0} \tag{7}$$

where *V* is the volume of the electrolytic bath (cm³), and m_{Ao} and m_{Af} are the masses of the chemical species A deposited at the cathode (g).

3. Results and discussions

3.1. Electroplating of Zn-Fe-Mo alloy

An initial study was proposed to determine the proper concentration of Mo in the bath with a current density of 50 mA·cm⁻² and rotating electrode of 45 rpm. Although the faradaic efficiency of the electrodeposition with a concentration of 0.01 mol·L⁻¹ Mo was 13.25 %, when compared to the obtained alloy of 0.005 mol·L⁻¹ concentration (ε - 26.01 %), the sample was more homogeneous and adherent. Thus, the concentration of 0.01 mol·L⁻¹ of Mo was used in all experiments. The literature reports that the increase of MoO_4^{2-} concentration promoted a decrease in electrodeposition efficiency [8, 13]. This phenomenon was observed for the ternary Zn-Ni-Mo alloy, in which the authors [8] verified the decrease in efficiency from 82 to 25 % when increasing the concentration of MoO_4^{2-} from 0.0025 to 0.05 mol·L⁻¹. The authors suggested that at pH close to 5.7 the uncomplexed MoO_4^{2-} ions can be the ionic form

of molybdenum. Therefore molybdate ions could block the surface of electrode and then suppress the deposition process.

The pH of the bath of 5.5 was obtained by analysis of metallic speciation diagrams from the Hydra and Medusa Software used for other studies [9, 14, 15], which demonstrated the formation of complexing species that favor the electrodeposition of the three metals. The complexation of Zn for the composition used occurs in the pH range 3 to 8 in the form of $Zn(cit)^-$, Fe in the pH range 3 to 10 in the form of $Fe(cit)^-$ and Mo in the pH range 3 to 7 in the form of $MoO_4(H_2cit)^{3-}$, as shown in Fig. 1. Values close to pH 5.5 Mo exist as mono-oxyanions and the deposition is thought to occur with decrease in the size of oxyanions, which allows easier deposition of Mo [16], and Zn does not form hydroxides [17].
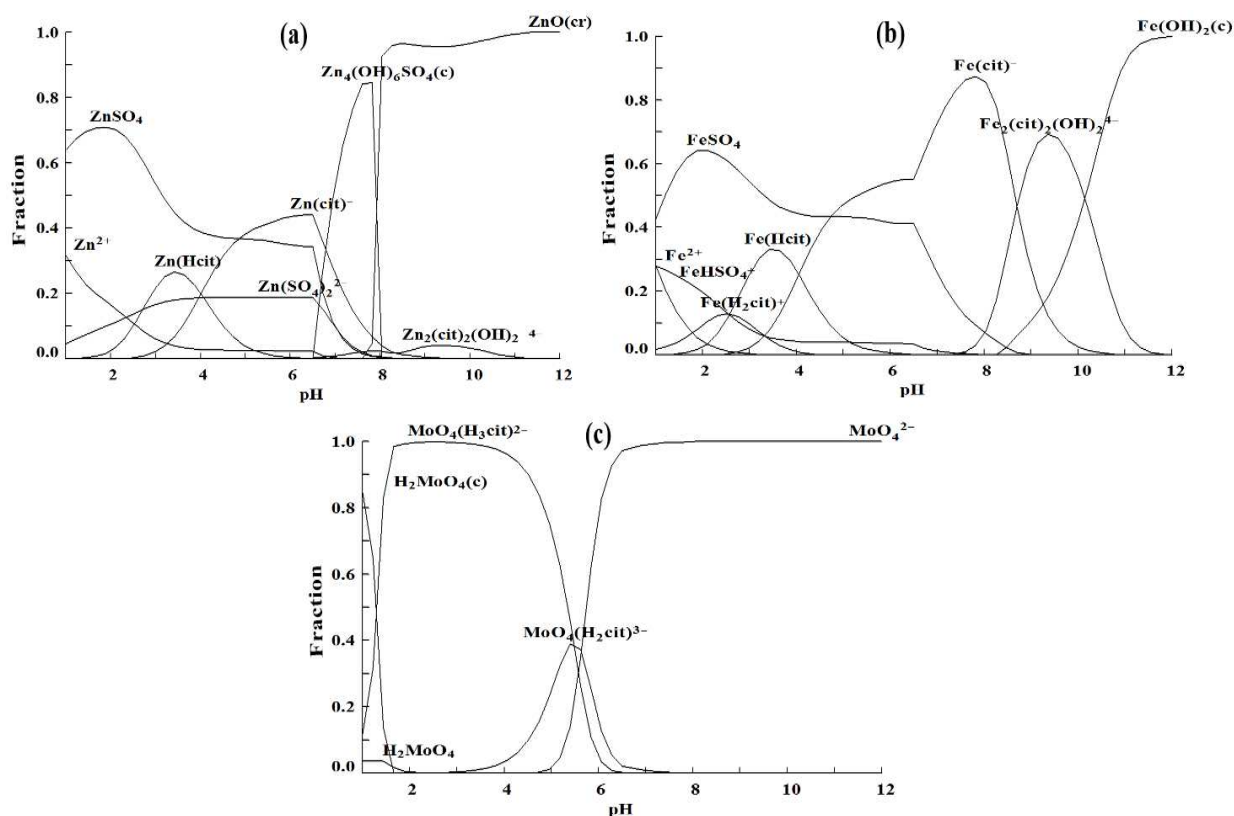
Figure 1. Chemical species of a) zinc, b) iron and c) molybdenum in the electrolytic bath obtained on Hydra and Medusa Softwares.

Table 2 correlates the tests with their respective electrodeposition efficiencies according to the mass proportions obtained in the EDX analysis. It was found that low current densities led to high faradaic efficiencies. However, for the same range of current density

studied by Kosugi, Hagio, Kamimoto and Ichino [17] (1 to 10 mA·cm^{-2}) it was observed that high efficiencies are associated with high current densities, which is in agreement with the authors. High current densities had low efficiencies due to the less adherent deposit, which changed the deposit mass used in the efficiency calculation.

The large proportion of Zn in the alloy suggested the anomalous codeposition phenomenon [18, 19]. This term, introduced by Brenner [4] is used to describe the preferential deposition of the less noble metal. In other words, the reduction of Mo or Fe is inhibited while the deposition of Zn is enhanced when compared with their individual deposition rates. However, there are experimental conditions, such as low current density and high temperatures, in which the codeposition becomes normal, with great increase in the content of the most noble metal [20].

Table 2. Matrix of central composite design and faradaic efficiency

Exp.	I(mA·cm^{-2})	R (rpm)	m_{Zn} ($\times 10^{-1}$ g)	m_{Fe} ($\times 10^{-3}$ g)	m_{Mo} ($\times 10^{-3}$ g)	ε (%)
1	10 (-1)	15 (-1)	0.6320	1.06	0.94	68
2	50 (+1)	15 (-1)	0.3814	1.84	1.92	9
3	10 (-1)	45 (+1)	0.3429	0.44	0.18	36
4	50 (+1)	45 (+1)	0.3247	1.72	1.81	8
5	30 (0)	30 (0)	1.5038	5.27	0.55	54
6	30 (0)	30 (0)	1.3960	4.90	0.51	50
7	30 (0)	30 (0)	1.2516	4.39	0.46	45
8	30 (0)	9 (-√2)	0.7878	2.62	1.49	29
9	30 (0)	51 (+√2)	1.8702	6.23	3.54	69
10	1.72 (-√2)	30 (0)	0.0447	0.15	0.08	29
11	58.28 (+√2)	30 (0)	0.5122	1.71	0.97	10

As can be observed in Table 2, the deposited proportion of zinc is high in comparison with the other metals, which is consistent with the work of Winiarski, Tylus, Krawczyk and Szczygieł [1]. It is noteworthy that experiments submitted to high current densities led to a percentage increase of iron and molybdenum in the alloy composition, and this was probably the factor that led to lower faradaic efficiency. Hegde, Venkatakrishna and Eliaz [5] suggested that this may occur due to the change in the local pH, caused by the variation of the applied current density, which interferes in the stability of the iron complexes and acts directly on the coating composition.

From the results of experiment 1 to 7, only the current density had an experimental significance, since its effect was found within the confidence interval and its absolute value of significance is above the 95% confidence level. As the statistical analysis for the linear adjustment model obtained low values of linear and adjusted coefficient of determination (R^2 - 78% and adjusted R^2 - 56%), a curvature adjustment was performed, resulting in a new model with R^2 - 96% and adjusted R^2 - 99%, which suggested a central composite design, with addition of the experiments 8, 9, 10 and 11. The new statistical analysis reaffirmed the experimental significance only for current density, which presented p-values less than 0.05, with a value of 0.012 for the linear term and 0.014 for the quadratic term. Rotating cathode had no significant effect with a 95% confidence interval and was not relevant in the model using central composite planning, however, the forced convection phenomenon contributed with a percentage of electrodeposition, according to item 3.3. The quadratic model proved to be significant, which can be confirmed by the normal distribution of the residues, according to Fig. 2, which the residual values are close to the straight line.
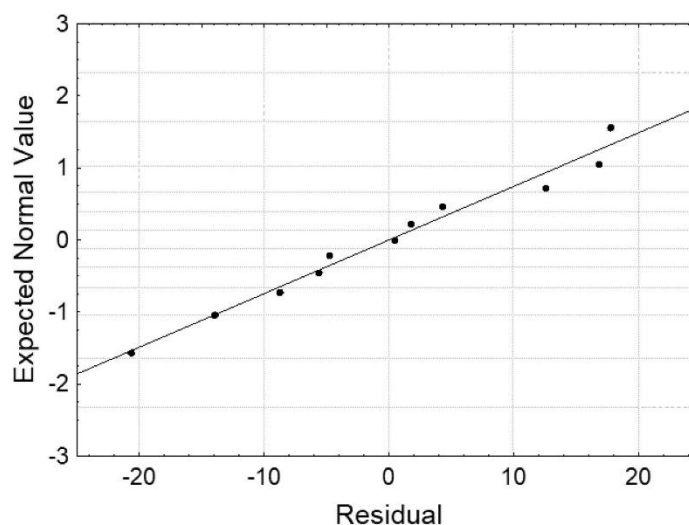
Figure 2. Normal plot of residues probability.

Fig. 3 shows the response surface for the central composite design, and confirms that low current densities result in high efficiencies, especially when the current density is between 10 mA·cm^{-2} (-1) and 30 mA·cm^{-2} (0).
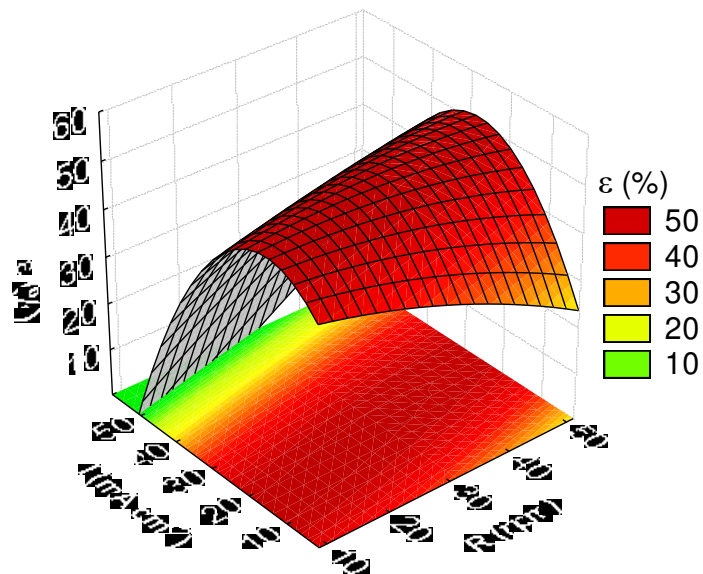
Figure 3. Response surfaces for the faradaic efficiency.

3.2. Crystallinity and morphology of Zn-Fe-Mo coating

Fig. 4 shows the X-ray diffractograms of the ternary alloy according to the variation of the parameters analyzed. Five samples with smaller and higher faradaic efficiencies were selected. The XRD patterns revealed well-defined metal zinc peaks at angles 2θ close to: 41.50, 43.47 and 55.60° with the presence of traces of the copper substrate. The positions of the reported peaks were smoothly displaced when compared to the diffractogram of other authors [21, 22], however this is a phenomenon that commonly occurs due to small differences in the procedure of the experiments.
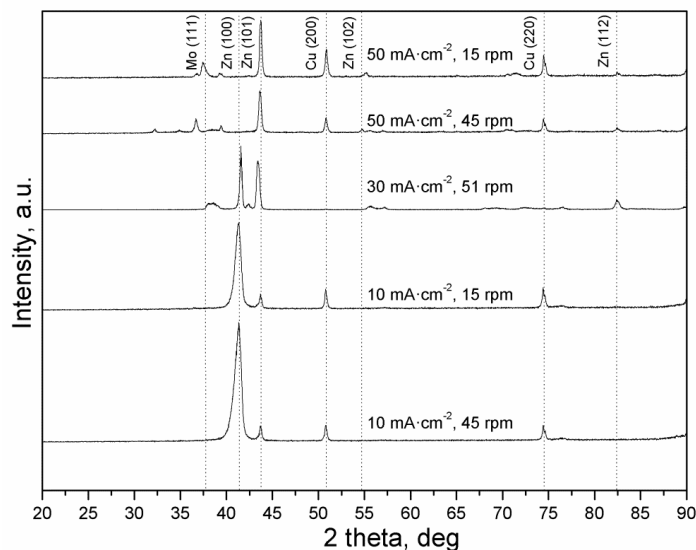
Figure 4. XRD patterns of Zn-Fe-Mo electrodeposited coatings.

From the analysis of Fig. 4, it was concluded that the increase in current density induced more intense peaks of Zn (100) at about 41.50° and less intense peaks of Zn (101) at 43.47°, (102) at 54.90° and (112) at 82.35°. The lattice constants are a - 2.66 Å and c - 4.95 Å; their ratio c/a ~ 1.86 is different to the ideal value for hexagonal close-packed cell c/a - 1.63, which suggests in the zinc matrix the presence of metal with higher atomic radius, such as molybdenum. The peak (100) for Zn was intense for sample 1, 3 and 9, however was absent to samples 2 and 4. This observation suggests that the peak occurs only at high faradaic efficiency, i.e., large amount of deposits. Peaks at 50.45 and 74.13° can be attributed to copper. These peaks correspond to the (200) and (220) planes of Cu (JCPDS card n° 85-1326) respectively, which shows the low adhesion of the alloy to the substrate in the depositions outside the central point. In sample 4 the peak of molibdenium (111) was observed, with 38.68° (JCPDS card n° 88-2331). This occurred due to the proportion of molybdenum being greater when compared to its proportions in the other samples. It is also observed that despite the addition of amorphizing agent in the electrolytic bath, the Zn-Fe-Mo alloy showed characteristics of crystalline structure. Most of diffractograms of the deposited coatings did not reveal pure iron and molybdenum peaks, a fact expected according to studies [1, 17], because these metals possibly dissolved in the zinc matrix.

Fig. 5 shows the scanning electron micrographs of the Zn-Fe-Mo alloy surfaces subjected to high and low current densities and rotating cathode, in order to verify the influence of the parameters on deposit morphology. As reported by Kosugi, Hagio, Kamimoto and Ichino

[17], at a pH close to 5 and applied current density of 10 mA·cm^{-2}, the structure of the deposits became more rough and fibrous, which can be verified in the SEM micrographs - Fig. 5 (c-d). It was notable the presence of irregular faults and determined porosity in the alloy. It was observed by the EDX analysis that, when the rotating cathode was 45 rpm, an alloy deposited at 10 mA·cm^{-2} obtained 0.5 mol % (w / w) of molybdenum, ten times lower than when subjected to 50 mA·cm^{-2}. This increase in the percentage of the metal probably induced the surface to become smoother and homogeneous, as shown in Fig. 5 (a-b). A similar result was observed by Laszczynska [8] in the morphology of the Zn-Ni and Zn-Ni-Mo alloys, where the presence of molybdenum in the composition of the metal alloys led to more regular surfaces.
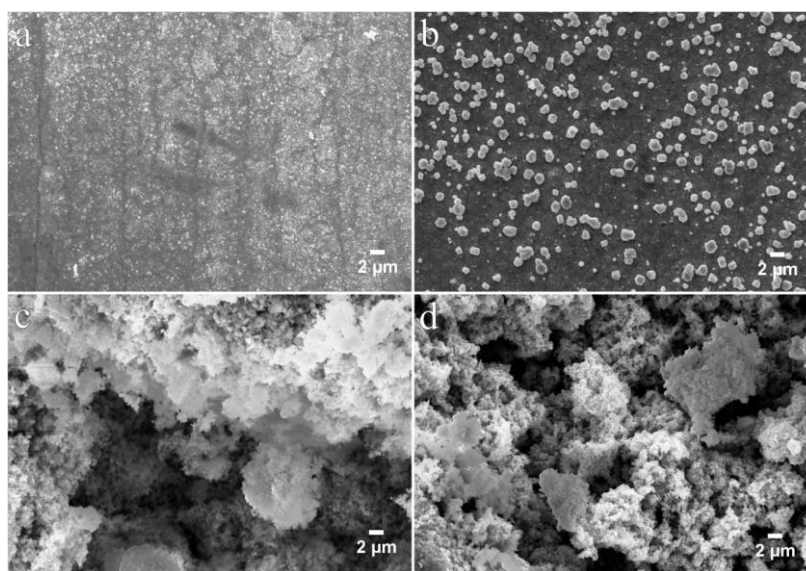
Figure 5. SEM micrographs of Zn-Fe-Mo coatings produced at: a) 45 rpm and b) 15 rpm, at 50 mA·cm^{-2}; and c) 45 rpm and d) 15 rpm, at 10 mA·cm^{-2}; with 5000 × amplification.

EDX mapping of the Zn-Fe-Mo alloy in Fig. 6-a shows the homogeneity of the electroplated sample at 15 rpm at 50 mA·cm^{-2}. The predominant color is blue, which zinc represents 91% of the deposit composition, followed by Fe (6%) and Mo (3%). The EDX spectrum graph in Fig. 6-b present the metal peaks Zn, Fe and Mo, and the copper substrate.
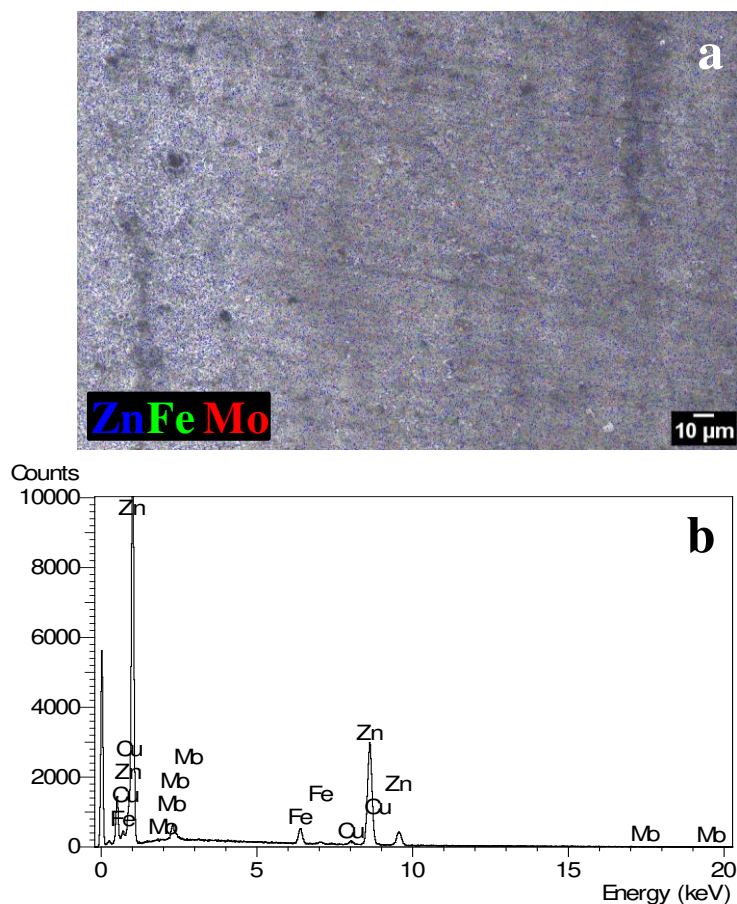
Figure 6. a) EDX mapping of Zn-Fe-Mo, and b) EDX spectrum, both at the electrodeposition condition of 15 rpm at 50 mA·cm^{-2}.

3.3. Deposition rate and fluid dynamic effects

The study on the influence of the amount of movement applied on the system by rotating electrode was performed, evaluating the actual deposition rate in comparison with the rate of deposition obtained by forced convection applied to the system. For this, the convective transfer coefficient (k_c), was calculated for each assay and for each alloying component (Zn, Fe and Mo). The kinematic viscosity of the water at 25 °C and the values of the diffusivity of the three ions in relation to water were obtained from the values tabulated by authors [23, 24]. The initial concentrations (C_{A0}) for the zinc, iron and molybdenum ions were, respectively, 0.023, 0.020 and 0.001 g·cm^{-3}.

Fig. 7 shows the comparison for the deposition rates (W_A) and real (W_R) obtained for the three metals in each experiment. The real deposition rate (W_R) was calculated by dividing the final mass of each element in the alloy by the deposition time (60 min).
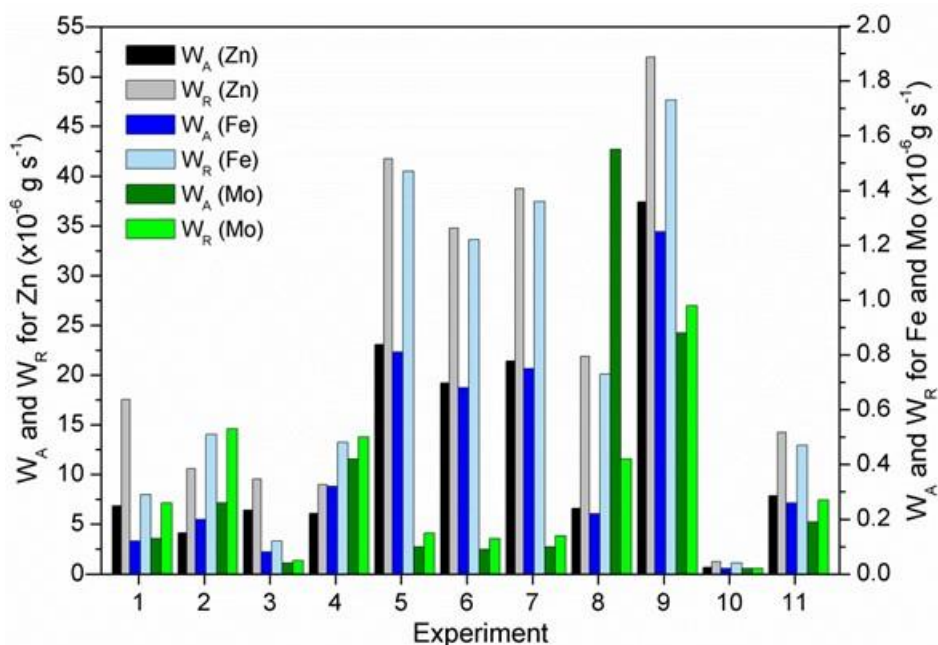
Figure 7. Comparison between the deposition rate obtained (W_A) and the real deposition rate (W_R) for each metal in the respective experiments.

Several values were obtained for the influence of rotation on the deposition, from 30 to 72 % for zinc and iron, and 38 to 90 % for molybdenum, and the low percentages were obtained in the experiment with the low rotation (9 rpm) and the high in the experiment with the high rotation (51 rpm). Studies analyzed the influence of forced convection on the electrodeposition process. The authors verified values of 61 % for cobalt and 74 % for tungsten electrodeposited with a cathodic rotation of 45 rpm [25]. Thus, according to the fluid dynamics analysis performed, forced convection was considered a significant phenomenon in the contribution of the mass transfer of the metals.

4. Conclusions

The evaluated parameters directly affected the faradaic efficiency, the morphology and the composition of the Zn-Fe-Mo ternary alloy obtained by the galvanostatic method. High

deposition efficiency was obtained at 30 mA·cm^{-2} current density and rotating cathode (51 rpm) and, although statistical analysis indicated that only current density was significant in the experiments, dynamic fluid analysis showed that the forced convection phenomenon contributed with electrodeposition of 30 to 90% according to the experimental conditions. All Zn-Fe-Mo coatings are composed of a zinc phase. Metallic molybdenum and iron dissolved in the zinc matrix according to XRD analysis. The alloys presented fibrous and porous appearance, with potential application as catalysts.

Acknowledgements

References

[1] J. Winiarski, W. Tylus, M.S. Krawczyk, B. Szczygieł, The influence of molybdenum on the electrodeposition and properties of ternary Zn–Fe–Mo alloy coatings, Electrochimica Acta 196 (2016) 708-726.

[2] J. Dou, X. Li, A. Tahmasebi, J. Xu, J. Yu, Desulfurization of coke oven gas using char-supported Fe-Zn-Mo catalysts: Mechanisms and thermodynamics, Korean Journal of Chemical Engineering 32 (2015) 2227-2235.

[3] Z. Abdel Hamid, Electrodeposition of cobalt–tungsten alloys from acidic bath containing cationic surfactants, Materials Letters 57 (2003) 2558-2564.

[4] A. Brenner, Electrodeposition of Alloys, Academic Press, New York, USA, 1963.

[5] A.C. Hegde, K. Venkatakrishna, N. Eliaz, Electrodeposition of Zn–Ni, Zn–Fe and Zn–Ni–Fe alloys, Surface and Coatings Technology 205 (2010) 2031-2041.

[6] J. Winiarski, W. Tylus, B. Szczygieł, EIS and XPS investigations on the corrosion mechanism of ternary Zn–Co–Mo alloy coatings in NaCl solution, Applied Surface Science 364 (2016) 455-466.

[7] J. Winiarski, B. Szczygieł, The effect of plating bath pH on the properties of protective ternary Zn-Fe-Mo alloy coatings deposited from citrate-sulphate solution, 4 (2015).

[8] A. Laszczynska, Influence of bath concentration and pH on electrodeposition process of ternary Zn-Ni-Mo alloy coatings AU - Szczygiel, B, Transactions of the IMF 92 (2014) 196-202.

[9] J. Winiarski, W. Tylus, A. Lutz, I. De Graeve, B. Szczygieł, The study on the corrosion mechanism of protective ternary ZnFeMo alloy coatings deposited on carbon steel in 0.5 mol dm^{-3} NaCl solution, Corrosion Science 138 (2018) 130-141.

[10] B.A. Oyejola, N. J.C., Selecting the right central composite design, Int. J. Stat. Appl. 5 (2015) 21-30.

[11] M.B. Porto, L.B. Alvim, A.F. de Almeida Neto, Nickel removal from wastewater by induced co-deposition using tungsten to formation of metallic alloys, Journal of Cleaner Production 142 (2017) 3293-3299.

[12] J.R. Welty, C.E. Wicks, R.E. Wilson, G.L. Rorrer, Fundamentals of Momemtum, Heat and Mass Transfer, 5th ed., Jhon Wiley and Sons, Hoboken, 2007.

[13] A. Laszczyńska, B. Szczygieł, An electrochemical study on the influence of sodium molybdate on electrodeposition process and phase composition of ternary Zn–Ni–Mo alloy coatings AU - Winiarski, J, Transactions of the IMF 93 (2015) 267-274.

[14] C.F. Baldessin, T.C. de Morais Nepel, A.F. de Almeida Neto, The influence of Ni and Co concentration in the electroplating bath on Ni-Co-W alloys properties, The Canadian Journal of Chemical Engineering 96 (2018) 1284-1289.

[15] H. Kazimierczak, A. Hara, A. Bigos, P. Ozga, Electrodeposition of Zn-Mn-Mo layers from citrate-based aqueous electrolytes, Electrochimica Acta 202 (2016) 110-121.

[16] H. Kazimierczak, P. Ozga, R.P. Socha, Investigation of electrochemical co-deposition of zinc and molybdenum from citrate solutions, Electrochimica Acta 104 (2013) 378-390.

[17] D. Kosugi, T. Hagio, Y. Kamimoto, R. Ichino, Effect of the Addition of Molybdenum on the Structure and Corrosion Resistance of Zinc–Iron Plating, 2017.

[18] M.M. Abou-Krisha, F.H. Assaf, S.A. El-Naby, Electrodeposition behavior of zinc–nickel–iron alloys from sulfate bath, Journal of Coatings Technology and Research 6 (2009) 391-399.

[19] M.M. Abou-Krisha, Effect of pH and current density on the electrodeposition of Zn–Ni–Fe alloys from a sulfate bath, Journal of Coatings Technology and Research 9 (2012) 775-783.

[20] R. Fratesi, G. Roventi, G. Giuliani, C.R. Tomachuk, Zinc–cobalt alloy electrodeposition from chloride baths, Journal of Applied Electrochemistry 27 (1997) 1088-1094.

[21] J. Winiarski, A. Leśniewicz, P. Pohl, B. Szczygieł, The effect of pH of plating bath on electrodeposition and properties of protective ternary Zn–Fe–Mo alloy coatings, Surface and Coatings Technology 299 (2016) 81-89.

[22] A. Roshanghias, M. Heydarzadeh Sohi, The effects of pulse plating variables on morphology and corrosion behavior of Zn–Fe alloy coatings, 2012.

[23] L. Yuan-Hui, S. Gregory, Diffusion of ions in sea water and in deep-sea sediments, Geochimica et Cosmochimica Acta 38 (1974) 703-714.

[24] J.C. Crittenden, R.R. Trussell, D.W. Hand, K.J. Howe, G. Tchobanoglous, MWH's Water Treatment: Principles and Design, 3 rd ed., Jhon Wiley and Sons, Hoboken, 2012.

[25] J.M. Costa, T.C. de Morais Nepel, A.F. de Almeida Neto, Influence of current density and W concentration on Co–W alloys used as catalysts in electrodes for Li–O_2 batteries, Chemical Papers 73 (2019) 1103-1112.

APPENDIX D

Effects of tungsten and cobalt concentration on microstructure and anticorrosive property of cobalt-tungsten alloys

Effects of tungsten and cobalt concentration on microstructure and anticorrosive property of cobalt-tungsten alloys

Josiel Martins Costa, Mariana Borges Porto, Rodolfo José Amancio,
and Ambrósio Florêncio de Almeida Neto

Abstract

The replacement of chrome coatings for materials that maintain the same properties has become the Co-W alloy relevant. In this context, we proposed to evaluate the effects of the Co and W concentration in the electrolytic bath on the faradaic efficiency, morphology, and anticorrosive properties of the Co-W alloy. The diffractograms indicated amorphous alloys when the W content increased from 0.1 to 0.3 M, and the faradaic efficiency achieved values close to 70%. Alloy surfaces demonstrated a homogeneous composition according to the Energy-Dispersive X-ray (EDX) mapping and the increase in the Co and W content promoted the formation of rounded structures and reduction of the space between the microcracks. Moreover, the high concentration of Co and W promoted greater corrosion resistance with a corrosion current (i_{corr}) of $1.83 \, \mu A \, cm^{-2}$.

Keywords: Co-W coatings; Corrosion; Direct current deposition; Electrodeposition.

1. Introduction

For decades, chromium has been applied as a coating to protect equipment, decorative objects, and ship hulls. However, due to the high toxicity of electrolytes containing hexavalent chromium, and the carcinogenic potential of chromates, the production of these coatings was restricted. To develop new materials capable of coating and maintaining the same properties, tungsten is an option owing to corrosion resistance, high thermal conductivity, and because it is not cancerous. However, the high melting point hinders the application of this metal in conventional processes for the formation of metal alloys, in which the W saturation in the cobalt matrix is low (1 wt.%) [1].

Electrodeposition is an alternative for the formation of an alloy containing W because the association of W with another metal in the iron group promotes beneficial results, such as the Co-W alloy which presents a high corrosion resistance in the saline environment and wear resistance [2, 3]. Electrodeposited metals have more negative corrosion potentials than molten metals, and a higher corrosion current [4].

Regarding the influence of the composition, semi-rigid Co-W alloys exhibited ferromagnetic behavior with ± 2 to 3 at.% W. On the other hand, high tungsten content makes the coatings softer and non-ferromagnetic (~ 30 at.% W) [5]. With the increase of W content, an increase in corrosion resistance is expected. Synthesizing a corrosion-resistant material is relevant from the viewpoint that corrosion determines the useful life of the product and is a deteriorating phenomenon for metals and alloys [6]. The applications of the Co-W alloy are vast and comprise valves, tools, gas turbines, dies, and jet engines [7].

Cobalt has been studied as a component of several metal alloys, such as Ni-Co[8], Ni-Co-W [9], Co-W [10], Zn-Co [11], among others. For Co-W alloys, W is used in the bath in the tungstate form, along with a complexing agent. The pH has a strong influence on the formation of complexes, which are the precursors in the synthesis of the coatings [12]. In addition to pH, other parameters also influence faradaic efficiencies, such as temperature, composition, electrical current density, and mechanical agitation. This allows the evaluation of the operational and chemical parameters of the electrodeposition process, aiming at improving the physical aspects of the formed alloy and the faradaic efficiency.

According to Ibrahim et al. (2003), the increased pH favors an increase in W content as well as the increase of temperature and Co concentration in the electrolyte solution [13]. The

substrate influences adhesion, which can lead to the formation of an intermediate Co layer, when deposited on the copper substrate, which does not occur on the steel substrate [14].

Thus, this study aimed to evaluate the effect of Co and W concentrations on faradaic efficiency, microstructure, and corrosion resistance. The alloys were characterized by scanning electron microscopy (SEM) and X-ray diffraction (XRD). Corrosion resistance was measured by the Tafel extrapolation method and electrochemical impedance spectroscopy (EIS).

2. Material and methods

2.1. Bath composition and electrodeposition assays

A process of cleaning and exposing the metallic area on the copper substrate allowed the activation of the surface. The first stage consisted of sanding with sandpaper with 320 and 400 granulometry. The second stage was the chemical treatment with the immersion of the plate in 10 wt.% NaOH and 1% (v/v) H_2SO_4, lasting 1 min both.

The electrolyte solution was composed of sodium tungstate (Na_2WO_4), from 0.1 to 0.3 M, cobalt sulfate ($CoSO_4$), from 0.1 to 0.3 M, sodium borate ($Na_2B_4O_7 \cdot 10H_2O$), 3.75×10^{-2} M, ammonium citrate ((NH_4)$_2C_6H_6O_7$), 0.3 M, and sodium 1-dodecyl sulfate ($NaC_{12}H_{25}SO_4$), 1×10^{-4} M. The faradaic efficiency (ε), determined according to previous studies [10, 15, 16], was the response for statistical analysis of the influence of the concentrations of Co (C_{Co}) and W (C_W) source. The experiments occurred using a 2^2 factorial design with triplicate in the central point with the C_{Co} level of 0.1 and 0.3 M, and C_W level of 0.1 and 0.3 M.

The electrodeposition tests were carried out with the application of direct electric current, with an electric current density of 50 mA cm^{-2} through a potentiostat/galvanostat VersaStat 3, Princeton Applied Research, and a rotating cathode of 15 rpm with the electrode rotator Princeton Applied Research, AMETEK, Model 616A. The deposition was performed at room temperature (25 °C), two-electrode cell configuration (hollow platinum mesh as a reference and counter electrode) and lasted for 1 h.

2.2. Co-W alloys characterization

The alloy composition, homogeneity, and topography of Co-W deposits were evaluated by SEM model Leo 440i, equipped with EDX LEO Electron Microscopy/Oxford, Cambridge, England model 6070. Physical characteristics such as crystallinity were performed by the XRD Philips Analytical X-Ray diffractometer and X'Pert-MPD model with K-α Cu scanning method, 40 kV voltage, 2θ and speed $0.033°$ s^{-1} with a wavelength of 1.54 Å.

2.3. Electrochemical corrosion tests in a saline environment

The saline environment was composed of 0.1 M NaCl in a 3-electrode cell configuration, with Ag/AgCl as a reference and Pt as a counter electrode. For the Tafel extrapolation method, potentials between ±250 mV were applied around the open circuit potential (OCP) with a scanning speed of 10 mV s^{-1}. For the EIS test, the OCP was applied for one hour with an amplitude of 10 mV and a frequency window of 10^6 Hz to 0.01 Hz.

3. Results and discussion

3.1. Influence of pH and statistical analysis

The pH of the electrolytic bath was determined from chemical speciation diagrams of metals by Hydra and Medusa software. The Co and W diagrams indicated the complex form of Co – Co(cit)$^-$ and W – HW$_6$O$_{21}$$^{5-}$, which were around the pH value equal to 6, the value used for the deposition tests. The complexing agent and the pH value significantly affect the coating properties [17]. Table 1 presents the faradaic efficiency and the weight of the deposit of Co and W. The efficiencies were high, achieving values close to 70%, however, a lower concentration of Co and W provided lower efficiencies such as the value of 31.5%.

Table 1. Faradaic efficiency for the Co-W coatings

Exp.	C_{Co} (M)	C_W (M)	M_{Co} ($\times 10^{-1}$ g)	M_W ($\times 10^{-2}$ g)	ε (%)
1	0.1	0.1	1.01	3.87	31.5
2	0.1	0.3	1.08	5.76	37.2
3	0.3	0.1	2.43	4.38	64.9
4	0.3	0.3	2.38	6.91	69.3
5	0.2	0.2	1.47	6.00	46.6
6	0.2	0.2	1.50	6.13	47.5
7	0.2	0.2	1.55	6.32	49.1

According to a previous study [18], the W concentration in the electrolytic bath influenced faradaic efficiency and the W amount in the deposit. A lower Na_2WO_4 concentration in the electrolytic bath led to high cathodic current efficiencies. On the other hand, the increase of the Na_2WO_4 concentration indicated a decrease in the efficiency and cathodic polarization, resulting in a reduction in the deposition rate and W content in the coating. This behavior occurred for the Na_2WO_4 concentration between 0.027 and 0.041 M, deposited at 5 and 25 µA cm^{-2}. For the present study, the W concentration range did not indicate a reduction in faradaic efficiency with the increase of W concentration. Comparing exp. 1 and 2 the faradaic efficiency increased, as well as when comparing exp. 3 and 4, which demonstrated the influence of the bath composition to obtain high efficiencies.

Statistical analysis in the Statistica 8.0 software considered pure error and a 95% confidence interval. The model presented a regression coefficient (R^2) of 98.3% and only the cobalt concentration influenced significantly. Equation 1 allows calculating the faradaic efficiency.

$$\varepsilon = 49.4 + 32.8\, C_{Co} \tag{1}$$

where C_{Co} is the cobalt concentration (M).

As indicated in Figure 1-a, the increase in the concentration of Co and W favors efficiency values of up to 65%. The linear distribution of the predicted efficiency values compared to the observed values is illustrated in Figure 1-b and indicates the adequacy of the data by Equation 2. Analysis of variance (ANOVA) and F test for $p < 0.05$ demonstrated the significance and prediction of the model.

Figure 1. a) Response countors for the variables C_{Co} and C_W and b) Observed versus predicted faradaic efficiency values.

3.2. Co-W coating morphology

The morphology of the deposit plays an important role in the structural characteristics and material properties. Figure 2-a indicates the presence of cracks, which are not beneficial for allowing the exposure of the substrate to the environment. Cracks occur owing to the high electric current density. A study developed alloys with uniform surfaces when the electric current density was decreased [19]. With the increase of the W concentration (Figure 2-b) the cracks remained, however, the deposit presented rounded shapes, as well as when the Co concentration increased (Figure 2-c). There is a high amount of microcracks, which can lead to the embrittlement of the alloy and compromise its performance as an anticorrosive coating. This network of microcracks is the result of internal stresses generated by high W content and hydrogen evolution during the electrodeposition process [20, 21].

With the increase of both concentrations (Figure 2-d) the rounded structures became more defined and the space between the cracks was reduced. With both concentrations at 0.2 M, the space between cracks is more reduced compared to 0.3 M, as illustrated in Figure 2-e. Electric current density and W content affect structure size [22]. The decrease in grain size promotes high uniformity and quality of the nanoscale coating. Although the electric current density was the same for the entire experiment, the increase in the W concentration decreased the rounded structures, as exp. 2 and 4 with a diameter size of 13.9 and 21.5 µm compared to exp. 3 - 29.2 µm.

Figure 2. SEM micrographs of a) Exp. 1 – C_{Co} - 0.1 M, C_W - 0.1 M; b) Exp. 2 – C_{Co} - 0.1 M, C_W - 0.3 M; c) Exp. 3 – C_{Co} - 0.3 M, C_W - 0.1 M; d) Exp. 4 – C_{Co} - 0.3 M, C_W - 0.3 M; e) Exp. 5 – C_{Co} - 0.2 M, C_W - 0.2 M.

The micrographs with EDX mapping, as illustrated in Figure 3-a, b, c, d, and e indicated the homogeneity of the deposit in terms of the composition distribution. EDX spectrum revealed the Co and W energy peaks in Figure 3-f. According to Figure 3-b and d, the cracks are close to the grain boundary region, which were similar results in other study [23]. The W content quantified by EDX indicated average values of 27.3, 34.1, 15.2, 22.0, and 28.3 wt.%, respectively for exp.1 to 5.Values greater than 40 wt.% of W present a tendency to amorphization, due to the energetically favorable content for the formation of disordered structures [24].

Figure 3. SEM micrographs with EDX mapping of: a) Exp. 1 – C_{Co} - 0.1 M, C_W - 0.1 M, b) Exp. 2 – C_{Co} - 0.1 M, C_W - 0.3 M; c) Exp. 3 – C_{Co} - 0.3 M, C_W - 0.1 M; d) Exp. 4 – C_{Co} - 0.3 M, C_W - 0.3 M; e) Exp. 5 – C_{Co} - 0.2 M, C_W - 0.2 M; f) EDX spectra for Exp. 4 – C_{Co} - 0.3 M, C_W - 0.3 M.

3.3. Crystallinity of Co-W alloy

Figure 4 illustrates the XRD patterns of the alloys from exp.1 to 5, which confirms the amorphous and crystalline structure of the alloy. Crystallinity was more evident in exp. 3 with defined peaks of the structure of Co_2, Co_3W, Co_3W, W and Co_2, with their crystallographic planes (010), (002), (201), (220) and (110) and Co_2, at their respective angles of 41.4, 43.8, 46.4, 64.9, and 75.4°. The Co_2 structure presented a hexagonal crystalline system (JCPDS card nº 01-1616), as well as Co_3W (JCPDS card nº 65-3520), and W was cubic (JCPDS card nº 88-2339). The Co_3W structure is known as a stable intermetallic compound and is generally amorphous and hard [5, 23].

Figure 4. XRD patterns of Co-W alloys.

The increase in Co and W concentration made the alloy amorphous, as exp. 5, as well as the crystallinity was reduced when the W concentration was greater than the Co concentration of 0.1 M (Exp. 2). Although the EDX mapping indicated W contents below 40 wt.%, amorphous alloys were obtained, as exp. 2 and 5. Materials with network disordered have high hardness, low coefficient of thermal expansion, and corrosion resistance. Crystallite size (Cs) of the structures was calculated by Equation 2, known as the Scherrer equation:

$$Cs = {K\lambda}/{\beta\cos\theta} \tag{2}$$
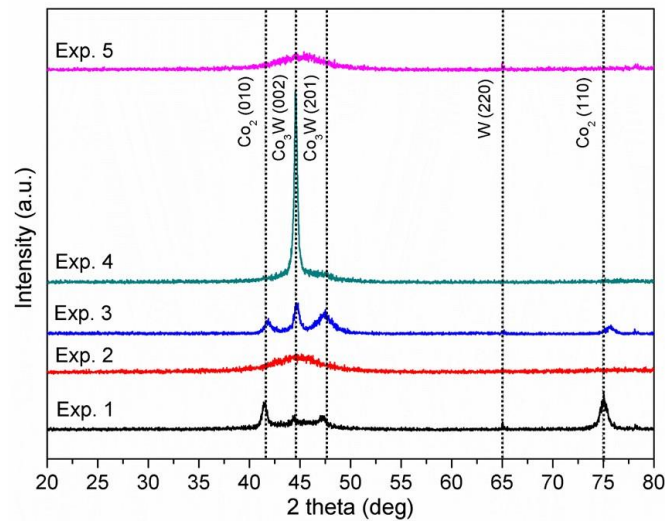
where K is the Scherrer constant (0.91), λ is the wavelength radiation (0.154156 nm), β is the width at half-height of the diffraction (rad) and θ is the Bragg angle (rad).

Crystallite size for the structures Co_2 (010), Co_3W (002), and W (220) in exp. 1 provided values of 6.8, 9.2, and 10.1 nm. The transition from coarse grain size to nanocrystalline occurs in a small composition range between 18 and 22 at.% W [23]. The exp. 1 presented a composition lower than this range (15.2 at.% W), in agreement with the micrograph of Figure 2-a, which did not indicate rounded structures as the others. The thickness of the coating structure can generate varied compositions owing to alkalinization close to the electrode, according to a study that deposited Co-W by a direct current with a value of 10 mA cm² and pH 6.7 [5]. In thick coatings, there is a facility to reduce tungstate, which increases the W content.

3.4. Corrosion assays

The evaluation of the alloy against corrosive environments is relevant to the application of these materials. According to Figure 5, the corrosion resistance is dependent on the composition of the alloy, because the increase in the Co concentration and the same Co and W concentration, both with 0.3 M had a better performance, as shown in the arches of exp. 3, 4 and 5. Besides the decrease in cracks and the spaces between them, exp. 3 and 4 indicated a higher Co content, with 84.3 and 75.9%. Although the experiments presented cracks, larger grains may have prevented the increase in internal stress generated by the reduction of grains and provides reasonable corrosion resistance.

The Nyquist diagrams with capacitive loops indicated a constant time in the electric double-layer capacitance. The loops indicated the formation of the semicircle and the absence of an inductive loop, a phenomenon verified by the corrosion of products. The heterogeneity of the electrode surface, such as the absence of globular structures in exp. 1 generated changes in the ideal capacitive behavior.
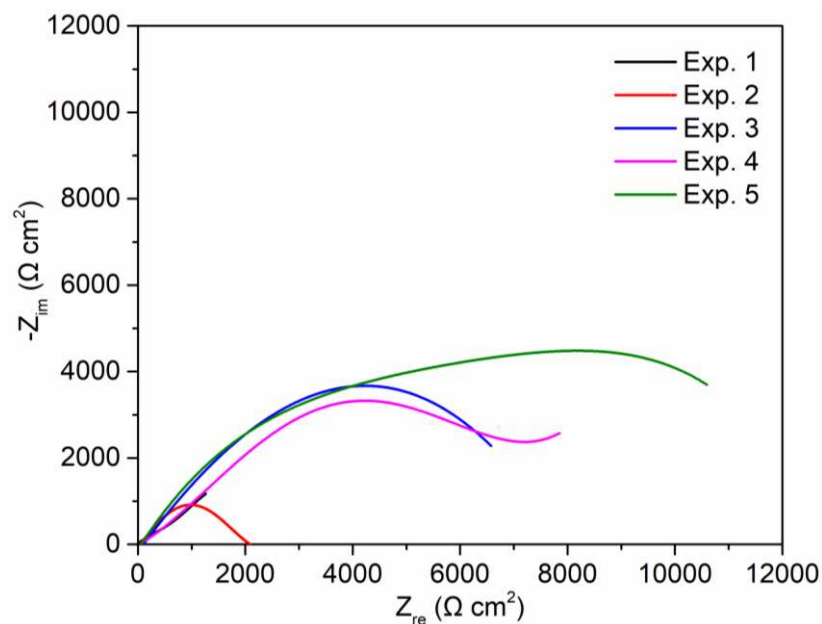
Figure 5. Nyquist diagrams for Co-W alloys in the corrosive medium.

To adjust the data, Randles equivalent circuits indicated except exp. 1, a circuit configuration that included a constant phase element (CPE), with characteristics of an imperfect capacitor, in which related to charge transfer (Q_{ct}), and the fractional power of the frequency

(n), in parallel with the coating resistance (R_{ct}), and in series with the electrolyte resistance (R_e). Exp.1 presented the Warburg impedance element (Z_w) with a value of $2868\ \Omega\ s^{-0.5}$, which relates the semi-infinite linear diffusion of corrosive processes, formed by a rectilinear section with an angle of $45°$ concerning the real axis [25]. In parallel, this circuit presented the double-layer capacitance (C_{dl}) with a value of $6.81\ \mu F\ cm^{-2}$. This characteristic was observed in the anomalous codeposition of W in Fe [26]. The highest R_{ct} value was $528.57\ \Omega\ cm^2$ in the Fe-W alloy with a faradaic efficiency of 11.55% and 69.39% of W content.

The data adjusted by the Spectrum Analyzer software shown in Table 2 indicated for experiments 3, 4, and 5 a greater corrosion resistance, according to the R_{ct} values. Values of n close to 1 indicated the electrode surface is rough, as in exp. 2 with n - 0.88 closest to this morphology.

Table 2. Simulation parameters obtained by Spectrum Analyzer software.

Exp.	R_e (Ω cm²)	R_{ct} (Ω cm²)	Q_{ct} ($\times 10^{-4}\ \Omega^{-1}\ s^n\ cm^{-2}$)
2	49	1805	4.46 (n=0.88)
3	100	11968	4.71 (n=0.69)
4	76	12777	3.47 (n=0.61)
5	66	13008	3.57 (n=0.75)

Tafel slopes of experiments 1 to 5 are illustrated in Figure 5. The main electrochemical parameters extracted from potentiodynamic polarization, such as corrosion current density (i_{corr}), corrosion potential (E_{corr}), anodic and cathodic β, are presented in Table 3. The E_{corr} values less than zero indicated that Co-W coatings are prone to exhibit active dissolution [27]. The i_{corr} values were significantly lower than the copper substrate value ($87.40\ \mu A\ cm^{-2}$) [28], indicating that this coating is capable of protecting copper against corrosion damage.

The change of Co concentration in the electrolytic bath produced a coating with less i_{corr}. The lowest value was obtained in exp. 3 - $1.83\ \mu A\ cm^{-2}$, with a concentration of Co - 0.3 M, W - 0.1 M and an electrical current density of $50\ mA\ cm^{-2}$, demonstrating to be superior to a previous study that deposited Co-W with an electric current density of $10\ mA\ cm^{-2}$ and

obtained i_{corr} of 1.96 µA cm^{-2} [29]. This result presented great performance, mainly owing to the high faradaic efficiency (64.9%).
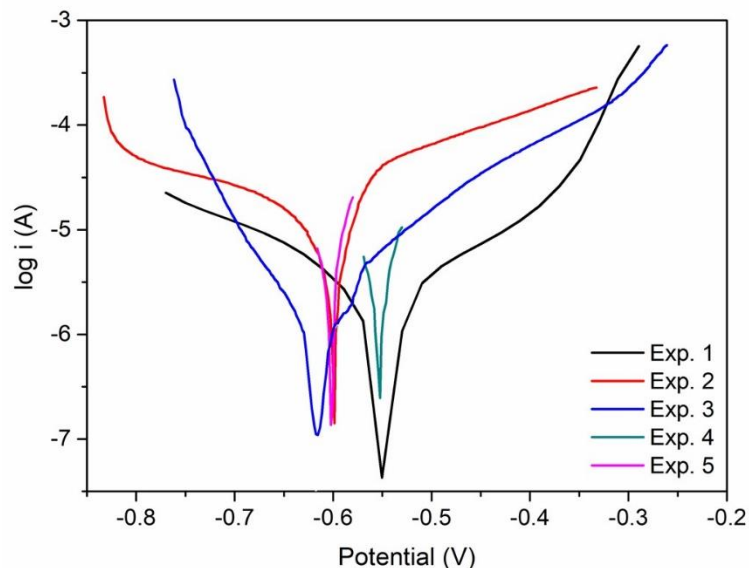
Figure 6. Tafel slopes for Co-W alloys in corrosive medium with 0.1 M NaCl.

Table 3. Results of the corrosion current and polarization resistance by Tafel extrapolation in a corrosive medium for Co-W alloys.

Experiment	$-E_{corr}$ (V)	i_{corr} (µA cm^{-2})	R_p (Ω cm^2)	β_{anodic} (mV)	$\beta_{cathodic}$ (mV)
1	0.549	3.87	15207	257	286
2	0.600	8.15	2229	60	153
3	0.616	1.83	13498	146	93
4	0.613	2.68	12571	157	153
5	0.668	3.55	11234	174	194

4. Conclusions

Co-W metal alloys were deposited by applying a direct electric current from an electrolytic bath containing citrate as a complexing agent. By statistical analysis, Co concentration significantly affected the faradaic efficiency, which obtained a value of 69.3% with the concentration of Co and W at 0.3 M. Micrographs of deposits with low concentrations of Co and W, at 0.1 M did not indicate rounded structures with grain outline. Amorphous alloys were obtained with increasing W content, and peaks of the Co$_3$W structure. According to the

Nyquist diagrams, the increase of the Co, or Co and W concentration, provided defined arches, indicating better performance. The adjusted EIS data were compatible with the experimental values since the lowest R_p was 2229 Ω cm^2 for the exp. 2, and for the R_f value.

Acknowledgments

References

[1] S.M.S.I. Dulal, C.B. Shin, J.Y. Sung, C.-K. Kim, Electrodeposition of CoWP film II. Effect of electrolyte concentration, Journal of Applied Electrochemistry, 38 (2008) 83-91.

[2] Y.S. Yapontseva, A.I. Dikusar, V.S. Kyblanovskii, Study of the composition, corrosion, and catalytic properties of Co-W alloys electrodeposited from a citrate pyrophosphate electrolyte, Surface Engineering and Applied Electrochemistry, 50 (2014) 330-336.

[3] H. Capel, P.H. Shipway, S.J. Harris, Sliding wear behaviour of electrodeposited cobalt–tungsten and cobalt–tungsten–iron alloys, Wear, 255 (2003) 917-923.

[4] J. Sinkeviciute, Corrosion study of electrodeposited W and Mo alloys with iron group metals, in, University of Vilnius, Lithuania, 2009, pp. 112.

[5] N. Tsyntsaru, H. Cesiulis, E. Pellicer, J.P. Celis, J. Sort, Structural, magnetic, and mechanical properties of electrodeposited cobalt–tungsten alloys: Intrinsic and extrinsic interdependencies, Electrochimica Acta, 104 (2013) 94-103.

[6] E. Vernickaite, N. Tsyntsaru, H. Cesiulis, Electrochemical co-deposition of tungsten with cobalt and copper: Peculiarities of binary and ternary alloys coatings formation, Surface and Coatings Technology, 307 (2016) 1341-1349.

[7] S.M. Mayanna, L. Ramesh, B.N. Maruthi, D. Landolt, AES investigation of electrochemically deposited Co--W layers on copper, Journal of Materials Science Letters, 16 (1997) 1305-1306.

[8] W. Li, J. Hao, S. Mu, W. Liu, Electrochemical behavior and electrodeposition of Ni-Co alloy from choline chloride-ethylene glycol deep eutectic solvent, Applied Surface Science, 507 (2020) 144889.

[9] D.G. Portela, M.B. Porto, A.F. de Almeida Neto, Parameters variation on Ni–Co–W coating electroplating to evaluate improvements in morphology and corrosion resistance, Journal of the Brazilian Society of Mechanical Sciences and Engineering, 41 (2019) 574.

[10] J.M. Costa, T.C. de Morais Nepel, A.F. de Almeida Neto, Influence of current density and W concentration on Co–W alloys used as catalysts in electrodes for Li–O_2 batteries, Chemical Papers, 73 (2019) 1103-1112.

[11] J.M. Costa, A.F. de Almeida Neto, Zn-Co electrocatalysts in lithium-O_2 batteries: temperature and rotating cathode effects on the electrodeposition, Journal of Solid State Electrochemistry, 23 (2019) 2533-2540.

[12] A.I. Shul'man, S.S. Belevskii, S.P. Yushchenko, A.I. Dikusar, Role of complexation in forming composition of Co-W coatings electrodeposited from gluconate electrolyte, Surface Engineering and Applied Electrochemistry, 50 (2014) 9-17.

[13] M.A.M. Ibrahim, S.S.A. El Rehim, S.O. Moussa, Electrodeposition of noncrystalline cobalt–tungsten alloys from citrate electrolytes, Journal of Applied Electrochemistry, 33 (2003) 627-633.

[14] M. Donten, T. Gromulski, Z. Stojek, The interface between metallic substrates and layers of electrodeposited Co–W amorphous alloys, Journal of Alloys and Compounds, 279 (1998) 272-278.

[15] J.M. Costa, M.S. Hori, A.F. de Almeida Neto, Effects of the forced convection and current density on the electrodeposition of Zn-Fe-Mo alloys, Chemical Physics, 527 (2019) 110502.

[16] M.B. Porto, L.B. Alvim, A.F. de Almeida Neto, Nickel removal from wastewater by induced co-deposition using tungsten to formation of metallic alloys, Journal of Cleaner Production, 142 (2017) 3293-3299.

[17] F. Su, C. Liu, P. Huang, Establishing relationships between electrodeposition techniques, microstructure and properties of nanocrystalline Co–W alloy coatings, Journal of Alloys and Compounds, 557 (2013) 228-238.

[18] Z. Abdel Hamid, Electrodeposition of cobalt–tungsten alloys from acidic bath containing cationic surfactants, Materials Letters, 57 (2003) 2558-2564.

[19] Z. Ghaferi, S. Sharafi, M.E. Bahrololoom, Effect of current density and bath composition on crystalline structure and magnetic properties of electrodeposited FeCoW alloy, Applied Surface Science, 355 (2015) 766-773.

[20] Z. Ghaferi, K. Raeissi, M.A. Golozar, H. Edris, Characterization of nanocrystalline Co–W coatings on Cu substrate, electrodeposited from a citrate-ammonia bath, Surface and Coatings Technology, 206 (2011) 497-505.

[21] P. Bera, H. Seenivasan, K.S. Rajam, V.K. William Grips, XRD, FESEM and XPS studies on heat treated Co–W electrodeposits, Materials Letters, 76 (2012) 103-105.

[22] N. Tsyntsaru, Electrodeposition of cobalt–tungsten alloys and their application for surface engineering, Russian Journal of Electrochemistry, 52 (2016) 1041-1047.

[23] N. Tsyntsaru, H. Cesiulis, A. Budreika, X. Ye, R. Juskenas, J.P. Celis, The effect of electrodeposition conditions and post-annealing on nanostructure of Co–W coatings, Surface and Coatings Technology, 206 (2012) 4262-4269.

[24] A. Singh, N. Iyer, S.P. Harimkar, Prediction of glass forming ability and glass forming range for electrodeposited binary Co-W alloys, Journal of Applied Physics, 111 (2012) 103508.

[25] E. McCafferty, Validation of corrosion rates measured by the Tafel extrapolation method, Corrosion Science, 47 (2005) 3202-3215.

[26] M.B. Porto, V.d.L. Bellia, T.C.d.M. Nepel, F.L. Moreira, A.F.d.A. Neto, The influence of anomalous codeposition on few coating alloys properties, Journal of Materials Research and Technology, 8 (2019) 4547-4555.

[27] H.D. Mejía V, A.M. Echavarría, J.A. Calderón, G. Bejarano G, Microstructural and electrochemical properties of TiAlN(Ag,Cu) nanocomposite coatings for medical applications deposited by dc magnetron sputtering, Journal of Alloys and Compounds, 828 (2020) 154396.

[28] X. Zhang, Q. Qian, L. Qiang, B. Zhang, J. Zhang, Comparison study of gold coatings prepared by traditional and modified galvanic replacement deposition for corrosion prevention of copper, Microelectronics Reliability, 110 (2020) 113695.

[29] M.B. Porto, D.G. Portela, A.F. de Almeida Neto, Temperature, current density and cobalt concentration effects on electrodeposited anticorrosive cobalt-tungsten alloys using factorial experiment design and ANOVA techniques, Transactions of the IMF, 97 (2019) 305-311.

APPENDIX E

Ultrasound-assisted electrodeposition and synthesis of alloys and composite materials: A review

Ultrasound-assisted electrodeposition and synthesis of alloys and composite materials: A review

Josiel Martins Costa and Ambrósio Florêncio de Almeida Neto

Abstract

The development of electrodeposited materials with improved technological properties has been attracting the attention of researchers and companies from different industrial sectors. Many studies have demonstrated that the electrodeposition and synthesis of alloys and composite materials assisted by ultrasound may promote the de-agglomeration of particles in the electrolytic solution due to microturbulence, microjets, shock waves, and breaking of Van der Waals forces. The sonoelectrochemical technique, in which the ultrasound probe acts as a working electrode, also has been used for the formation of nanostructures in greater quantity, in addition to accelerating the electrolysis process and eliminating the reaction products on the electrode surface. Regarding the morphological aspects, the acoustic cavitation promotes the formation of smooth and uniform surfaces with incorporated particles homogeneously distributed. These changes have a direct impact on the composition and physical properties of the material, such as corrosion resistance, magnetization, wear, and microhardness. Despite the widespread use of acoustic cavitation in the synthesis of nanostructured materials, the discussion of how process variables such as acoustic power, frequency, and type of ultrasound device, as well as their effects still are scarce. In this sense, this review discusses the influence of ultrasound technology on obtaining electrodeposited coatings. The trends and challenges in this research field were reviewed from 2014 to 2019. Moreover, the effects of process variables in electrodeposition and how these ones change the technological properties of these materials were evaluated.

Keywords: Acoustic cavitation; Coatings; Electrodeposition process; Metallic materials; Particles.

1. Introduction

The electrodeposited coatings include nanostructured materials, with multilayer, and ceramic particles in the metallic, or polymeric matrix. The matrix is usually composed of metal, alloy, ceramic, or polymer, while the particles may have a spheroidal, layered, plate-like, or core-coated shape, with a size order from sub-millimeters to nanometers [1]. These composite coatings are anticorrosive, wear-resistant, hydrophobicity, and have a good tribological performance that make them applicable in the manufacturing process of many industrial sectors [2]. Recent studies have demonstrated the diverse applications of the composite materials [3-8], as illustrated in Figure 1. The development of nanometer-scale composites with different morphological structures, composition, and size distribution, can be obtained through the application of acoustic cavitation originated by ultrasound treatment.
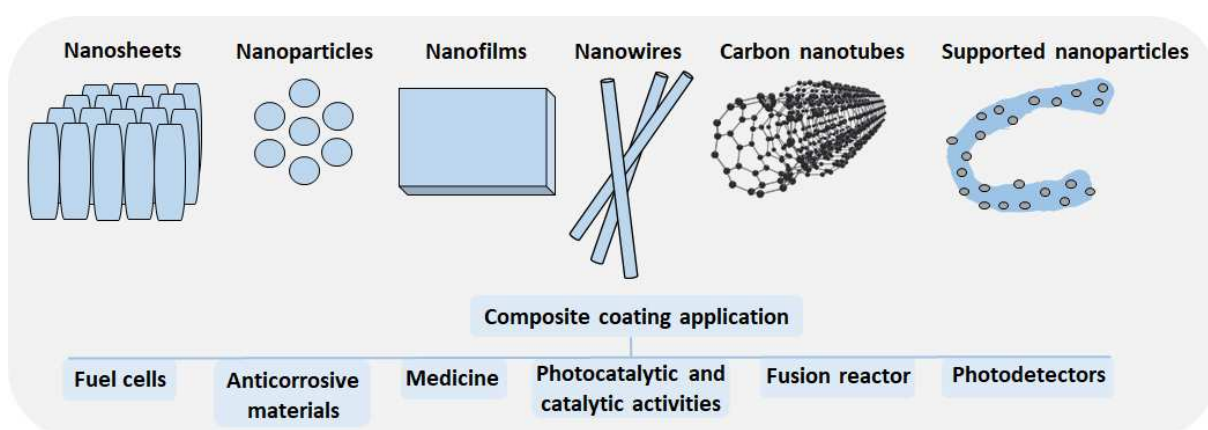
Figure 1. Applications of composite materials and their nanostructures that may be produced using ultrasound technology.

Galvanized coatings can significantly improve their physical properties such as hardness, resistance to wear and corrosion when the particles are dispersed in the solution [9]. Promising novel coatings have been developed in last years. Some studies have sought to focus on different operational parameters during the electrodeposition process to increase the concentration of particles in the coating [10]. However, process parameters such as the increase in particle concentration in the electrolytic bath and decrease in the concentration of electroactive species were discarded due to instability of the dispersion at high concentrations of particles and problems related to mass transport affected by reduced conductivity of the

solution [11]. The agglomeration of particles leads to an increase in the sedimentation rate, impairing thermophysical properties, such as viscosity and thermal conductivity, and pressure drop [12].

The use of ultrasound technology has shown high potential for this purpose, since it can prevent particle agglomeration, promoting uniform surfaces with higher particle content [13]. Also, the use of ultrasound during the electrodeposition leads to the size reduction of porous structures through the hydrogen absorption in the deposit, as well as the formation of a homogeneous microstructure, composed of fine and crystalline granules, with uniform distribution. Ultrasonic waves can play a relevant role in the orientation of crystals and stability related to adhesion between the film and the substrate [14]. This emerging technology has been applied in the fabrication of materials for drug delivery [15], scaffolds for gingival cells growth [16]; environmental process of wastewater treatment [17]; food sector, for the extraction of compounds [18] and dairy products processing [19], and in the gas production, such as H_2 [20].

During the process, acoustic waves are propagated in the liquid medium, causing the vibrational movement of compression and expansion of the molecular structure. Therefore, the distance between the molecules varies according to the oscillation. If this vibrational intensity reaches the state in which the molecular structure becomes unstable, the formation of bubbles occurs, generating the acoustic cavitation phenomenon [21]. Thus, the application of ultrasound in liquid media can alter physical and chemical aspects through the generation of turbulent convection and temperature increase due to the formation and subsequent collapse of bubbles [22]. These changes decrease the thickness of the diffusion layer and improve the mass transport, degassing the electrode surface, and promoting an increase in the reaction rate and generation of hydroxyl radicals [23]. The basic forms of emitting ultrasonic waves and promoting changes in the material can occur directly by converting mechanical energy into acoustic from the transducer to the probe, inducing vibrations in the material; and indirectly, through the cavitation induced in the liquid medium, by the propagation of acoustic waves [24]. However, the influence of ultrasound process parameters on the electrodeposition of composites and metal alloys was poorly studied and requires further studies. In this context, this review presents trends in the application of ultrasound technology in the electrodeposition of metallic coatings and how this emerging technology could improve the technological properties of these materials.

2. Fundamentals of ultrasound technology

The phenomenon of acoustic cavitation occurs due to the propagation of ultrasonic waves in the liquid medium, increasing its pressure and temperature, as shown in Figure 2. Gaseous nuclei in the liquid initiate the cavitation bubbles, which are subsequently enlarged and expanded until a consequent rupture, generating waves of shocks, microturbulence, and microjets [25]. Physical forces such as vibration, rise of experimental temperature from 2000 to 10,000 K, and agitation are generated by acoustic cavitation. In addition, reactive radicals can be formed from cavitation bubbles [26].
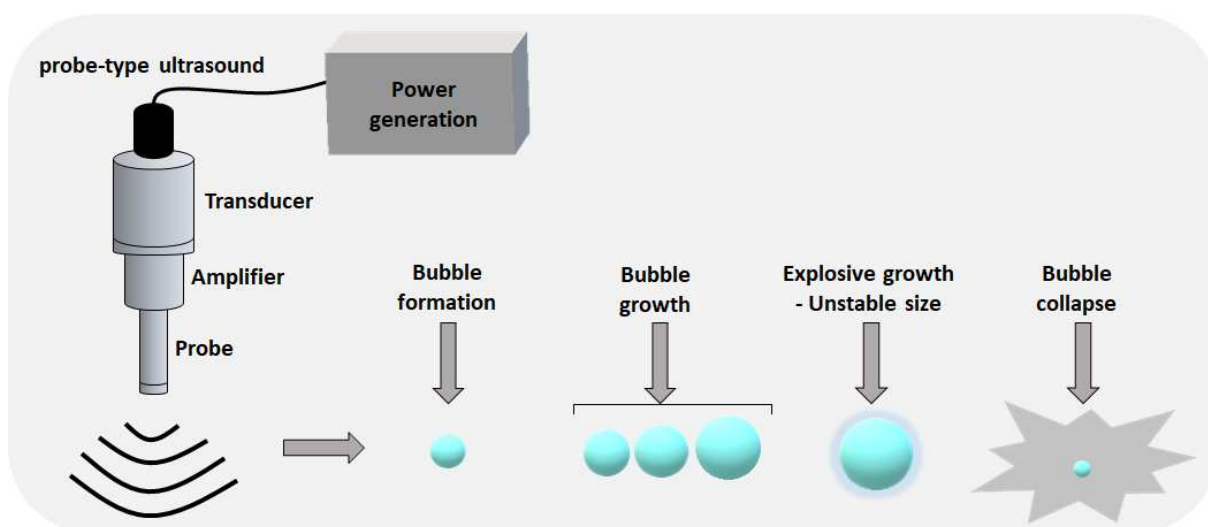
Figure 2. Summary of bubble implosion under ultrasonic conditions.

The frequency range of the ultrasound can be divided into two classifications. High frequency (100 kHz - 1 MHz) applies an intensity level of 1 W cm^{-2}. Low frequency (16 - 100 kHz) intensity levels from 10 to 1000 W cm^{-2} are applied [27]. These frequencies determine the interaction with matter, conferring physical and chemical changes caused by fluctuation of pressure, growth, and collapse of bubbles. The ultrasonic device shown in Figure 2 used during the electrodeposition process consists of a power generator, a transducer, an amplifier, and an ultrasonic probe [28]. The generator supplies high-frequency electrical energy, which is converted into mechanical vibrations by the transducer. These vibrations are amplified in the amplifier and propagated by the probe in the form of acoustic waves into the liquid medium [29].

Another acoustic wave propagating device is the bath ultrasound, which differs from the probe-type ultrasound in terms of efficiency and process capacity. In bath ultrasound, cavitation is propagated uncontrolled in the liquid medium, presenting low intensity and uneven spreading. Probe-type ultrasound provides intense effects, with the homogeneous and reproducible distribution. For application in particle dispersion, sonication by the probe is indicated, due to differences in power density, which for the ultrasonic bath reaches a value of 40 W L^{-1} and for the probe-type - 20000 W L^{-1} [12].

3. Use of ultrasound in electrodeposition process

Ultrasonic waves in a liquid medium promote the acoustic cavitation, in which the mechanical wave is propagated in cycles that generate positive and negative pressure. High energy promotes the formation of bubbles during negative pressure cycles. When the microbubble reaches a critical size, it collapses and ruptures [30]. This point is known as a hot spot, which can reach high pressures and temperatures. The events arising from this formation of bubbles are the basis for the application of ultrasound technology in the most diverse industrial sectors, such as food [31, 32], chemical [33, 34], electrochemical [13, 35], among others.

Walker and Walker [36] found when testing different operating conditions that the effect of acoustic cavitation on the deposited coating depends on the metal, electrochemical parameters, and the acoustic fields. Ultrasound promotes the removal of hydrogen bubbles and oxide films, protecting locations for electrodeposition, with a consequent increase in cathodic efficiency. The porosity is improved due to the collapse of the hydrogen bubbles and the acoustic flow on the electrode surface. The hardness and luster of the coatings, in general, increase due to ultrasonic agitation, while the porosity decreases.

In recent years, many research groups have studied the effect of sonication and the dispersion of particles in electrolytic baths for the dissolution of metallic coatings, nanocomposites, films, and nanosheets. Table 1 presents the effects of the ultrasound on the coating properties, as well as the bath composition, and the ultrasound parameters. Ni compounds and their alloys have been highlighted in the last six years and the absence of surfactant in the bath demonstrates the ability of ultrasound to promote the dispersion of particles.

As shown in Table 1, the use of ultrasound can promote specific characteristics depending on the material. Ni and Ni-Mo coatings deposited under different ultrasound intensities (20, 30, and 40 W cm^{-2}) evidenced the non-dependence of ultrasound for the Ni coating [37]. For the Ni-Mo coating, the ultrasound impacted the deposition kinetics, increasing the Mo content from 14.5 Mo wt% without ultrasound to 19.5 Mo wt% with an ultrasound intensity of 40 W cm^{-2}. The increase in the ultrasound intensity led to a gradual increase in microhardness from 720 to 820 HV in Ni-Mo alloys. The introduction of Mo modified and reduced the grain size in the Ni. The greatest hardness was related to the mechanical action generated by the acoustic cavitation close to the cathode in the deposition process [38].

Table 1. Summary of deposited materials prepared with ultrasound.

Deposited material	Electrolyte composition	Process variables	Effects on the technological properties of the material	Reference
Ni-Co alloy	Cobalt sulfate, nickel sulfate, ascorbic acid, sulfanilic acid, and glycerol	- System: probe - Frequency: 20 kHz - Power intensity: 0.6, 0.9 and 1.2 W cm^{-2}	- Corrosion resistance was improved by inducing the effect of ultrasound parallel to electrodeposition.	[24]
Ni and Ni-Mo alloy	Nickel sulfate, sodium citrate (Ni coating), and sodium tungstate (Ni-Mo coating)	- System: probe - Frequency: N/A - Power intensity: 20, 30 and 40 W cm^{-2}	- Ultrasound promoted an increase in the Mo content, refinement of the structure, and an increase in the hardness of the coating from 720 to 820 HV.	[37]
Ni-W/ZrO$_2$ nanocomposites	Nickel sulfate, sodium tungstate, sodium citrate, and sodium chloride	- System: bath - Frequency: 35 and 130 kHz - Power: N/A	- Ultrasound operating at 35 kHz promoted the incorporation of ZrO$_2$ particles in the coating, which resulted in a smooth surface with a homogeneous and compact microstructure.	[39]
Cu$_3$Se$_2$ nanosheets	Sodium selenite and copper chloride	- System: probe - Frequency: 20 kHz - Nominal power: 20 W	- Ultrasound increased the crystallites size, decreased the thickness of the thin film composed of nanoparticles, and improved the packaging and compressive stress of the nanosheets.	[40]
Co–W/MWCNTs nanocomposite	Cobalt sulfate, sodium tungstate, boric acid, sodium sulfate, sodium citrate, sodium dodecylbenzenesulfonate, and saccharin	- System: N/A - Frequency: 20 kHz - Nominal power: 200, 400 and 500 W	- Ultrasonic agitation was more favorable than mechanical agitation due to the homogeneous incorporation of MWCNTs in the layer and on the surface of the coatings. The composite showed greater hardness, resistance to wear, and reduced friction, in addition to a smoother surface.	[41]
Ni-Cu/TiN composite	Nickel sulfate, copper sulfate, boric acid, titanium nitride, sodium lauryl sulfate, and saccharin	- System: bath - Frequency: 40 kHz - Power intensity: from 0 to 12 W cm^{-2}	- Ultrasound improved anti-corrosive performance.	[42]

Ni-doped TiN coating	Nickel amido sulfate, nickel chloride, boric acid, titanium nitride nanoparticles, and sodium dodecyl sulfate	- System: N/A - Frequency: 42 kHz - Power intensity: 0, 20 and 40 W cm^{-2}	- Modulus and microhardness of Young increased when the ultrasound power changed from 0 to 20 W cm^{-2}, however it decreased when the ultrasound intensity increased from 20 to 40 W cm^{-2}. - Moderate values of ultrasonic intensity induced the homogeneous dispersion of TiN in the coating, which increases the hardness of the material.	[43]
Cu-Ni films	Copper sulfate, nickel sulfate, and boric acid	- System: probe - Frequency: 20 kHz - Power: N/A	- Ultrasound promoted an increase in hardness in the films, even with a large amount of Cu in the material. The increase in hardness resulted from the refinement of the crystallite size provided by ultrasound.	[44]
Zn and Zn-TiO$_2$ coatings	Zinc chloride, potassium chloride, boric acid, and TiO$_2$ powder	- System: bath - Frequency: 38 kHz - Nominal power: 200 W	- Ultrasound combined with high-speed deposition provided a batter particle incorporation and distribution, besides the improvement of the hardness.	[45]
Ni-B/TiC composite	Nickel sulfate, nickel chloride, dimethylamine borane, saccharine, sodium dodecyl sulfate, and TiC particles	- System: bath - Frequency: 40 kHz - Power intensity: from 0 to 12 W cm^{-2}	Ultrasound reduced the agglomeration generated by the cavitation dispersion. The morphology showed a lateral migration of the grains due to ultrasonic waves. As a result, the structure had a refined appearance with reduced gaps.	[46]
Ni/graphene oxide	Nickel sulfamate, nickel chloride, boric acid, and sodium dodecyl sulfate	- System: bath - Frequency: 40 kHz - Power: 50 W	Ultrasound increased 1.8 times in the hardness of Ni/graphene oxide, the refinement of grains, and the quality of the coating surface.	[47]
Zn-Ni-Al$_2$O$_3$ nanocomposites	Zinc chloride, nickel chloride, boric acid, potassium chloride, ammonium chloride, sodium dodecyl sulfate, and Al$_2$O$_3$-α particles	- System: horn - Frequency: N/A - Nominal power: 30, 90 and 150 W	- Low ultrasonic power combined with high current density (16-17 A dm^{-2}) and lower pulse frequency increase the alumina content in composite coatings.	[48]

Cu-Sn alloy	Copper sulfate pentahydrate, tin sulfate, ammonium oxalate, sodium acetate, sodium acetate, gelatin, and methylene blue	- System: probe - Frequency: 26 kHz - Power density: 0.008, 0.016, 0.032 and 0.040 W cm^{-3}	- Increasing the ultrasound intensity from 0.008 to 0.040 W cm^{-3}, the mass transfer was intensified and the deposition rate increased from 2 to 8 times.	[49]
Pt-Pd alloy nanoparticles on reduced graphene oxide	Sodium chloride, chloroplatinic acid, and palladium chloride	- System: N/A - Frequency: N/A - Power: N/A	- Minimizing of the nanoparticles size. - Electrode surface cleaning and radical formation. -High loading and uniform distribution.	[50]
SnS thin films	Tin chloride and sodium thiosulfate	- System: probe - Frequency: 20 kHz - Power: N/A	- The smaller grain size of SnS orthorhombic polycrystalline structures. - Thin plans with vertical growth and increased conversion efficiency of solar cells, improving the photovoltaic property.	[51]
Fe-nano ZrO$_2$ coating	Iron chloride, sodium chloride, boric acid, sodium lauryl sulfate, and ZrO$_2$ nanoparticles	- System: N/A - Frequency: N/A - Nominal power: 120, 180, 240 and 300 W	The parameters with the nominal power of 180 W, ZrO$_2$ concentration of 10 g L^{-1}, current density of 4 A dm^{-2}, and duty cycle of 20% promoted a coating with 5.5 wt% of nanoparticles.	[52]
NiCrTiO$_2$ alloy	Nickel sulfate, potassium dichromate, and TiO$_2$ nanoparticle	- System: probe - Frequency: 32 kHz - Power: N/A	- Ultrasonic waves refined the grain size and improved the quality of the coating, avoiding the reduction of Cr ions in precipitates composed of chromium oxides and hydroxides.	[53]
Ni-SiC nanocomposites	Nickel sulfate, nickel chloride, boric acid, and SiC nanoparticles	- System: probe - Frequency: 30 kHz - Nominal power: 300 W	- Ultrasound improved the concentration of metal ions in the solution and the microhardness.	[54]

3.1. Sonoelectrochemical method

The direct participation of the ultrasonic probe in electrolysis is known as the sonoelectrochemical process. The ultrasound probe is used as a vibrating working electrode, in a three-electrode cell configuration [55]. The cell is composed of a reference electrode and a counter electrode that is placed close to the vibrating working electrode, as illustrated in Figure 3. In the production of metallic nanoparticles, only the flat circular area of the probe is exposed to the electrolytic bath. This area acts as a cathode and ultrasonic source. The reduction of metal ions occurs at the cathode and after the explosion generated by ultrasound, the metal nanoparticles are removed, the surface is cleaned and then the double layer is replenished with metal ions [56]. Thus, by controlling process parameters such as processing time, acoustic power, and electrolysis current, physical properties such as particle size distribution and morphology can be changed.
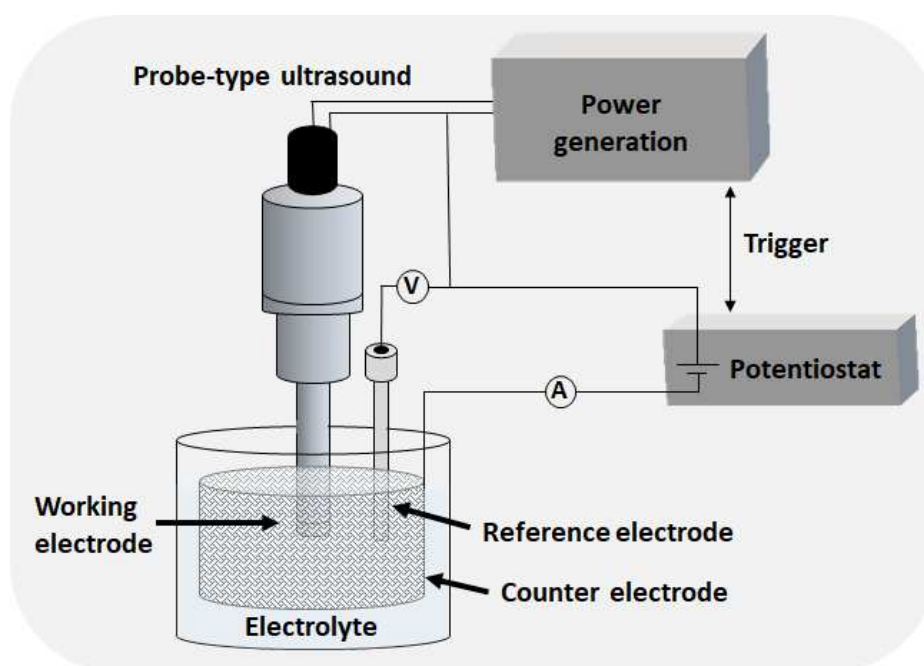
Figure 3. Schematic configuration of the sonoelectrochemical process. Adapted from Zin, Pollet and Dabalà [57], with permission from Elsevier.

The application of sonoelectrochemistry allows high yields compared to conventional processes that apply constant current and depends on the concentration of salts in the solution [58-60]. Pt nanoparticles were produced in the presence of the Ti electrode as a

cathode and ultrasonic probe with a frequency of 20 kHz [57]. Ultrasonic pulses after short pulses of current produced nanoparticles from 11 to 15 nm. Acoustic cavitation allowed the production of Pt nanoparticles with high purity, homogeneous crystallite size, and controlled structure. Ag nanoparticles were also deposited by the sonoelectrochemical method [61]. They presented spherical, nanorods, and nanostructured dendrites shapes. The sonication time and the concentrations of silver nitrate and nitrilotriacetate were crucial for the shape of the Ag nanoparticles.

In the sonoelectrodeposition process, the increase in electrochemical current and changes in voltammetric curves determine whether the acoustic cavitation has improved mass transfer in the system [62]. Cavitation close to the electrode surface generates a rupture of bubbles resulting in corrosion and the formation of a new surface, verified by the increased current pulses. Turbulence, microjets, and shock waves together decrease the diffusion layer (δ), as shown in Figure 4, just as microjets are the most efficient effect for removing absorbed material and have the ability to passivate the material, due to the high pressure on the electrode surface [63]. The mass transport model at the electrode interface is composed of a laminar sublayer and a concentration gradient adjacent to the electrode. The occurrence of acoustic cavitation promotes the transfer of energy to the molecules [64].
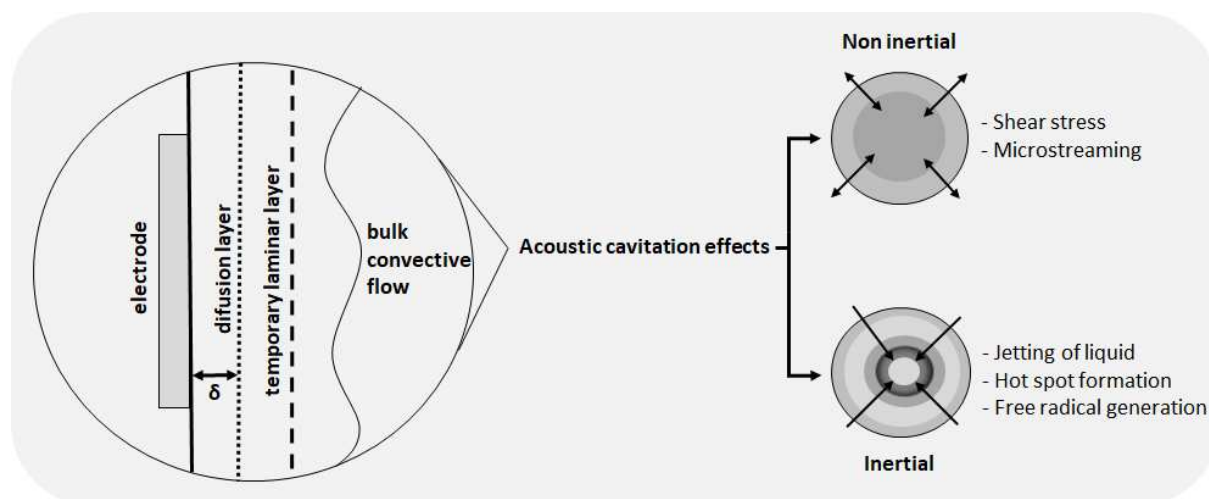
Figure 4. Diffusion layer at the solution-electrode interface and effects of acoustic cavitation.

The pulsed sonoelectrochemistry technique consists of the application of a current or potential pulse to the cathode with cation reduction, with the deposition of metallic nuclei occurring and with the titanium probe acting as an electrode in this period (T_{on}) [65]. After the

T_{on}, a short ultrasound pulse occurs, capable of removing the metallic particles from the surface and replenishing the double layer of metallic cations, with simultaneous agitation. A rest time (T_{off}) can be applied to promote the restoration of the initial conditions of the electrode.

CuO nanostructures were deposited without ultrasound and by the sonoelectrochemical technique [66]. The sonoelectrodeposition eliminated the products of the electrochemical reaction and accelerated the electrolysis process, producing 4.2 times more CuO nanostructures. Moreover, it can improve properties such as magnetization, according to the study by Hajnorouzi and Modaresi [67], which synthesized Fe_3O_4 nanoparticles by the direct sonoelectrochemical method and without ultrasound. The ultrasonic probe increased the saturation magnetization by 24.9% at high current density compared to the conventional method. The deposition rate increased up to 15 times without changing the purity and crystallinity of the nanoparticles.

3.2. Effects of ultrasound on the particles dispersion

Ultrasound technology is widely applied in the dispersion of particles due to de-agglomeration promoted in the suspension system. In addition to the use of ultrasound during the electrodeposition process to improve certain properties, ultrasonic irradiation as the step before the dispersed deposition of particles and can also promote the total dissolution of compounds in the electrolytic bath. This de-agglomeration and dispersion of particles are due to microturbulences that generate oscillating acoustic pressure and cavitation, in addition to the breakdown of Van der Waals forces by the collision of particles induced by acoustic streaming, microjetting and shock waves [68]. Compared with conventional magnetic stirring deposition, ultrasound optimizes and accelerates the dispersion of particles by increasing mass transport, impacting coatings with greater hardness, and better tribological performance [69, 70]. However, although acoustic cavitation improves the dispersion of particles in the solution, it may not be sufficient to promote de-agglomeration in certain cases [71].

Several studies [72-74] have obtained galvanized coatings with dispersed incorporated particles and distributed homogeneously with the use of ultrasound. Composite Ni-B/Ti-C coatings were synthesized by ultrasound-assisted deposition to improve their microstructure and electrochemical properties [46]. Analyzes by atomic force microscopy identified protrusions and nodular pits dispersed in the coating. These protrusions and pits

occurred due to particle agglomeration and preferential adsorption of metal ions in "tip" locations and reduced to metal, forming protuberances. Moreover, the formation of acoustic cavitation by ultrasound decreased the agglomeration and the size of the protrusions. The average and square root roughness size indicated smooth and compact coatings. Ni-B grains, which more than 90% had a dimension less than 220 nm, involved TiC nanoparticles.

3.3. Effects of ultrasound on the morphology and microstructure

The microstructure and morphology of the deposited coating are also affected by the use of ultrasound in the electrodeposition process. Many studies have reported the application of ultrasound technology as a solution to provide smooth surfaces due to uniform particle distribution and refinement in grain size [39, 44, 69, 75]. Acoustic cavitation, microjets, and acoustic streaming generated by ultrasound prevent the formation of microspheres and lead to the production of semi-microspherical nanoparticles, with an application as sites for electron transfer [76]. Co-W/MWCNTs nanocomposite was deposited by applying mechanical and ultrasonic agitation [41]. The Co-W coating produced under mechanical agitation indicated nodules ranging in size from 5 to 10 µm. Co-W/MWCNTs nanocomposite had a rough surface with uneven Co-W grains and MWCNT clusters. Under acoustic cavitation conditions, the nanocomposite surface had a more uniform appearance with nodules ranging in size from 5 to 25 µm. However, the increase in ultrasonic power has made the nodular size uneven. According to Figure 5-a, mechanical agitation led to the formation of dispersed and agglomerated carbon nanotubes. With the use of ultrasound, a uniform distribution of MWCNTs occurred in the coating (Figure 5-b-d). Increasing the nominal power from 200 to 400 W, the microstructure of the nanocomposite surface obtained was more homogeneous (Figure 5-c). However, for the nominal power of 500 W, the nanoparticles incorporated in the matrix have become inconsistent, resulting in the detachment of the material and emphasizing that there is ideal nominal power for the system.
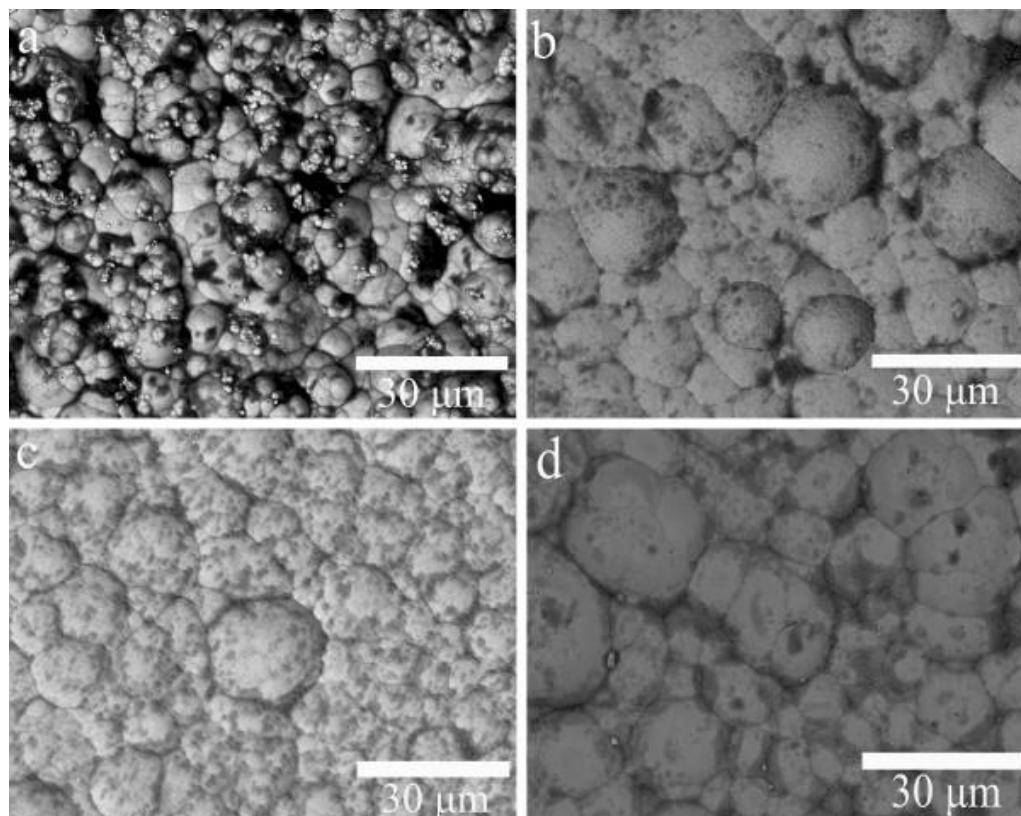
Figure 5. Backscattered SEM images of Co–W/MWCNTs composite under several process conditions: a) mechanical agitation; b) 200 W; c) 400 W); and d) 500 W.

Bismuth sulfide films were synthesized by conventional electrodeposition and sonoelectrodeposition [76]. XRD diffractograms identified the orthorhombic phase of Bi_2S_3 without impurities. The electrodeposition treatment without ultrasound showed less intense peaks compared to the film obtained with a 30% amplitude of the ultrasound, which indicated that the acoustic cavitation led to the growth of Bi_2S_3 crystalline plates. The opposite result occurred in the ultrasound-assisted electrodeposition of TiO_2 nanotubes containing calcium phosphate [77]. The acoustic cavitation reduced the rate of growth of CaP crystals and inhibited the accumulation of CaP in specific regions of the nanotubes. When the nucleation rate was higher than the growth rate, there was a greater number of crystals with smaller sizes. The growth rate higher than the nucleation rate provided a smaller number of larger crystals.

MnO$_2$ nanowires and nanosheets deposited in Ni foam with and without the application of ultrasound presented a dense morphology, composed of stacked nanosheets generated by acoustic cavitation [75]. The ultrasonic treatment promoted the transfer of Mn ions to the working electrode, resulting in larger MnO_2 particles. Although larger particles

decrease the specific surface area, they have smaller pores, which are ideal for electrochemical reaction sites. Furthermore, the electrodes produced by sonoelectrodeposition showed better adhesion to the substrate, proving to be stable for the electrochemical performance. The active sites allowed energy storage, resulting in high rate charges due to the rapid transport of ions and electrons.

In non-conductive substrates, the low adhesion promoted by the presence of high-level internal stress is a relevant indicator [78]. The internal tension of the coating results from the atomic and crystalline structure of the deposit during its formation. The high temperatures of the substrate, such as copper at 48 °C, present thermal stress greater than the coating. The hydrogen content is the crucial factor, as it affects the substrate layer, decreasing the free energy of the resin surface, with consequent loss of adhesion and increased porosity.

3.4. Effects of ultrasound on corrosion resistance

Corrosion resistance can be improved with the incorporation of particles [10, 79] and during the material synthesis by applying ultrasonic treatment [80]. Shetty and Chitharanjan Hegde [24] studied the multilayer Ni-Co alloy and found that the corrosion rate can be increased by decreasing the ultrasound processing time since the sonication promotes homogeneity and modulates mass transport. According to the potentiodynamic polarization graph (Figure 6), the corrosion rate decreased with an increase of up to 150 layers, then increased by 300 layers. The lower corrosion rate was attributed to the increase in the interfacial surface area due to the layers formed by the periodic pulsation of ultrasonic waves, which allowed the separation of layers with different compositions. The authors concluded that the multilayer coating tends to be more homogeneous and there is a certain optimal level of layers (150 layers). The sonication effect increased coating thickness by 3 µm.
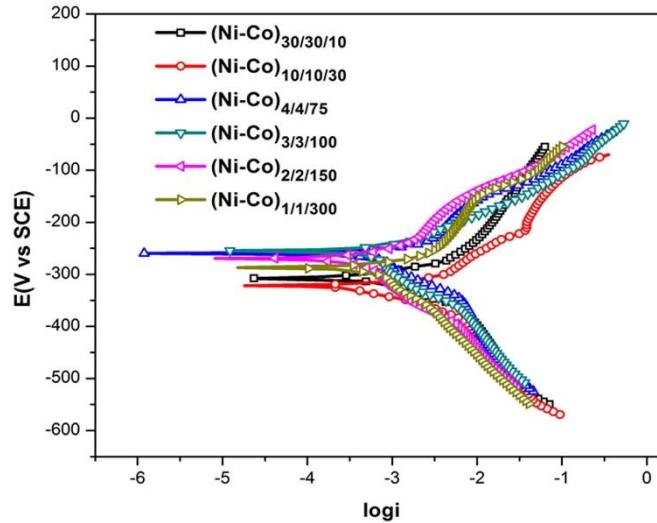
Figure 6. Potentiodynamic polarization of multilayer Ni-Co alloy coatings with different number of layers. Adapted from Shetty and Chitharanjan Hegde [24], with permission from Elsevier.

Other process variables such as current density during electrodeposition, combined with ultrasonic agitation can improve corrosion resistance. When the current density was increased from 2 to 5 A dm^2, the charge transfer resistance of the nanocomposite increased from 37 to 796 kΩ cm^2 in the electrodeposition of Ni-Cu nanocomposites with embedded TiN particles [42]. In the same way that a value greater than 5 A dm^2 of current density provided a decrease in the charge transfer resistance, demonstrating an ideal value for the system. Although corrosion resistance is dependent on several factors, the chemical composition and microstructure of the material are relevant factors that influence corrosion resistance [81] and are directly related to the current density and ultrasonic agitation.

Graphene oxide-hydroxyapatite (GO-HA) composite was deposited in titanium for medical applications [82]. The bare samples of Ti, the pretreated Ti, and the pre-treated ones containing GO, HA, and GO-HA indicated the anticorrosive behavior. The pretreatment performed through ultrasonic waves and agitation at 120 rpm, to promote dispersion of the GO phase. The pulsed electrodeposition assisted by ultrasound occurred in a galvanostatic form with a current density of 15 mA cm^{-2}, t$_{on}$: 1 s and t$_{off}$: 9 s and nominal powers of 0, 20, 60, and 100 W. The polarization curves demonstrated that the potential of corrosion (E$_{corr}$) increased from the bare sample to pre-treated, from -559 to -423 mV. The HA-coated pretreated surface sample showed an E$_{corr}$ of -415 mV and corrosion current density (i$_{corr}$) of 0.17 μA cm^{-2}. For

the authors, the application of the coating restricts the contact of corrosive fluids from the body with the implant surface, increasing the protection against corrosion. The GO-HA composite showed an E_{corr} of -358 mV and an i_{corr} of 0.09 µm cm^{-2}, demonstrating greater resistance to corrosion among the analyzed samples.

4. Influence of ultrasound process parameters on the electrodeposition of the coatings

Although the previous section discussed the application of ultrasound treatment during the electrodeposition process as well as its effects on particle dispersion, morphology and microstructure, and improvement in corrosion resistance. Ultrasonic conditions, such as type of ultrasound, frequency and power ultrasonic, and equipment coupling region still are scarce. These process conditions are crucial for understanding and suggesting changes in the ultrasound configuration to achieve beneficial results in coatings and its industrial scale-up.

4.1. Ultrasonic frequency

The ultrasonic frequency has not been explored in the electrodeposition of coatings. There are few studies focused on this process variable. An example is the work of Suliţanu, Pîrghie and Brînză [83], who studied the effect of ultrasonic frequency on the microstructure of deposited Ni-Zn thin films. Conditions without and with ultrasound at frequencies of 20 kHz and 1 MHz were studied. The frequency of 20 kHz in the ultrasound bath allowed to obtain Ni-Zn films with fine granulation and denser morphology when compared to a deposition without ultrasound. The higher frequency (1 MHz) showed interference in the formation of granulated films. The different frequencies provided control of the microstructure and physico-chemical properties of the films.

Beltowska-Lehman, Indyka, Bigos, Kot and Tarkowski [84] deposited nanocrystalline Ni-W alloys with Al$_2$O$_3$ particles. The experimental conditions applied ultrasonic frequency of 35 and 130 kHz. Working at 35 kHz improved the mechanical performance of the coating and promoted the de-agglomeration of the ceramic phase onto the matrix, resulting in a uniform distribution of the composite. Increasing ultrasonic frequency, the intensity of the acoustic cavitation was reduced due to a short compression cycle, which forms smaller microbubbles. On the other hand, the larger microbubbles collapse quickly,

which indicates that mechanical agitation is a more frequent phenomenon with lower ultrasonic frequencies [85].

Three deposition processes were applied to obtain Ni-B coatings to analyze the impact of the ultrasound frequency [86]. The authors investigated deposition under magnetic stirring (0 Hz), with probe ultrasound (20 kHz) and thermostatic bath ultrasound (35 kHz). The ultrasonic agitation in greater frequency resulted in smoother surfaces, with few areas similar to the structure of the cauliflower type, in addition to increasing the deposition efficiency with a thickness of 25.13 ± 2.02 µm. Corrosion tests at 0.1 M NaCl revealed that the coating produced at a frequency of 35 kHz indicated less corrosion damage and a large plateau before the pitting potential, which occurred due to the smooth surface of the coating, decreasing the risk of inter-columnar attack.

4.2. Ultrasonic power

The studies on ultrasound-assisted electrodeposition generally provide only the ultrasound power, known as the nominal power, in other words, it is the power consumed by the equipment. The amount of energy supplied to the system is less than the nominal power and is known as acoustic power or real power, specifically, it is the amount of power transmitted to the sonicated liquid medium. This power should be provided in the studies since it relates the specific heat, the mass, and the temperature change of the liquid medium concerning processing time. The ultrasonic intensity calculated through the acoustic power with the probe area is not mentioned in most studies and could demonstrate the effects of the analyzed variables. Similarly, the influence of the amount of energy per volume unit known as energy density was little discussed. For example, the use of a greater volume of liquid medium results in the application of less power density for the same processing time.

Energy density is a useful parameter for the evaluation of ultrasound energy performance and should be evaluated in electrodeposition studies. Although the nominal power is provided in the studies, it would be relevant to consider the energy dissipated by sample volume for comparison purposes [87]. Thus, energy density should be calculated from acoustic power to increase the accuracy of the energy balance. Besides, the temperature change over the processing time is neglected, according to previous studies [88, 89]. The temperature profile

provides the real temperatures achieved with the ultrasound treatment, allowing a suitable interpretation of its effects on the chemical changes of the sonicated system.

Regarding the studies involving ultrasonic power, the ultrasound-assisted deposition of hydroxyapatite (HA) in PVA/PLA braids was compared using nominal power levels of 0 and 20 W with an electric current density of 2.5, 5 and 7.5 mA cm^{-2} [90]. The nucleation rate with a consequent increase in crystal formation occurred with the highest current density. However, the coatings obtained at 0 W, for the current densities of 5 and 7.5 mA cm^{-2}, detaching HA from the PVA/PLA braids. The nominal power at 20 W decreased the weight of the deposit and provided uniformity of ions in the electrolyte. Ultrasound supplemented the ions when these were consumed by the cathode, which generated dense acicular crystalline structures [91]. The increase in current density combined with the nominal power of 20 W favored the increase in crystallinity from 68.70 ± 5.23% at 0 W to 73.52 ± 7.64% at 20 W applying a current density of 7.5 mA cm^{-2}.

Sn was deposited on a 316 L stainless steel substrate under 40 kHz ultrasonic frequency and with different nominal powers of 0, 20, 40, 60, 80, and 100 W [92]. Three different electrochemical techniques such as chronoamperometry, cyclic voltammetry, and linear scanning voltammetry indicated the diffusion-controlled three-dimensional nucleation as an electrochemical mechanism of Sn deposition. Besides changing the electrodeposition reaction generated by ultrasound. The current efficiency was increased from 85.84 to 95.11% when the ultrasound was coupled. The ultrasound-assisted electrodeposition provided smooth and compact surfaces, with the optimum condition at 35 °C, 100 W, and H$^+$ concentration of 3.5 M, while in the treatment without ultrasound, microstructures composed of irregularly shaped whiskers were obtained.

Although ultrasound in most cases favored particle de-agglomeration, the study of Zheng, Wang, Song, Wu, Liu and Tan [93], involving the deposition of the Co-Cr$_3$C$_2$ composite, found that the increase in nominal power from 20 to 60 W decreased the content of Cr$_3$C$_2$ particles from 31.4 to 11.5% in the coating. The process took place by jet electroplating at 40 °C in carbon steel, without and with ultrasound, frequency of 20 kHz, in the nominal powers from 20 to 60 W, without a pulse-on time, with a pulse-on time of 1, 4, 8 s, and continuous. In general, the acoustic cavitation promoted the dispersion of particles; however, high power values promote the separation of the particles at the cathode, with a consequent decrease in their content [94]. The hardness coefficient decreased with an increase in nominal

power from 20 to 60 W, as well as the friction coefficient decreased. Composites produced with nominal power greater than 40 W showed lower hardness than the coating produced without ultrasound (586 HV). Despite the morphology of particles prepared at 60 W having shown a better distribution of particles when compared to those produced without ultrasound, the coating presented a loose structure with high porosity.

Zhang, Zhang and Fang [47] studied the impact of nominal power from 0 to 50 W on the morphology of the nickel/graphene oxide coating. As shown in Figure 7-a the SEM image for pure nickel shows a coarse surface, with a pyramid appearance [95]. With the increase in ultrasonic power to 20 W the structure tends to become more compact and smaller (Figure 7-b-f). The pore formation occurs due to the hydrogen trapped in the deposit and the instability of the electro-hydrodynamic system. Ultrasound decreases the absorption of hydrogen in the deposit, reducing porous structures. However, high ultrasonic potentials can cause defects, due to microvapors generated by the acoustic cavitation (Figure 7-e-f).
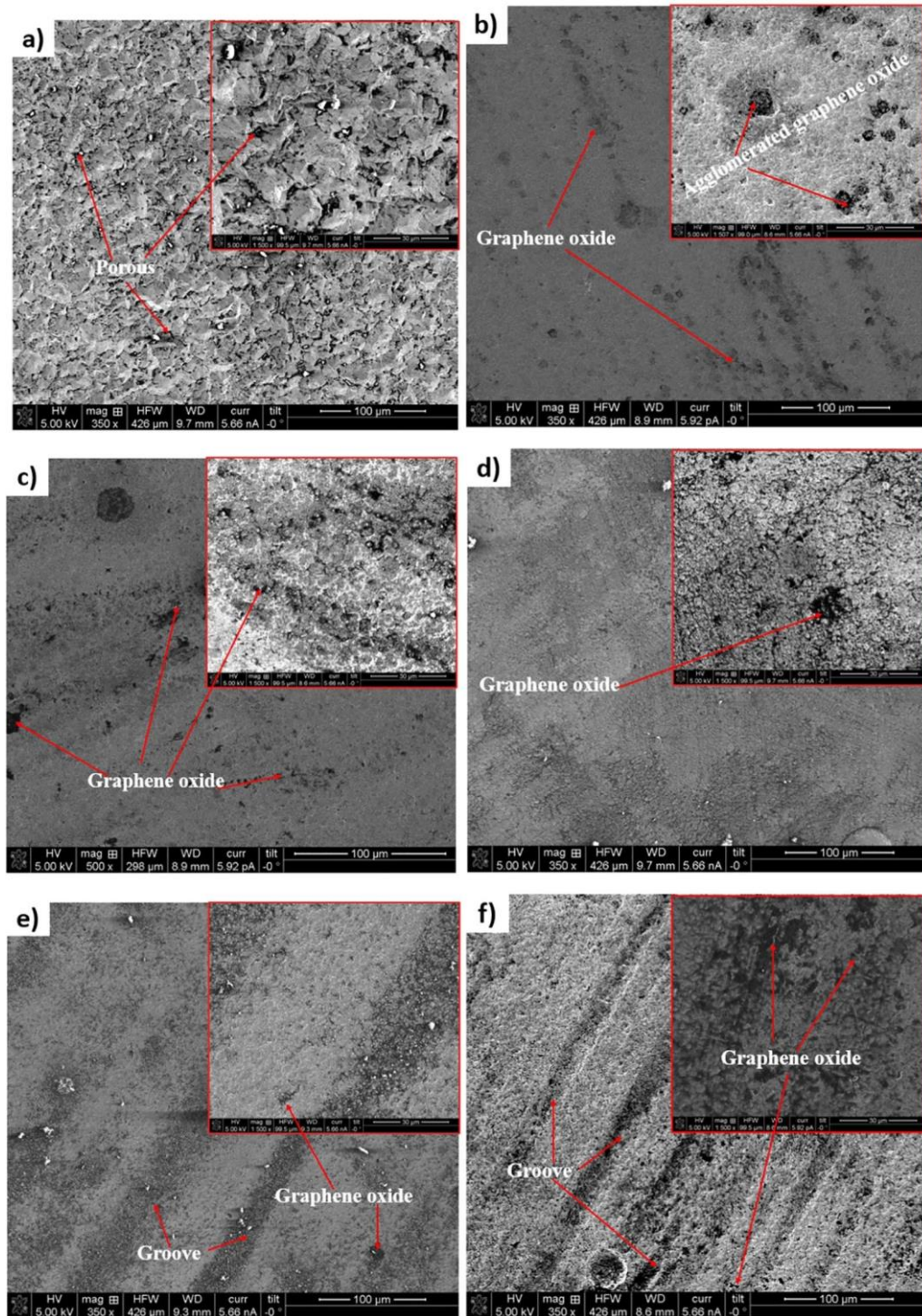
Figure 7. SEM micrographs of the nickel/graphene oxide coatings under the different nominal powers: a) Pure nickel, 0 W, b) 20 W, c) 30 W, d) 35 W, e) 45 W, f) 50 W. Adapted from Zhang, Zhang and Fang [47], with permission from Elsevier.

Besides changes in morphology, the ultrasonic power affects the crystallinity of the deposited coatings. Ni-doped TiN coatings were deposited with different ultrasonic intensities [43]. The increase from 0 to 20 W cm^{-2}, according to XRD diffractograms, led to an increase in Ni peaks and a decrease in intensity, indicating a decrease in the size of Ni crystals. On the other hand, with the increase to 40 W cm^{-2}, the Ni diffraction peaks increased.

Another impact of the ultrasonic power intensity is the increase in corrosion resistance. Sn-Ni alloys deposited in mild steel under ultrasound intensities of 0.6, 0.9, and 1.2 W cm^{-2} revealed that sonoelectrodeposition generated coatings more corrosion resistant compared to coatings produced without ultrasound [80]. Sn-Ni alloy deposited at 0.9 W cm^{-2} showed the lowest corrosion rate (7.81×10^{-2} mm year^{-1}), while without ultrasound treatment the value was 16.63×10^{-2} mm year^{-1}. This difference in the corrosion rate occurred due to the high degree of stratification, composed of 300 layers, which were deposited due to the diffusion mechanism between the layers, generated by the ultrasonic field. Pulsed electrodeposition combined with ultrasound promoted the diffusion of metal ions towards the cathode, which they discharged in their metallic form of Sn^{2+} and Ni^{2+}. This process occurred by diffusion mass transport and was controlled by acoustic cavitation.

4.3. Ultrasound type effect and application mode

Regarding the operational configuration, although the ultrasonic bath has been widely used according to the literature, electrodepositions assisted by probe-type ultrasound are more efficient, resulting in shorter processing times and greater electrodeposition efficiencies, due to the higher energy density supplied to the system in this type of configuration. The probe diameter can influence the system, because smaller diameters dissipate less energy, resulting in less heating in the sonicated liquid medium. A larger area probe dissipates more energy in the heat form to the system, increasing the temperature of the solution.

The large volume of liquid required for the operation of the ultrasound baths and the indirect treatment of the electrodeposition medium reduces the applied energy densities and the effects on the working electrode, respectively. However, a higher density of applied energy provides violent acoustic cavitation, which can have a negative effect, since the rapid propagation of the acoustic wave can collide the particles immediately on the electrode surface, promoting lesser incorporation of particles, although they distribute evenly within the coating

[96]. In electrochemistry, both configurations are widely applied, as the bath ultrasound promotes sonication of the electrolyte while the probe-type ultrasound provides vibrations on the solid surface of the electrode.

An alternative is also to apply the combined ultrasound system, consisting of the bath and probe configuration. This system promotes the highest level of acoustic cavitation than a single device. According to Ao, Xue, Li and Zhang [97], Ni-Nd$_2$O$_3$ nanocomposites were deposited on a stainless steel plate using the bath and probe type configuration. The surface morphology of the coatings showed a smooth appearance, fine and compact grains. The coupling of bath-type and probe-type ultrasound with a nominal power of 240 and 30 W, respectively, provided a high content of 3.48% Nd$_2$O$_3$ particles.

Regarding the application mode of ultrasound during coating deposition, the continuous or pulse form may be applied. Bi$_2$MoO$_6$ nanofilms were deposited in stainless steel by both modes with and without ultrasound [14]. The film prepared by sono-pulsed electrodeposition showed high photocatalytic efficiency for the degradation of sodium diclofenac attributed to high roughness and morphology composed of mustache structures. The electron transfer and light scattering occurred due to these structures, which were absent in films prepared by using conventional electrodeposition. Pulsed ultrasound (t_{on}: 4 s and t_{off}: 8 s) combined with pulsed electrodeposition (t_{on}: 4 s and t_{off}: 8 s) demonstrated high crystal growth in XRD patterns compared to conventional deposition. Ultrasonic waves promoted greater nucleation which led to the growth of plates in different directions.

As previously described, the lack of studies and information on ultrasonic conditions makes the technological expansion of ultrasound challenging. Even so, research has been widely developed with sonochemical reactors [98, 99]. In large-scale reactors, the introduction of ultrasound is more complex and studies on a smaller scale may at first serve as a comparison study.

Sonochemical reactors are more effective with the use of multiple transducers and multiple frequencies, which can enhance the cavitational effect [100]. In low-frequency reactors, acoustic cavitation promotes a stirring contribution greater than 90%. In high-frequency reactors, the production of less cavitation in the focal zone, if it concerns high intensity focused ultrasound, the cavitation reaches values close to the ultrasonic probe and low-frequency sonoreactors [101]. Despite the great potential, the industrial use of sonoreactors is scarce, mainly in electrochemical processes, due to lack of information on performance, and

difficulty in uniform distribution of cavitational activity. The applications are specific according to the type of the sonochemical reactor and its dimensions and position of the ultrasonic transducers must consider hydrodynamic characteristics and the behavior of the mixture.

Although ultrasound is an emerging, non-toxic, safe, and environmentally friendly technology, its consolidation on an industrial scale specifically in the synthesis of electrodeposited nanostructures still is a challenge. Although experiments on a laboratory scale are carried out in batch reactors, on an industrial scale the ideal is continuous reactors, due to the limited depth of cavitation waves, which may have reduced efficiency [102]. The lack of industries that manufacture suitable equipment, technical specialists, and startup companies, as well as high capital expenditure, are limiting factors for the development of this technology. On the other hand, the electroplating industry is consolidated for macro-structured materials, however, for the production of nanomaterials, the laboratory scale has greater operational control related to morphology, composition, and crystallinity.

5. Patents on the deposition process using ultrasound

The method of depositing material on a substrate under ultrasonic conditions has been few patented for the past two decades. McLamore and Taguchi [103] patented the method of pulsed sonoelectrodeposition and sonoelectropolymerization, with the application of a galvanic potential pulse alternating with the sonication pulse, to form a plurality of structures. A pause in the processing time can optionally be included between the coating pulse and the sonication pulse. Nanoparticles were produced from a metal (Pt, Ni, Au, Ag, Pd, or a combination thereof) and a conductive polymer.

The Y_2SiO_5/$MoSi_2$ composite coating preparation by sonoelectrodeposition was patented for presenting a simple control for the formation of a uniform coating that allowed a better connection property for application in products with complex surface [104]. The coating protected carbon-based materials, functioning as an antioxidant, with an oxidative weight of less than 0.5% after oxygenation for 200 h at 1600 °C. Other patents have shown the relevance of electrodeposition with ultrasound, as in the synthesis of Pt-based catalysts [105], ferromagnetic nanocomposite materials [106], and chromium alloys [107]. The methods produce materials with a metallic matrix of superior multilayer and simplify the production

technique, saving raw material and reducing costs, besides improving the catalytic activity and dispersion of the particles.

6. Critical observations and economic approaches

The main process variables affecting the incorporation of particles and the formation of nanostructured materials are ultrasound power, frequency, processing time, and mode of sonication. The suitable incorporation of particles in the metallic matrix is achieved through the de-agglomeration caused by ultrasonic waves. However, most studies carried out to date have not evaluated the synergy between process variables using ultrasound technology. The diameter of the probe is rarely described, as well as the energy density has been neglected, despite their significant effects on process performance.

In sonoelectrochemical processes, further studies could better describe the reason for choosing the ultrasonic probe as a working electrode. In recent studies (2014-2019), ultrasound has been used more for dispersion of the liquid medium, presenting better results in the synthesis of materials compared to magnetic agitation. Studies have focused on a batch operating model, moreover, studies in continuous mode may be relevant from the viewpoint of acoustic cavitation flux.

Although the ultrasound-assisted electrodeposition has been demonstrated to produce materials from the most diverse structures, there is no economic feasibility study of the process, which could attract investments from the industrial sector. The mathematical models of different unit operations linked to the chemicals database comprise different commercial simulation software, such as Cadsim Plus®, Aspen Plus®, Wingems®, and Super Pro Design®. Economic evaluation has occurred for processes involving extraction [108, 109], distillation of azeotropic mixture [110], and biorefinery processes [111] assisted by ultrasound.

The SuperPro Designer® software, for example, simulates the process according to the input variables and provides costs (US\$ kg^{-1}) as responses. The cost of manufacture considers the sum of direct, fixed, and general costs. The components are estimated in terms of fixed investment capital, labor costs, raw materials, public services, and waste treatment. The service cost would include the energy needed to convert the ionized metal to the solid-state on the substrate. This approach would have major impacts on the scale-up study of this technology in the area of materials development. In terms of energy impacts, a shorter sonication time in

addition to saving energy promotes homogeneity and sufficient mass transport to improve the anticorrosive property of the coating.

7. Conclusions

The article reviewed the technological applications of ultrasound-assisted electrodeposition from 2014 to 2019. The effects of acoustic cavitation on particle de-agglomeration, as well as the impacts on the properties of composites, such as hardness and corrosion resistance, were discussed. The sonoelectrodeposition has valuable potential for transforming irregular surfaces into uniform and smooth surfaces through ultrasonic cavitation in the electrolyte. This review showed that, in recent years, few studies have been carried out on ultrasound-assisted deposition of composites, metal alloys, and polymeric structures. Given the global problem, which is the corrosion of materials and as discussed that the use of ultrasound is beneficial for this property, more research is expected to be developed in this segment. Also, more information about the ultrasound configuration needs to be provided to understand the impact and provide optimizations in the electrodeposition process.

References

[1] F.C. Walsh, Modern developments in electrodes for electrochemical technology and the role of surface finishing, Transactions of the IMF, 97 (2019) 28-42.

[2] F.C. Walsh, S. Wang, N. Zhou, The electrodeposition of composite coatings: Diversity, applications and challenges, Current Opinion in Electrochemistry, 20 (2020) 8-19.

[3] J.-J. Huang, C.-H. Lin, Y.-R. Ho, Y.-H. Chang, Aluminium oxide passivation films by liquid phase deposition for TiO_2 ultraviolet solid–liquid heterojunction photodetectors, Surface and Coatings Technology, 391 (2020) 125684.

[4] H.D. Mejía V, A.M. Echavarría, J.A. Calderón, G. Bejarano G, Microstructural and electrochemical properties of TiAlN(Ag,Cu) nanocomposite coatings for medical applications deposited by dc magnetron sputtering, Journal of Alloys and Compounds, 828 (2020) 154396.

[5] J. Wang, Y. Ling, Z. Lu, Q. Zhou, R. Wang, Z. Zhang, Enhanced formation of α-Al_2O_3 at low temperature on Cr/Al coating by controlling oxygen partial pressure, Applied Surface Science, 515 (2020) 146053.

[6] K. Sahu, A. Bisht, A. Pandey, A. Dutta, S.A. Khan, R. Singhal, T. Som, S. Mohapatra, RF magnetron sputtered Ag-Cu$_2$O-CuO nanocomposite thin films with highly enhanced photocatalytic and catalytic performance, Applied Surface Science, 517 (2020) 146169.

[7] M.A. Deyab, G. Mele, Stainless steel bipolar plate coated with polyaniline/Zn-Porphyrin composites coatings for proton exchange membrane fuel cell, Scientific Reports, 10 (2020) 3277.

[8] F. Mohsenifar, H. Ebrahimifar, Effect of titanium oxide ceramic particles concentration on microstructure and corrosion behaviour of Ni–P–Al$_2$O$_3$–TiO$_2$ composite coating, Bulletin of Materials Science, 43 (2020) 99.

[9] V.N. Tseluikin, Composite electrochemical coatings: Preparation, structure, properties, Protection of Metals and Physical Chemistry of Surfaces, 45 (2009) 312-326.

[10] C.T.J. Low, R.G.A. Wills, F.C. Walsh, Electrodeposition of composite coatings containing nanoparticles in a metal deposit, Surface and Coatings Technology, 201 (2006) 371-383.

[11] M.K. Camargo, U. Schmidt, R. Grieseler, M. Wilke, A. Bund, Electrodeposition of Zn-TiO$_2$ Dispersion Coatings: Study of Particle Incorporation in Chloride and Sulfate Baths, Journal of The Electrochemical Society, 161 (2014) D168-D175.

[12] A. Asadi, F. Pourfattah, I. Miklós Szilágyi, M. Afrand, G. Żyła, H. Seon Ahn, S. Wongwises, H. Minh Nguyen, A. Arabkoohsar, O. Mahian, Effect of sonication characteristics on stability, thermophysical properties, and heat transfer of nanofluids: A comprehensive review, Ultrasonics Sonochemistry, 58 (2019) 104701.

[13] M. Lekka, R. Offoiach, F. Revelant, L. Fedrizzi, Effect of the plating parameters on the electrodeposition of Ni matrix coatings containing Ti nanoparticles, Transactions of the IMF, 97 (2019) 73-81.

[14] M. Zargazi, M.H. Entezari, Bi2MoO6 nanofilms on the stainless steel mesh by PS-PED method: Photocatalytic degradation of diclofenac sodium as a pharmaceutical pollutant, Ultrasonics Sonochemistry, 62 (2020) 104867.

[15] S. He, S. Zhong, L. Xu, Y. Dou, Z. Li, F. Qiao, Y. Gao, X. Cui, Sonochemical fabrication of magnetic reduction-responsive alginate-based microcapsules for drug delivery, International Journal of Biological Macromolecules, 155 (2020) 42-49.

[16] R.R. Huerta, E.K. Silva, I. Ekaette, T. El-Bialy, M.D.A. Saldaña, High-intensity ultrasound-assisted formation of cellulose nanofiber scaffold with low and high lignin content

and their cytocompatibility with gingival fibroblast cells, Ultrasonics Sonochemistry, 64 (2020) 104759.

[17] P.R. Gogate, P.D. Thanekar, A.P. Oke, Strategies to improve biological oxidation of real wastewater using cavitation based pre-treatment approaches, Ultrasonics Sonochemistry, 64 (2020) 105016.

[18] H.S. Arruda, E.K. Silva, G.A. Pereira, C.F.F. Angolini, M.N. Eberlin, M.A.A. Meireles, G.M. Pastore, Effects of high-intensity ultrasound process parameters on the phenolic compounds recovery from araticum peel, Ultrasonics Sonochemistry, 50 (2019) 82-95.

[19] S.H.M.C. Monteiro, E.K. Silva, J.T. Guimarães, M.Q. Freitas, M.A.A. Meireles, A.G. Cruz, High-intensity ultrasound energy density: How different modes of application influence the quality parameters of a dairy beverage, Ultrasonics Sonochemistry, 63 (2020) 104928.

[20] M.H. Islam, O.S. Burheim, B.G. Pollet, Sonochemical and sonoelectrochemical production of hydrogen, Ultrasonics Sonochemistry, 51 (2019) 533-555.

[21] D. Peters, Ultrasound in materials chemistry, Journal of Materials Chemistry, 6 (1996) 1605-1618.

[22] C.E. Banks, R.G. Compton, Ultrasonically Enhanced Voltammetric Analysis and Applications: An Overview, Electroanalysis, 15 (2003) 329-346.

[23] J.P. Lorimer, B. Pollet, S.S. Phull, T.J. Mason, D.J. Walton, The effect upon limiting currents and potentials of coupling a rotating disc and cylindrical electrode with ultrasound, Electrochimica Acta, 43 (1998) 449-455.

[24] A.R. Shetty, A. Chitharanjan Hegde, Ultrasound induced multilayer Ni-Co alloy coatings for better corrosion protection, Surface and Coatings Technology, 322 (2017) 99-107.

[25] V.S. Nalajala, V.S. Moholkar, Investigations in the physical mechanism of sonocrystallization, Ultrasonics Sonochemistry, 18 (2011) 345-355.

[26] J. Chandrapala, C. Oliver, S. Kentish, M. Ashokkumar, Ultrasonics in food processing, Ultrasonics Sonochemistry, 19 (2012) 975-983.

[27] A.C. Soria, M. Villamiel, Effect of ultrasound on the technological properties and bioactivity of food: a review, Trends in Food Science & Technology, 21 (2010) 323-331.

[28] E.K. Silva, M.T.M.G. Rosa, M.A.A. Meireles, Ultrasound-assisted formation of emulsions stabilized by biopolymers, Current Opinion in Food Science, 5 (2015) 50-59.

[29] S. Abbas, K. Hayat, E. Karangwa, M. Bashari, X. Zhang, An Overview of Ultrasound-Assisted Food-Grade Nanoemulsions, Food Engineering Reviews, 5 (2013) 139-157.

[30] I. Tudela, Y. Zhang, M. Pal, I. Kerr, A.J. Cobley, Ultrasound-assisted electrodeposition of composite coatings with particles, Surface and Coatings Technology, 259 (2014) 363-373.

[31] E.K. Silva, A.L.R. Costa, A. Gomes, M.A. Bargas, R.L. Cunha, M.A.A. Meireles, Coupling of high-intensity ultrasound and mechanical stirring for producing food emulsions at low-energy densities, Ultrasonics Sonochemistry, 47 (2018) 114-121.

[32] A. Taha, T. Hu, Z. Zhang, A.M. Bakry, I. Khalifa, S. Pan, H. Hu, Effect of different oils and ultrasound emulsification conditions on the physicochemical properties of emulsions stabilized by soy protein isolate, Ultrasonics Sonochemistry, 49 (2018) 283-293.

[33] J. Yoo, H.-S. Kim, S.-Y. Park, S. Kwon, J. Lee, J. Koo, Y.-S. Seo, Instantaneous integration of magnetite nanoparticles on graphene oxide assisted by ultrasound for efficient heavy metal ion retrieval, Ultrasonics Sonochemistry, 64 (2020) 104962.

[34] Y. Liu, R. Li, Study on ultrasound-assisted liquid-phase exfoliation for preparing graphene-like molybdenum disulfide nanosheets, Ultrasonics Sonochemistry, 63 (2020) 104923.

[35] H.R. Bakhshandeh, S.R. Allahkaram, A.H. Zabihi, An investigation on cavitation-corrosion behavior of Ni/β-SiC nanocomposite coatings under ultrasonic field, Ultrasonics Sonochemistry, 56 (2019) 229-239.

[36] C.T. Walker, R. Walker, Effect of ultrasonic agitation on some properties of electrodeposits, Electrodeposition and Surface Treatment, 1 (1973) 457-469.

[37] A. Bigos, E. Beltowska-Lehman, E. García-Lecina, M. Bieda, M.J. Szczerba, J. Morgiel, Ultrasound-assisted electrodeposition of Ni and Ni-Mo coatings from a citrate-ammonia electrolyte solution, Journal of Alloys and Compounds, 726 (2017) 410-416.

[38] I. Tudela, Y. Zhang, M. Pal, I. Kerr, T.J. Mason, A.J. Cobley, Ultrasound-assisted electrodeposition of nickel: Effect of ultrasonic power on the characteristics of thin coatings, Surface and Coatings Technology, 264 (2015) 49-59.

[39] E. Beltowska-Lehman, A. Bigos, P. Indyka, A. Chojnacka, A. Drewienkiewicz, S. Zimowski, M. Kot, M.J. Szczerba, Optimisation of the electrodeposition process of Ni-W/ZrO$_2$ nanocomposites, Journal of Electroanalytical Chemistry, 813 (2018) 39-51.

[40] F. Monjezi, F. Jamali-Sheini, R. Yousefi, Ultrasound-assisted electrodeposition of Cu$_3$Se$_2$ nanosheets and efficient solar cell performance, Journal of Alloys and Compounds, 780 (2019) 626-633.

[41] F. Su, C. Liu, P. Huang, Ultrasound-assisted pulse electrodeposition and characterization of Co–W/MWCNTs nanocomposite coatings, Applied Surface Science, 309 (2014) 200-208.

[42] B. Li, T. Mei, D. Li, S. Du, Ultrasonic-assisted electrodeposition of Ni-Cu/TiN composite coating from sulphate-citrate bath: Structural and electrochemical properties, Ultrasonics Sonochemistry, 58 (2019) 104680.

[43] W. Cui, Y. Zhang, R. Song, P. Wang, Ultrasonic assisted pulse electrodeposited Ni-doped TiN coatings, Ceramics International, 44 (2018) 14767-14773.

[44] P. Nath, D.K. Sahu, A. Mallik, Physicochemical and corrosion properties of sono-electrodeposited Cu-Ni thin films, Surface and Coatings Technology, 307 (2016) 772-780.

[45] M.K. Camargo, I. Tudela, U. Schmidt, A.J. Cobley, A. Bund, Ultrasound assisted electrodeposition of Zn and Zn-TiO$_2$ coatings, Electrochimica Acta, 198 (2016) 287-295.

[46] B. Li, W. Zhang, Facile synthesis and electrochemical properties of a novel Ni-B/TiC composite coating via ultrasonic-assisted electrodeposition, Ultrasonics Sonochemistry, 61 (2020) 104837.

[47] H. Zhang, N. Zhang, F. Fang, Fabrication of high-performance nickel/graphene oxide composite coatings using ultrasonic-assisted electrodeposition, Ultrasonics Sonochemistry, 62 (2020) 104858.

[48] S.A. Ataie, A. Zakeri, RSM optimization of pulse electrodeposition of Zn-Ni-Al$_2$O$_3$ nanocomposites under ultrasound irradiation, Surface and Coatings Technology, 359 (2019) 206-215.

[49] A.A. Kasach, I.I. Kurilo, D.S. Kharitonov, S.L. Radchenko, I.M. Zharskii, Effect of Sonochemical Treatment Modes on the Electrodeposition of Cu–Sn Alloy from Oxalic Acid Electrolyte, Russian Journal of Applied Chemistry, 91 (2018) 591-596.

[50] Y. Sun, H. Zheng, C. Wang, M. Yang, A. Zhou, H. Duan, Ultrasonic-electrodeposition of PtPd alloy nanoparticles on ionic liquid-functionalized graphene paper: towards a flexible and versatile nanohybrid electrode, Nanoscale, 8 (2016) 1523-1534.

[51] H. Kafashan, M. Azizieh, H. Nasiri Vatan, Ultrasound-assisted electrodeposition of SnS: Effect of ultrasound waves on the physical properties of nanostructured SnS thin films, Journal of Alloys and Compounds, 686 (2016) 962-968.

[52] S. Yan, M.H. Wu, Z. Ning, Y.G. Wang, Ultrasound-Pulse Electrodeposition Preparation of Fe-Nano ZrO2 Functional Gradient Coating, Applied Mechanics and Materials, 556-562 (2014) 222-227.

[53] W. Sassi, H. Boubaker, S. Bahar, M. Othman, A. Ghorbal, R. Zrelli, J.Y. Hihn, A challenge to succeed the electroplating of nanocomposite Ni–Cr alloy onto porous substrate under ultrasonic waves and from a continuous flow titanium nanofluids, Journal of Alloys and Compounds, 828 (2020) 154437.

[54] W.Q. Liu, W.N. Lei, C.Y. Wang, H.F. Qian, L.H. Ding, Ni-SiC Nanocomposites Electroplating Process under Ultrasonic and Agitation, Integrated Ferroelectrics, 167 (2015) 192-198.

[55] J. Zhu, S.T. Aruna, Y. Koltypin, A. Gedanken, A Novel Method for the Preparation of Lead Selenide: Pulse Sonoelectrochemical Synthesis of Lead Selenide Nanoparticles, Chemistry of Materials, 12 (2000) 143-147.

[56] M. Hujjatul Islam, M.T.Y. Paul, O.S. Burheim, B.G. Pollet, Recent developments in the sonoelectrochemical synthesis of nanomaterials, Ultrasonics Sonochemistry, 59 (2019) 104711.

[57] V. Zin, B.G. Pollet, M. Dabalà, Sonoelectrochemical (20kHz) production of platinum nanoparticles from aqueous solutions, Electrochimica Acta, 54 (2009) 7201-7206.

[58] L. Hostert, G.d. Alvarenga, L.F. Marchesi, A.L. Soares, M. Vidotti, One-Pot sonoelectrodeposition of poly(pyrrole)/Prussian blue nanocomposites: Effects of the ultrasound amplitude in the electrode interface and electrocatalytical properties, Electrochimica Acta, 213 (2016) 822-830.

[59] V. Zin, K. Brunelli, M. Dabalà, Characterization of Cu–Ni alloy electrodeposition and synthesis of nanoparticles by pulsed sonoelectrochemistry, Materials Chemistry and Physics, 144 (2014) 272-279.

[60] S. Levi, V. Mancier, C. Rousse, O.L. Garcia, J. Mejia, M. Guzman, S. Lucas, P. Fricoteaux, Synthesis of spherical copper-platinum nanoparticles by sonoelectrochemistry followed by conversion reaction, Electrochimica Acta, 176 (2015) 567-574.

[61] J. Zhu, S. Liu, O. Palchik, Y. Koltypin, A. Gedanken, Shape-Controlled Synthesis of Silver Nanoparticles by Pulse Sonoelectrochemical Methods, Langmuir, 16 (2000) 6396-6399.

[62] J.C. Eklund, F. Marken, D.N. Waller, R.G. Compton, Voltammetry in the presence of ultrasound: A novel sono-electrode geometry, Electrochimica Acta, 41 (1996) 1541-1547.

[63] K. Macounova, J. Klima, C. Bernard, C. Degrand, Ultrasound-assisted anodic oxidation of diuron, Journal of Electroanalytical Chemistry, 457 (1998) 141-147.

[64] A. Magdziarz, C.J. Colmenares, In Situ Coupling of Ultrasound to Electro- and Photo-Deposition Methods for Materials Synthesis, Molecules, 22 (2017).

[65] V. Sáez, J.T. Mason, Sonoelectrochemical Synthesis of Nanoparticles, Molecules, 14 (2009).

[66] A. Hajnorouzi, Two ultrasonic applications for the synthesis of nanostructured copper oxide (II), Ultrasonics Sonochemistry, 64 (2020) 105020.

[67] A. Hajnorouzi, N. Modaresi, Direct sono electrochemical method for synthesizing Fe3O4 nanoparticles, Journal of Magnetism and Magnetic Materials, 505 (2020) 166732.

[68] T. Hielscher, Ultrasonic production of nano-size dispersions and emulsions, European Nano Systems, (Paris, France, 14-16 December) (2005).

[69] E. García-Lecina, I. García-Urrutia, J.A. Díez, J. Morgiel, P. Indyka, A comparative study of the effect of mechanical and ultrasound agitation on the properties of electrodeposited Ni/Al$_2$O$_3$ nanocomposite coatings, Surface and Coatings Technology, 206 (2012) 2998-3005.

[70] Q. Cheng, Z. Yao, F. Zhang, S. Zhang, M. Oleksander, Microstructure and tribological property of Ni–MoS2 composite coatings prepared by ultrasonic and mechanical stirring electrodeposition, Materials Research Express, 6 (2020) 126434.

[71] M.-C. Chou, M.-D. Ger, S.-T. Ke, Y.-R. Huang, S.-T. Wu, The Ni–P–SiC composite produced by electro-codeposition, Materials Chemistry and Physics, 92 (2005) 146-151.

[72] X. Zhou, Y. Wang, X. Liu, Z. Liang, H. Jin, Electrodeposition Kinetics of Ni/Nano-Y2O3 Composite Coatings, Metals, 8 (2018).

[73] S.A. Ataie, A. Zakeri, Improving tribological properties of (Zn–Ni)/nano Al$_2$O$_3$ composite coatings produced by ultrasonic assisted pulse plating, Journal of Alloys and Compounds, 674 (2016) 315-322.

[74] L.N. Bengoa, A. Ispas, J.F. Bengoa, A. Bund, W.A. Egli, Ultrasound Assisted Electrodeposition of Cu-SiO$_2$ Composite Coatings: Effect of Particle Surface Chemistry, Journal of The Electrochemical Society, 166 (2019) D244-D251.

[75] J. Liu, L. Yang, Z. Song, C. Xu, Microstructures and capacitance performance of MnO$_2$ films fabricated by ultrasonic-assisted electrodeposition, Applied Surface Science, 478 (2019) 94-102.

[76] M. Zargazi, M.H. Entezari, Sono-electrodeposition of novel bismuth sulfide films on the stainless steel mesh: Photocatalytic reduction of Cr (VI), Journal of Hazardous Materials, 384 (2020) 121300.

[77] J. Chen, Z. Zhang, J. Ouyang, X. Chen, Z. Xu, X. Sun, Bioactivity and osteogenic cell response of TiO_2 nanotubes coupled with nanoscale calcium phosphate via ultrasonification-assisted electrochemical deposition, Applied Surface Science, 305 (2014) 24-32.

[78] J.Y. Hihn, F. Touyeras, M.-L. Doche, C. Costa, B.G. Pollet, Sonoelectrodeposition: The Use of Ultrasound in Metallic Coatings Deposition, in: B. Pollet (Ed.) Power Ultrasound in Electrochemistry, Wiley, 2012, pp. 169-214.

[79] T. He, Y. He, H. Li, Z. Su, Y. Fan, Z. He, Fabrication of $Ni-W-B_4C$ composite coatings and evaluation of its micro-hardness and corrosion resistance properties, Ceramics International, 44 (2018) 9188-9193.

[80] S. Shetty, M.M. Jaffer Sadiq, D.K. Bhat, A.C. Hegde, Development of multilayer Sn–Ni alloy coating by pulsed sonoelectrolysis for enhanced corrosion protection, RSC Advances, 6 (2016) 77465-77473.

[81] E. Beltowska-Lehman, P. Indyka, A. Bigos, M.J. Szczerba, J. Guspiel, H. Koscielny, M. Kot, Effect of current density on properties of Ni–W nanocomposite coatings reinforced with zirconia particles, Materials Chemistry and Physics, 173 (2016) 524-533.

[82] L. Fathyunes, J. Khalil-Allafi, Characterization and corrosion behavior of graphene oxide-hydroxyapatite composite coating applied by ultrasound-assisted pulse electrodeposition, Ceramics International, 43 (2017) 13885-13894.

[83] N. Suliţanu, C. Pîrghie, F. Brînză, Effect of ultrasounds sonication on surface microstructure of the electrodeposited Ni-Zn thin films, Journal of Optoelectronics and Advanced Materials, 8 (2006) 1889-1891.

[84] E. Beltowska-Lehman, P. Indyka, A. Bigos, M. Kot, L. Tarkowski, Electrodeposition of nanocrystalline Ni–W coatings strengthened by ultrafine alumina particles, Surface and Coatings Technology, 211 (2012) 62-66.

[85] K.V.B. Tran, T. Kimura, T. Kondo, S. Koda, Quantification of frequency dependence of mechanical effects induced by ultrasound, Ultrasonics Sonochemistry, 21 (2014) 716-721.

[86] L. Bonin, N. Bains, V. Vitry, A.J. Cobley, Electroless deposition of nickel-boron coatings using low frequency ultrasonic agitation: Effect of ultrasonic frequency on the coatings, Ultrasonics, 77 (2017) 61-68.

[87] E. Keven Silva, G.L. Zabot, A.A.C. Toledo Hijo, M.A.A. Meireles, Chapter 13 - Encapsulation of Bioactive Compounds Using Ultrasonic Technology, in: D. Bermudez-

Aguirre (Ed.) Ultrasound: Advances for Food Processing and Preservation, Academic Press, 2017, pp. 323-350.

[88] E.K. Silva, H.S. Arruda, G.M. Pastore, M.A.A. Meireles, M.D.A. Saldaña, Xylooligosaccharides chemical stability after high-intensity ultrasound processing of prebiotic orange juice, Ultrasonics Sonochemistry, 63 (2020) 104942.

[89] M. Martins Strieder, M. Isabel Landim Neves, E. Keven Silva, M. Angela A. Meireles, Low-frequency and high-power ultrasound-assisted production of natural blue colorant from the milk and unripe Genipa americana L, Ultrasonics Sonochemistry, (2020) 105068.

[90] T.-T. Li, L. Ling, M.-C. Lin, Q. Jiang, Q. Lin, C.-W. Lou, J.-H. Lin, Effects of ultrasonic treatment and current density on the properties of hydroxyapatite coating via electrodeposition and its in vitro biomineralization behavior, Materials Science and Engineering: C, 105 (2019) 110062.

[91] S. Pang, Y. He, P. He, X. Luo, Z. Guo, H. Li, Fabrication of two distinct hydroxyapatite coatings and their effects on MC3T3-E1 cell behavior, Colloids and Surfaces B: Biointerfaces, 171 (2018) 40-48.

[92] T. Nan, J. Yang, B. Chen, Electrochemical mechanism of tin membrane electrodeposition under ultrasonic waves, Ultrasonics Sonochemistry, 42 (2018) 731-737.

[93] X. Zheng, M. Wang, H. Song, D. Wu, X. Liu, J. Tan, Effect of ultrasonic power and pulse-on time on the particle content and mechanical property of Co-Cr$_3$C$_2$ composite coatings by jet electrodeposition, Surface and Coatings Technology, 325 (2017) 181-189.

[94] C. Zanella, M. Lekka, p.l. Bonora, Effect of ultrasound vibration during electrodeposition of Ni–SiC nanocomposite coatings, Surface Engineering, 26 (2010) 511-518.

[95] Z. Chen, L. Wang, Z. Ma, J. Song, G. Shao, Ni–reduced graphene oxide composite cathodes with new hierarchical morphologies for electrocatalytic hydrogen generation in alkaline media, RSC Advances, 7 (2017) 704-711.

[96] E. García-Lecina, I. García-Urrutia, J.A. Díez, J. Fornell, E. Pellicer, J. Sort, Codeposition of inorganic fullerene-like WS2 nanoparticles in an electrodeposited nickel matrix under the influence of ultrasonic agitation, Electrochimica Acta, 114 (2013) 859-867.

[97] Z.H. Ao, Y.J. Xue, X.H. Li, D.Y. Zhang, Effect of Ultrasound Power on Ni-Nd2O3 Nanocomposite Coatings Prepared by Electrodeposition in Combination Ultrasonic Field, Applied Mechanics and Materials, 678 (2014) 597-600.

[98] S.J. Coleman, S. Roy, Design of an ultrasonic tank reactor for copper deposition at electrodes separated by a narrow gap, Ultrasonics Sonochemistry, 42 (2018) 445-451.

[99] A. Li, R. Zhong, X. Li, J. Zhang, Enhancement of sonochemical efficiency using combination of ultrasound with ultraviolet irradiation and water flow in a horn-type reactor, Chemical Engineering and Processing - Process Intensification, 150 (2020) 107884.

[100] S. Asgharzadehahmadi, A.A. Abdul Raman, R. Parthasarathy, B. Sajjadi, Sonochemical reactors: Review on features, advantages and limitations, Renewable and Sustainable Energy Reviews, 63 (2016) 302-314.

[101] J.Y. Hihn, M.L. Doche, A. Mandroyan, L. Hallez, B.G. Pollet, Respective contribution of cavitation and convective flow to local stirring in sonoreactors, Ultrasonics Sonochemistry, 18 (2011) 881-887.

[102] T. Belwal, F. Chemat, P.R. Venskutonis, G. Cravotto, D.K. Jaiswal, I.D. Bhatt, H.P. Devkota, Z. Luo, Recent advances in scaling-up of non-conventional extraction techniques: Learning from successes and failures, TrAC Trends in Analytical Chemistry, 127 (2020) 115895.

[103] E.S. McLamore, M. Taguchi, Pulsed sonoelectrodeposition and sonoelectropolymerization methods and structures formed therefrom, WO2017132507A1, United States (2017).

[104] H. Jianfeng, W. Yaqin, C. Liyun, Y. Qiang, X. Changkui, Y. Lixiong, L. Jing, W. Jianpeng, Method for preparing $Y_2SiO_5/MoSi_2$ composite coat by sonoelectrodeposition, CN101514474B, China (2009).

[105] X. Ren, Q. Lv, L. Liu, B. Liu, A kind of method that pulse electrodeposition prepares Pt base catalyst under ultrasound condition, CN109331820A, China (2018).

[106] F. Yang, L. Xingong, W. Menghua, J. Weiping, W. Yuangang, Method for preparing ferromagnetic nano composite material with pulse-ultrasound electrodeposition, CN102002748A, China (2010).

[107] H. Xinkui, Method for electrodepositing chromium and chromium alloy composite coating through ultrasound-pulse for trivalent chromium plating liquid system, CN101392394A, China (2008).

[108] A. Galviz-Quezada, A.M. Ochoa-Aristizábal, M.E. Arias Zabala, S. Ochoa, J.F. Osorio-Tobón, Valorization of iraca (Carludovica palmata, Ruiz & Pav.) infructescence by ultrasound-

assisted extraction: An economic evaluation, Food and Bioproducts Processing, 118 (2019) 91-102.

[109] S. Ochoa, M.M. Durango-Zuleta, J. Felipe Osorio-Tobón, Techno-economic evaluation of the extraction of anthocyanins from purple yam (Dioscorea alata) using ultrasound-assisted extraction and conventional extraction processes, Food and Bioproducts Processing, (2020).

[110] T. Mahdi, A.E. Al-Kawaz, A Simulation Study of Enhanced Distillation Using Ultrasound Waves for the Separation of Azeotropic Mixtures, American Journal of Engineering and Applied Sciences, 11 (2017) 97-107.

[111] A. García, M. Alriols, W. Wukovits, A. Friedl, J. Labidi, Process Simulation Tools for the Assessment of Biorefinery Process Intensification by Ultrasound Technology, Chemical Engineering Transactions, 35 (2013) 67.

APPENDIX F

Nanocatalysts deposition assisted by supercritical carbon dioxide technology: A review

Nanocatalysts deposition assisted by supercritical carbon dioxide technology:
A review

Josiel Martins Costa and Ambrósio Florêncio de Almeida Neto

Abstract

The impregnation of active compounds such as phytochemicals, drugs, and metals using supercritical CO_2 technology has been a promising alternative for developing new products of high-technological standards. In this sense, the incorporation of metals in several support materials has been explored to produce novel powerful catalysts. This non-thermal and clean emerging technology allows obtaining unique and varied morphologies as dispersed species, films, and high-surface-area nanoparticles. They are beneficial for use as electrocatalysts of oxygen reduction/evolution reactions in energy storage systems such as batteries, supercapacitors, and fuel cells, surpassing the results of commercial catalysts. In this context, firstly, this review presents a brief introduction of supercritical fluid applications, fundamental aspects, and the combination of deposition techniques. Moreover, kinetic control in modifying the advanced materials was approached. The discussion of how the temperature, pressure, and contact time, and their effects, is still scarce. The CO_2 volume rate is not considered a process variable and may improve the performance of supercritical CO_2 in the synthesis of deposited nanoparticles. Therefore, we reported the supercritical process conditions in the synthesis of nanostructured nanocomposites materials from 2014 to 2020.

Keywords: electrocatalysis, energy storage materials, nanoparticles, supercritical fluids.

1. Introduction

The search and development of innovative catalysts that exhibit stability, high catalytic activity, and ease of synthesis have been the main challenge in recent decades for several reactions, including energy storage devices such as fuel cells, metal-air batteries, and supercapacitors. In general, the purpose of the catalysts in energy systems is to reduce the overpotential generated during the charging and discharging process in the device, maintaining a stable cycle, and retaining energy more efficiently.

Catalysts are synthesized by several methods, such as electrodeposition [1, 2] sol-gel chemistry [3], deposition-precipitation [4], coprecipitation [5], sonochemical reduction [6], chemical vapor deposition [7], atomic layer deposition [8], among others. In addition to these methods, supercritical fluid deposition technology has emerged as a promising environmentally friendly alternative. It consists of pure or a mixture of substances in their supercritical state to impregnate the active material into desirable support based on their transport properties like higher diffusion coefficients and good solubility [9].

The supercritical fluid deposition (SCFD) technique provides the formation of well-defined nanoscale metal structures on the solid support by hydrogenating metal salts or organometallic precursors of their solutions under supercritical process conditions. The hydrogen as a reducing agent allows the synthesis of pure films or nanoparticles of low pollution due to the organic binders formed from the precursors [10]. Moreover, thermal decomposition in an inert atmosphere and chemical reduction with air after pressurization can also occur after deposition [11, 12].

The nanoparticles easily penetrate and diffuse into the support pores, from precursors, resulting in highly dispersed materials supported on substrates. In conventional processes, the regular particle distribution onto the support material and the particle design control such as morphology and particle size distribution present several difficulties [13]. Supercritical technology has been recognized as a powerful technique for particle engineering and design. Several studies demonstrated that particles with controlled properties like morphology, size distribution, porosity, density, and others might be produced using this emerging technology [14-16].

Characterization techniques such as X-ray diffraction and spectroscopy (Raman, infra-red or ultraviolet-visible) allow for *in situ* monitoring thermodynamic phenomena and

particle nucleation and growth. However, conventional metal reactors are "blind" to these techniques. The reactors used are capillaries and sapphire/fused silica tubes and on-chip high-pressure microreactors [17].

A variety of pure substances may be used as SCFs, for example, water and hydrocarbons. However, they are generally corrosive, toxic, and flammable. Supercritical fluids demonstrate interesting physicochemical properties, such as low viscosity and surface tension, and high diffusivity, which are abruptly altered by temperature and pressure. Moreover, they exhibit solvation behavior and dielectric properties [18]. Carbon dioxide is a compound frequently used due to its "green solvent" properties and does not exhibit the potential to cause the greenhouse effect and can be recovered during processing [19]. It is non-flammable, inert, and non-polar, with relatively moderate values of critical pressure and temperature ($T_c = 31$ °C, $P_c = 7.38$ MPa) [20].

In this sense, this review presents the trends, perspectives, and challenges of using supercritical CO_2 (scCO_2) to synthesize high-technological performance catalysts. The process variables' effects on the synthetized systems and their potential applications in several industrial sectors and research fields were summarized.

2. Supercritical technology fundamentals

A supercritical fluid is defined as any fluid that presents itself at conditions above its critical point. Viscosity and diffusivity exhibit values between liquid and gaseous; however, the density value is the order of magnitude of the one of a liquid, and the surface tension is close to zero. Solvents in their supercritical state exhibit the combination of gaseous outflow and solvent properties similar to liquids, according to Table 1. Thus, the state of high homogeneity resulting from intrinsic transport allows the control of the particle growth process [21].

Table 1. Physical properties of gases, SCFs, and liquids

Fluid properties	Gas	SCFs	Liquid
Density (g cm^{-3})	0.6-2 × 10^{-3}	0.2-0.9	0.6-1.6
Diffusivity (m^2 s^{-1})	1-4 × 10^{-5}	2-7 × 10^{-8}	10^{-9}
Viscosity (Pa s^{-1})	1-3 × 10^{-5}	1-9 × 10^{-5}	10^{-3}

From these transport properties, SCFs present several applications, such as nanoparticle synthesis, extraction, and chromatography [14], and have attracted considerable attention from the pharmaceutical, biomedical, and food industries [22-24]. Other applications include extraction of phytochemical compounds, particle engineering and design, impregnation of active compounds, microbial and enzymatic inactivation [25-27]. According to Figure 1, as temperature and pressure increase, the gas state becomes denser, and the liquid state's density decreases. At the critical point, the liquid state and the gas state are identical, and a state differentiation is difficult. Above the critical point, the fluid is named as a supercritical fluid.
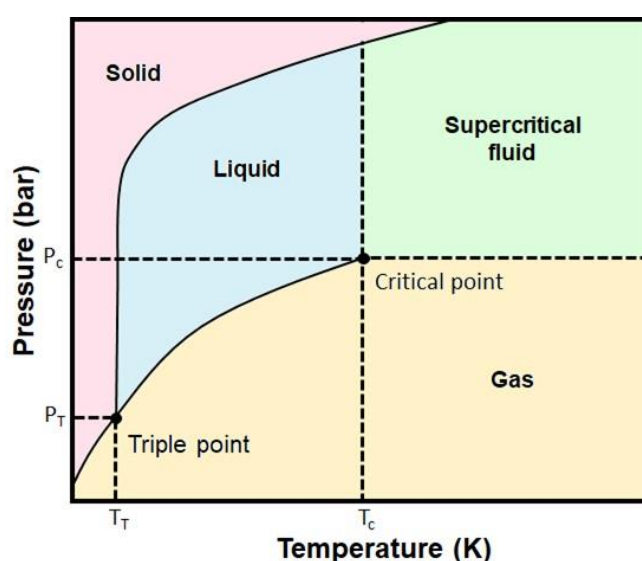
Figure 1. Schematic representation of the pressure-temperature phase diagram.

According to Table 2, several pure substances can be applied in SCF technology, and the choice depends on the critical point [28]. Water has been applied as SCF due to its low cost, non-toxicity, and high availability. However, it has a high critical point with T_c 374.15 °C and P_c 22.05 MPa. Thus, $scCO_2$ has been noted for presenting these advantages and, additionally, due to the easy separation of the product after depressurization. Besides that, the low critical temperature of the CO_2 allows its application in non-thermal processing. It has been explored in several applications involving thermosensitive compounds, such as phytochemicals and drugs. Criteria such as flammability, corrosivity, and toxicity are taken into consideration for suitable solvent selection. Material manufacturing companies seek alternatives to toxic and hazardous solvents due to environmental concerns. As a non-toxic solvent, $scCO_2$ has enormous potential for material synthesis processes [29].

Table 2. Critical properties of different SCFs

Compound	T_c (°C)	P_c (MPa)	Remarks
Ammonia	132.4	11.29	Irritant and corrosive
Benzene	289.1	4.9	Carcinogen and high critical temperature
Carbon dioxide	31	7.38	Low critical temperature
Chlorotrifluoromethane	111.8	3.9	Ozone-depleting potential
Ethanol	243.1	6.39	High critical temperature
Isopropanol	235.6	5.37	High critical temperature and low toxicity
Methanol	240.6	7.9	High critical temperature
n-Propane	93.9	4.3	Asphyxiant
Propane	96.8	4.26	Asphyxiant
Water	374.1	22.1	Corrosive properties and high critical temperature

3. Supercritical CO_2 impregnation and kinetic control of the compounds

The impregnation is a penetration or saturation process of a specific active compound or particle onto a desirable support surface. The support materials may have their physical and chemical properties modified according to the impregnated adsorbed onto the surface or bulk material. Despite having low diffusion, long contact time, and impregnated overload, impregnation can be more effective and sustainable using the $scCO_2$ process [30]. Although $scCO_2$ as a reaction medium has some disadvantages such as low solubility of reagents in dense CO_2 and enzymatic deactivation, it has the advantage of non-toxicity, low cost, and inflammability. Factors involving reagent solubility can be solved using co-solvents [31].

As illustrated in Figure 2, the impregnation must occur by compression and mixing with pressurized gas in the supercritical state for the impregnated material's sorption. The impregnation step occurs at the appropriate temperature to allow the profound reach and concentration necessary to obtain specific substrate properties. Decreasing pressure can open the vessel and remove the substrate, as the temperature decrease due to the Joule-Thompson effect (isoenthalpy expansion) causes the solvent to evaporate. After impregnation, impregnations, additives, or other compounds in the material gas are removed. The expansion of the container containing the impregnated material is crucial, as it influences the final

product's quality. Post-treatment of the product can be useful for removing residual solvents and deodorizing the material [30].
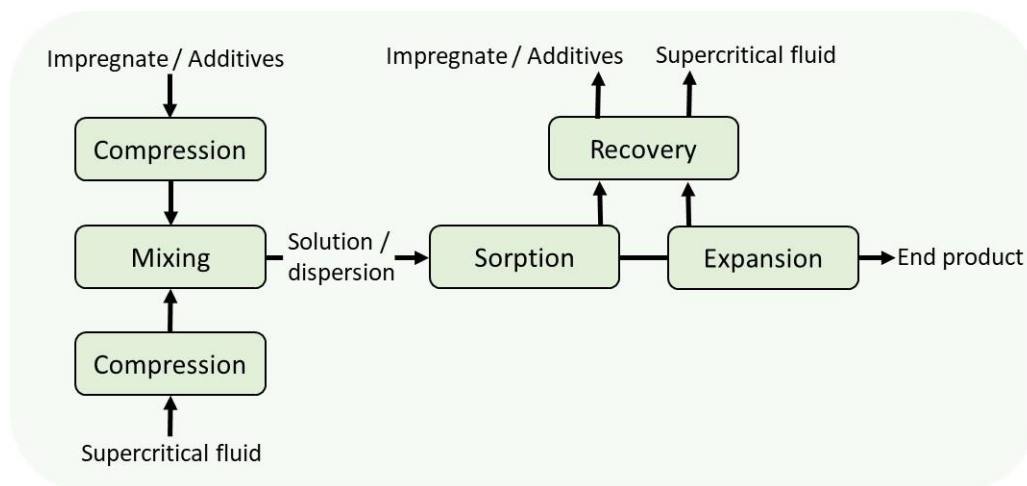
Figure 2. Schematic representation of the impregnation/sorption process under supercritical conditions.

The thermodynamic control of the surface occurs in the metal's adsorption/sorption, followed by the precursor's transformation into the metallic form. Figure 3 illustrates the different ways of converting the metallic precursor to its metallic form. The transformations involve chemical reduction with an SCF or pure hydrogen, thermal reduction at atmospheric pressure, or an SCF. Thermal reduction in an inert atmosphere results in smaller spherical nanoparticles. Growth occurs by superficial diffusion of metal atoms and/or precursor molecules. The chemical reduction in $scCO_2$ with hydrogen provides surfaces coated with nanoparticles dispersed within a porous structure [32].
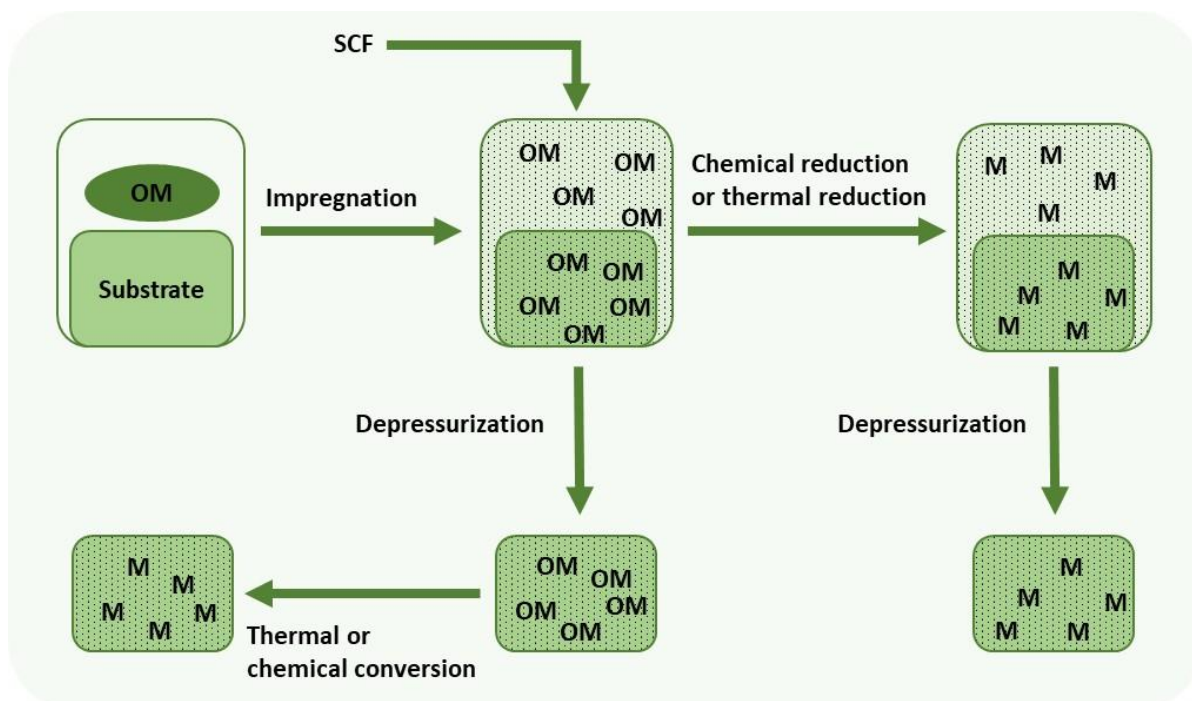
Figure 3. Scheme of the synthesis of nanoparticles by deposition using SCF as a solvent. Adapted from Zhang and Erkey [12], with permission from Elsevier.

In addition to thermodynamic control, the modification of the materials' surface can occur through kinetic control. Copper nanoparticle decorated silica was developed in a supercritical medium for application as advanced nanostructured materials [33]. The precursor's kinetic decomposition model considered the initial homogeneous nucleation and the rapid heterogeneous growth on the silica particles' surface. According to the simulated model, the experimentally synthesized nanoparticles exhibited a controlled size between 100 and 125 °C.

In the absence of silica interaction with copper, spherical Cu nanoparticles are formed depending on the reaction temperature. Pascu, Cacciuttolo, Marre, Pucheault and Aymonier [34] studied the control of surface morphology, composition, and properties under kinetic control. The metal charge (wt.%) and the metal type (Cu, Sn, Pt, and Pd) supported on SiO_2, and Pd supported on different oxides (SiO_2, CeO_2, TiO_2, Fe_2O_3) exhibited different material architectures. The authors reported that homogeneous kinetics, followed by heterogeneous growth in the formation and deposition of nanoparticles, did not depend on the support type. The increased precursor load increased the nanoparticles' size since for 1 and 5 wt.% of Pd, the Pd nanoparticles' size in SiO_2 was 4.5 and 9 nm. Metallic nanoparticles supported on oxides by SCFD proved to be a versatile way to manufacture active materials.

Sorption of magnesium surfaces decorated with Pd, Ni, and Cu nanoparticles is widely studied to improve hydrogen storage [35-37]. The biggest challenge is to keep these catalytic nanoparticles close to the magnesium surface. Denis, Sellier, Aymonier and Bobet [37] studied the hydrogen sorption properties of magnesium particles decorated with metallic nanoparticles (Cu, Ni, and Pd). The authors used the first-order Avrami-Erofeev model, which considers the Fick equation and the Johnson-Mehl-Avrami model. The Cu particles indicated good sorption kinetics at high temperatures (300 °C - absorption and 330 °C - desorption), resulting from improved chemical bonds between Cu and Mg.

Pd nanoparticles were deposited in magnesium-scandium alloys by SCFD to improve hydrogen sorption [38]. Tetravalent metal ions, such as Sc, destabilize the MgH_2 compound, inducing the conversion of the rutile structure of MgH_2 to the fluorite structure $MgScH_2$. Therefore, this phenomenon improves kinetics due to the formation of octahedral and tetrahedral sites in the compound $MgScH_2$ [39]. The sites facilitated the transfer of hydrogen atoms, acting as a transport channel. The sample's absorption kinetics produced at 80 °C, P_{H_2} - 0.5 MPa, P_{CO_2} - 23.5, Pd - 1 wt.%, time - 2 h, is illustrated in Figure 4 [38]. The authors reported that the $Pd@Mg_{0.65}Sc_{0.35}$ nanocomposites absorbed 4.7 wt.% hydrogen during the activation cycle. The passivation of the sample caused by treatment with SCFD affected the experimental comparison with the theoretical. The kinetic curve consisted of two stages, indicating two different hydrogenation reactions. The first was regarding the decomposition of $Mg_{0.65}Sc_{0.35}$, and the second corresponded to the reaction between hydrogen magnesium.
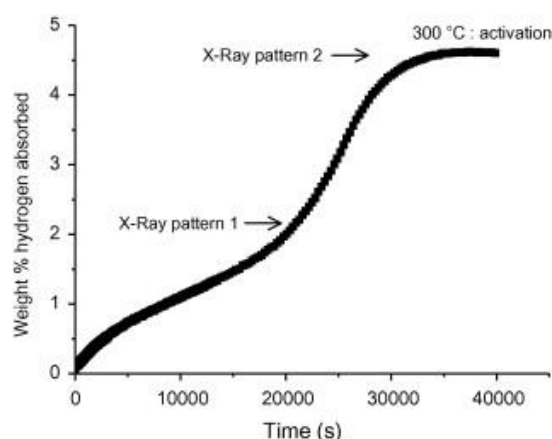
Figure 4. Hydrogen activation kinetic for $Pd@Mg_{0.65}Sc_{0.35}$ compound, under 1 MPa of H_2 and 300 °C. Adapted from Couillaud et al. [38], with permission from Elsevier.

4. ScCO₂ applications in the synthesis of catalytic nanoparticles

The obtaining and design of metallic nanoparticles are of interest to the scientific community and industrial sectors. They display high surface area at the nanometer scale, and the optical, magnetic, photocatalytic, and electrical properties of these materials become sensitive due to the particle's size and shape [12, 40-42]. Supercritical technology for particle engineering and design is recognized for being environmentally friendly and offering an effective path to sustainability, due to the non-generation of contaminant residues that can cause pollution of air, soil, and water-lint [43]. The metal nanoparticles' catalytic properties depend on the nature of the particles' bonding to the substrate's surface. Hence it is closely related to the manufacturing process. The use of supercritical fluid to synthesize catalysts allows generating materials with high catalytic activity in chemical reactions [44].

Particle formation can occur through various processes using $scCO_2$. They are classified according to the role of $scCO_2$ in the process, as illustrated in Figure 5. $ScCO_2$ can act as a solvent, anti-solvent, solution nebulizer, extractor and anti-solvent, and solute [14].
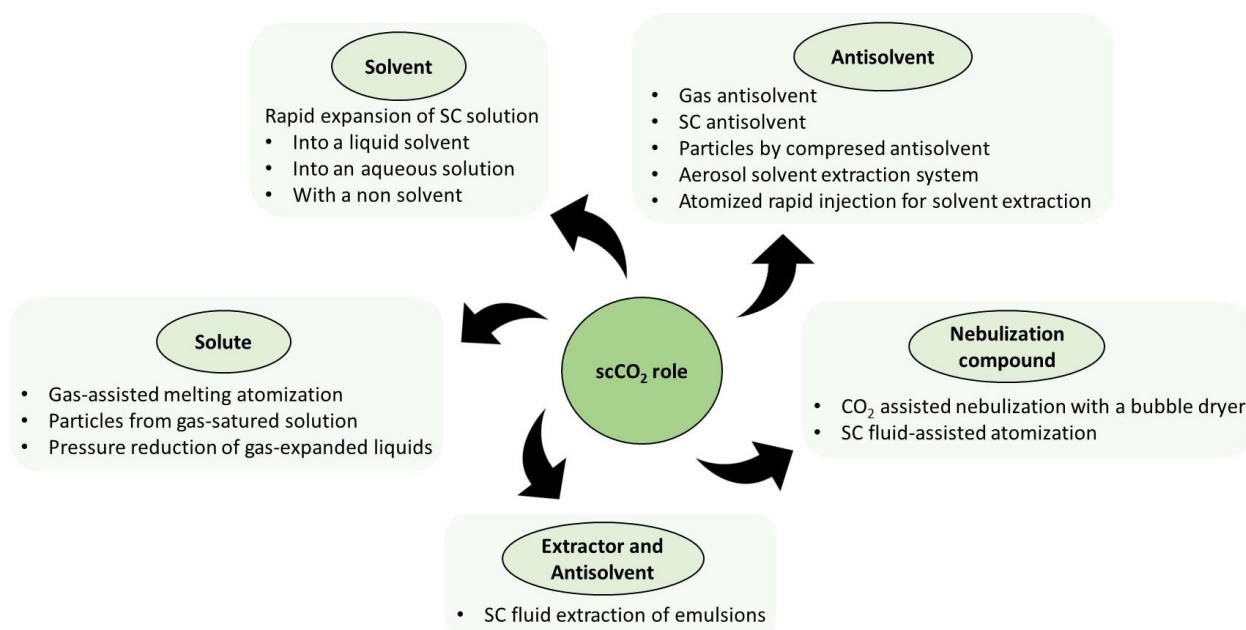
Figure 5. Several $scCO_2$ roles on the particle formation.

4.1. Adsorption and conversion of metal complexes on surfaces in the presence of scCO₂

The thermodynamic equilibrium represented by the adsorption isotherm is the limiting factor in determining the amount of metal complexes loaded into the adsorbent. The metal complexes' affinity with $scCO_2$ and the adsorbent support and the interaction forces related to temperature and pressure changes are determined by an adsorption isotherm [45]. Thus, it is essential to understand the thermodynamics behavior for the process development using $scCO_2$ technology. High-surface area substrates, usually carbon-based materials, the adsorption of metal complexes occurs within the pores, which results in the formation of a surface monolayer coating, represented by Langmuir-type isotherms when the precursor metal exhibits moderate solubility in $scCO_2$ [46].

Metal loading during supercritical impregnation can be adjusted by loading the support with the metal complexes. The amount depends on the adsorption isotherm of the precursors. The adsorbed precursors are converted to metal by the *ex-situ* pathway, usually at low pressure after the depressurization process [12]. *In situ* conversion consists of the precursor being initially converted to the metal in the vessel using conversion agents such as H_2 gas or organic substances (alcohol) in $scCO_2$.

4.3. Effect of process variables

High-performance catalytic system applications under supercritical process conditions offer viable alternatives for developing sustainable industrial processes based on green chemistry applications [47]. Process conditions, such as the type of metal precursor, temperature, pressure, and deposition time, were optimized in the deposition of Pt nanoparticles dispersed in γ-Al_2O_3 [48]. The authors used inorganic metal precursor salt, justified by the high cost and complexity of synthesis when using organic metal precursor salt. The largest dispersion of Pt particles (41.8%) occurred from the precursor Na_2PtCl_6, while the smallest used $Pt(cod)Cl_2$ as the Pt precursor salt, indicating 25.6% Pt dispersion. The largest Pt charge (0.37 wt.%) and smaller particle size (1.5 ± 0.4 nm) were also obtained from the precursor Na_2PtCl_6. The authors attributed the high particle dispersion due to the ethanol used as a co-solvent, which improved the inorganic precursor solubility in $scCO_2$ [49].

Regarding the temperature, the increase from 35 to 40 °C increased the Pt precursor's dispersion because of the increased diffusion coefficient of scCO$_2$ [48]. The smallest particle size was obtained at 40 °C. The pressure analyzed from 9 to 17 MPa indicated a decrease in the Pt particle size, followed by an increase. The time of 3 h led to the formation of smaller particles. A short time will not allow the diffusion of Pt in the support. The Pt/Al$_2$O$_3$-Na$_2$PtCl$_6$ catalysts exhibited high catalytic activity in cyclohexane dehydrogenation with increasing Pt load, demonstrating future industrial applications.

Table 3 displays the metal catalysts impregnated in the last seven years using supercritical technology, such as Pd and Pd-Ag in Al$_2$O$_3$ at 45 to 60 °C of temperature and 15 to 24 MPa of pressure for application in the acetylene ethylene hydrogenation reaction [50]. The authors assumed that the reaction occurred on the catalyst surface and not inside the pores. The increased temperature and pressure for Pd impregnation decreased the degree of acetylene hydrogenation. Ag impregnation after Pd impregnation improved the hydrogenation degree (close to 96%) and decreased pore volume to 0.289 cm^3 g^{-1}.

Cobalt oxide nanoparticles were deposited on porous silica support through supercritical fluid [51]. The first stage (deposition) consisted of using the temperature at 70 °C, with a pressure of 11 MPa for 3 h. A study with different pressures (6, 11, 14, 17, and 20 MPa) for the second stage (decomposition) demonstrated that the maximum content was 2.90 wt.% with the pressure of 14 MPa at 200 °C lasting 3 h. The authors found that metal loading increased with the thermal degradation time of the precursor. The maximum value was 3.4 wt.% Co at 120 min, demonstrating that the decomposition step should not exceed 1 h. When the variable analyzed was time, the combination of 3 h in the first stage (70 °C, 11 MPa) and 1 h in the second stage (200 °C, 14 MPa) presented 4.30 wt.%.

According to Table 3, current studies little explore the process variables during impregnation to synthesize metal catalysts. TiO$_2$ dispersed Pt was synthesized in supercritical condition at 300 °C and 20 MPa for photocatalytic application in solar fuels [52]. The study proposes to compare Pt in TiO$_2$ with commercial TiO$_2$ catalysts. The results were better or similar, producing a catalyst with high surface area and pore volume. The authors pointed out that the supercritical impregnation method was more ecological and scalable than traditional techniques that are expensive and laborious procedures.

For studies that verified the influence of variables, Pt, Ru and Ni were impregnated in graphene oxide under different experimental conditions varying pressure and temperature in

3 steps: impregnation using scCO$_2$ and reduction with H$_2$/N$_2$ or H$_2$/CO$_2$ [53]. The particle size evidenced by transmission electron microscope (TEM) was increased from 4.6 ± 0.1 to 5.4 ± 0.2 nm compared to the reduction step at H$_2$/N$_2$ at 200 °C with H$_2$/CO$_2$ at 80 °C. The initial precursor concentration in CO$_2$ was relevant as the metal charge increased from 0.4 ± 0.2 to 6.6 ± 0.2 wt.% when the concentration changed from 2.2 10^{-5} to 4.5 10^{-5} y. The catalytic activity of metals in reduced graphene oxide (rGO) was observed in the limonene hydrogenation reaction. The catalyzed reaction for 60 min using Pt/rGO, reduced in H$_2$/CO$_2$, showed 78% conversion. For the same scenario using Ru/rGO, the conversion was 77%. Compared with commercial Ru/C catalysts, for the same reaction time of 60 min, the conversion was 42%. The authors associated the high activity and selectivity with the support structure's 2D opening, which promoted the adsorption of compounds and desorption of intermediate products.

The temperature, pressure, and reduction medium were analyzed for mesoporous silica impregnated Pt bimetallic catalysts for application in the furfural hydrogenation reaction [54]. For reaction time of 150 and 180 min, the Pt catalyst demonstrated the highest conversion (73% for both times), impregnated at 60 °C and 13.0 MPa, and reduced in H$_2$/CO$_2$ at 80 °C. The authors observed that the nanoparticles deposited by the H$_2$/CO$_2$ reduction methodology grew larger than the reduction in H$_2$/N$_2$. Even though the CuPt and RuPt bimetallic catalysts showed lower activity to furfuryl alcohol than Pt, they were the more selective and reduced cost when incorporated into Pt.

Table 3. Summary of catalysts obtained by scCO$_2$

Catalyst	Temperature (°C)	Pressure (MPa)	Contact time (h)	Reduction/ conversion medium	Reduction/ conversion temperature (°C)	Reduction/ conversion time (h)	Application	Reference
Ru on C	80	8	4	H$_2$–N$_2$ (10%-90%)	350	3	Hydrogenation of butanone	[20]
Pd and Pd-Ag at Al$_2$O$_3$	45, 50, 55 and 60	15 to 24	0.33	H$_2$	250	2	Hydrogenation of acetylene	[50]
Co$_x$O$_y$ on MCM41 (mesoporous sílica)	70 and 200	9 to 30	1-3	N/A	N/A	N/A	Catalysts	[51]
Pt dispersed on TiO$_2$	300	20	2	N/A	N/A	N/A	Solar cell production	[52]
Pt, Ru, and Ni on graphene	60 and 80	10 and 13.5	24	H$_2$/N$_2$	200 (Pt) and 400 (Ru, Ni)	5	Partial Hydrogenation of limonene	[53]
Pt, Ru, Cu, Pt-Ru, and Pt-Cu on mesoporous SiO$_2$	60 to 80	13 and 13.5	1 to 4	H$_2$/N$_2$	200 (Pt) and 400 (Ru, Cu, and Pt bimettalics)	4	Hydrogenation of furfural	[54]
Co on MCM41	70	11	3	N/A	N/A	N/A	CO oxidation reactions	[55]
Al$_2$O$_3$ supported MoP	300 and 400	25	1-2	10 % H$_2$/Ar	500	4	Hydrodesulfurization of methyl-3- thiophene	[56]
Pd on pristine graphene, reduced graphene oxide, C nanotubes, and C black	50	18	5	N/A	N/A	N/A	Electro-oxidation of formic acid and methanol	[57]
Pt-Ru-Ni, Pt-Ru, and Pt on graphene	50	16	4	N/A	N/A	N/A	Oxidation of methanol	[58]
Pd supported on amphiphilic functional copolymer	40	25	N/A	H$_2$	35	3	Heck reaction	[59]

Pt on Vulcan XC-72 (carbon)	50	13.2	12	H_2, N_2, and $scCO_2$	Room and 200 (H_2) 200 (N_2) 120 ($scCO_2$)	4 (H_2) 4 (N_2) 6 ($scCO_2$)	Proton Exchange membrane fuel cells	[60]
Pt on TiO_2, Al_2O_3, and mesoporous silica	80	15.5	20	H_2 and $scCO_2$	25 and 80	2	Catalyst	[61]
Pt on graphene	200 ($H_2 + CO_2$)	16 ($H_2 + CO_2$)	N/A	$H_2 + CO_2$	300	1.5	Direct methanol fuel cells	[62]
Pt-Ru on graphene	200 ($H_2 + CO_2$)	16 ($H_2 + CO_2$)	0.5	N/A	N/A	N/A	Direct methanol fuel cells	[63]
Rh-Pt on SBA-15 (mesoporous silica)	40	17.24	2	H_2	400	2	Hydrogenation of terephthalic acid in water	[64]
Pd on mesoporous SiO_2	80	17.2	N/A	$H_2 + CO_2$	80	8	Catalysts	[65]
Pt on mesoporous graphene aerogel	35	10.7		N_2	200, 400, 600 and 800	4	Oxygen reduction reaction	[66]
Au and Au-Ag nanoparticles on BP2000 (carbon black), γ-Al_2O_3, TiO_2, and β- cyclodextrin	80	15.5	20	$H_2 + CO_2$	80	2	Chemical reactions	[67]
Pt-Cu on mesoporous carbon aerogel	35	10.7	N/A	H_2 (Cu) N_2 (Pt)	200	2	Oxygen reduction reaction	[68]
Pt and Pd-Pt nanoparticles on porous carbon	40-70	N/A	0.5	N/A	N/A	N/A	Hydrogenation of furfural	[69]
PtIrCo nanoparticles into 3D carbon aerogel	82	20	48	10% H_2/ 90% Ar	600 and 900	1	Methanol oxidation and oxygen reduction reaction	[70]
$Pt_{40}Fe_{60}$ on 3D graphene	60	15.2	2	N/A	N/A	N/A	Oxygen reduction reaction	[71]
Pt/graphene sheet composites	70	24.5	6	N_2	200	4	Methanol electrooxidation	[72]
Carbon aerogel supported Pt nanoparticles	80	27.6	N/A	N_2	200, 400, 600, 800, and 1000	4	Oxygen reduction reaction	[73]

Pt on C nanotubes	200	10	1	5% H_2 in CO_2	200	0.5	CO_2 electroreduction	[74]
Ag nanoparticles on lignin-derived electrospun carbon nanofibers	36	17.2	24	10% N_2/H_2	180	2	Oxygen reduction reaction in alkaline fuel cells	[75]
N, Co, and N-Co carbon aerogel nanostructures	70	20	N/A	H_2 and N_2	800	2 and 4	Oxygen reduction reaction	[76]
Fe_3O_4 nanoparticles on hierarchical porous carbon	200	20	2	N/A	N/A	N/A	Lithium coin cells	[77]
Pt-Cu on carbon aerogel and Vulcan XC-72 (carbon)	80	17.2	24	H_2 and $scCO_2$	135	6	Polymer electrolyte membrane fuel cells	[78]
Pt-Fe and Pt-Fe-Co on porous graphene cellular monolith	50	25.3	2	borane tetrahydro furan and $scCO_2$	60	1	Oxygen reduction reaction	[79]
Pb on C nanotubes	200	10	1	5% H_2 in CO_2	200	0.5	CO_2 electroreduction	[80]
Ru/polydimethylsiloxane nanocomposites	40	10.34	24	N_2	250	6	Catalytic growth of semi-conductor nanowires and biomedical applications	[81]
Pt-Fe, Pt-Ni, and Pt-Cu decorated graphene	60	24	24	N_2	400	4	Polymer electrolyte membrane fuel cells	[82]
Cu nanoparticles on C nanotubes	200	10	1	4.5% H_2 in CO_2	200	0.5	CO_2 electroreduction	[83]
Al-modified SBA-15-supported Ru	40	17.24	2	H_2	400	2	Hydrogenation of dimethyl terephthalate in water	[84]
Pt nanoparticles on graphene nanoplatelets and carbon black	35	12	N/A	N_2	400	4	Polymer electrolyte membrane fuel cells	[85]

Pd nanoparticles on SBA-15 (mesoporous silica)	80	17.2	1	H_2 and CO_2	80	24	Suzuki–Miyaura C-C cross-coupling reaction of a phenylboronic acid and bromobenzene	[86]
Pd on multi-walled C nanotubes	90	27.6	N/A	H_2 and CO_2	N/A	4	Suzuki cross-coupling reaction of a phenylboronic acid and bromobenzene	[87]
Ru on C nanotubes	45	17	4	H_2-N_2 (10-90%)	350	3	Chemical industry	[88]
Pt nanoparticles over polyethylenedioxythiophene /carbon composites	70	24	N/A	N_2	200	4	Proton exchange membrane fuel cells	[89]
V_2O_5 on C nanotubes	170	28.96	2	N/A	N/A	N/A	Electrochemical capacitors	[90]
Nanosilicon and carbon nanotubes incorporated in the folded graphite layer (Si/CNTs@FG)	70	12	2	N/A	N/A	N/A	CR2025 coin-type half cells	[91]
Alumina-supported Pt-CeO$_x$	60	14.2	20	5% H_2 in N_2	350	N/A	Water-gas shift reaction	[92]
Undoped and Cu-doped TiO_2 nanofibers	40, 60, and 80	20 and 24	24	N/A	N/A	N/A	Photocatalytic reduction of CO_2	[93]
Pd nanoparticles in the mesopores of hierarchical porous SiO_2	60	20	24	H_2 and N_2	200	5	Hydrogenation of styrene to ethylbenzene in methanol	[94]
Copper selenide decotared with graphene oxide	200 (reduction)	20 (reduction)	1	N/A	N/A	N/A	Electrochemical sensing of eugenol	[95]
γ-Alumina supported Pd nanoparticles	90	27.6	1	H_2 and CO_2	900	4	Suzuki-Miyaura coupling reactions	[96]
Reduced graphene oxide-C black	35	12	N/A	N_2	400	4	Proton exchange membrane fuel cells	[97]

Ru nanoparticles onto SiO_2 SBA-15	80 (scCO2) 80 (scH$_2$-CO$_2$) 35 (sc 10% EtOH + CO$_2$)	13.5-19.3 (scCO$_2$) 14 (scH$_2$-CO$_2$) 8.5 (sc 10% EtOH + CO$_2$)	24, 2, and 2-4	H$_2$/N$_2$	150, 200 and 400	3 and 5	Hydrogenation reactions of benzene and limonene	[98]
Ru nanoparticles supported on activated C	45	10	4	H$_2$-N$_2$ (10-90%)	350	3	Hydrogenation reactions	[99]
Pt nanoparticles over graphene nanoplatelets	35	12	N/A	N$_2$	400	4	Proton exchange membrane fuel cells	[100]
Cu on C nanotubes	200	10	1	5% H$_2$ in CO$_2$	200	0.5	CO$_2$ electroreduction	[101]

4.4. Electrocatalysts for energy storage systems

ScCO$_2$ deposition results in highly dispersed nanoparticles with limited particle size [73]. Besides, this method does not disturb the nanostructure, which can be disrupted due to capillary pressures during impregnation drying. To obtain electrical conductivity, high electrode-specific surface area, and chemical stability, carbon-based materials such as reduced graphene oxide must be homogeneously dispersed to promote effective charge transfer between the nanoparticles and graphene sheets [95, 102]. In this context, supercritical deposition has been a solution to this need, and it has been a viable technique for producing electrocatalysts that outperform commercial electrocatalysts.

Pt nanoparticles were deposited on a Vulcan VX-72 carbon support at 13.2 MPa and 50 °C for application to proton exchange membrane combustible cells (PEMFCs) [60]. Three precursor conversion routes were evaluated: 1) thermal conversion to N$_2$; 2) thermal conversion to scCO$_2$; 3) chemical conversion to H$_2$. The mean Pt nanoparticle diameters evidenced by TEM were smaller for route 1 (1.7 nm) and larger for route 3 (6 nm). The Pt electrocatalyst deposited by route 1 presented the highest peak power density with a value 190 mW cm^{-2}, proving to be a suitable route for preparing PEMFCs catalysts.

The deposition of Pt in graphene nanoplatelets (GNP) and carbon black (CB) occurred under lower temperature and pressure of scCO$_2$ [85]. For this purpose, Pt was deposited in different GNP/CB (w:w%) ratios at 35 °C and 12 MPa. The 60:40 ratio carrying 0.4 g Pt cm^{-2} indicated the best performance in the polymer electrolyte membrane fuel cell, comparable to the commercial ETEK catalyst. The high surface area and small pore volume resulted in greater accessibility of the Pt nanoparticles. The nanoparticles for all ratios were well distributed in the support. However, some of them were electrochemically inactive due to the surface's occlusion caused by the support.

Sarac Oztuna et al. [66] evaluated the precursor conversion temperatures to metal. The average particle size increased from 1.2 to 2.9 nm when the temperature was changed from 400 to 800 °C. The authors deposited Pt in porous graphene aerogel for application in the ORR. The sample impregnated at 600 °C and 10.7 MPa exhibited the largest electrochemical surface area (102 m^2 g^{-1}). The sample impregnated at 800 °C demonstrated the lowest mass activity (12 mA mg$_{Pt}^{-1}$) and electrochemical surface area (43 m^2 g^{-1}) due to Pt nanoparticle agglomeration,

resulting in a high specific activity. scCO$_2$ deposition techniques allow controlled modification of nanoparticle size distribution.

In general, SCFD studies evaluate the metal charge in the catalyst composition. Ag nanoparticles' catalytic activity deposited on lignin-derived electrophilic nanofibers under supercritical conditions was evaluated for alkaline cells [75]. The deposition in the scCO$_2$ environment at 36 °C and 17.2 MPa followed by heat treatment in H$_2$/N$_2$ at 180 °C analyzed Ag and nanofibers ratios (1:1, 2:1, and 3:1). scCO$_2$ promoted Ag reduction, and heat treatment allowed conversion into Ag nanoparticles. Scanning electron microscopy (SEM) characterization indicated that increasing the Ag ratio increased nanoparticle size from 35 to 73 nm, as illustrated in Figure 6. ORR's electrochemical results in 0.1 M KOH indicated a high catalytic activity by the theoretical pathway with a value close to four electrons. The composition containing 15 wt.% Ag on the nanofibers exhibited the highest mass activity (119 mA mg^{-1}) with better results than the commercial Pt/C catalyst (98 mA mg^{-1}).
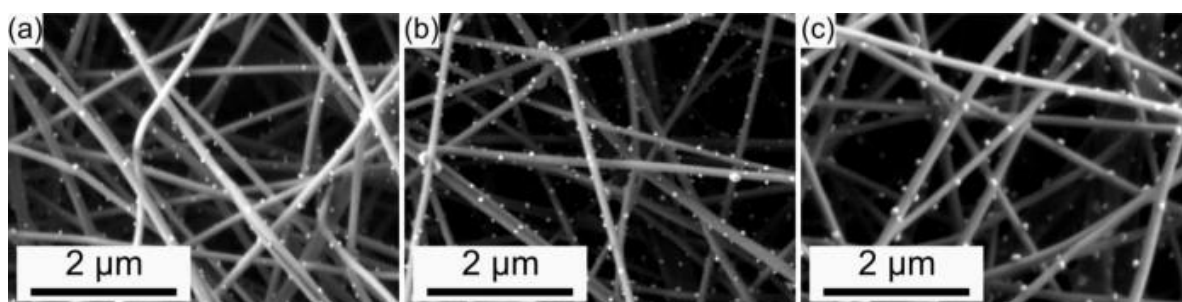
Figure 6. SEM micrographs of the Ag/electrospun carbon nanofibers electrocatalytic systems with the Ag loading amount a) 11, b) 15, and c) 25 wt.%. Adapted from Lai et al. [75], with permission from Elsevier.

Three electrocatalyst synthesis methods were compared to demonstrate the advantages of SCFD [83]. Cu nanoparticles deposited in CNT were synthesized by precipitation, microemulsion, and supercritical deposition for application in the electrochemical reduction of CO$_2$. The highest yield of Cu deposition in CNT occurred by precipitation (89.7%), followed by SCFD (85.1%). The microemulsion method showed the lowest yield (59.3%). The highest CO$_2$ conversion rate occurred with the catalyst produced by SCFD, while the lowest rate occurred with the catalyst obtained by precipitation. Diffractogram peaks corresponding to metallic copper nanoparticles were only obtained by SCFD. The precipitation method led to the

formation of a mixture of copper oxides. To the authors, the SCFD method demonstrated great potential for the synthesis of electrocatalysts.

The comparison of methods for the synthesis of Pt electrocatalysts was also studied by Daş et al. [103]. The authors compared the SCFD (Pt/G2) and microwave irradiation (Pt/G1) method in the synthesis of Pt supported on graphene nanoplatelets for converting the energy in PEMFCs. The catalyst synthesized by SCFD had a smaller particle size (1.5 nm) than synthesis by microwave irradiation (3.4 nm). The SCFD method led to a decrease in the degree of agglomeration of nanoparticles during the reduction process, caused by the high interaction of the adsorbed precursor ions and the support material's surface. Cyclic voltammograms are illustrated in Figure 7-a-b. The electrochemical surface area (ESA) of the catalysts was calculated from the hydrogen adsorption and desorption peaks. Before aging, the ESA of Pt/G2 ESA was 87.2 m^2 g^{-1}, while Pt/G1 24.2 m^2 g^{-1}. After aging, the value obtained was 51.4 and 10.7 m^2 g^{-1}, respectively. The higher ESA of Pt/G2 resulted from the smaller particle size and better interaction between Pt nanoparticles and graphene. Moreover, the Pt/G2 catalyst demonstrated better performance in regions of higher and lower current density in PEMFCs.
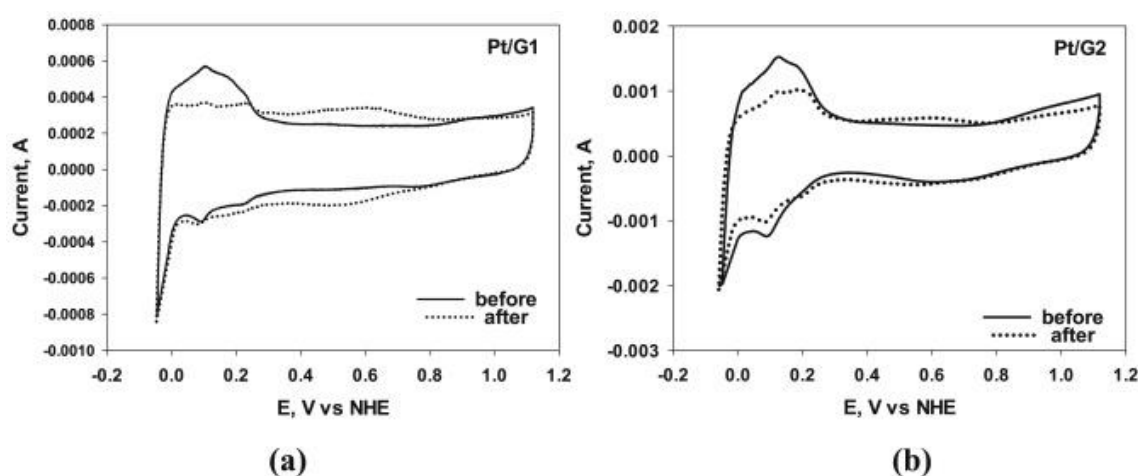
Figure 7. Cyclic voltammograms taken before and after the aging test in 1 M H_2SO_4 at a scan rate of 50 mV s^{-1} for the synthesized a) Pt/G1 and b) Pt/G2 catalysts. Adapted from Daş et al. [103], with permission from Elsevier.

5. Combination of deposition techniques

A combination of techniques can be used with scCO$_2$, such as electrodeposition consisting of a power supply, anode, and a cathode within the vessel to obtain specific material characteristics. The addition of surfactants to the electrolyte enables emulsion formation that provides improved properties and better aesthetic finish to metal alloys [104]. However, this technique is made difficult when applied on a large scale by the high cost of pressure equipment. Large-scale production has been suggested to use high-intensity ultrasound technology to form a homogeneous emulsion [105]. The application of ultrasound in a liquid medium promotes the acoustic cavitation phenomenon, promoting the formation and subsequent collapse of microbubbles, increasing the fluidity in the fluid medium [106, 107].

6. Patents on nanoparticles deposition and production using scCO$_2$

The invention of methods and devices for nanomaterials involving supercritical fluid has been patented in the last decade. Hæggström et al. [108] developed a device for the nanoparticles' production by the controlled expansion of pressurized solutions. The system consists of 1) pressure chamber - Mix the organic substance with the supercritical fluid; 2) nanoparticle collection chamber; 3) outlet tube - Connects the pressure chamber to the collection chamber; 4) one or more second nozzles. The outlet tube was configured to control the mixture's pressure, and the first nozzle is configured to allow expanding the mixture into the collection chamber. The invention allowed the production of nanoparticles smaller than 20 nm using a gradient pressure reduction process.

Su et al. [109] developed a scCO$_2$ deposition method of gold nanocrystals adsorbed on the graphene sheet. The deposition occurred between 115 - 125 °C, 10 - 12 MPa, with the mutual electrostatic attraction of gold ions and graphene oxide. The uniform distribution of nanocrystals and minuscule grain size makes applying this method in areas such as catalysis, energy storage, and lubrication.

Nano-silver/graphene composites were prepared by SCFD. The conditions for deposition occurred between 10 ~ 15MPa and 60 ~ 90 °C [110]. The nanocomposites exhibited controllable load capacity, single-phase and small grain size, and uniform distribution between graphene nanofibers' layers. The authors report that the preparation method is simple, fast, and

provides minuscule-sized nanoparticles, with a 5-10 nm diameter. Other applications of $scCO_2$ include the control of agglomeration of nanoparticles in the electroplating process [111], methods of preparing graphene composites/metal oxide nanoparticles [112], and the production of cadmium sulfide nanoparticles [113]. In general, patents report uniform particle size, simplicity, and low cost of the process.

7. Critical discussion and economic approaches

The morphology, surface area, and pore volume are affected by $scCO_2$ process variables such as pressure, temperature, and processing time. The metal precursor's solubility is a relevant issue in successfully using $scCO_2$ technology for effective impregnation. However, most studies conducted have not yet evaluated the synergistic effects among the main process variables. The volume rate of CO_2 is most often not considered a process variable. Bilalov et al. [50] reported that impregnation efficiency decreased as the CO_2 flow rate increased. A higher solvent flow indicated a shorter contact time between CO_2 and the substance to be developed, resulting in a lower concentration of palladium chloride in CO_2. The ideal range of CO_2 flow rate was 1 to 5 mL min^{-1}. The contact time had a greater hydrodynamic effect of improving mass transfer than the high flow rates. The intensification of turbulence in the high-pressure reactor is another essential factor that can increase the diffusion of CO_2 inside the material, increasing the mass transfer coefficients.

Although the results in recent years have proven the $scCO_2$ impregnation technique's viability, there are no reports involving the process's financial viability for nanoparticles. Economic evaluation has been applied to several $scCO_2$ processes, such as extracting bioactive compounds [114, 115] and phytonutrients [116]. Commercial software such as SuperPro Designer® estimates the economic viability (US\$ kg^{-1}) considering the fixed capital investment, raw material costs, equipment, operational labor, waste treatment, and utilities (water, electricity, and steam). Direct costs (electrical installations, instrumentation, and installation, etc.) and indirect costs (insurance, human resources, engineering, and construction, etc.) are also considered in the simulation of the economic evaluation [116]. Promoting economic feasibility studies in a materials synthesis process is necessary to attract investment from the industrial sector and large-scale production.

8. Conclusions and future perspectives

This review demonstrated the potential of $scCO_2$ for the impregnation of metal nanoparticles, oxides, among other materials. The nanoparticles' morphological and physicochemical characteristics can be changed depending on the metal complexes' interaction with the support material's surface, the reactions that occur on the surface, and the nanoparticle conversion method. Studies involving these mechanisms are limited and need further study. Computational simulation, along with experimental methods, could be an alternative to describe through modeling the properties of nanoparticles, such as selectivity and reaction conversion, according to the SCF state. Exploring the synergy between process variables (flow rate, contact time, temperature, and pressure) and economic feasibility studies are relevant to promoting this fashionable ecological technology.

Acknowledgments

References

[1] J.M. Costa, A.F. de Almeida Neto, Electrocatalysis, 10 (2019) 532-539.

[2] J.M. Costa, A.F. de Almeida Neto, Journal of Solid State Electrochemistry, 23 (2019) 2533-2540.

[3] W. Hu, S. Chen, Q. Xia, International Journal of Hydrogen Energy, 39 (2014) 6967-6976.

[4] Z. Huang, F. Cui, J. Xue, J. Zuo, J. Chen, C. Xia, Catalysis Today, 183 (2012) 42-51.

[5] Y. Sim, J. Yoo, J.-M. Ha, J.C. Jung, Journal of Energy Chemistry, 35 (2019) 1-8.

[6] L. Karuppasamy, C.-Y. Chen, S. Anandan, J.J. Wu, International Journal of Hydrogen Energy, 44 (2019) 30705-30718.

[7] K.-T. Li, P.-H. Lin, S.-W. Lin, Applied Catalysis A: General, 301 (2006) 59-65.

[8] J. Chen, Z. Li, Y. Chen, J. Zhang, Y. Luo, G. Wang, R. Wang, Chemical Physics Letters, 755 (2020) 137793.

[9] J.M. Campelo, D. Luna, R. Luque, J.M. Marinas, A.A. Romero, ChemSusChem, 2 (2009) 18-45.

[10] M. Majimel, S. Marre, E. Garrido, C. Aymonier, Chemical Vapor Deposition, 17 (2011) 342-352.

[11] Y. Zhang, D. Kang, C. Saquing, M. Aindow, C. Erkey, Industrial & Engineering Chemistry Research, 44 (2005) 4161-4164.

[12] Y. Zhang, C. Erkey, The Journal of Supercritical Fluids, 38 (2006) 252-267.

[13] S. Marre, F. Cansell, C. Aymonier, Nanotechnology, 17 (2006) 4594-4599.

[14] A. Tabernero, E.M. Martín del Valle, M.A. Galán, Chemical Engineering and Processing: Process Intensification, 60 (2012) 9-25.

[15] S.Y. Lee, L.C. Abdullah, R. Abdul Rahman, F. Abas, W.K. Tan, G.H. Chong, Chemical Engineering Research and Design, 138 (2018) 176-189.

[16] E. Reverchon, G. Della Porta, Chemical Engineering & Technology, 26 (2003) 840-845.

[17] C. Aymonier, G. Philippot, A. Erriguible, S. Marre, The Journal of Supercritical Fluids, 134 (2018) 184-196.

[18] Y. Xu, V. Musumeci, C. Aymonier, Reaction Chemistry & Engineering, 4 (2019) 2030-2054.

[19] S.P. Nalawade, F. Picchioni, L.P.B.M. Janssen, Progress in Polymer Science, 31 (2006) 19-43.

[20] Y. Zhang, H. Jiang, Y. Wang, G. Li, M. Zhang, Catalysis Communications, 56 (2014) 86-91.

[21] Y. Qiao, N. Said, M. Rauser, K. Yan, F. Qin, N. Theyssen, W. Leitner, Green Chemistry, 19 (2017) 977-986.

[22] L. Padrela, M.A. Rodrigues, A. Duarte, A.M.A. Dias, M.E.M. Braga, H.C. de Sousa, Advanced Drug Delivery Reviews, 131 (2018) 22-78.

[23] E.K. Silva, M. Martelli-Tosi, R. Vardanega, G.C. Nogueira, G.L. Zabot, M.A.A. Meireles, Journal of Cleaner Production, 189 (2018) 231-239.

[24] E.K. Silva, M.A.A. Meireles, M.D.A. Saldaña, Trends in Food Science & Technology, 97 (2020) 381-390.

[25] E.K. Silva, H.S. Arruda, M.N. Eberlin, G.M. Pastore, M.A.A. Meireles, Food Research International, 125 (2019) 108561.

[26] N. Koch, O. Jennotte, B. Grignard, A. Lechanteur, B. Evrard, European Journal of Pharmaceutical Sciences, 150 (2020) 105332.

[27] L. Baldino, M. Scognamiglio, E. Reverchon, The Journal of Supercritical Fluids, 165 (2020) 104960.

[28] K. Li, Z. Xu, Journal of Cleaner Production, 227 (2019) 794-809.

[29] S.B. Barim, E. Uzunlar, S.E. Bozbag, C. Erkey, Journal of The Electrochemical Society, 167 (2020) 054510.

[30] E. Weidner, The Journal of Supercritical Fluids, 134 (2018) 220-227.

[31] Ž. Knez, M. Pantić, D. Cör, Z. Novak, M. Knez Hrnčič, Chemical Engineering and Processing - Process Intensification, 141 (2019) 107532.

[32] P. Oana, M. Samuel, A. Cyril, Nanotechnology Reviews, 4 (2015) 487-515.

[33] S. Marre, A. Erriguible, A. Perdomo, F. Cansell, F. Marias, C. Aymonier, The Journal of Physical Chemistry C, 113 (2009) 5096-5104.

[34] O. Pascu, B. Cacciuttolo, S. Marre, M. Pucheault, C. Aymonier, The Journal of Supercritical Fluids, 105 (2015) 84-91.

[35] J.L. Bobet, C. Aymonier, D. Mesguich, F. Cansell, K. Asano, E. Akiba, Journal of Alloys and Compounds, 429 (2007) 250-254.

[36] C. Aymonier, A. Denis, Y. Roig, M. Iturbe, E. Sellier, S. Marre, F. Cansell, J.L. Bobet, The Journal of Supercritical Fluids, 53 (2010) 102-107.

[37] A. Denis, E. Sellier, C. Aymonier, J.L. Bobet, Journal of Alloys and Compounds, 476 (2009) 152-159.

[38] S. Couillaud, M. Kirikova, W. Zaïdi, J.-P. Bonnet, S. Marre, C. Aymonier, J. Zhang, F. Cuevas, M. Latroche, L. Aymard, J.-L. Bobet, Journal of Alloys and Compounds, 574 (2013) 6-12.

[39] P.H.L. Notten, M. Ouwerkerk, H. van Hal, D. Beelen, W. Keur, J. Zhou, H. Feil, Journal of Power Sources, 129 (2004) 45-54.

[40] F. Cansell, C. Aymonier, The Journal of Supercritical Fluids, 47 (2009) 508-516.

[41] S. Kashiwaya, C. Aymonier, J. Majimel, C. Olivier, A. Klein, W. Jaegermann, T. Toupance, New Journal of Chemistry, 42 (2018).

[42] E. Garrido, C. Aymonier, L. Roiban, O. Ersen, C. Labrugère, P. Gaillard, M. Lamirand-Majimel, The Journal of Supercritical Fluids, 101 (2015) 110-116.

[43] M. Türk, C. Erkey, The Journal of Supercritical Fluids, 134 (2018) 176-183.

[44] S. Lang, M. Türk, B. Kraushaar-Czarnetzki, Journal of Catalysis, 286 (2012) 78-87.

[45] S.E. Bozbağ, C. Erkey, The Journal of Supercritical Fluids, 96 (2015) 298-312.

[46] B. Cangül, L.C. Zhang, M. Aindow, C. Erkey, The Journal of Supercritical Fluids, 50 (2009) 82-90.

[47] T. Dang-Bao, D. Pla, I. Favier, M. Gómez, Catalysts, 7 (2017).

[48] H. Jiang, C. Yao, Y. Wang, M. Zhang, The Journal of Supercritical Fluids, (2020) 105014.

[49] J. Ming, C. Wu, H. Cheng, Y. Yu, F. Zhao, The Journal of Supercritical Fluids, 57 (2011) 137-142.

[50] T.R. Bilalov, F.M. Gumerov, F.R. Gabitov, Russian Journal of Physical Chemistry B, 12 (2018) 1287-1293.

[51] S. Aspromonte, A. Sastre, A. Boix, M.J. Cocero, E. Alonso, The Journal of Supercritical Fluids, 110 (2016) 47-55.

[52] S. Tostón, R. Camarillo, F. Martínez, C. Jiménez, J. Rincón, Chinese Journal of Catalysis, 38 (2017) 636-650.

[53] J. Morère, E. Sánchez-Miguel, M.J. Tenorio, C. Pando, A. Cabañas, The Journal of Supercritical Fluids, 120 (2017) 7-17.

[54] E. Sánchez-Miguel, M.J. Tenorio, J. Morère, A. Cabañas, Journal of CO_2 Utilization, 22 (2017) 382-391.

[55] S.G. Aspromonte, M.D. Mizrahi, E. Alonso, J.M. Ramallo-López, A.V. Boix, Microporous and Mesoporous Materials, 239 (2017) 147-157.

[56] B. Motos-Pérez, C. Quilfen, D. Uzio, C. Aymonier, ChemCatChem, 9 (2017) 2352-2357.

[57] J. Zhao, Z. Liu, H. Li, W. Hu, C. Zhao, P. Zhao, D. Shi, Langmuir, 31 (2015) 2576-2583.

[58] J. Zhao, H. Li, Z. Liu, W. Hu, C. Zhao, D. Shi, Carbon, 87 (2015) 116-127.

[59] F. Gasc, S. Clerc, E. Gayon, J.-M. Campagne, P. Lacroix-Desmazes, The Journal of Supercritical Fluids, 105 (2015) 136-145.

[60] S.E. Bozbağ, T. Gümüşoğlu, S. Yılmaztürk, C.J. Ayala, M. Aindow, H. Deligöz, C. Erkey, The Journal of Supercritical Fluids, 97 (2015) 154-164.

[61] S. Wolff, M. Crone, T. Muller, M. Enders, S. Bräse, M. Türk, The Journal of Supercritical Fluids, 95 (2014) 588-596.

[62] J. Zhao, L. Zhang, T. Chen, H. Yu, L. Zhang, H. Xue, H. Hu, The Journal of Physical Chemistry C, 116 (2012) 21374-21381.

[63] J. Zhao, H. Xue, L. Zhang, J. Yu, H. Hu, Journal of Nanoparticle Research, 14 (2012) 935.

[64] W. Yu, Y.-P. Hsu, C.-S. Tan, Applied Catalysis B: Environmental, 196 (2016) 185-192.

[65] F. Ulusal, B. Güzel, The Journal of Supercritical Fluids, 133 (2018) 233-238.

[66] F.E. Sarac Oztuna, S.B. Barim, S.E. Bozbag, H. Yu, M. Aindow, U. Unal, C. Erkey, Electrochimica Acta, 250 (2017) 174-184.

[67] S. Müller, M. Türk, The Journal of Supercritical Fluids, 96 (2015) 287-297.

[68] S.B. Barim, S.E. Bozbag, H. Yu, R. Kızılel, M. Aindow, C. Erkey, Catalysis Today, 310 (2018) 166-175.

[69] D. Hu, H. Xu, Z. Yi, Z. Chen, C. Ye, Z. Wu, H.F. Garces, K. Yan, ACS Sustainable Chemistry & Engineering, 7 (2019) 15339-15345.

[70] P. Kolla, A. Smirnova, Electrochimica Acta, 182 (2015) 20-30.

[71] Y. Zhou, C.H. Yen, Y.H. Hu, C. Wang, X. Cheng, C.M. Wai, J. Yang, Y. Lin, Journal of Materials Chemistry A, 4 (2016) 18628-18638.

[72] J. Zhao, H. Yu, Z. Liu, M. Ji, L. Zhang, G. Sun, The Journal of Physical Chemistry C, 118 (2014) 1182-1190.

[73] Ş.B. Barım, A. Bayrakçeken, S.E. Bozbağ, L. Zhang, R. Kızılel, M. Aindow, C. Erkey, Microporous and Mesoporous Materials, 245 (2017) 94-103.

[74] C. Jiménez, J. García, R. Camarillo, F. Martínez, J. Rincón, Energy & Fuels, 31 (2017) 3038-3046.

[75] C. Lai, P. Kolla, Y. Zhao, H. Fong, A.L. Smirnova, Electrochimica Acta, 130 (2014) 431-438.

[76] S. Ünsal, M.B. Yağcı, S.E. Bozbağ, B. Deljoo, M. Aindow, C. Erkey, Energy Technology, 7 (2019) 1900450.

[77] L. Wang, L. Zhuo, C. Zhang, F. Zhao, Chemistry – A European Journal, 20 (2014) 4308-4315.

[78] S.B. Barim, S.E. Bozbag, B. Deljoo, M. Aindow, C. Erkey, Fuel Cells, 20 (2020) 285-299.

[79] Y. Zhou, X. Cheng, C.H. Yen, C.M. Wai, C. Wang, J. Yang, Y. Lin, Journal of Power Sources, 347 (2017) 69-78.

[80] J. García, C. Jiménez, F. Martínez, R. Camarillo, J. Rincón, Journal of Catalysis, 367 (2018) 72-80.

[81] M. Ge, S.E. Bozbag, C.J. Ayala, M. Aindow, C. Erkey, Materials Chemistry and Physics, 180 (2016) 1-4.

[82] E. Daş, S. Alkan Gürsel, A. Bayrakçeken Yurtcan, The Journal of Supercritical Fluids, 165 (2020) 104962.

[83] C. Jiménez, J. García, F. Martínez, R. Camarillo, J. Rincón, Electrochimica Acta, 337 (2020) 135663.

[84] W. Yu, S. Bhattacharjee, W.-Y. Lu, C.-S. Tan, ACS Sustainable Chemistry & Engineering, 8 (2020) 4058-4068.

[85] E. Daş, B.Y. Kaplan, S.A. Gürsel, A.B. Yurtcan, Renewable Energy, 139 (2019) 1099-1110.

[86] F. Ulusal, E. Erünal, B. Güzel, Journal of Nanoparticle Research, 20 (2018) 219.

[87] B. Tezcan, F. Ulusal, A. Egitmen, B. Guzel, Journal of Nanoparticle Research, 20 (2018) 145.

[88] Y. Zhang, H. Jiang, G. Li, M. Zhang, RSC Advances, 6 (2016) 16851-16858.

[89] G. Bozkurt, F. Memioğlu, A. Bayrakçeken, Applied Surface Science, 318 (2014) 223-226.

[90] Q.H. Do, C. Zeng, Industrial & Engineering Chemistry Research, 57 (2018) 6863-6869.

[91] X. Wang, K. Wen, T. Chen, S. Chen, S. Zhang, Applied Surface Science, 522 (2020) 146507.

[92] J.W. Deal, P. Le, C.B. Corey, K. More, C.W. West, The Journal of Supercritical Fluids, 119 (2017) 113-121.

[93] R. Camarillo, D. Rizaldos, C. Jiménez, F. Martínez, J. Rincón, The Journal of Supercritical Fluids, 147 (2019) 70-80.

[94] K. Matsuyama, S. Tanaka, T. Kato, T. Okuyama, H. Muto, R. Miyamoto, H.-z. Bai, The Journal of Supercritical Fluids, 130 (2017) 140-146.

[95] K. Murtada, V. Moreno, Á. Ríos, M. Zougagh, The Journal of Supercritical Fluids, 153 (2019) 104597.

[96] F. Ulusal, B. Darendeli, E. Erünal, A. Egitmen, B. Guzel, The Journal of Supercritical Fluids, 127 (2017) 111-120.

[97] A. Bayrakçeken Yurtcan, E. Daş, International Journal of Hydrogen Energy, 43 (2018) 18691-18701.

[98] J. Morère, M.J. Torralvo, C. Pando, J.A.R. Renuncio, A. Cabañas, RSC Advances, 5 (2015) 38880-38891.

[99] Y. Zhang, H. Jiang, Y. Wang, M. Zhang, Industrial & Engineering Chemistry Research, 53 (2014) 6380-6387.

[100] E. Daş, S. Alkan Gürsel, L. Işıkel Şanlı, A. Bayrakçeken Yurtcan, International Journal of Hydrogen Energy, 42 (2017) 19246-19256.

[101] C. Jiménez, J. García, F. Martínez, R. Camarillo, J. Rincón, The Journal of Supercritical Fluids, 166 (2020) 104999.

[102] Y. Duan, S. Li, S. Lei, J. Qiao, L. Zou, B. Ye, Journal of Electroanalytical Chemistry, 827 (2018) 137-144.

[103] E. Daş, S. Alkan Gürsel, L. Işikel Şanli, A. Bayrakçeken Yurtcan, International Journal of Hydrogen Energy, 41 (2016) 9755-9761.

[104] B.-W. Wang, C.-Y. Lee, H.-B. Lee, Surface and Coatings Technology, 337 (2018) 232-240.

[105] H.-C. Chuang, G.-W. Jiang, J. Sanchez, Ultrasonics Sonochemistry, 60 (2020) 104805.

[106] M.T. Timko, S. Marre, A.R. Maag, The Journal of Supercritical Fluids, 109 (2016) 51-60.

[107] K.V.B. Tran, T. Kimura, T. Kondo, S. Koda, Ultrasonics Sonochemistry, 21 (2014) 716-721.

[108] E. Hæggström, J. Yliruusi, K. Falck, H. Räikkönen, J. Pessi, I. Lassila, A. Meriläinen, EP3204150A1, Finland (2017).

[109] F. Su, Y. Meng, Y. Chen, CN107096926A, China (2017).

[110] F. Su, Y. Meng, Y. Chen, CN105397103A, China (2016).

[111] W. Lei, W. Liu, X. Li, C. Wang, H. Qian, L. Liu, Y. Shen, (2016).

[112] J. Kim, Y. Dohyeon, W. Li, J. Hwang, US20160099466A1, United States of America (2016).

[113] S. Yan, Z. Shuai, F. Yang, D. Hu, X. Xu, J. Wang, J. Wu, CN104045106B, China (2015).

[114] G.L. Zabot, M.N. Moraes, M.A.A. Meireles, Food and Bioproducts Processing, 109 (2018) 122-138.

[115] G.L. Zabot, I.P. Bitencourte, M.V. Tres, M.A.A. Meireles, The Journal of Supercritical Fluids, 119 (2017) 261-273.

[116] J. Viganó, G.L. Zabot, J. Martínez, The Journal of Supercritical Fluids, 122 (2017) 88-98.

APPENDIX G

Ni-Co-W alloys: Influence of Operational Process Conditions on their Electroplating

Ni-Co-W alloys:

Influence of Operational Process Conditions on their Electroplating

Josiel Martins Costa, Daniella Gonçalves Portela, and Ambrósio Florêncio de Almeida Neto

Abstract

The search for innovative technologies to meet the needs of efficient and sustainable production motivates the development of research on new materials. Ni-Co-W alloys have been studied for replacing chromium due to their superior wear, hardness and corrosion properties. In addition to these properties, Ni-Co-W alloys have remarkable mechanical resistance and thermal stability, which confers the various applications, such as microsensors, thermostable films, anticorrosive coatings, electrocatalysts, and generation of electronic images, among others. However, the management of the parameters that influence the electrodeposition of metallic layers, whose features can be obtained by the optimization of the operational and solution parameters, have attracted the attention of researchers. The change of parameters such as speed agitation, electric current density, temperature, reagent concentration, and pH can modify and improve the features of the electrodeposited layer (accession to the substrate, homogeneity, hardness, corrosion resistance and embrittlement by hydrogen), which is of great importance for industrial applications. In this sense, this chapter aims to demonstrate the effect of operational parameters on morphology, corrosion resistance, and composition.

Keywords: Anti-corrosive materials; microstructure; magnetic materials; electrochemical synthesis; electrodeposition; adhesion; corrosion resistance; bath composition.

1. Introduction

Coatings containing chromium are widely applied in engineering due to the anti-corrosive properties and for presenting a low coefficient of friction and detachable hardness [1]. However, the solution contains toxic chromium ions and by European directives legislation (2000/53/WE and 2011/37/UE) should no longer be used. With the challenge of replacing chromium by other metals, Ni coatings combined with refractory metals have become a source of study for appropriate, promising and environmentally friendly alternatives [2, 3]. Other common challenge is to use less current density without impairing the alloy characteristics.

The electrodeposition of alloys using electrolytes allows uniform coatings to be obtained, being an economical and simple method, and quite applicable when the melting point of the metals involved has a larger range (Ni - 1445 °C, Co - 1495 °C, W - 3410 °C). In addition, the conventional method could lead to the embrittlement by hydrogen, due to the release of hydrogen that would diffuse between the lattice of the substrate, generating failures in the sample [4]. Industrially the electrodeposition using direct current it is the most applied. Savale (2018) considered that this method is easier to reproduce and can provide more control over film thickness when compared to methods as anodization or sputtering deposition [5]. Moreover, metals used to form alloys have an important role to attribute specific characteristics.

Ni-Co alloys have been studied because of the characteristics of a micro mechanically hard material. The researchers have sought to investigate correlations between operating conditions that confer microstructure, microhardness and specific mechanical properties in the material [6-10]. Besides, the electrodeposition process is complex, which involves transport phenomena, material and surface science, and solid-state physics [11]. Thus, there is a range of parameters that can influence the alloy, according to Figure 1, so that the variation of these provides the fabrication of materials with specific properties and applications.
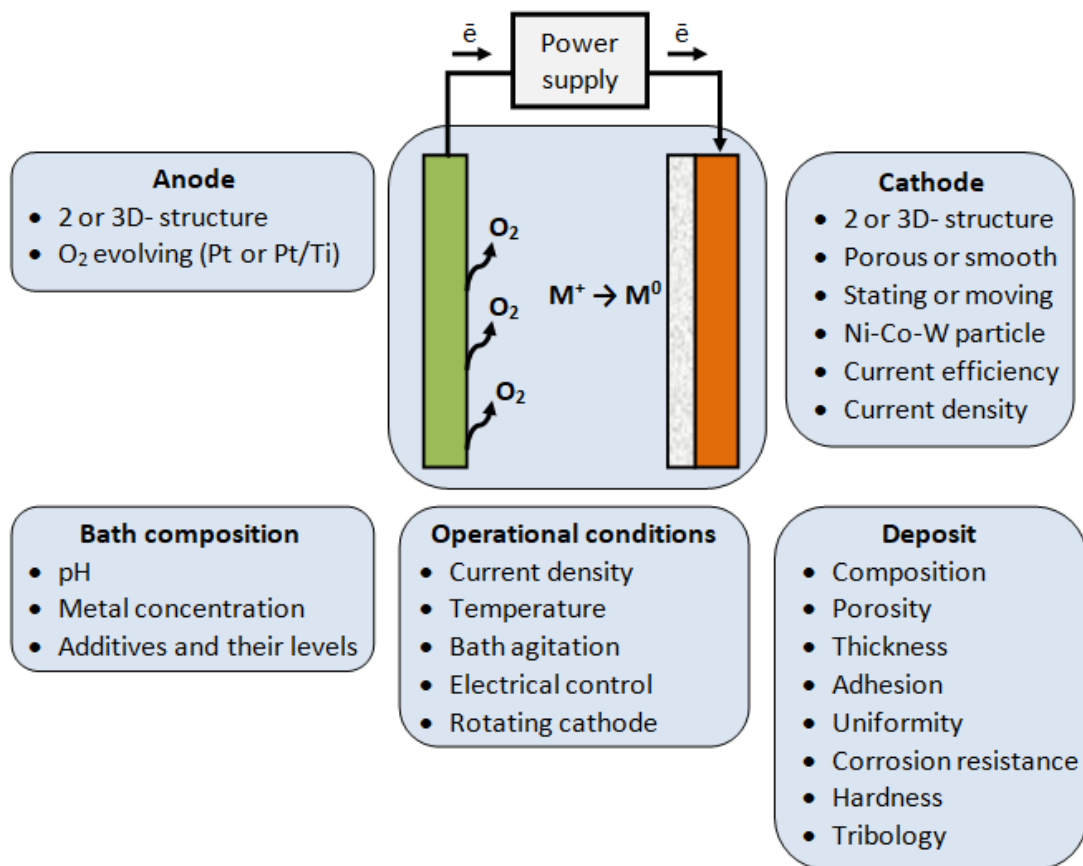
Figure 1. Representation of the parameters studied in the electrodeposition process of Ni-Co-W alloys. Adapted [12] Copyright 2019, Surface & Coatings Technology

In this sense, this chapter approaches with the Ni-Co-W ternary alloy development techniques and studies addressing each metal isolated and together with another metal, highlighting the tendencies of the use of these materials and the influence that the electrodeposition parameters have on the characteristics of the final material.

2. Metallic alloys

The electrodeposition of coatings allows the synthesis of materials for various applications, such as computer industry, anti-corrosion materials, heat conduction, anti-erosion coatings, fuel cells, anti-wear and magnetic materials, connectors and electrocatalysts [12]. In the coating of metallic parts, the electrodeposition is quite accepted and relatively simple, which produces coatings with nanocrystalline or amorphous structures. There are cases which the

alloy structure can be modified by the operating parameters such as the change in current density, which produced different crystal structures, as shown in Figure 2.
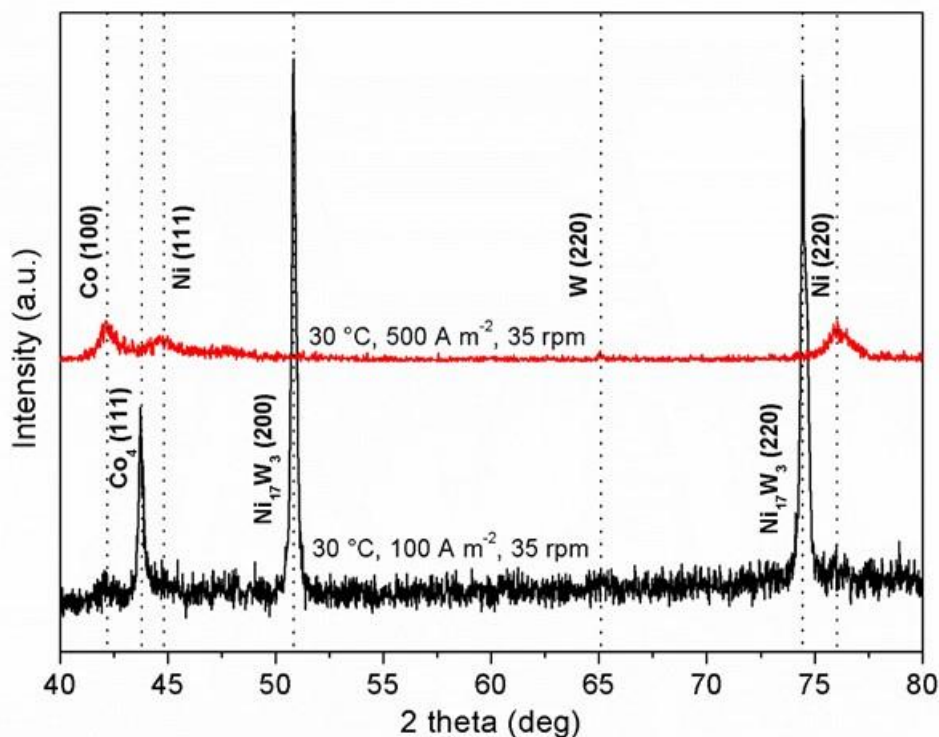
Figure 2. X-ray diffraction patterns of the Ni-Co-W alloys under different electrodeposition conditions.

At 100 A m^{-2} the Ni$_{17}$W$_3$ with crystallographic planes (200), 50.88°; (220) 74.82° (JCPDS n° 65-4228); and Co$_4$ (111) 43.90° (JCPDS n° 01-2927) indicated a cubic crystalline system for both elements. For the same temperature of 30 °C, 15 rpm and 500 A m^{-2} were obtained crystalline structures of Co (100), 41.68° (JCPDS n° 05-0727); Ni (111), 44.60° (JCPDS n° 03-1043); and W (220), 64.91° (JCPDS n° 88-2339) indicating hexagonal crystalline system for cobalt and cubic for nickel and tungsten.

2.1. Nickel alloys

Nickel is one of the most commonly used metals in the galvanizing process and can be introduced into various metal alloys. Binary or ternary alloys are commonly found with combinations of nickel, iron, zinc, cobalt, copper, and aluminum. Ni coatings with other metals

promote modifications in the crystalline structure of Ni. The nickel binary alloy containing iron is commonly studied since it can the junction of these metals promote the formation of a cubic crystalline structure with a centered body, which attributes hardness to the material. However, the combinations between metals must be evaluated, since, during the formation of coatings with two or more metals, the interaction of the particles does not occur in the same way as if there were only one metal. For example, the Fe-Ni alloy provides improvements in the characteristics of the material, however, in the electrodeposition process, microcracks can arise due to internal stress during the formation of the crystalline lattice [13, 14].

One of the main applications of nickel in industry and the urban environment is in anti-corrosive materials. The corrosive process in metals, especially in more aggressive environments, can be controlled with nickel-enriched sacrificial alloys, replacing toxic alloys composed of chromium and cadmium. In Ni alloys used to retard corrosion, the weight percent of that metal is between 10 and 15%. This amount of nickel allows the formation of a more evident γ phase in the morphology, which consequently makes the coating more regular and hard [15].

Ni-Fe and Ni-Zn binary alloys are preferably used to improve the corrosion resistance of metals such as steel, which is one of the metals most consumed. Other combinations, such as the Ni-Co-Fe ternary alloy, impart ferromagnetic properties to the material; however, in ternary alloys, strict control is required during electrodeposition, since these are more susceptible to cause changes in the material due to phenomena such as anomalous co-deposition [16].

2.2. Tungsten alloys

Tungsten has the characteristic of being co-deposited only with other metals, that is, it is not deposited alone, and this characteristic is known as induced co-deposition, as shown in the diagram of Figure 3. The process of co-deposition occurs because a metal, generally, of the ferrous group begins to undergo reduction and forms a layer that catalyzes the tungsten allowing its deposition. As a consequence of the induced co-deposition process, the tungsten alloys are not able to reach 100% of the faradaic efficiency, because during the electrodeposition of this metal, even with low currents, the hydrogen evolution and the increase of the tungsten percentage in the alloy form oxide plates [17]. During the electrodeposition the

hydrogen can be adsorbed on the inductive metal layer, requiring a greater transfer of the payload and decreasing the faradaic efficiency [18].
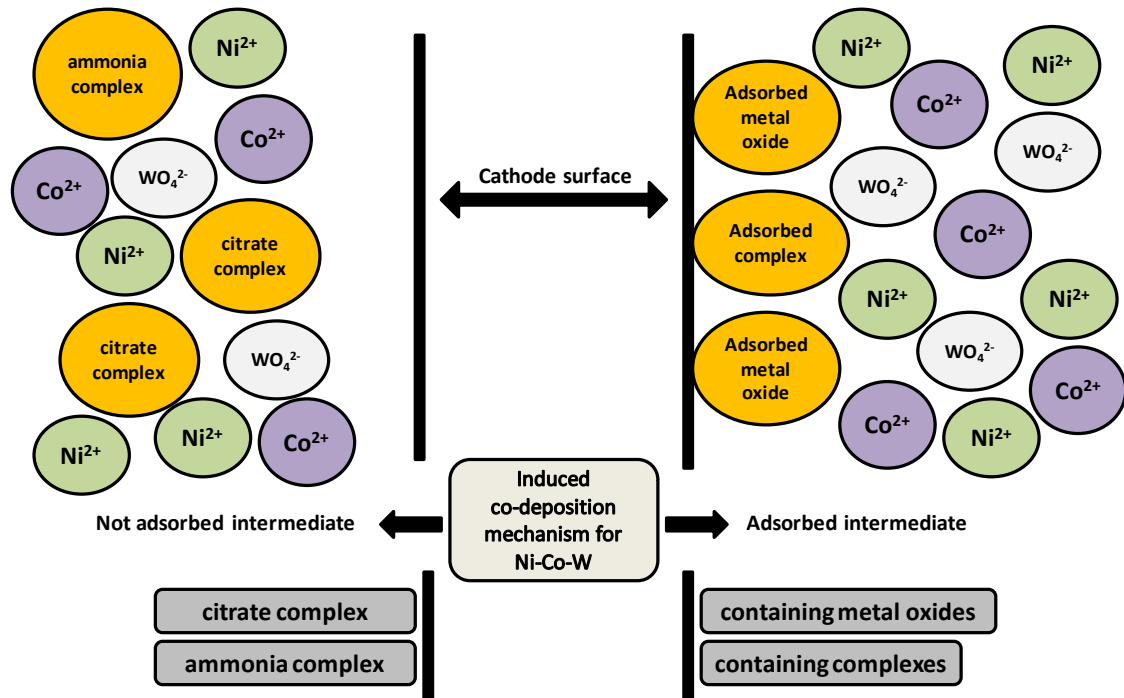
Figure 3. Proposal for an electrodeposition mechanism of Ni-Co-W alloy. Adapted [19] Copyright 2016, Surface & Coatings Technology

Despite the specificities to occur the electrodeposition of tungsten, this metal can be easily deposited and attribute improvements to the characteristics of the coating. Studies indicate that materials containing a certain amount of tungsten have amorphous properties, producing a material with thermodynamically stable intermetallic components [17]. An amorphous structure can be active incorporating tungsten into the crystalline layer of metals such as iron, nickel, and cobalt. Tungsten atoms can increase the main internal distance of the atoms and changes crystals arrangement. The crystallinity of the coating directly interferes with the abrasion resistance and corrosion protection. Corrosion resistance can be improved in alloys with percentages tungsten about 18%, with structure is partially amorphous. Due to certain concentrations of the induced metal, large deformations of the intermetallic structure can be caused, being able to form partially amorphous structures with percentages between 10 and 20% of tungsten, and amorphous structures with percentages above 20% [20].

Depending on the internal structure of the tungsten alloys, the coating has similar mechanical and tribological properties to the chromium-containing materials, and tungsten has the advantage of being non-toxic and does not harm the environment. These characteristics of the metal are also added to the corrosion resistance, temperature resistance and magnetism of the alloy, which allows the use of tungsten alloys in electronic equipment. Other uses for these alloys are the electrocatalysis of hydrogen, deposition in the reentrance of microstructures and electrodeposition of alloys in nanotubes, foams, and gas diffusion layers for application as electrocatalysts in oxygen reduction/evolution reactions [21, 22].

The parameters of the electrodeposition (rotation, current density, temperature) of metals interfere in the formation of the material, for example, tungsten alloy with cobalt deposited at a low current value tends to be magnetic. Nevertheless, it is not only the tungsten that modifies the coating properties, but the association between this metal and the parameters used is also another important factor.

2.3. Cobalt alloys

The use of cobalt is common in superalloys applied in gas turbines and aerospace vehicles. Cobalt superalloys were originally used to withstand internal stress arising from temperature. With the development of new materials and the need to replace toxic metals, other properties of cobalt were explored, some of them were the resistance of the metal to oxidation and corrosion. Ni coatings containing W and P, and Co-W have become potential substitutes for hard chromium, while cobalt-rich alloys have stood out due to low coefficients of friction and good properties related to wear. Sliding wear tests on the Co-W alloy, presented better results in wear rate for high loads, with a lower coefficient of friction, compared to chromium [23]. These tribological properties of the alloy containing cobalt are associated with its compact hexagonal structure and the resistance of adhesive interactions with the counterface of the coating.

Cobalt coatings can be obtained by applying alternative methods to electrodeposition, however, this makes the process of formation of hexagonal structures more unpredictable. With the use of electrodeposition to apply thin layers of cobalt, there is a control of the magnetic properties of the coating, creating ideal materials to be applied in electronic equipment. Current applications in electrocatalysis suggest cobalt as one of the elements

responsible to the catalysis in the oxygen evolution/reduction reaction in metal-air cells [24-28].

Cobalt magnetic films with low coercivity, which applications are ideal for motors and generators were prepared from an electrolytic bath. The authors proved the direct relationship between magnetic morphology, structure, and property, with control of the electrodeposition parameters [29]. Saturation magnetization and coercivity are dependent on the amount of cobalt in the film and the electrodeposition temperature [30].

In the electrodeposition of cobalt and its alloys, nanocrystalline materials can be obtained with grains smaller than 100 nm, and as the grains decrease there is a tendency to increase hardness. Polycrystalline (4.8 μm) and nanocrystalline (12 nm) cobalt coatings were studied [31]. In the stress of the nanocrystalline coating due to deformation was made difficult, due to the need for greater energy to promote grain slip. Tensile and elasticity tests on nanocrystalline coatings were better, suggesting that the plastic deformation properties of the material may be altered.

Cobalt is preferably deposited with lower currents and in some situations its co-deposition is anomalous. Generally, the anomalous co-deposition aim to be avoided, because it occurs when the less noblest metal is dominate. In these case, the concentrations of metals obtained in the deposit have non-linear proportions, and inverse to the concentrations of the metals added in the bath [30].

3. Ni-Co-W alloys

The control of the coating characteristics towards electrodeposition parameters is still established trough experimental process. The effects of several parameters on the passive behavior of alloys have been studied to better understand the phenomena attributed to the characteristics of the alloy [13, 14, 17].

Results published on Ni-Co [12, 32] and Ni-W [19, 33] alloys indicated an improvement of properties of Ni coating, by adding Co or W. Ni-Co-W alloys demonstrated a substantial reduction of microcracks on their nodular surface when compared to Co-W alloys [34]. Studies indicate the application of Ni-Co alloys in parts requiring ductility, wear-resistance, and electrocatalytic activity, whereas Ni-W alloys present amorphous microstructure, excellent corrosion resistance, hardness and magnetic properties [35-37]. Thus,

it is important to consider that the combination of these metals may promote specific properties in the material.

When there is a soluble anode, the metal ions are generated according to Equations 1 and 2:

$$Ni + 2\bar{e} \rightarrow Ni^{2+} \tag{1}$$

$$Co + 2\bar{e} \rightarrow Co^{2+} \tag{2}$$

When there is an insoluble anode, such as a platinum electrode, the oxygen is evolved:

$$2H_2O + 4\bar{e} \rightarrow O_2 + 4H^+ \tag{3}$$

In the cathode, the main reaction is the electrodeposition of Ni and Co, according to Equations 1 and 2. In some cases when the target is a ternary alloy these are accompanied by deposition of another element such as phosphorus, boron or tungsten.

The hydrogen evolution occurs secondarily in the cathode surface:

$$2H^+ + 2\bar{e} \rightarrow H_2 \tag{4}$$

This reaction decreases pH and efficiency and can result in porous deposits if there is no surfactant in the bath composition. Other consequences of the hydrogen evolution are the cracks that are caused by hydrogen embrittlement due to stress among the ions [38]. High current efficiency means that the metal deposition reaction is dominant, which minimizes the electrochemical hydrogen source, preventing cracks to appears [39].

The variation of Ni and Co in the bath alters the coating of the metal alloy [40]. Studies used the fixed experimental conditions used were 5 A dm^{-2} and 20 rpm for 60 min at room temperature, as shown in Table 1, which shows the most recent studies of ternary / quaternary alloys containing Ni-Co in the composition. By varying the concentrations of Ni and Co, a direct relationship between higher faradaic efficiency in baths with a higher proportion of nickel was observed. During the study, it was concluded that in the higher Ni level of the

factorial design, Co and W were deposited with greater difficulty, however in the inverse situation, ie, for the lower proportion of nickel of the planning, there was a high deposition rate of tungsten and higher deposition of cobalt. For the authors, the crystallinity of the coating depended on the presence of boron and the Ni and Co concentration in the solution, which provided a greater deposition of Co and W with a disordered arrangement. Moreover, although amorphous alloys were more suitable for corrosion resistance, corrosion tests proved to be better in crystalline alloys with higher nickel concentration.

Table 1. Summary of Ni-Co-X deposits

Alloy	Source of the third/fourth element	Temperature (°C)	pH	Current density (A dm^{-2})	Reference
Ni-Co-W	Na_2WO_4	25	7.5 - 8.0	5 (DC)	[40]
Ni-Co-W	-	30 - 60	4.5	2.6 (DC)	[43]
Ni-Co-Fe	$FeSO_4 \cdot 7H_2O$	55	4	4 (DC)	[44]
Ni-Co-P	H_3PO_3 and/or NaH_2PO_2	80	2	6.25 (DC)	[45]
Ni-Co-Fe-P	$FeSO_4 \cdot 7H_2O$	65	1.8	2 (DC)	[46]
Ni-Co-Cr	$Cr_2(SO_4)_3$	30	6	0.25 (DC)	[47]
	$Cr_2(SO_4)_3 \cdot 6H_2O$	25	2.4, 2.8, and 3.2	6 (DC)	[48]
Ni-Co-Cu	$CuSO_4$	25	3.25	-0.58 V vs. SCE for Cu between -1.00 and -1.5 V vs. SCE for Ni-Co	[49]
Ni-Co-Cu	$CuSO_4 \cdot 5H_2O$	40	5	-1 to -5	[50]
Ni-Co-Al	-	Room	4	1.6 (DC)	[51]
Ni-Co-Mn	$MnSO_4 \cdot H_2O$	55	4.5	3 (DC)	[52]
Ni-Co-Sn	$SnSO_4$	50	5, 6, and 7	5 (DC)	[53]

(DC) - Direct current
SCE - Saturated Calomel Electrode

The current density applied and adsorption of active species can alter the morphology and features of Ni-Co, Ni-W and Ni-Co-W alloys [33]. The current density used by the authors in the assays was between 2.5 to 50 mA cm^{-2} with W concentrations varying from 11.3 to 4.2%, Co ranging from 28.2 to 11.9% and Ni ranging from 62.3 to 84.9%. The evolution of the corrosion resistance obtained in the linear potentiodynamic polarization provided the values of corrosion current 3, 4.5 and 4.5 μA cm^{-2}, values referring to the

increasing order of the current densities used. Observations regarding the electrochemically active species of the Ni-W and Ni-Co-W alloys demonstrated that during the electrodeposition the adsorption of complex ions containing tungsten plays an important function in the morphological formation of the coatings. It was concluded that under the same deposition conditions Ni-Co-W coating presented a high Co content in the deposit, compared to Ni-Co binary alloy, thus raising the hypothesis that tungsten acts as a catalyst. The authors reported that in Ni-Co-W alloys some characteristics such as the size of the nodules (6-10 nm), the orientation of the grains and the spherical morphological structure are not directly related to the variations of current density, because the elements Co and W have opposite and simultaneous effects.

The composition phases of the electrodeposited coatings, the microstructure, the nucleation and growth mechanisms of the grain were studied for Ni-Co-W alloy [37]. The electrodepositions were performed on a polished copper surface, from a solution of sulfuric acid with the addition of sodium tungstate and citrate, pH 6 - 7, temperature 20 - 30 °C and current density between 50 - 400 A m^{-2}. The studies were carried out based on the data obtained by scanning electron microscopy associated with an electron transmission microscope and X-ray diffraction. The amorphous alloys had a composition of $Co_{38}Ni_{36}W_{26}$ and $Ni_{50}Co_{25}W_{25}$.

In the composition phase of the ternary alloy, solid solutions are formed, in which the cobalt replaces the nickel, as much in the crystalline state as in the amorphous state. Tungsten has catalytic action on cobalt, facilitating the deposition of cobalt.

A heterogeneous phase, centered and hexagonal cubic, in the ternary alloy with tungsten concentrations between 12% and 14% and an amorphous homogeneous phase with tungsten concentrations above 20%, which tends to occur with the highest incidence of the hexagonal phase was obtained in Ni-Co-W coatings [37]. The ternary alloy presented a network of microstructures, which varied according to the percentage of elements in the coating. The crystalline structure was altered as the cobalt concentration was increased.

The relation of the operational parameters with the corrosion resistance and alloy co-deposition efficiency was discussed in the literature [32]. For this, some techniques were used, such as scanning electron microscopy, chemical analysis by X-ray dispersive energy, X-ray diffraction, linear potentiodynamic polarization, and electrochemical impedance spectroscopy. The pH was maintained at 8, the temperature ranged from 30 to 70 °C and the current density from 200 to 600 A m^{-2}. Corrosion tests were performed at 0.1 g mol^{-1} sodium

chloride at room temperature and linear potentiodynamic polarization and electrochemical impedance spectroscopy measure the tendency for corrosion in a three-electrode cell. Through statistical analysis of a complete factorial design, the authors obtained results for the Ni-Co-W alloy behavior varying temperature and current density. They observed that the current density variable had little influence on electrodeposition, however, the interaction of the applied current density with the solution temperature was significant in the process, evidencing a synergistic involvement. The deposited alloy presented good adherence and quality, certified by the outcomes of X-ray diffraction that presented an amorphous structure. The values optimized for the operational conditions in terms of deposition efficiency were a cathodic current density of 600 A m^{-2}, solution temperature of 30 °C, 8.0 pH and rotating cathode of 20 rpm, with 46% of deposition efficiency. The optimum coating in terms of corrosion resistance of the alloy had a deposition efficiency of 36% and was obtained with a current density of 600 A m^{-2}, the temperature of 70 °C, 8.0 pH and rotating cathode - 20 rpm. The average composition of the most corrosion-resistant alloy was 70% Ni, followed by 22% W, and Co at a lower proportion (8%). The corrosion potential and bias resistance for this corrosion efficiency were respectively -508 mV and 4.56×10^4 ohm.

The pH values between 2 and 9 could be correlated with their effects on electrodeposition [41]. In the baths, with higher acid concentration the reduction of the faradaic efficiency occurred and the tungsten concentration remained constant. Varying the percentage of each metal in the electrolyte can increase the tungsten concentrations in the alloy, however, the increase of tungsten in the bath allowed the evolution of hydrogen. The composition of the alloy also changed with variations in current density and temperature. The study of the current density was carried out with a density between 20 and 400 A m^{-2}. The deposits were bright and adherent with 150 A m^{-2}, and for values of current density above 150 A m^{-2} the deposited tungsten concentrations were higher. The temperature directly influenced the adhesion, composition and alloy efficiency. Alloys deposited at temperatures above 35 °C were more adherent, in addition to the decrease of the cobalt concentration and increase of the other compounds, there was an improvement in the faradaic efficiency.

The chemical composition and crystallite size can be altered according to the thickness of the Ni-W-Co (Al$_2$O$_3$) nanocomposite by the electrochemical technique of reverse pulse [42]. The authors verified that cathodic and zero current times altered the percentage of elements, impacting the thickness, while the anodic reverse current promoted the reduction of

the cracks in the coatings, removing the hydrogen from the cathode surface and taking away the residual stresses. Corrosion and wear properties were also affected by the parameters of the electrochemical procedure.

4. Operational parameters in the electrodeposition of alloys

Crystalline structure control, morphology, and composition of metal coatings is important to maintain quality in the production of the alloys. Among the several studies, some affirm that solution composition, temperature, and current density indirectly influence the structure of the alloy [54]. Other studies indicate that the change of parameters, such as current density, causes direct changes in grain nucleation [55]. Therefore, operational parameters of electrodeposition are still widely studied, to understand the changes generated in the material, whether due to the variation of an isolated parameter or their association.

4.1. Temperature

The temperature interferes in the diffusion and migration of the metal ions. The increase in temperature accelerates the availability of ions on the cathode since the movement of ions at the interface of the cathode is a function of temperature. Thus, there is an increase in the kinetic energy of the particles, which reduces the cathodic overpotential and the electric field. In experiments with nickel, the increase in temperature led to an increase in the Ni content in the coating.

Figure 4-a shows micrographs of Ni-Co-W alloy deposited on the copper substrate under temperature conditions at 60 °C, a current density of 500 A m^{-2}, and rotating cathode 10 rpm with the presence of chips and cracks. Figure 4-b occurred at 80 °C, showing similarity in morphology, however, the faradaic efficiency increased from 53.35 to 68.46% as the bath temperature was increased by 20 °C. Figure 4-c shows the Energy-Dispersive X-Ray (EDX) mapping to the ternary alloy at 60 °C and figure 4-d at 80 °C, which composition of the three metals were Ni - 72.68, Co - 9.47, and W-17.85% for temperature at 60 °C and Ni - 74.02, Co - 5.57, and W - 20.41% for temperature at 80 °C, agreeing with the literature that the percentage of nickel is favored with temperature increase.
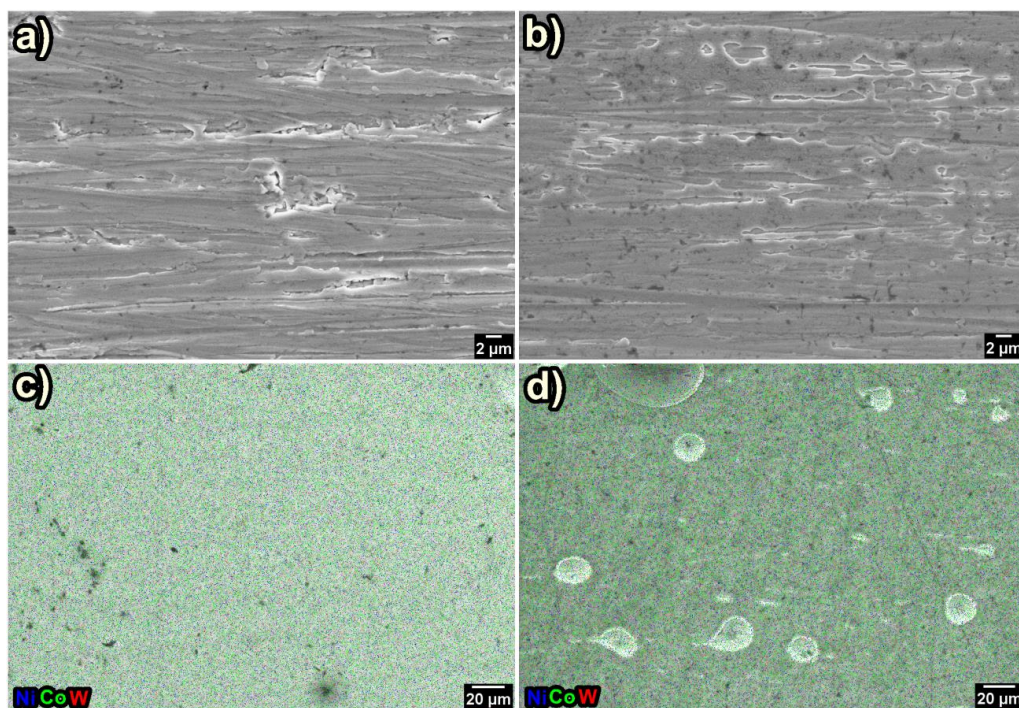
Figure 4. a) Ni-Co-W alloy electrodeposited at 60 °C, 50 mA cm^{-2}, and 10 rpm; b) Ni-Co-W alloy electrodeposited at 80 °C, 50 mA cm^{-2}, and 10 rpm; c) EDX mapping of the Ni-Co-W at 80 °C; d) EDX mapping of the Ni-Co-W at 80 °C.

In addition to the coating composition, the temperature can alter the crystal structure of the film. During the electrodeposition, the increase in the temperature of the solution leaves the coating more crystalline and increases the growth of the grains. The structure tends to be more crystalline, since the temperature promotes the incorporation of more atoms of metal in the layer of the host metal, distorting the diffraction peaks, commonly seen in X-Ray diffraction patterns [30].

High temperatures positively influence the cathodic efficiency of the deposition process of the metal phase, although it is not the most significant parameter to alter the cathodic efficiency [34]. Some metals are favored by the intense mobility of the ions, in tungsten co-depositions, the increase in temperature favors the concentration of reducible species present in the diffusion layer, which reduces the viscosity of the electrolyte, increases the formation of the film and makes the co-deposition of the atoms easier and more solid [18]. On the other hand, some metals are harmed by the rise in temperature, as with cobalt. In the experiments conducted at 48 °C demonstrated the decrease of the adsorption of complexed cobalt species on the cathodic surface [32].

Performing electrodeposition without heating the electrolyte, or with little heating can help to obtain some expected results since it allows greater control of the hydrogen evolution (release of H_2 bubbles). High temperatures increase the hydrogen evolution, being able to surpass the deposition rate and to decrease the faradaic efficiency in the electrodepositions in which the cobalt is present in a great amount [56]. Jeffrey et al. (2000) studied the temperature effect on the electrowinning process efficiency and observed that hydrogen evolution reactions increasing in electrodeposition process as cobalt concentrations and temperatures increases [56]. Inhibition of some molecules may also occur due to the elevation in temperature, and surface energy of crystallines. During electrodeposition at high temperatures, the grains become coarser, due to the decrease of the generation of new nuclei and acceleration of the development of the nucleus of existing grains.

4.2. Rotating cathode

Rotating cathode ensures homogenization of the electrolyte and current density at the cathode surface. The particles transfer step from the dispersed metal in the electrolyte to the cathode surface differs according to the variables used in the electrodeposition. Among the variables can be cited the effects of rotation under a perspective of kinetics, hydrodynamics, and control of mass transport during electrodeposition. A study indicates the increase of metal particles in the deposit due to the increase of the agitation, however, the excessive agitation can also damage the deposition of the particles, caused by the hydrodynamic forces in the solution that give off micro particles already deposited [57].

The vigorous agitation of an electrolyte which has in its composition a surfactant facilitates the release of bubble and can control the hydrogen pites [58]. The intense stirring of the fluid generates a turbulent flow with a high Reynolds (*Re*) number, which can interfere with the potential difference measurements in a galvanostatic electrodeposition system. However, for rotations less than or equal to 11 rpm, the *Re* number is below 50 and the mass transfer occurs mainly through natural convection [59]. The rotation used during electrodeposition has a participation in the deposition rate and can be calculated considering a diffusivity coefficient (D_{AB}), the Reynolds number (*Re*), which describes the flow of the fluid, and the number of Schmidt (*Sc*), which describes the transport properties of the electrolyte.

One of the complexities of analyzing ionic mass transfer in the electrodeposition of alloys is due to the formation of intermediate complexes, reduced in parallel and simultaneous stages during adsorption, which increases the resistance to mass transfer [59]. Besides, this parameter should not be studied singly, since it will be at least related to current density. Therefore, the study of mass transfer is necessary, since just as the effects of the rotation variation can change the rate of deposition, there can also be changed in the characteristics of the alloy.

4.3. Current density

Applied current can directly affect morphology and consequently alloy structure. The application of the current density in the electrodeposition can be carried out potentiostatically, where the potential is kept constant in the system, or galvanostatically, in which current is applied in the system. The galvanostatic form is the most used for the deposition of alloys, which the current can be applied using techniques of direct current, pulsed current or reverse pulsed current, being the first technique the most industrially employed. The choice of technique and how it is applied may affect the deposited final mass and grain size, being a relevant tool to control the crystallinity of the material. Depending on the value of current density and the technique used, the size of the deposited grains can be gradually reduced or increased. The outcome of current density on the grain size occurs, because at a high cathodic overpotential the nucleation process is accelerated and the grains are refined, this electrocrystallisation theory has already been observed in several studies [58, 60, 61]. The hydrogen evolution may also increase the size of Ni grains and the tensile strength of the coating [14].

The function of current in the deposition of metal atoms has significant interferences caused by variables such as metal concentrations, pH and temperature. The set of parameters that will promote the catalysis of this metal needs to be considered. For deposition of tungsten, for example, the electrodeposition needs to be under high currents and the solution pH is close to 8 for the generation of the tungstate complexes.

The impact of current density, in the range of 50 - 1000 A m^{-2}, on the morphology and magnetic features of the $(Co_{100-x}Ni_x)_{100-y}W_y$ electrodeposited alloys were evaluated from a glycine - containing solution [62]. The W content decreases with increasing current density

magnitude. The current density variation allowed the formation of two-phase structural transitions: the hexagonal close-packed that occurred at a current density of 200 A m^{-2} and cubic crystalline phase at 500 A m^{-2}. The observed Co face-centered cubic phase depended on the adsorption / incorporation and the effect of grain size reduction. The relation between current density and crystallinity was observed by Sakita et al. (2013), which proved that an amorphous state occurs for values higher than 500 A m^{-2} [62].

As in the other parameters, the hydrogen evolution affects the deposition of metals, mainly with the use of high currents. The incorporation of hydrogen in the deposit causes changes in the surface energy, in the mechanisms of growth and the distribution of the applied current [14, 60, 63].

4.4 Bath composition and pH

The initial concentration of metal add into the bath is an important parameter and can interfere directly on morphology [40]. However, the final proportion of the metal which composes the alloy also have an intrinsic dependence with the cathodic overpotential during electrodeposition. Qiao et al. (2013) observed a constancy in the alloy composition when the cathodic potential was fixed during electrodeposition [64]. Together with the salt source of a metal that composes the bath can add other reagents to improve electrodeposition efficiency. Their addition is with the purpose of complexation, bath stabilization, the formation of amorphous structures in the alloy and surfactants to reduce hydrogen bubbles during deposition [32, 65]. Lupi, Dell'Era, and Pasquali (2017) analyzed the electrodeposition with and without sodium citrate, a complexing agent [43]. The use of a complexing agent promoted high efficiency and specific energy consumption. Using citrate in solution the tungsten contents increased with temperature, however, without citrate W remain quite constant.

The pH adjustment is necessary to obtain better current efficiency and avoid anomalous electrodeposition due to the chemical species correlation with the potential [66]. In Ni-Co-W alloys, ammonium hydroxide is used for pH adjustment due to its complexing action [32]. Baths such as Watts type, have low pH and high nickel concentration. Authors who tested different alloys using acid baths showed good results for the deposits [33, 66-68].

5. Conclusions and Future Perspectives

Researchers have spared no effort to develop new materials capable of replacing coatings that use toxic metals that harm human health and the environment. Ni-Co electroplated alloys have been widely applied in magnetic devices such as sensors and inductors. Ni-W alloys demonstrate high hardness and corrosion resistance. The introduction of W in Ni-Co coatings favors durability, increases hardness and resistance to high temperatures.

It was discussed the tendencies of Ni-Co-W ternary alloy applications including electrodeposition conditions, parameters affecting various properties (magnetic, mechanical and thermal stability) and nanocrystalline morphology. The topics implicit in this chapter are some among a huge list of study objects potentially innovative for future research. We hope that this chapter will motivate the research in the field of metallic alloys, in particular in the influence of the electrodeposition parameters, since the literature is still deficient of recent studies.

References

[1] Anicai, L., Ni-W alloys coatings as ecological alternative for chromium plating - Evalution of corrosion behaviour, *Corros. Rev.*, 25, 607, 2007.

[2] Kirihara, S., Umeda, Y., Tashiro, K., Honma, H., Takai, O., Development of Ni-W alloy plating as a substitution of hard chromium plating, *Trans. Mater. Res. Soc. Jpn*, 41, 35, 2016.

[3] Wasekar, N.P., Sundararajan, G., Sliding wear behavior of electrodeposited Ni–W alloy and hard chrome coatings, *Wear*, 342-343, 340, 2015.

[4] Hillier, E.M.K., Robinson, M.J., Permeation measurements to study hydrogen uptake by steel electroplated with zinc–cobalt alloys, *Corros. Sci.*, 48, 1019, 2006.

[5] Savale, P., Comparative Study of Various Chemical Deposition Methods for Synthesis of Thin Films: A Review, *Asian J. Res. Chem.*, 11, 195, 2018.

[6] Karpuz, A., Kockar, H., Alper, M., Effect of film thickness on properties of electrodeposited Ni–Co films, *Appl. Surf. Sci.*, 258, 5046, 2012.

[7] Rafailović, L.D., Karnthaler, H.P., Trišović, T., Minić, D.M., Microstructure and mechanical properties of disperse Ni–Co alloys electrodeposited on Cu substrates, *Mater. Chem. Phys.*, 120, 409, 2010.

[8] Vijayakumar, J., Mohan, S., Yadav, S.S., Effects of primary dicarboxylic acids on microstructure and mechanical properties of sub-microcrystalline Ni–Co alloys, *J. Alloys Compd.*, 509, 9692, 2011.

[9] Lokhande, A.C., Bagi, J.S., Studies on enhancement of surface mechanical properties of electrodeposited Ni–Co alloy coatings due to saccharin additive, *Surf. Coat. Tech.*, 258, 225, 2014.

[10] Khazi, I., Mescheder, U., Micromechanical properties of anomalously electrodeposited nanocrystalline Nickel-Cobalt alloys: a review, *Mater. Res. Express*, 6, 082001, 2019.

[11] Messier, R., Electrodeposition - The materials science of coatings and substrates. By Jack W. Dini, *Adv. Mater.*, 6, 88, 1994.

[12] Karimzadeh, A., Aliofkhazraei, M., Walsh, F.C., A review of electrodeposited Ni-Co alloy and composite coatings: Microstructure, properties and applications, *Surf. Coat. Tech.*, 372, 463, 2019.

[13] Li, H., Ebrahimi, F., Synthesis and characterization of electrodeposited nanocrystalline nickel–iron alloys, *Mater. Sci. Eng.: A*, 347, 93, 2003.

[14] Ebrahimi, F., Ahmed, Z., The effect of current density on properties of electrodeposited nanocrystalline nickel, *J. Appl. Electrochem.*, 33, 733, 2003.

[15] Gavrila, M., Millet, J.P., Mazille, H., Marchandise, D., Cuntz, J.M., Corrosion behaviour of zinc–nickel coatings, electrodeposited on steel, *Surf. Coat. Tech.*, 123, 164, 2000.

[16] Hanafi, I., Daud, A.R., Radiman, S., Potentiostatic Electrodeposition of Co-Ni-Fe Alloy Particles Thin Film in a Sulfate Medium, *Port. Electrochim. Acta*, 35, 1, 2017.

[17] Donten, M., Bulk and surface composition, amorphous structure, and thermocrystallization of electrodeposited alloys of tungsten with iron, nickel, and cobalt, *J. Solid State Electrochem.*, 3, 87, 1999.

[18] Ibrahim, M.A.M., El Rehim, S.S.A., Moussa, S.O., Electrodeposition of noncrystalline cobalt–tungsten alloys from citrate electrolytes, *J. Appl. Electrochem.*, 33, 627, 2003.

[19] Allahyarzadeh, M.H., Aliofkhazraei, M., Rezvanian, A.R., Torabinejad, V., Sabour Rouhaghdam, A.R., Ni-W electrodeposited coatings: Characterization, properties and applications, *Surf. Coat. Tech.*, 307, 978, 2016.

[20] Królikowski, A., Płońska, E., Ostrowski, A., Donten, M., Stojek, Z., Effects of compositional and structural features on corrosion behavior of nickel–tungsten alloys, *J. Solid State Electrochem.*, 13, 263, 2009.

[21] Tsyntsaru, N., Cesiulis, H., Donten, M., Sort, J., Pellicer, E., Podlaha-Murphy, E.J., Modern trends in tungsten alloys electrodeposition with iron group metals, *Surf. Eng. Appl. Electrochem.*, 48, 491, 2012.

[22] Costa, J.M., de Morais Nepel, T.C., de Almeida Neto, A.F., Influence of current density and W concentration on Co–W alloys used as catalysts in electrodes for Li–O$_2$ batteries, *Chem. Pap.*, 73, 1103, 2019.

[23] Weston, D.P., Shipway, P.H., Harris, S.J., Cheng, M.K., Friction and sliding wear behaviour of electrodeposited cobalt and cobalt–tungsten alloy coatings for replacement of electrodeposited chromium, *Wear*, 267, 934, 2009.

[24] Cho, Y.-B., Moon, S., Lee, C., Lee, Y., One-pot electrodeposition of cobalt flower-decorated silver nanotrees for oxygen reduction reaction, *Appl. Surf. Sci.*, 394, 267, 2017.

[25] Costa, J.M., de Almeida Neto, A.F., Ag–Co Electrocatalysts for Rechargeable Lithium–O$_2$ Batteries: O$_2$ Pressure and Current Density Effects, *Electrocatalysis*, 10, 532, 2019.

[26] Xiong, M., Ivey, D.G., Composition effects of electrodeposited Co-Fe as electrocatalysts for the oxygen evolution reaction, *Electrochim. Acta*, 260, 872, 2018.

[27] Costa, J.M., de Almeida Neto, A.F., Zn-Co electrocatalysts in lithium-O$_2$ batteries: temperature and rotating cathode effects on the electrodeposition, *J. Solid State Electrochem.*, 23, 2533, 2019.

[28] Zhong, B., Zhang, L., Yu, J., Fan, K., Ultrafine iron-cobalt nanoparticles embedded in nitrogen-doped porous carbon matrix for oxygen reduction reaction and zinc-air batteries, *J. Colloid Interf. Sci.*, 546, 113, 2019.

[29] Gómez, E., Vallés, E., Thick cobalt coatings obtained by electrodeposition, *J. Appl. Electrochem.*, 32, 693, 2002.

[30] Tian, L., Xu, J., Qiang, C., The electrodeposition behaviors and magnetic properties of Ni–Co films, *Appl. Surf. Sci.*, 257, 4689, 2011.

[31] Karimpoor, A.A., Erb, U., Aust, K.T., Palumbo, G., High strength nanocrystalline cobalt with high tensile ductility, *Scripta Mater.*, 49, 651, 2003.

[32] Santana, R.A.C., Campos, A.R.N., Medeiros, E.A., Oliveira, A.L.M., Silva, L.M.F., Prasad, S., Studies on electrodeposition and corrosion behaviour of a Ni–W–Co amorphous alloy, *J. Mater. Sci.*, 42, 9137, 2007.

[33] Farzaneh, M.A., Zamanzad-Ghavidel, M.R., Raeissi, K., Golozar, M.A., Saatchi, A., Kabi, S., Effects of Co and W alloying elements on the electrodeposition aspects and properties of nanocrystalline Ni alloy coatings, *Appl. Surf. Sci.*, 257, 5919, 2011.

[34] Vernickaite, E., Tsyntsaru, N., Cesiulis, H., Electrochemical co-deposition of tungsten with cobalt and copper: Peculiarities of binary and ternary alloys coatings formation, *Surf. Coat. Tech.*, 307, 1341, 2016.

[35] Mizushima, I., Tang, P.T., Hansen, H.N., Somers, M.A.J., Residual stress in Ni–W electrodeposits, *Electrochim. Acta*, 51, 6128, 2006.

[36] Wang, L., Gao, Y., Xu, T., Xue, Q., A comparative study on the tribological behavior of nanocrystalline nickel and cobalt coatings correlated with grain size and phase structure, *Mater. Chem. Phys*, 99, 96, 2006.

[37] Grabchikov, S.S., Potuzhnaya, O.I., Sosnovskaya, L.B., Sheleg, M.U., Microstructure of amorphous electrodeposited Co-Ni-W films, *Russ Metall (Metally)*, 2009, 164, 2009.

[38] Eliaz, N., Sridhar, T.M., Gileadi, E., Synthesis and characterization of nickel tungsten alloys by electrodeposition, *Electrochim. Acta*, 50, 2893, 2005.

[39] Gabe, D.R., The role of hydrogen in metal electrodeposition processes, *J. Appl. Electrochem.*, 27, 908, 1997.

[40] Baldessin, C.F., de Morais Nepel, T.C., de Almeida Neto, A.F., The influence of Ni and Co concentration in the electroplating bath on Ni-Co-W alloys properties, *Can. J. Chem. Eng.*, 96, 1284, 2018.

[41] Singh, V.B., Singh, L.C., Tikoo, P.K., Studies on Electrodeposition of Nickel-Cobalt-Tungsten Alloys, *J. Electrochem. Soc.*, 127, 590, 1980.

[42] Allahyarzadeh, M.H., Aliofkhazraei, M., Rouhaghdam, A.R.S., Torabinejad, V., Electrochemical tailoring of ternary Ni-W-Co(Al2O3) nanocomposite using pulse reverse technique, *J. Alloys Compd*, 705, 788, 2017.

[43] Lupi, C., Dell'Era, A., Pasquali, M., Effectiveness of sodium citrate on electrodeposition process of NiCoW alloys for hydrogen evolution reaction, *Int. J. Hydrogen Energ.*, 42, 28766, 2017.

[44] Kong, A.N.G., Gong, B.-K., Wang, G., Cui, H.-W., Influence of surface roughness of substrate on the properties of Ni-Co-Fe electrodeposition coating on copper, *Surf. Rev. Lett.*, 25, 1850120, 2017.

[45] Ignatova, K., Kozhukharov, S., Alakushev, M., Barrier ability and durability of NiCoP coatings in accordance to the content of H_3PO_3 and NaH_2PO_2 as phosphorus sources, *Mater. Chem. Phys.*, 219, 175, 2018.

[46] Ji, X., Yan, C., Duan, H., Luo, C., Effect of phosphorous content on the microstructure and erosion–corrosion resistance of electrodeposited Ni-Co-Fe-P coatings, *Surf. Coat. Tech.*, 302, 208, 2016.

[47] Meena, S.P., Ashokkumar, R., Ranjith Kumar, E., Effects of Cr Doping Concentration on Structural, Morphology, Mechanical and Magnetic Properties of Electrodeposited NiCoCr Thin Films, *J. Inorg. Organomet. Polym. Mater.*, 29, 1094, 2019.

[48] Yang, T., Peng, C.Z., Xiang, L., Cao, H., Fabrication and Corrosion Properties of Electroplated Ni-Co-Cr Alloy Coatings, *Appl. Mech. Mater.*, 456, 438, 2014.

[49] Zsurzsa, S., Pellicer, E., Sort, J., Péter, L., Bakonyi, I., Electron Microscopy Characterization of Electrodeposited Homogeneous and Multilayered Nanowires in the Ni-Co-Cu System, *J. Electrochem. Soc.*, 165, D536, 2018.

[50] Goranova, D., Lefterova, E., Rashkov, R., Electrocatalytic activity of Ni-Mo-Cu and Ni-Co-Cu alloys for hydrogen evolution reaction in alkaline medium, *Int. J. Hydrogen Energ.*, 42, 28777, 2017.

[51] Srivastava, M., Balaraju, J.N., Ravisankar, B., Anandan, C., William Grips, V.K., High temperature oxidation and corrosion behaviour of Ni/Ni–Co–Al composite coatings, *Appl. Surf. Sci.*, 263, 597, 2012.

[52] Xi, X., Zhang, R., Sun, F., Effect of phosphorus content on suspension of Ni-P coated diamond (NPCD) and wear resistance of electrodeposited Ni-Co-Mn/NPCD composite coatings, *Diam. Relat. Mater.*, 74, 164, 2017.

[53] Liu, Y., Lu, H., Kou, X., Electrodeposited Ni-Co-Sn alloy as a highly efficient electrocatalyst for water splitting, *Int. J. Hydrogen Energ.*, 44, 8099, 2019.

[54] Younes, O., Zhu, L., Rosenberg, Y., Shacham-Diamand, Y., Gileadi, E., Electroplating of Amorphous Thin Films of Tungsten/Nickel Alloys, *Langmuir*, 17, 8270, 2001.

[55] Ghaferi, Z., Sharafi, S., Bahrololoom, M.E., Effect of current density and bath composition on crystalline structure and magnetic properties of electrodeposited FeCoW alloy, *Appl. Surf. Sci.*, 355, 766, 2015.

[56] Jeffrey, M.I., Choo, W.L., Breuer, P.L., The effect of additives and impurities on the cobalt electrowinning process, *Miner. Eng.*, 13, 1231, 2000.

[57] Low, C.T.J., Wills, R.G.A., Walsh, F.C., Electrodeposition of composite coatings containing nanoparticles in a metal deposit, *Surf. Coat. Tech.*, 201, 371, 2006.

[58] Elias, L., Chitharanjan Hegde, A., Electrodeposition of laminar coatings of Ni–W alloy and their corrosion behaviour, *Surf. Coat. Tech.*, 283, 61, 2015.

[59] Belevskii, S.S., Cesiulis, H., Tsyntsaru, N.I., Dikusar, A.I., The role of mass transfer in the formation of the composition and structure of CoW coatings electrodeposited from citrate solutions, *Surf. Eng. Appl. Electrochem.*, 46, 570, 2010.

[60] Rashidi, A.M., Amadeh, A., The effect of current density on the grain size of electrodeposited nanocrystalline nickel coatings, *Surf. Coat. Tech.*, 202, 3772, 2008.

[61] Tsyntsaru, N., Electrodeposition of cobalt–tungsten alloys and their application for surface engineering, *Russ. J. Electrochem.*, 52, 1041, 2016.

[62] Sakita, A.M.P., Passamani, E.C., Kumar, H., Cornejo, D.R., Fugivara, C.S., Noce, R.D., Benedetti, A.V., Influence of current density on crystalline structure and magnetic properties of electrodeposited Co-rich CoNiW alloys, *Mater. Chem. Phys.*, 141, 576, 2013.

[63] Wasekar, N.P., Haridoss, P., Seshadri, S.K., Sundararajan, G., Influence of mode of electrodeposition, current density and saccharin on the microstructure and hardness of electrodeposited nanocrystalline nickel coatings, *Surf. Coat. Tech.*, 291, 130, 2016.

[64] Qiao, X., Li, H., Zhao, W., Li, D., Effects of deposition temperature on electrodeposition of zinc–nickel alloy coatings, *Electrochim. Acta*, 89, 771, 2013.

[65] Porto, M.B., Alvim, L.B., de Almeida Neto, A.F., Nickel removal from wastewater by induced co-deposition using tungsten to formation of metallic alloys, *J. Clean. Prod.*, 142, 3293, 2017.

[66] Robotin, B., Ispas, A., Coman, V., Bund, A., Ilea, P., Nickel recovery from electronic waste II Electrodeposition of Ni and Ni–Fe alloys from diluted sulfate solutions, *Waste Manage.*, 33, 2381, 2013.

[67] Seo, M.H., Kim, D.J., Kim, J.S., The effects of pH and temperature on Ni–Fe–P alloy electrodeposition from a sulfamate bath and the material properties of the deposits, *Thin Solid Films*, 489, 122, 2005.

[68] Bai, A., Hu, C.-C., Effects of electroplating variables on the composition and morphology of nickel–cobalt deposits plated through means of cyclic voltammetry, *Electrochim. Acta*, 47, 3447, 2002.

ATTACHMENTS

Copyright

Copyright Clearance Center — RightsLink®

Home | Help | Email Support | Josiel Costa ∨

SPRINGER NATURE

New Approaches for Renewable Energy Using Metal Electrocatalysts for Lithium-O2 and Zinc-Air Batteries

Author: Josiel Martins Costa, Ambrósio Florêncio de Almeida Neto
Publication: Springer eBook
Publisher: Springer Nature
Date: Jan 1, 2020

Copyright © 2020, Springer Nature Switzerland AG

Order Completed

Thank you for your order.

This Agreement between Mr. Josiel Costa ("You") and Springer Nature ("Springer Nature") consists of your license details and the terms and conditions provided by Springer Nature and Copyright Clearance Center.

Your confirmation email will contain your order number for future reference.

License Number	4847670930305	🖶 Printable Details
License date	Jun 14, 2020	

✅ Licensed Content

Licensed Content Publisher	Springer Nature
Licensed Content Publication	Springer eBook
Licensed Content Title	New Approaches for Renewable Energy Using Metal Electrocatalysts for Lithium-O2 and Zinc-Air Batteries
Licensed Content Author	Josiel Martins Costa, Ambrósio Florêncio de Almeida Neto
Licensed Content Date	Jan 1, 2020

📖 About Your Work

Title	Development of Co-W, Ag-Co, and Zn-Co electrocatalysts for oxygen reduction / evolution reactions in Zn-air and Li-O2 batteries
Institution name	University of Campinas
Expected presentation date	Feb 2021

📋 Order Details

Type of Use	Thesis/Dissertation
Requestor type	academic/university or research institute
Format	print and electronic
Portion	full article/chapter
Will you be translating?	no
Circulation/distribution	50000 or greater
Author of this Springer Nature content	yes

📁 Additional Data

📍 Requestor Location

Requestor Location	Mr. Josiel Costa Avenida Albert Einstein, 500 Campinas, São Paulo 13083852 Brazil Attn: Mr. Josiel Costa

🖥 Tax Details

$ Price

Total	0.00 USD

Total: 0.00 USD

CLOSE WINDOW | ORDER MORE

Copyright
Clearance
Center

RightsLink®

My Orders   My Library   My Profile   **Welcome** josiel.martins.costa@gmail.com   Log out | Help

My Orders > Orders > All Orders

License Details

This Agreement between Mr. Josiel Costa ("You") and Springer Nature ("Springer Nature") consists of your license details and the terms and conditions provided by Springer Nature and Copyright Clearance Center.

Print   Copy

License Number	4664511427730
License date	Sep 08, 2019
Licensed Content Publisher	Springer Nature
Licensed Content Publication	Chemical Papers
Licensed Content Title	Influence of current density and W concentration on Co–W alloys used as catalysts in electrodes for Li–O2 batteries
Licensed Content Author	Josiel Martins Costa, Thayane Carpanedo de Morais Nepel, Ambrósio Florêncio de Almeida Neto
Licensed Content Date	Jan 1, 2018
Licensed Content Volume	73
Licensed Content Issue	5
Type of Use	Thesis/Dissertation
Requestor type	academic/university or research institute
Format	print and electronic
Portion	full article/chapter
Will you be translating?	no
Circulation/distribution	50000 or greater
Author of this Springer Nature content	yes
Title	Development of Co-W, Ag-Co, and Zn-Co electrocatalysts for oxygen reduction / evolution reactions in Zn-Air and Li-O2 batteries
Institution name	University of Campinas
Expected presentation date	Feb 2021
Requestor Location	Mr. Josiel Costa Avenida Albert Einstein, 500 Campinas, São Paulo 13083852 Brazil Attn: Mr. Josiel Costa
Total	**0.00 USD**

BACK

Copyright Clearance Center · RightsLink®

My Orders   My Library   My Profile

My Orders > Orders > All Orders

License Details

This Agreement between Mr. Josiel Costa ("You") and Springer Nature ("Springer Nature") consists of your license details and the terms and conditions provided by Springer Nature and Copyright Clearance Center.

Print   Copy

License Number	4664521083325
License date	Sep 08, 2019
Licensed Content Publisher	Springer Nature
Licensed Content Publication	Electrocatalysis
Licensed Content Title	Ag–Co Electrocatalysts for Rechargeable Lithium–O2 Batteries: O2 Pressure and Current Density Effects
Licensed Content Author	Josiel Martins Costa, Ambrósio Florêncio de Almeida Neto
Licensed Content Date	Jan 1, 2019
Licensed Content Volume	10
Licensed Content Issue	5
Type of Use	Thesis/Dissertation
Requestor type	academic/university or research institute
Format	print and electronic
Portion	full article/chapter
Will you be translating?	no
Circulation/distribution	50000 or greater
Author of this Springer Nature content	yes
Title	Development of Co-W, Ag-Co, and Zn-Co electrocatalysts for oxygen reduction / evolution reactions in Zn-Air and Li-O2 batteries
Institution name	University of Campinas
Expected presentation date	Feb 2021
Requestor Location	Mr. Josiel Costa Avenida Albert Einstein, 500 Campinas, São Paulo 13083852 Brazil Attn: Mr. Josiel Costa
Total	**0.00 USD**

BACK

Copyright Clearance Center — RightsLink®

My Orders   My Library   My Profile   **Welcome** josiel.martins.costa@gmail.com   Log out | Help

My Orders > Orders > All Orders

License Details

This Agreement between Mr. Josiel Costa ("You") and Springer Nature ("Springer Nature") consists of your license details and the terms and conditions provided by Springer Nature and Copyright Clearance Center.

Print   Copy

License Number	4664520475646
License date	Sep 08, 2019
Licensed Content Publisher	Springer Nature
Licensed Content Publication	Journal of Solid State Elecrochemistry
Licensed Content Title	Zn-Co electrocatalysts in lithium-O2 batteries: temperature and rotating cathode effects on the electrodeposition
Licensed Content Author	Josiel Martins Costa, Ambrósio Florêncio de Almeida Neto
Licensed Content Date	Jan 1, 2019
Licensed Content Volume	23
Licensed Content Issue	8
Type of Use	Thesis/Dissertation
Requestor type	academic/university or research institute
Format	print and electronic
Portion	full article/chapter
Will you be translating?	no
Circulation/distribution	50000 or greater
Author of this Springer Nature content	yes
Title	Development of Co-W, Ag-Co, and Zn-Co electrocatalysts for oxygen reduction / evolution reactions in Zn-Air and Li-O2 batteries
Institution name	University of Campinas
Expected presentation date	Feb 2021
Order reference number	4664511427730
Requestor Location	Mr. Josiel Costa Avenida Albert Einstein, 500 Campinas, São Paulo 13083852 Brazil Attn: Mr. Josiel Costa
Total	**0.00 USD**

BACK

Copyright Clearance Center

RightsLink®

Home | Help | Email Support | Josiel Costa ∨
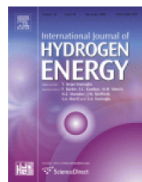
In-situ transformation of electrodeposited W–Co oxide to ZnCo2O4 nanoparticles as an effective bifunctional catalysts in Zn-air batteries

Author:
Josiel Martins Costa,Michael Patrick Clark,Ambrósio Florêncio de Almeida Neto,Douglas Gordon Ivey

Publication: International Journal of Hydrogen Energy

Publisher: Elsevier

Date: 11 June 2020

BACK   CLOSE WINDOW

RightsLink®

Home | Account Info | Help | LIVE CHAT
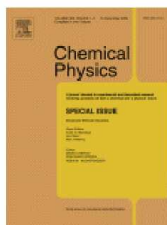
Title: Effects of the forced convection and current density on the electrodeposition of Zn-Fe-Mo alloys

Author: Josiel Martins Costa, Mariana Sayuri Hori, Ambrósio Florêncio de Almeida Neto

Publication: Chemical Physics

Publisher: Elsevier

Date: 1 November 2019

© 2019 Elsevier B.V. All rights reserved.

Logged in as:
Josiel Costa

LOGOUT

BACK | CLOSE WINDOW

Copyright Clearance Center

RightsLink®

Home | Help | Email Support | Josiel Costa ⌄

Effects of tungsten and cobalt concentration on microstructure and anticorrosive property of cobalt-tungsten alloys

Author:
Josiel Martins Costa,Mariana Borges Porto,Rodolfo José Amancio,Ambrósio Florêncio de Almeida Neto

Publication: Surfaces and Interfaces

Publisher: Elsevier

Date: September 2020

BACK   CLOSE WINDOW

Copyright Clearance Center

RightsLink®

Home | Help | Email Support | Josiel Costa ∨

Ultrasound-assisted electrodeposition and synthesis of alloys and composite materials: A review

Author: Josiel Martins Costa,Ambrósio Florêncio de Almeida Neto

Publication: Ultrasonics Sonochemistry

Publisher: Elsevier

Date: November 2020

© 2020 Elsevier B.V. All rights reserved.

BACK   CLOSE WINDOW

Copyright Clearance Center RightsLink®

My Orders > Orders > All Orders

License Details

This Agreement between Mr. Josiel Costa ("You") and Elsevier ("Elsevier") consists of your license details and the terms and conditions provided by Elsevier and Copyright Clearance Center.

Print   Copy

License Number	4965261068863
License date	Dec 10, 2020
Licensed Content Publisher	Elsevier
Licensed Content Publication	Synthetic Metals
Licensed Content Title	Nanocatalysts deposition assisted by supercritical carbon dioxide technology: A review
Licensed Content Author	Josiel Martins Costa, Ambrósio Florêncio de Almeida Neto
Licensed Content Date	Available online 13 November 2020
Licensed Content Volume	n/a
Licensed Content Issue	n/a
Licensed Content Pages	1
Type of Use	reuse in a thesis/dissertation
Portion	full article
Circulation	999999
Format	both print and electronic
Are you the author of this Elsevier article?	Yes
Will you be translating?	No
Title	Development of Co-W, Ag-Co, and Zn-Co electrocatalysts for oxygen reduction / evolution reactions in Zn-air and Li-O2 batteries
Institution name	University of Campinas
Expected presentation date	Feb 2021
Requestor Location	Mr. Josiel Costa Avenida Albert Einstein, 500 Campinas, São Paulo 13083852 Brazil Attn: Mr. Josiel Costa
Publisher Tax ID	GB 494 6272 12
Billing Type	Invoice
Billing address	Mr. Josiel Costa Avenida Albert Einstein, 500 Campinas, Brazil 13083852 Attn: Mr. Josiel Costa
Total	0.00 USD

BACK

Copyright Clearance Center — RightsLink®

? Help	Email Support	Josiel Costa ⌄

WILEY

Book: Ni-Co-W Alloys
Author:
Josiel Martins Costa, Daniella Gonçalves Portela, Ambrósio Florêncio Almeida Neto
Publisher: John Wiley and Sons
Date: May 11, 2020

Copyright © 2020, John Wiley and Sons

Order Completed

Thank you for your order.

This Agreement between Josiel Costa ("You") and John Wiley and Sons ("John Wiley and Sons") consists of your order details and the terms and conditions provided by John Wiley and Sons and Copyright Clearance Center.

License number	Reference confirmation email for license number
License date	May, 26 2020

🗹 Licensed Content

Licensed Content Publisher	John Wiley and Sons
Licensed Content Publication	Wiley Books
Licensed Content Title	Ni-Co-W Alloys
Licensed Content Author	Josiel Martins Costa, Daniella Gonçalves Portela, Ambrósio Florêncio Almeida Neto
Licensed Content Date	May 11, 2020
Licensed Content Pages	22

📋 Order Details

Type of use	Dissertation/Thesis
Requestor type	University/Academic
Format	Print and electronic
Portion	Text extract
Number of Pages	21
Will you be translating?	No

📄 About Your Work

Title	Development of Co-W, Ag-Co, and Zn-Co electrocatalysts for oxygen reduction / evolution reactions in Zn-Air and Li-O2 batteries
Institution name	University of Campinas
Expected presentation date	Feb 2021

📁 Additional Data

Portions	all the text

📍 Requestor Location

Requestor Location	Mr. Josiel Costa Avenida Albert Einstein, 500 Campinas, São Paulo 13083852 Brazil Attn: Mr. Josiel Costa

🖥 Tax Details

Publisher Tax ID	EU826007151

💳 Billing Information

Billing Type	Invoice
Billing address	Mr. Josiel Costa Avenida Albert Einstein, 500 Campinas, Brazil 13083852 Attn: Mr. Josiel Costa

$ Price

Total	0.00 USD

Total: 0.00 USD

CLOSE WINDOW